Techniques for Controlling Structural Vibrations

Shafic Sami Oueini

Dissertation submitted to the Faculty of the
Virginia Polytechnic Institute and State University
in partial fulfillment of the requirements for the degree of

Doctor of Philosophy
in
Engineering Mechanics

Ali H. Nayfeh, Chairman
Scott L. Hendricks
Daniel J. Inman
Werner E. Kohler
Dean T. Mook

April 19, 1999
Blacksburg, Virginia

Keywords: Active Control, Vibration Absorber, Nonlinear Dynamics,
Parametric Excitation, Saturation, Smart Structures, PZT, Terfenol-D

Techniques for Controlling Structural Vibrations

Shafic Sami Oueini

(ABSTRACT)

We tackle the problem of suppressing high-amplitude vibrations of cantilever beams when subjected to either primary external or principal parametric resonances. Guided by results of previous investigations into the nonlinear dynamics of single- and multi-degree-of-freedom structures, we design mechatronic systems of sensors, actuators, and electronic devices and implement nonlinear active feedback control.

In the case of external excitation, we devise two vibration absorbers based on either quadratic or cubic feedback. We conduct theoretical analyses and demonstrate that when a two-to-one (one-to-one) internal resonance condition is imposed between the plant and the quadratic (cubic) absorber, there exists a saturation phenomenon. When the plant is forced near its resonant frequency and the forcing amplitude exceeds a certain small threshold, the nonlinear coupling creates an energy-transfer mechanism that limits (saturates) the response of the plant.

Our theoretical studies reveal that the cubic absorber creates regimes of high-amplitude quasiperiodic and chaotic responses, thereby limiting its utility. However, we show that superior results can be achieved when the natural frequency of the quadratic absorber is set equal to one-half the excitation frequency. Consequently, we apply the quadratic technique through a variety of linear and nonlinear actuators, sensors, and electronic devices.

We design and build second-order analog circuits that emulate the quadratic absorber. Using a DC motor, piezoelectric ceramics, and Terfenol-D struts as actuators and potentiometers, strain gages, and accelerometers as sensors, we demonstrate successful single- and multi-mode vibration control.

In order to realize a more versatile implementation of the control strategy, we resort to a digital signal processing (DSP) board. We compose a code in C and design a digital absorber

by developing algorithms that, in addition to replacing the analog circuit, automatically detect the amplitude and frequency of oscillation of the plant and fine-tune the absorber parameters. We take advantage of the digital realization, implement a linear absorber, and compare the performance of the quadratic absorber with that of its linear counterpart.

In the case of parametric excitation, we investigate two techniques. First, we explore application of the quadratic absorber. We prove theoretically and demonstrate experimentally that this control scheme is not reliable. Then, we propose an alternate approach. We devise a control law based on cubic velocity feedback. We conduct theoretical and experimental investigations and show that the latter strategy leads to effective vibration suppression and bifurcation control.

In memory of my father

Sami Bachir Oueini

Acknowledgments

I feel very fortunate to have witnessed my academic career mature under the supervision of two exceptional men: Dr. Ali Nayfeh and Dr. Farid Golnaraghi. In their own way, they have shaped the course of my life.

My interest and respect for Dr. Nayfeh emerged upon reading through one of his textbooks seven years ago. It is the content of that same textbook that inspired the topic of this Dissertation. His insight and inquisitive mind have enriched my work and his intellect has augmented my knowledge. Truly, working under his auspices has been a privilege.

I am indebted to Dr. Farid Golnaraghi for introducing me to graduate school and the fascinating topic of nonlinear dynamics. His unique lifestyle, friendship, and encouragement are surely the reasons why I sought a higher education.

I thank Professors Scott Hendricks, Dan Inman, Werner Kohler, and Dean Mook for serving on my committee and reading my Dissertation. A word of appreciation goes to Mrs. Sally Shrader for her indispensable help and friendship.

The accomplishment of this work would not have been possible without the assistance of two very talented individuals, Dr. Jon Pratt for his experimental wisdom and Dr. Char-Ming Chin for his ingenuity. Both have contributed directly to the content of this Dissertation.

I also thank my past and present labmates Dr. Haider Arafat, Osama Ashour, Ayman El-Badawy, Sean Fahey, Jimmy Fung, Benjamin Hall, and Ryan Krauss. In addition to their stimulating conversations and friendship, their questions and suggestions helped me understand better my work and myself.

This work was funded by the Army Research Office, the Air Force Office of Scientific Research, and the National Science Foundation.

Finally, I thank my family for their love and patience over the last twelve years.

Shafic Sami Oueini
April 1999

Table of Contents

List of Figures

List of Tables

Chapter 1

Introduction

1.1 Motivation and Background

Airplane wings, helicopter blades, bridges, and buildings are examples of engineering structures that are prone to vibrations caused by wind gusts, rotating engines, high-speeding cars, or many other environmental disturbances. These disturbances lead to high-amplitude motions that may cause degradation or catastrophic failure of the structures' components. Therefore, the task of suppressing these undesirable vibrations is of prime importance to the engineering and science communities.

With the fast advancements in the electronics and material-science technologies, it has become possible to implement what is known as *active* feedback control. Active feedback control consists of designing and implementing sophisticated vibration control techniques using a variety of sensors, electronic hardware, and actuators. The sensor measures the vibrations of the structure and creates the so-called feedback signal. The electronic device, an analog circuit or a digital computer, for instance, samples the feedback signal, processes it mathematically, and provides a corresponding output signal. Then, the output of the circuit or the computer is fed to the actuator, which imparts an opposing force to the structure, thereby reducing its high-amplitude vibrations. Since this discipline brings together

concepts and developments from within the fields of mechanical, electrical, and electronics engineering, it has been coined *mechatronics*.

One of the main research areas in mechatronics is the development of safe and feasible mathematical algorithms that, once evaluated by the electronic device, can be applied as part of an active vibration suppression strategy. A more challenging task is to devise techniques which are effective but, more importantly, easy to understand and simple to analyze. The goal of our research is to develop such algorithms. More specifically, we devise what are usually thought-of as unconventional *nonlinear* control strategies.

Nonlinearities in dynamical systems are the source of a wealth of interesting phenomena. Scientists and engineers have always considered them detrimental, and almost all of their efforts have been confined to understanding and documenting any unusual or potentially catastrophic phenomena nonlinearities may lead to. The question that arises then is: can the results of these studies be used to advance the state-of-the-art from the "reporting" stage to the "application" stage?

It is our aim in this Dissertation to draw upon previously reported findings and demonstrate that nonlinearities *can* be exploited for devising active vibration control techniques. More specifically, we will show that simple yet effective nonlinear feedback strategies can be implemented for suppressing high-amplitude motions resulting from primary external or principal parametric resonances, the two most common and damage-incurring phenomena in structural systems. The advantage of our approach lies in the fact that the nature of the nonlinearities and their magnitudes are defined and adjusted by the user. Therefore, our techniques will yield predictable suppression schemes.

Before reviewing the history of controlling these resonances, we briefly present some of the relevant research in order to understand the implications of nonlinearities on the response of forced systems. First, we consider single-degree-of-freedom models.

The most basic system that exhibits interesting characteristics is the externally forced Duffing oscillator. It typically arises in the context of modeling pendulums, nonlinear springs, or

beams. Its dynamics are governed by

$$\ddot{u} + 2\,\mu\,\dot{u} + \omega^2 u + \alpha\,u^3 = F\cos(\Omega t), \tag{1.1}$$

where μ is the linear damping term, ω is the natural frequency, α is a positive or negative constant, and F and Ω are the forcing amplitude and frequency, respectively. A straightforward perturbation analysis of this system will reveal that, in addition to the linear resonance that occurs when $\Omega \approx \omega$, there exists two other resonances that lead to high-amplitude motions when $3\,\Omega \approx \omega$ or $\Omega \approx 3\,\omega$, also known as superharmonic and subharmonic resonances, respectively. If quadratic nonlinearities are included in the model to account for an initial curvature in a beam, for example, then resonances may develop when $2\,\Omega \approx \omega$ or $\Omega \approx 2\,\omega$. Moreover, when $\Omega \approx \omega$ and $\alpha < 0$, the analysis shows that the frequency-response curve of this system bends to the left, thereby exhibiting the so-called softening behavior. When $\alpha > 0$, the curve bends to the right, thereby exhibiting the so-called hardening behavior. The nonlinearity gives rise to coexisting high- and low-amplitude motions, jumps, and hysteresis [1]. The manuscripts by Minorsky [2] and Nayfeh and Mook [3] contain excellent reviews and analyses of these and other nonlinear models.

Nonlinearities play also a major role in the dynamics of systems subjected to parametric excitation. Unlike its external counterpart, parametric forcing is due to an excitation that is orthogonal to the coordinate in question, as it was first observed by Faraday [4]. He noted that a fluid in a vertically oscillating container develops horizontal surface waves. This resonance is peculiar because it occurs when the forcing frequency is close to twice one of the natural frequencies of the excited system, and it leads to high-amplitude motions. Mathieu [5] developed the first linear model exhibiting such a behavior. It is given by

$$\ddot{u} + 2\,\mu\,\dot{u} + \omega^2 u = uF\cos(\Omega t). \tag{1.2}$$

The analysis of this model reveals that, unlike systems subjected to a primary external excitation, viscous damping does not limit the amplitude of the response. The linear damping, however, delays the on-set of the instability [3].

In a realistic situation, such as the case of structural vibrations, the growth of the response is limited by nonlinearities that are not accounted for by any Mathieu-type model. Zavodney,

Nayfeh, and Sanchez [6] studied the response of a model given by

$$\ddot{u} + 2\,\mu\,\dot{u} + \omega^2 u + \alpha_1 u^2 + \alpha_2 u^3 = uF\cos(\Omega t). \tag{1.3}$$

They found that stable limit cycles can exist. They also showed that the system can exhibit quasiperiodic and chaotic motions. Zavodney and Nayfeh [7] investigated the dynamics of a cantilever beam carrying a lumped mass. They modeled the structure with cubic geometric and inertia nonlinearities, conducted experiments, and reported results that were in general agreement with the theory. Anderson, Nayfeh, and Balachandran [8] improved the model proposed by Zavodney and Nayfeh [7] and considered the effect of quadratic damping on the response of the system. Their theoretical results agreed very well with the experiments. Yabuno, Ide, and Aoshima [9] reconsidered the problem tackled by Zavodney and Nayfeh [7] and included quadratic damping in their model. They performed theoretical and experimental studies and showed that increasing the tip mass reduces the stabilizing effect of quadratic damping.

In multi-degree-of-freedom systems, nonlinearities create energy-transfer mechanisms that set the stage for interactions among two or more modes. Depending on the degree of the nonlinearities and type of excitation, several scenarios may be possible. Nayfeh and Mook [10] identified three energy transfer mechanisms between modes. They attributed them to either internal resonances, combination resonances, or energy exchange among widely spaced modes.

Arafat, Nayfeh, and Chin [11] studied the nonplanar dynamics of symmetric cantilever beams subjected to a principal parametric excitation. They considered the case of one-to-one internal resonance between the first in- and first out-of-plane flexural modes. Using analytical and numerical techniques, they investigated the response of the structure and found that the system exhibits complicated dynamics, such as Hopf and cyclic-fold bifurcations and period-doubling routes to chaos.

Anderson, Balachandran, and Nayfeh [12] subjected a cantilever beam to simultaneous principal parametric resonance of its third mode and primary external resonance of its fourth mode. They found that the response of the beam contained contributions from the first

mode. In their case, the ratio of the fourth frequency to the first frequency was 50-to-1. Nayfeh and Nayfeh [13, 14] and Nayfeh and Chin [15] proposed a paradigm that explains this phenomenon. They developed simple two-degree-of-freedom models possessing widely spaced frequencies and demonstrated theoretically and experimentally that energy transfer between the two modes is possible.

Of particular interest to us are systems coupled with quadratic nonlinearities subjected to primary resonances and possessing a two-to-one internal resonance. Sethna [16] was one of the first researchers to study such systems. He conducted theoretical studies, performed analog-computer simulations, and showed that nonperiodic motions may exist. In the context of analyzing coupling between the roll and pitch motions of ships, Nayfeh, Mook, and Marshall [17] discovered a saturation phenomenon that manifests itself in quadratically coupled systems. They modeled the dynamics of the ship with two second-order differential equations coupled with quadratic nonlinearities. They found that, when the frequency of pitch is twice the frequency of roll (two-to-one internal resonance) and the ship is subjected to head-seas at an encounter frequency equal to the pitch frequency (primary resonance of the higher mode), there exists a saturation phenomenon. For a certain threshold of the forcing amplitude, the amplitude of the directly excited mode (pitch) saturates, and the remaining excitation energy is channeled to the roll mode. As the forcing amplitude increases, the response of the unexcited roll mode increases, while the response amplitude of the directly excited mode remains constant. This behavior, although first identified in ship dynamics, can occur in other physical systems.

Haddow, Barr, and Mook [18] conducted analytical and experimental studies on an L-shaped beam structure and were the first to validate experimentally the results reported in [17]. Nayfeh and Zavodney [19] and Balachandran and Nayfeh [20] conducted experiments on a similar structure. They reported the occurrence of quasiperiodic and chaotic regimes whenever certain frequency conditions are violated.

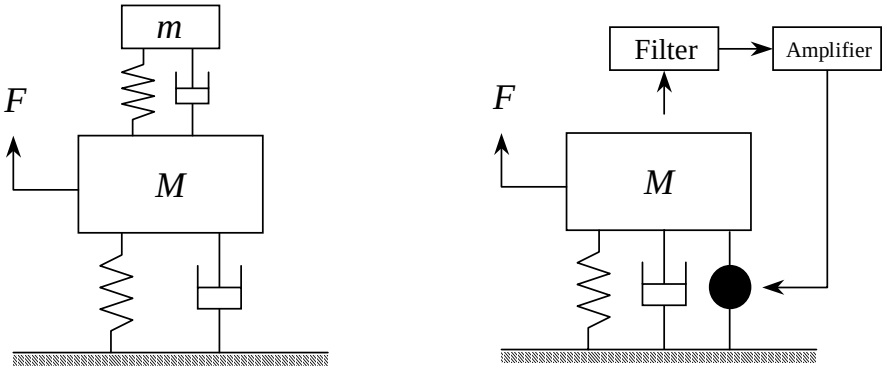

Figure 1-1. Typical configurations of a vibration absorber. (a) Passive and (b) active.

1.2 Control of Primary Resonance

Controlling the high-amplitude response of resonantly forced systems has been the subject of numerous theoretical and experimental studies. A recent survey by Sun, Jolly, and Norris [21] reveals that most control methods rely on the concept of a vibration absorber.

A vibration absorber may be passive or active. In the passive case, as illustrated in Figure 1-1a, a physical device m is attached to the primary structure M through an elastic component. By properly choosing the system parameters, the device is made to limit the vibration of the main mass by "absorbing" the external energy imparted to it. Depending on the material and the geometry of the assembly, the absorber may be linear or nonlinear.

In the case of active absorbers, the device is replaced by a control system of sensors, actuators, and filters that counteract the undesired vibrations, as shown in Figure 1-1b. Active vibration absorbers are typically more flexible than their passive counterparts, but the fundamental principle of transferring vibrational energy from a primary system to a secondary system remains intact. Depending on the control algorithms, active absorbers may be linear or nonlinear, as well.

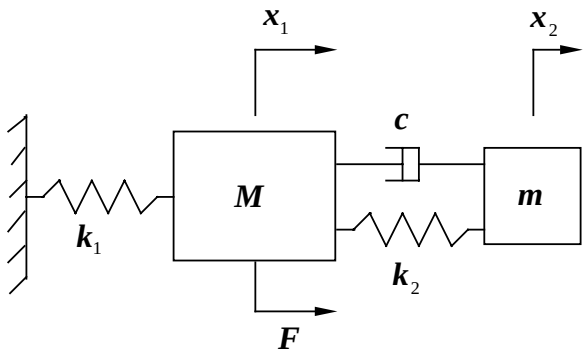

Figure 1-2. The classical vibration absorber.

In the next three sections, we present a review of vibration absorbers. First, we discuss the classical vibration absorber and its derivatives. Second, we present autoparametric nonlinear absorbers. Lastly, we summarize the results of the literature survey, discuss disadvantages of existing methods, and propose a solution.

1.2.1 Classical Vibration Absorbers

The classical linear vibration absorber as we know it today is due to Frahm [22]. He augmented the vibrating system under consideration with an auxiliary mass-spring-dashpot system that counteracted the effect of the applied external force. The vibrating mass and the absorber are shown in Figure 1-2.

The equations of motion of the system are

$$M\ddot{x}_1 + c\,(\dot{x}_1 - \dot{x}_2) + k_1\,x_1 + k_2\,(x_1 - x_2) = F_0\cos(\Omega t), \tag{1.4}$$

$$m\ddot{x}_2 - c\,(\dot{x}_1 - \dot{x}_2) - k_2(x_1 - x_2) = 0, \tag{1.5}$$

where M is the mass of the main vibrating system, m is the mass of the absorber, c is a damping constant, k_1 and k_2 are spring stiffnesses, F_0 is the forcing amplitude, and Ω is the forcing frequency. The case of resonant excitation is considered (i.e., $\Omega \approx \sqrt{k_1/M}$).

In its original and most simple application, the absorber damping is not implemented (i.e., $c = 0$). The response of the main mass is completely suppressed by setting the absorber

frequency equal to the frequency of excitation; that is,

$$\sqrt{\frac{k_2}{m}} = \Omega \approx \sqrt{\frac{k_1}{M}}.$$

However, due to the linear coupling between equations (1.4) and (1.5), the combined system will possess two resonant frequencies at which the absorber becomes a vibration amplifier. In order to circumvent this potentially dangerous situation, Den Hartog [23] augmented the absorber with a dashpot. The addition of the dashpot reduces the amplitudes of the two resonant peaks at the expense of allowing the main mass to vibrate at a small non-zero amplitude. Subsequently, researchers focused on investigating variations of the linear absorber in an effort to enhance its performance.

Roberson [24] and Arnold [25] analyzed undamped absorbers fitted with a nonlinear cubic spring. The resulting equations of motion are

$$M\ddot{x}_1 + k_1 x_1 + k_2 (x_1 - x_2) + k_3 (x_1 - x_2)^3 = F_0 \cos(\Omega t), \tag{1.6}$$

$$m\ddot{x}_2 - k_2(x_1 - x_2) - k_3 (x_1 - x_2)^3 = 0, \tag{1.7}$$

where k_3 is a constant. Roberson introduced the notion of *suppression bandwidth*; the region in the frequency-response curve between the two resonant peaks where

$$\frac{x_1 k_1}{F_0} \leq 1.$$

He analyzed equations (1.6) and (1.7) by the Duffing iteration method, while Arnold resorted to a Ritz method. Their results indicate that a soft spring ($k_3 < 0$) improves the performance of the absorber by widening the suppression bandwidth.

Hunt and Nissen [26] implemented a practical nonlinear damped absorber. They developed a spring by stacking steel Belleville washers. When mounted as shown in Figure 1-3, the washer assembly exhibits a complicated softening force-deflection characteristic. By properly choosing the washers' thickness s and the undeformed height h and fine tuning the absorber damping coefficient, they were able to double the suppression bandwidth.

Semercigil, Lammers, and Ying [27] modified the classical absorber by introducing an impact damper to the secondary mass. The system is shown in Figure 1-4. Through conservation

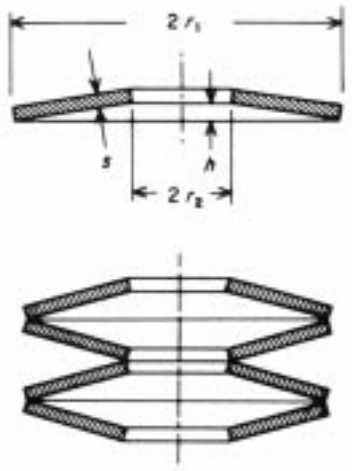

Figure 1-3. A Belleville washer and a spring stack.

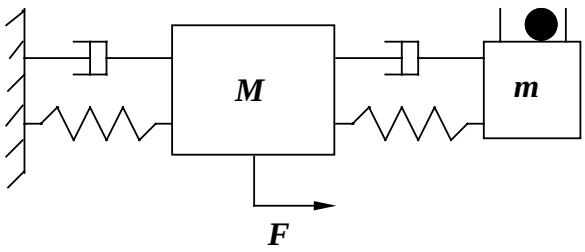

Figure 1-4. The impact-damper absorber.

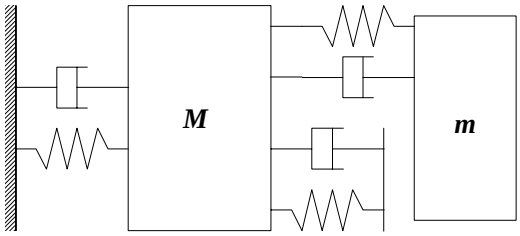

(a)

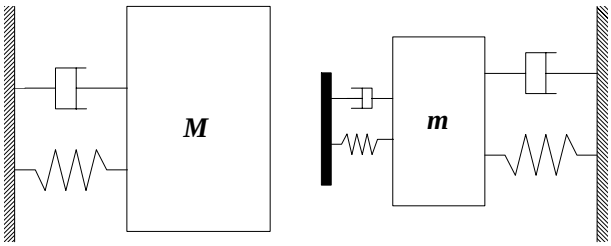

(b)

Figure 1-5. The discontinuous absorbers. (a) Setup analyzed by Galhoud *et al.* and Gonsalves *et al.* and (b) setup analyzed by Luo and Hanagud.

of momentum, the energy from the absorber is transferred to the smaller mass where it is dissipated through the impact.

In a similar effort, Galhoud, Masri, and Anderson [28] and Gonsalves, Neilson, and Barr [29] augmented the classical linear absorber with a discontinuously contacting spring, as shown in Figure 1-5a. To solve the resulting discontinuous (contact/no-contact) system of equations, Galhoud, Masri, and Anderson and Gonsalves, Neilson, and Barr developed a decision criterion based on the gap between the absorber mass and the spring-stop. Luo and Hanagud [30] improved the method of solution. They considered the motion of the stop as an additional degree of freedom, as illustrated in Figure 1-5b, and proposed a criterion based on the contact force. They conducted analytical and experimental studies and showed that the absorber creates regimes of quasiperiodic and chaotic responses.

Natsiavas [31] analyzed combinations of linear or nonlinear absorbers attached to linear or

nonlinear plants. He found that a softening absorber spring is effective when the excitation frequency is slightly smaller than the natural frequency of the plant, while a hardening spring is effective when the excitation frequency is slightly larger than the natural frequency of the plant. He also identified regions in the parameter space where the closed-loop system exhibited quasiperiodic and unbounded responses.

Olgac and Holm-Hansen [32] adopted an unconventional active absorber based on time-delayed feedback. The equation of the delayed resonator (absorber) takes the form

$$\ddot{x} + 2\zeta\omega\dot{x} + \omega^2 x + Gx(t-\tau) = 0, \tag{1.8}$$

where G and τ are user-defined constant gain and time delay, respectively. Due to the time delay, there are an infinite number of eigenvalues associated with equation (1.8). For a given delay, a value of the gain G can be chosen to place two eigenvalues at a specified location on the imaginary axis, while the rest remain in the left-hand plane. Thus, it is possible to implement an actively tuned absorber. Since the user possesses two parameters to vary, the gain and the time delay, Olgac, Elmali, and Vijayan [33] proposed to place four eigenvalues at prescribed locations on the imaginary axis. This freedom allowed them to design an absorber capable of simultaneous suppression at two forcing frequencies.

The development of the piezoceramic material PZT (Lead-Zirconium-Titanate) has lead to a significant amount of research investigating its application. PZT is a capacitive material that strains when a current is applied through it. Conversely, it generates a current whenever it is strained. It is therefore ideally suited for applications as an actuator and/or a sensor.

Fanson and Caughey [34] developed a linear suppression scheme based on positive position feedback (PPF). PPF is the active counterpart of the classical absorber. In this case, the coupling between the structure and the compensator need not be governed by the assembly of the system. Rather, the user is free to chose simple feedback and control signals that realize the necessary linear coupling. The equations governing the plant and the compensator are

$$\ddot{x}_1 + 2\zeta_1\omega_1\dot{x}_1 + \omega_1^2 x_1 = G\omega_1^2 x_2, \tag{1.9}$$

$$\ddot{x}_2 + 2\zeta_2\omega_2\dot{x}_2 + \omega_2^2 x_2 = \omega_2^2 x_1, \tag{1.10}$$

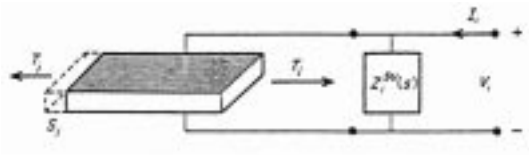

Figure 1-6. Shunted piezoceramics.

where x_1 is the structure's generalized coordinate, x_2 is the compensator coordinate, the ζ_i are damping coefficients, the ω_i are natural frequencies, and G is a user-defined gain. Following Den Hartog, they developed a design methodology for calculating the gain G and the damping coefficient ζ_2. They utilized PZT actuators and sensors, and they were one of the first researchers to implement active single- and multi-mode control of a cantilever beam.

Hagood and von Flotow [35] investigated the performance of passive piezoceramic linear absorbers. They mounted PZT patches on a cantilever beam and exploited their electromechanical behavior by shunting their terminals, as illustrated in Figure 1-6. They considered two possible shunts: resistive and combined resistive/inductive. The former is equivalent to adding viscoelastic damping to the structure. The latter introduces an electric resonance that can be tuned to the structure's frequency. Hence, it is analogous to the damped vibration absorber.

Dosch, Inman, and Garcia [36] developed a self-sensing PZT actuator. They designed analog bridge circuits that allow measurement of either the strain or the strain rate of the structure. They successfully applied their techniques to control vibrations of a cantilever beam fitted with one ceramic PZT.

The natural capacitance of PZT requires high inductance values for implementing an optimally tuned absorber. However, the inherent resistive value of any coil increases with the inductance value. Therefore, any usage of highly inductive components leads to an automatic increase of the equivalent absorber damping, thereby imposing a practical limitation on the application of the passively shunted piezoactuators.

To circumvent this anomaly, Hollkamp and Starchville [37] introduced a linear self-tuning

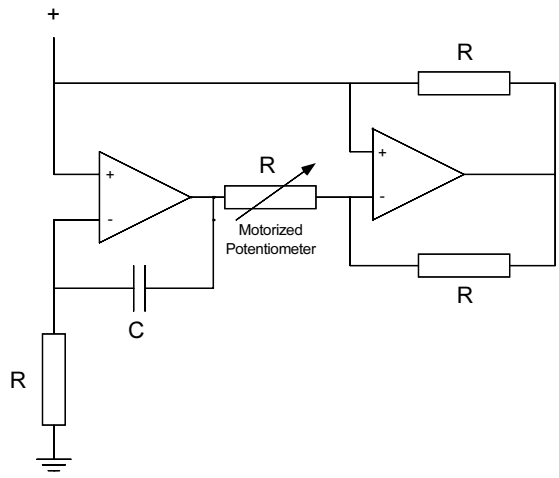

Figure 1-7. A synthetic inductor.

PZT absorber. They expanded the development of Hagood and von Flotow and implemented an active shunt by coupling the PZT actuators with a resistor and an electronic circuit that emulates an inductor. The circuit is shown in Figure 1-7. A computer senses the frequency of the structure and, through a motor-driven potentiometer, adjusts the shunt's frequency and optimizes the absorber. This application eliminates the introduction of unwanted absorber damping.

Recently, Agnes [38] studied passive PZT absorbers. He derived a model that accounts for quadratic and cubic capacitance and carried out a parametric investigation using perturbation methods and numerical simulations. When the plant is linear, he found that good vibration suppression can be achieved through the addition of either a softening or a hardening absorber nonlinearity. The choice depends on whether the frequency of the absorber is higher or lower than the plant's frequency. When the plant is nonlinear and for certain values of the forcing amplitude and absorber damping, he found regions where the absorber creates regimes of quasiperiodic or chaotic motions. These regimes can be eliminated by introducing a hardening absorber spring when the plant possesses softening characteristics or a softening absorber spring when the plant possesses hardening characteristics.

Other smart materials have also been developed. One popular material is Terfenol-D.

Terfenol-D, an Iron-Terbium-Dysprosium alloy, is a magnetostrictive material that manifests the so-called "butterfly" constitutive relationship between the applied magnetic field and the strain. This material exhibits quadratic and hysteretic characteristics. Researchers have been circumventing its nonlinear behavior by biasing the actuator with either a current or installing a magnet in the assembly and operating in a range, considered linear, around the biased point.

Hiller, Bryant, and Umegaki [39] were the first to use a biased magnetostrictive Terfenol-D actuator for active vibration isolation. Flatau, Hall, and Schlesselman [40] utilized a similar actuator to actively control the vibrations of a cantilever beam.

Pratt and Nayfeh [41] resorted to similar actuators for suppressing vibrations in a metal machining process. They attached, horizontally and vertically, two actuators to the cutting tool mount and implemented active control of chatter using modified linear absorbers.

1.2.2 Autoparametric Vibration Absorbers

Haxton and Barr [42] were the first to propose a passive vibration absorber based on two-to-one (autoparametric) resonance. Their technique amounts to attaching a cantilever beam with a tip mass to the primary system. The configuration is depicted in Figure 1-8. Assuming small beam deflections, one can write the dimensionless equations of motion as

$$\ddot{x} + 2\zeta_1\,\omega_1\,\dot{x} \;+\; \omega_1^2\,x \;-\; \alpha_1\,(\dot{y}^2 - y\ddot{y}) \;=\; \omega_1^2\cos(\Omega t), \tag{1.11}$$

$$\ddot{y} + 2\zeta_2\,\omega_2\,\dot{y} \;+\; (\omega_2^2 - \alpha_2\ddot{x})\,y \;+\; \alpha_3 y\,(\dot{y}^2 + y\ddot{y}) \;=\; 0, \tag{1.12}$$

where x is the displacement of the main mass, y is the horizontal deflection of the tip of the beam, ω_1 is the free undamped natural frequency of the entire system (absorber blocked), ω_2 is the free undamped natural frequency of the absorber, the ζ_i are damping coefficients, and the α_i are constants. They were able to achieve vibration suppression by either adjusting the mass or the length of the absorber so that $2\omega_2 \approx \omega_1$. Their implementation replaces the two resonant peaks with regions of local jumps whose amplitudes can be minimized by increasing the absorber damping. The model derived for their analysis considers only

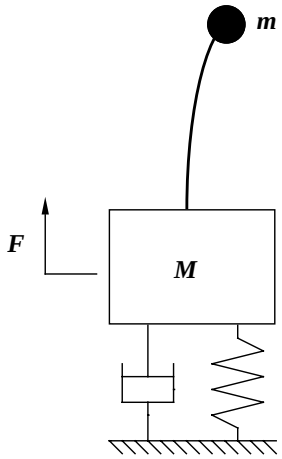

Figure 1-8. The autoparametric vibration absorber.

small absorber deflections. When a moderately large forcing amplitude is imparted to the system, the validity of their theoretical analysis is questionable. In this case, possibly other strong nonlinear terms become important, which may lead to performance degradation of the absorber.

Hatwal, Mallik, and Ghosh [43, 44] considered a system similar to the one explored by Haxton and Barr, but replaced the beam with a rigid pendulum. A diagram of their model is illustrated in Figure 1-9. They analyzed two cases where the restoring force is due to either gravity or to a torsional spring. Thus, their equations of motion contain quadratic, cubic, and circular nonlinear terms. They used the method of harmonic balance to find a second-order approximate solution to the governing equations. Their results indicate that both configurations can effectively suppress the resonant vibrations of the main mass. For large forcing amplitudes, the gravity-controlled pendulum exhibited transient non-oscillatory as well as non-periodic motions, whereas the spring-controlled pendulum introduced secondary peaks in the frequency-response curves.

Bajaj, Chang, and Johnson [45] and Banerjee, Bajaj, and Davies [46] reconsidered the gravity-controlled pendulum of Hatwal, Mallick, and Ghosh. They used first- and second-order averaging methods to analyze the dynamics of the system. In addition to reporting

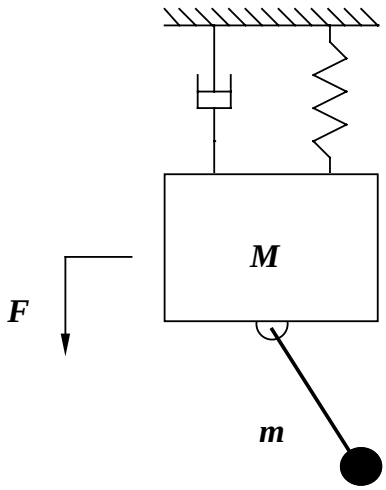

Figure 1-9. A pendulum absorber.

the occurrence of periodic and chaotic motions, they found that the saturation phenomenon predicted by the first-order averaging technique is lost when the effect of higher-order nonlinearities is included in the model.

Cartmell and Lawson [47] expanded the absorbers of Haxton and Barr and Hatwal, Mallik and Ghosh by installing a stepper motor that actuates a slider mass on the rigid pendulum. Their apparatus is shown in Figure 1-10. Horizontal springs are installed to insure a stable upright pendulum position. Their semi-active strategy consists of sensing the acceleration of the main mass and analyzing it through a computer. The computer determines the amplitude of the response and directs the motor to move the slider, thereby inducing small changes in the natural frequency of the absorber. This implementation, although successful, is costly because it requires the design and assembly of a rather delicate sliding mechanism. Another possible configuration amounts to replacing the slider mass by a servomotor attached to the pendulum. Then the absorber frequency can be fine-tuned by connecting the motor in position feedback mode and varying the feedback gain.

Cuvalci and Ertas [48] used a pendulum absorber for a flexible cantilever beam. The configuration is depicted in Figure 1-11. They used a one-mode Galerkin expansion procedure to reduce the system to two coupled equations. Their numerical and experimental results indi-

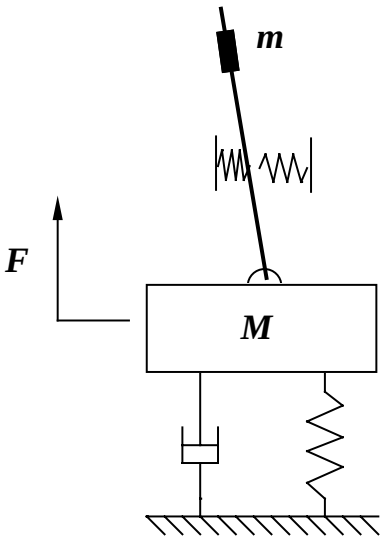

Figure 1-10. The semi-active pendulum absorber.

Figure 1-11. A pendulum absorber attached to a cantilever beam.

cate that the absorber is very effective when an autoparametric condition is present. They also noted that, for either a very small mass ratio or a forcing frequency largely detuned from resonance, the system response becomes chaotic.

Khajepour and Golnaraghi [49] proposed an active nonlinear control strategy based on modal coupling between a structure and a virtual second-order controller implemented through a computer. They used the method of normal forms to derive a quadratic control law that maximizes the modal coupling between the plant and the controller. Subsequently, they composed a software algorithm that updates the initial conditions of the controller and used it to suppress free and forced vibrations of a cantilever beam actuated with PZT patches.

1.2.3 Synopsis

Our review reveals that researchers have adopted two major avenues in designing new absorbers. In the first one, they developed passive and active variations of the classical absorbers in the aim of achieving two goals: widening the suppression bandwidth and reducing the amplitudes of the resonant peaks. This is accomplished by introducing damping mechanisms or some form of nonlinearity in the absorber. These techniques suffer from a number of limitations. The damping methods sacrifice amplitude reduction for bandwidth, while the nonlinearities, due either to the design of the absorber or to the plant characteristics, make the system prone to undesirable responses by creating regimes of quasiperiodic and chaotic motions.

In the second approach, inherently nonlinear passive absorbers have been developed. Here, the nonlinearity is due to the geometric construction of the absorber mechanisms rather than the material properties. The resulting governing equations are linearly uncoupled, but nonlinearly coupled through quadratic, cubic, and circular functions. Consequently, the absorbers suppress the plant's response amplitude without creating any additional resonances. However, they too suffer from an unavoidable disadvantage. When either the forcing amplitude is large or the system's frequency conditions are violated, the cubic and circular nonlinearities sever the absorber's suppression capability and replace the low-amplitude response with a quasiperiodic or a chaotic motion.

Following these findings, we propose to develop an absorber that resolves the shortfalls of the previous design methods. We consider implementation of an active nonlinear absorber. In contrast with passive techniques, we will be able to choose only the combination of nonlinear coupling terms that insures predictable system responses. More specifically, we will devise quadratic feedback control laws that induce the well-understood saturation phenomenon. To our knowledge, this is the first instance where the phenomenon is exploited for active vibration suppression.

1.3 Control of Parametric Resonance

Our search in the literature yielded considerably fewer studies reporting control of parametric resonance. Asfar and Masoud [50] implemented a Lanchester-type damper to suppress the vibrations of a single-degree-of-freedom system subjected to a principal parametric resonance. They conducted numerical studies and demonstrated effective suppression and bifurcation control. Mustafa and Ertas [51] proposed controlling the response of a cantilever beam with the addition of a tip-pendulum. They conducted experiments and showed that the closed-loop system exhibited chaotic responses. Thomsen [52] considered a string and used a sliding-mass nonlinear absorber. His studies revealed that, for moderate forcing amplitudes, successful suppression is possible. For high forcing amplitudes or a large slider mass, the system exhibited modulated responses. Yabuno [53] proposed a control law based on linear and cubic position feedback and linear velocity feedback. He showed that velocity feedback stabilizes the trivial solution in the frequency-response curves, while nonlinear position feedback reduces the response amplitude in the force-response curves.

1.4 Organization of the Dissertation

The Dissertation is divided into two parts. In Part I, we consider systems subjected to primary resonance, and in Part II, we consider systems subjected to principal parametric resonance.

We begin Part I by developing a nonlinear quadratic absorber. In Chapter 2, we present the theoretical background for the strategy. We consider the problem of suppressing the vibrations of a single-degree-of-freedom plant subjected to a primary resonance, develop the control law, and investigate the dynamics of the closed-loop system. Furthermore, we compare the performance of the quadratic absorber with that of a linear tuned absorber.

As a proof-of-concept, we design and build analog circuits that emulate the quadratic absorber and apply the control law through different actuation mechanisms and feedback sen-

sors. In Chapter 3, we describe application of the quadratic absorber using a DC motor, piezoelectric ceramics, and Terfenol-D struts. In each case, we develop and analyze a model of the implementation. Furthermore, we extend the theory to multi-degree-of-freedom plants.

In Chapter 4, we consider a versatile implementation of the quadratic absorber. We use a digital signal processing (DSP) board and develop a software-based absorber that replaces the analog circuit. First, we describe the hardware and the various functions of the program. Second, we perform experimental studies and compare the performance of a quadratic absorber with the performance of a linear absorber. Finally, we investigate the consequences of actuator saturation on the effectiveness of the quadratic absorber.

We end Part I with devising a different nonlinear absorber. In Chapter 5, we consider implementation of a technique where the plant and the absorber are coupled with a specific set of cubic nonlinearities. We conduct theoretical analyses and show that when a one-to-one internal resonance condition is imposed, the system exhibits a multi-valued saturation phenomenon.

In Part II, we present two techniques for controlling principal parametric resonance. Motivated by the results of Part I, we explore using the quadratic absorber for controlling a parametrically forced system. In Chapter 6, we conduct theoretical analyses and show that the quadratic absorber in this case does not constitute an effective control strategy. However, our studies reveal that the system exhibits interesting dynamics. Therefore, we carry out experiments and report results that are in agreement with the theory.

In Chapter 7, we propose an alternate control law. We demonstrate theoretically and experimentally that a simple technique based on cubic velocity feedback leads to effective vibration suppression and bifurcation control.

We end the Dissertation in Chapter 8 with a summary of our findings and suggestions for future work.

Part I

External Excitation

Chapter 2

Development of the Quadratic Absorber

In this chapter, we develop the quadratic absorber control strategy. We use the method of multiple scales [1, 54] to obtain an approximate solution to the governing equations. Then, we conduct a stability analysis and investigate theoretically the performance of the control technique.

For simplicity, we consider an externally forced single-degree-of-freedom plant governed by

$$\ddot{u} + 2\,\hat{\mu}\,\dot{u} + \omega_2^2\,u = \hat{F}\cos(\Omega t + \tau) + \hat{\delta}\,F_c(t), \tag{2.1}$$

where u is a generalized coordinate, $\hat{\mu}$ is the linear damping coefficient, ω_2 is the natural frequency, $\hat{F}$ and Ω are the amplitude and frequency of the excitation, respectively, τ is a constant phase, $\hat{\delta}$ is a constant gain, and $F_c(t)$ is a control signal.

Table 2-1. Feedback signals for the quadratic absorber.

Sensor	$F_f(t)$
Position	$uv, u\ddot{v}$
Velocity	$\dot{u}\dot{v}$
Acceleration	$\ddot{u}v, \ddot{u}\ddot{v}$

2.1 Development of Strategy

We consider the case of primary resonance (i.e., $\Omega \approx \omega_2$) and introduce a controller of the form

$$\ddot{v} + 2\,\hat{\zeta}\,\dot{v} + \omega_1^2\,v = \hat{\alpha}\,F_f(t), \tag{2.2}$$

where the controller's natural frequency ω_1 is chosen such that $2\,\omega_1 \approx \omega_2$, $\hat{\zeta}$ is the controller damping coefficient, $\hat{\alpha}$ is a constant gain, and $F_f(t)$ is a feedback signal. The form of $F_f(t)$ depends on the available sensor signal. We list its possible forms in Table 2-1. The control signal $F_c(t)$ may take the form v^2, $\dot{v}^2$, or $\ddot{v}^2$.

2.2 Perturbation Analysis

We consider the case of position feedback and analyze, without loss of generality, solutions of the system of equations

$$\ddot{u} + 2\,\hat{\mu}\,\dot{u} + \omega_2^2\,u = \hat{F}\cos(\Omega t + \tau) + \hat{\delta}v^2, \tag{2.3}$$

$$\ddot{v} + 2\,\hat{\zeta}\,\dot{v} + \omega_1^2\,v = \hat{\alpha}uv. \tag{2.4}$$

To determine an approximate solution of equations (2.3) and (2.4), we use the method of multiple scales. First, we scale the damping and forcing terms by letting

$$\hat{\mu} = \epsilon\,\mu, \quad \hat{\zeta} = \epsilon\,\zeta, \quad \hat{F} = \epsilon^2\,F, \tag{2.5}$$

where ϵ is a dimensionless bookkeeping parameter. Second, we seek approximate solutions to u and v in the form

$$u \approx \epsilon u_1(T_0, T_1) + \epsilon^2 u_2(T_0, T_1), \tag{2.6}$$

$$v \approx \epsilon v_1(T_0, T_1) + \epsilon^2 v_2(T_0, T_1), \tag{2.7}$$

where $T_0 = t$ is a fast time scale and $T_1 = \epsilon t$ is a slow time scale describing the time evolution of the amplitudes and phases of the response. The derivatives with respect to time are expressed in term of the new time scales as

$$\frac{d}{dt} = D_0 + \epsilon D_1 + \cdots \quad \text{and} \quad \frac{d^2}{dt^2} = D_0^2 + 2\epsilon D_0 D_1 + \cdots, \tag{2.8}$$

where $D_k \equiv \partial/\partial T_k$. Substituting equations (2.5)–(2.8) into equations (2.3) and (2.4) and equating coefficients of like powers of ϵ leads to
Order (ϵ):

$$D_0^2 u_1 + \omega_2^2 u_1 = 0, \tag{2.9}$$

$$D_0^2 v_1 + \omega_1^2 v_1 = 0, \tag{2.10}$$

Order (ϵ^2):

$$D_0^2 u_2 + \omega_2^2 u_2 = -2 D_0(D_1 u_1 + \mu u_1) + F\cos(\Omega t + \tau) + \hat{\delta} v_1^2, \tag{2.11}$$

$$D_0^2 v_2 + \omega_1^2 v_2 = -2 D_0(D_1 v_1 + \zeta v_1) + \hat{\alpha} u_1 v_1. \tag{2.12}$$

The solutions of equations (2.9) and (2.10) can be expressed as

$$u_1 = A_2(T_1) e^{i\omega_2 T_0} + \overline{A}_2(T_1) e^{-i\omega_2 T_0}, \tag{2.13}$$

$$v_1 = A_1(T_1) e^{i\omega_1 T_0} + \overline{A}_1(T_1) e^{-i\omega_1 T_0}. \tag{2.14}$$

The complex-valued functions $A_1(T_1)$ and $A_2(T_1)$ are unknown at this stage of the analysis. They will be determined by eliminating the secular terms at the next level of approximation.

Substituting equations (2.13) and (2.14) into equations (2.11) and (2.12) yields

$$D_0^2 u_2 + \omega_2^2 u_2 = -2 i \omega_2 (D_1 A_2 + \mu A_2) e^{i\omega_2 T_0}$$

$$+\ \hat{\delta}\ \left(A_1^2\, e^{2i\omega_1 T_0}\ +\ A_1\,\overline{A}_1\right)\ +\ \frac{1}{2}\,F\, e^{i(\Omega T_0+\tau)}\ +\ \text{cc}, \tag{2.15}$$

$$\begin{aligned} D_0^2\, v_2\ +\ \omega_1^2\, v_2\ =\ &-\ 2\, i\, \omega_1\, (D_1 A_1\ +\ \zeta\, A_1)\ e^{i\omega_1 T_0} \\ &+\ \hat{\alpha}\ \left(A_1\, e^{i\omega_1 T_0}\ +\ \overline{A}_1\, e^{-i\omega_1 T_0}\right)\ A_2\, e^{i\omega_2 T_0}\ +\ \text{cc}, \end{aligned} \tag{2.16}$$

where cc stands for the complex conjugate of the preceding terms. To describe quantitatively the nearness of $2\omega_1$ to ω_2 and Ω to ω_2, we introduce two detuning parameters σ_1 and σ_2 defined by

$$2\,\omega_1\ =\ \omega_2\ -\ \epsilon\,\sigma_1 \quad \text{and} \quad \Omega\ =\ \omega_2\ +\ \epsilon\,\sigma_2. \tag{2.17}$$

Then, substituting equations (2.17) in equations (2.15) and (2.16), we find that secular terms are eliminated from u_2 and v_2 if

$$2\, i\, (D_1 A_1 + \zeta A_1)\ +\ 4\,\alpha\, A_2 \overline{A}_1\, e^{i\sigma_1 T_1}\ =\ 0, \tag{2.18}$$

$$2\, i\, (D_1 A_2 + \mu A_2)\ +\ 4\,\delta\, A_1^2\, e^{-i\sigma_1 T_1}\ -\ f\, e^{i(\sigma_2 T_1+\tau)}\ =\ 0, \tag{2.19}$$

where

$$f\ =\ \frac{F}{2\,\omega_2}, \quad \delta\ =\ \frac{\hat{\delta}}{4\,\omega_2}, \quad \alpha\ =\ \frac{\hat{\alpha}}{4\,\omega_1}. \tag{2.20}$$

Care must be taken in choosing the coupling coefficients to insure that α and δ have the same sign. Nayfeh and Mook [3] have shown that A_1 and A_2 are unbounded if $\alpha\,\delta < 0$. In this case, the system contains regenerative terms that lead to a growth in the response.

Next, we express equations (2.18) and (2.19) in real variables by letting

$$A_j\ =\ \frac{1}{2}\, a_j(T_1)\, e^{i\beta_j(T_1)}. \tag{2.21}$$

Substituting equation (2.21) into equations (2.18) and (2.19) and separating real and imaginary parts yields

$$a_1'\ =\ -\,\zeta a_1\ -\ \alpha\, a_1\, a_2 \sin\gamma_1, \tag{2.22}$$

$$a_2'\ =\ -\,\mu a_2\ +\ \delta\, a_1^2 \sin\gamma_1\ +\ f \sin\gamma_2, \tag{2.23}$$

$$a_1\,\beta_1'\ =\ \alpha\, a_1\, a_2\ \cos\gamma_1, \tag{2.24}$$

$$a_2\,\beta_2'\ =\ \delta\, a_1^2\ \cos\gamma_1\ -\ f \cos\gamma_2, \tag{2.25}$$

where

$$\gamma_1 \;=\; \sigma_1 T_1 - 2\beta_1 + \beta_2 \quad \text{and} \quad \gamma_2 \;=\; \sigma_2 T_1 \;- \beta_2 + \tau, \tag{2.26}$$

and the prime represents differentiation with respect to the slow time variable T_1.

The system of equations (2.22)–(2.26) arose in the context of analyzing many physical systems, such as the motion of ships and the vibration of structures. In these cases, the magnitude of the nonlinear coupling terms α and δ, the damping coefficients μ and ζ, and the internal detuning σ_1 are determined by the physics of the problem at hand. In the present case, the absorber and the nonlinear coupling terms are conveniently introduced. Thus, it is possible for the user to adjust these parameters and hence devise adequate control laws to suppress any unwanted oscillations.

The control strategy is evaluated by analyzing the steady-state response of the closed-loop system. Setting $a_1' = a_2' = 0$ and $\gamma_1' = \gamma_2' = 0$ and solving the resulting equations yields the following two possibilities for the fixed points. First,

$$a_1 \;=\; 0, \tag{2.27}$$

$$a_2 \;=\; \frac{f}{\sqrt{\sigma_2^2 \;+\; \mu^2}}. \tag{2.28}$$

This is the solution of the linear problem; the amplitude of the directly excited mode varies linearly with the excitation amplitude, while the absorber (the unexcited mode) is not exhibiting any motion. Second,

$$a_1 \;=\; (\alpha\,\delta)^{-\frac{1}{2}}\,\sqrt{\Lambda_1 \pm (\alpha^2 f^2 \;-\; \Lambda_2^2)^{\frac{1}{2}}}, \tag{2.29}$$

$$a_2 \;=\; |\alpha|^{-1}\,\sqrt{\zeta^2 \;+\; \frac{1}{4}\,(\sigma_1 + \sigma_2)^2}, \tag{2.30}$$

where

$$\Lambda_1 \;=\; \frac{1}{2}\,\sigma_2\,(\sigma_1 + \sigma_2) \;-\; \zeta\,\mu \quad \text{and} \quad \Lambda_2 \;=\; \frac{1}{2}\,\mu\,(\sigma_1 + \sigma_2) \;+\; \zeta\,\sigma_2. \tag{2.31}$$

Using equations (2.17), we rewrite equation (2.30) as

$$a_2 \;= |\alpha|^{-1}\,\sqrt{\zeta^2 \;+\; \frac{(\Omega \;-\; 2\,\omega_1)^2}{4\epsilon^2}}. \tag{2.32}$$

In contrast with the linear solution, equation (2.32) indicates that the amplitude of the plant is a function of the controller's damping ζ and the deviation of twice the frequency of the controller from the excitation frequency. Thus, the response of the plant can be suppressed by properly adjusting the damping and frequency of the absorber. By making $\Omega - 2\,\omega_1 = 0$, the response of the excited mode can be reduced when the natural frequency of the controller is set equal to one-half the excitation frequency. In a real experiment, the plant's natural frequency may not be constant due to small structural changes or environmental effects. However, the plant will oscillate at the frequency of excitation. Thus, when the forcing is close to resonance, implementation of the technique is rendered very effective by tuning the frequency of the absorber equal to one-half the frequency of oscillation of the structure. Then, the resulting fixed points are

$$a_1 \;=\; \sqrt{\frac{-\,\zeta\,\mu \pm [(\alpha f)^2 \;-\; (\sigma_2 \zeta)^2]^{\frac{1}{2}}}{\alpha\,\delta}}, \tag{2.33}$$

$$a_2^* \;=\; \frac{\zeta}{|\alpha|}. \tag{2.34}$$

2.3 Stability Analysis

Next, we investigate the stability of the fixed points. We follow the analysis performed by Nayfeh [55] and determine when the roots of equation (2.33) are real. We define a critical value for the forcing f by

$$f_c \;=\; \sqrt{\frac{\zeta^2(\sigma_2^2 + \mu^2)}{\alpha^2}}. \tag{2.35}$$

Then, the only possible real solution of a_1 is given by

$$a_1^* \;=\; \sqrt{\frac{-\,\zeta\,\mu + [(\alpha f)^2 \;-\; (\sigma_2 \zeta)^2]^{\frac{1}{2}}}{\alpha\,\delta}}, \tag{2.36}$$

when $f > f_c$.

The analysis is simplified by recasting the modulation equations in Cartesian coordinates using the transformation

$$A_1 \;=\; \frac{1}{2}(p_1 - i q_1)\, e^{i[\nu_1 T_1 + \tau/2]} \quad \text{and} \quad A_2 \;=\; \frac{1}{2}(p_2 - i q_2)\, e^{i[\nu_2 T_1 + \tau]}, \tag{2.37}$$

where the p_n and q_n are real and

$$\nu_1 \;=\; \frac{1}{2}(\sigma_1 + \sigma_2) \quad \text{and} \quad \nu_2 \;=\; \sigma_2. \tag{2.38}$$

The transformed modulation equations take the form

$$p_1' \;+\; \zeta\, p_1 \;+\; \nu_1\, q_1 \;+\; \alpha\,(p_2 q_1 - p_1 q_2) \;=\; 0, \tag{2.39}$$

$$q_1' \;+\; \zeta\, q_1 \;-\; \nu_1\, p_1 \;+\; \alpha\,(p_1 p_2 + q_1 q_2) \;=\; 0, \tag{2.40}$$

$$p_2' \;+\; \mu\, p_2 \;+\; \nu_2\, q_2 \;-\; 2\,\delta\, p_1 q_1 \;=\; 0, \tag{2.41}$$

$$q_2' \;+\; \mu\, q_2 \;-\; \nu_2\, p_2 \;+\; \delta\,(p_1^2 - q_1^2) \;=\; f. \tag{2.42}$$

The stability of a given fixed point to a disturbance proportional to $e^{\lambda T_1}$ is determined by the roots of

$$\begin{vmatrix} \lambda+\zeta-\alpha\, q_2 & \nu_1+\alpha p_2 & \alpha\, q_1 & -\alpha p_1 \\ -\nu_1+\alpha p_2 & \lambda+\zeta+\alpha q_2 & \alpha\, p_1 & \alpha q_1 \\ -2\,\delta\, q_1 & -2\,\delta\, p_1 & \lambda+\mu & \nu_2 \\ 2\,\delta\, p_1 & -2\,\delta\, q_1 & -\nu_2 & \lambda+\mu \end{vmatrix} \;=\; 0. \tag{2.43}$$

The eigenvalues corresponding to the linear solution ($a_1 = 0$ and $a_2 \neq 0$) are given by

$$\lambda \;=\; -\zeta \pm \sqrt{\frac{\alpha^2 f^2}{\mu^2+\nu_2^2} - \nu_1^2} \quad \text{and} \quad -\mu \pm i\,\nu_2. \tag{2.44}$$

The linear solution is a stable focus provided that $f \leq f_c$ or $a_2 \leq a_2^*$. When $f > f_c$ or $a_2 > a_2^*$, the fixed point is a saddle. We note that the value of ζ must be minimized but not set exactly equal to zero in order to avoid a codimension-two bifurcation when $f = f_c$.

The stability of the nonlinear solution ($a_1 \neq 0$ and $a_2 \neq 0$) is investigated by substituting equations (2.34) and (2.36) into equation (2.43) and obtaining

$$\begin{aligned} &\lambda^4 \;+\; 2\,(\mu+\zeta)\,\lambda^3 \;+\; (\mu^2 + 4\mu\zeta + \nu_2^2 + 4\,\alpha\delta a_1^{*2})\,\lambda^2 \\ &\quad +\; \left[2\,\zeta\,(\mu^2+\nu_2^2) \;+\; 4\,\alpha\delta\,(\mu+\zeta)\,a_1^{*2}\right]\,\lambda \;+\; 4\,\alpha\delta\, a_1^{*2}\left(\alpha\delta\, a_1^{*2} + \mu\zeta - \nu_1\nu_2\right) \;=\; 0. \end{aligned} \tag{2.45}$$

Because a closed-form solution of the roots of the polynomial (2.45) is not available, we use the Routh-Hurwitz criterion to establish the stability of the fixed point. Accordingly, the

necessary and sufficient conditions that none of the roots of equation (2.45) has a positive real part are

$$2\,(\mu+\zeta) > 0, \tag{2.46}$$

$$2\,\mu\,(2\,\zeta+\mu)^2 + 2\,\mu\,\nu_2^2 + 4\,(\zeta+\mu)\,\alpha\delta\,a_1^2 > 0, \tag{2.47}$$

$$\alpha\,\delta\,a_1^2 \;+\; \zeta\,\mu \;-\; \nu_1\,\nu_2 \;>\; 0, \tag{2.48}$$

$$4\,\zeta\,\mu\,(\mu^2+\nu_2^2)\,(4\zeta^2+4\mu\zeta+\mu^2+\nu_2^2) \;+\; 8\,(\mu+\zeta)^2\,(\mu^2+2\mu\zeta+2\nu_1\nu_2+\nu_2^2)\,\alpha\delta\,a_1^2 > \;0. \tag{2.49}$$

Conditions (2.46) and (2.47) are always satisfied. The violation of condition (2.48) implies the existence of an eigenvalue with a positive real part. Substituting equation (2.36) into condition (2.48), we find that the solution is always stable. The violation of condition (2.49) implies the existence of two complex eigenvalues with positive real parts, which is a characteristic of a Hopf bifurcation. However, a careful examination of condition (2.49) reveals that the occurrence of such a bifurcation can be eliminated when

$$\nu_1\nu_2 \;=\; \frac{1}{2}\sigma_2\,(\sigma_2+\sigma_1) \geq \;0.$$

This condition is automatically satisfied by the fundamental design methodology and operation of the absorber.

2.4 Performance of the Control Strategy

2.4.1 Scaling of the Modulation Equations

To gain insight into the dynamics of the system, we seek to eliminate or reduce the number of parameters in the modulation equations. Thus, we introduce two scaling schemes that enable us to characterize both the transient and steady-state behavior of the solution.

We start from the complex-valued form of the modulation equations, introduce the scaling [56]

$$A_1 \;=\; c_1\,\tilde{A}_1, \;\; A_2 \;=\; c_2\,\tilde{A}_2, \;\; T_1 \;=\; c_3\,T, \tag{2.50}$$

where the c_i are real constants, and obtain

$$2\,i\left(D_1\tilde{A}_1 + \tilde{\zeta}\tilde{A}_1\right) + 4\,\alpha\,c_2c_3\tilde{A}_2\overline{\tilde{A}}_1\,e^{i\tilde{\sigma}_1 T} = 0, \tag{2.51}$$

$$2\,i\left(D_1\tilde{A}_2 + \tilde{\mu}\tilde{A}_2\right) + 4\,\frac{\delta c_1^2 c_3}{c_2}\,\tilde{A}_1^2\,e^{-i\tilde{\sigma}_1 T} - \frac{c_3 f}{c_2}\,e^{i(\tilde{\sigma}_2 T+\tau)} = 0, \tag{2.52}$$

where

$$\tilde{\zeta} = c_3\,\zeta, \quad \tilde{\mu} = c_3\,\mu, \quad \tilde{\sigma}_1 = c_3\,\sigma_1, \quad \tilde{\sigma}_2 = c_3\,\sigma_2. \tag{2.53}$$

To scale out α, δ, and f, we choose

$$|\alpha|c_2c_3 = 1, \quad \frac{|\delta|c_1^2c_3}{c_2} = 1, \quad \text{and} \quad \frac{c_3\,f}{c_2} = 1. \tag{2.54}$$

It follows from equations (2.54) that

$$c_1 = \sqrt{\frac{f}{|\delta|}}, \quad c_2 = \sqrt{\frac{f}{|\alpha|}}, \quad \text{and} \quad c_3 = \frac{1}{\sqrt{f|\alpha|}}. \tag{2.55}$$

The modulation equations are transformed into a four-dimensional system with the state variables

$$\tilde{a}_1 = a_1\sqrt{\frac{|\delta|}{f}}, \quad \tilde{a}_2 = a_2\sqrt{\frac{|\alpha|}{f}}, \tag{2.56}$$

$$\tilde{\gamma}_1 = \tilde{\sigma}_1 T - 2\,\beta_1 + \beta_2 \quad \text{and} \quad \tilde{\gamma}_2 = \tilde{\sigma}_2 T - \beta_2 + \tau, \tag{2.57}$$

and the parameters

$$\tilde{\zeta} = \frac{\zeta}{\sqrt{f|\alpha|}}, \quad \tilde{\mu} = \frac{\mu}{\sqrt{f|\alpha|}}, \quad \tilde{\sigma}_1 = \frac{\sigma_1}{\sqrt{f|\alpha|}}, \quad \text{and} \quad \tilde{\sigma}_2 = \frac{\sigma_2}{\sqrt{f|\alpha|}}. \tag{2.58}$$

The scaling in (2.55) eliminates the bifurcation control parameter f from the modulation equations. Consequently, it obscures the phenomenon of saturation. However, its importance is evident in defining the scaling of time. The last equation in (2.55) indicates that for a constant time scale, the gain α and the forcing f are inversely proportional. Thus for a given forcing level, the transient behavior is dependent on the choice of α. The issue of determining a suitable value of c_3, and thus α, is addressed in Section 2.4.3.

Next, we introduce a second scaling that maintains the dependency on the forcing f. We set $c_3 = 1$ and obtain

$$c_1 = \frac{1}{\sqrt{\alpha\delta}} \quad \text{and} \quad c_2 = \frac{1}{|\alpha|}. \tag{2.59}$$

The modulation equations are transformed into a four-dimensional system with the state variables

$$\tilde{a}_1 \;=\; a_1\sqrt{\alpha\delta}, \quad \tilde{a}_2 \;=\; a_2\,|\alpha|, \tag{2.60}$$

$$\gamma_1 \;=\sigma_1\,T \;-\; 2\,\beta_1 +\; \beta_2 \quad \text{and} \quad \gamma_2 \;=\; \sigma T - \beta_2 + \tau, \tag{2.61}$$

and the parameters

$$\sigma_1, \quad \sigma_2, \quad \zeta, \quad \mu, \quad \text{and} \quad \tilde{f} \;=\; f\,|\alpha|. \tag{2.62}$$

This latter scaling scheme is used in the next section to analyze the steady-state behavior of the system.

2.4.2 Steady-State Analysis

The steady-state performance of the control technique is evaluated by varying the forcing level $\tilde{f}$ and the external detuning σ_2, thereby generating the force- and frequency-response curves, respectively. In the following analysis, we present qualitative performance results of the absorber. We choose $\mu = 0.05$, $\zeta = 0.001$, and let $\alpha = \delta = 1$, leading to $\tilde{f} = f$, $\tilde{a}_1 = a_1$, and $\tilde{a}_2 = a_2$.

In Figure 2-1, we show the force-response curves. Figure 2-1 illustrates the well-known saturation phenomenon. Initially, the response of the directly excited mode varies linearly with the forcing level while the controller is inactive. When the forcing level exceeds the threshold f_c, the controller is activated, and the excited mode saturates. The value of f_c is given by

$$f_c \;=\; \sqrt{\frac{\zeta^2(\mu^2 + \sigma_2^2)}{\alpha^2}}.$$

Thus, the level above which the absorber is activated depends on the damping and the external detuning in the system. We note that f_c can be minimized by reducing the damping in the absorber or increasing α.

In Figure 2-2, we show the frequency-response curves when $f = 0.01$. The bandwidth of the absorber (the region between the points R and S) can be calculated by solving equation (2.36)

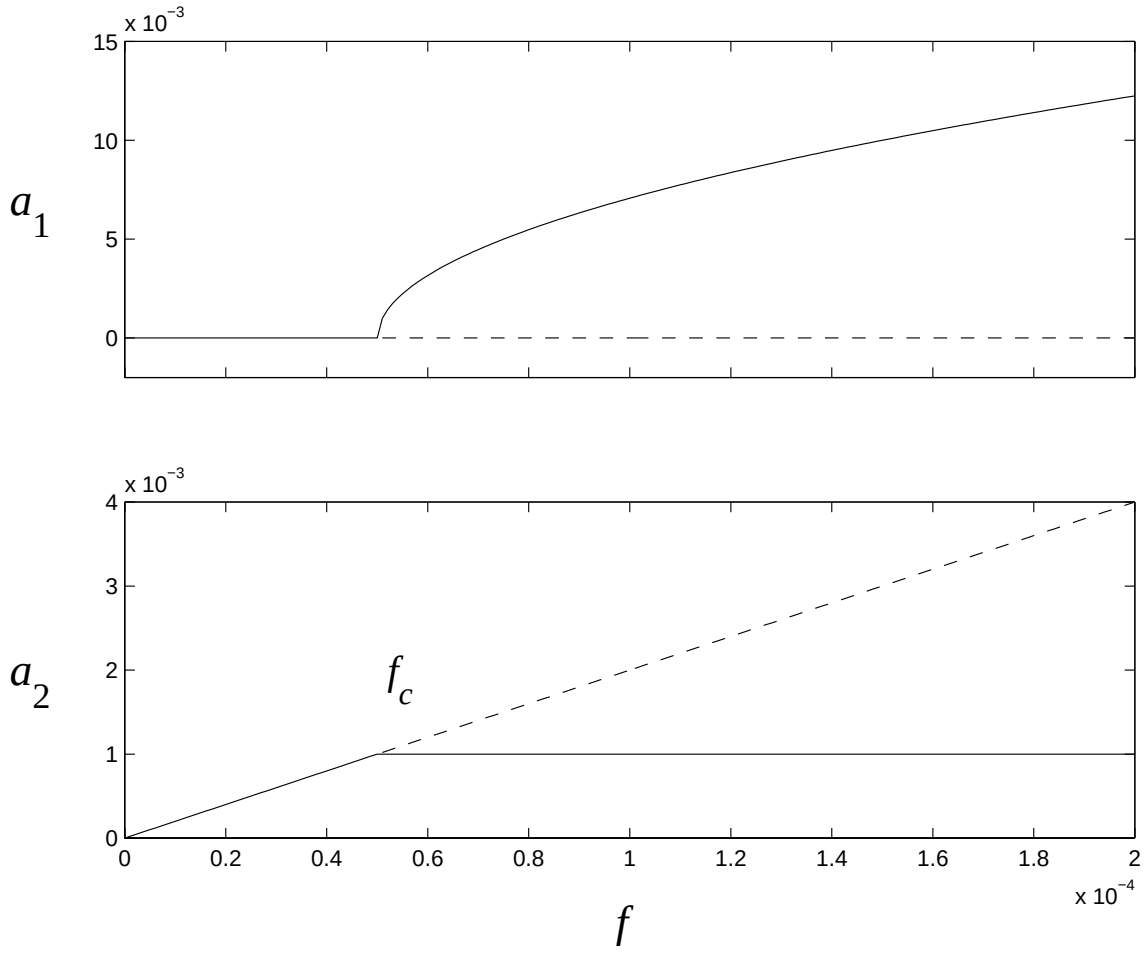

Figure 2-1. Force-response curves when $\mu = 0.05$, $\zeta = 0.001$, and $\alpha = \delta = 1$. (—) Stable and (– –) unstable solutions.

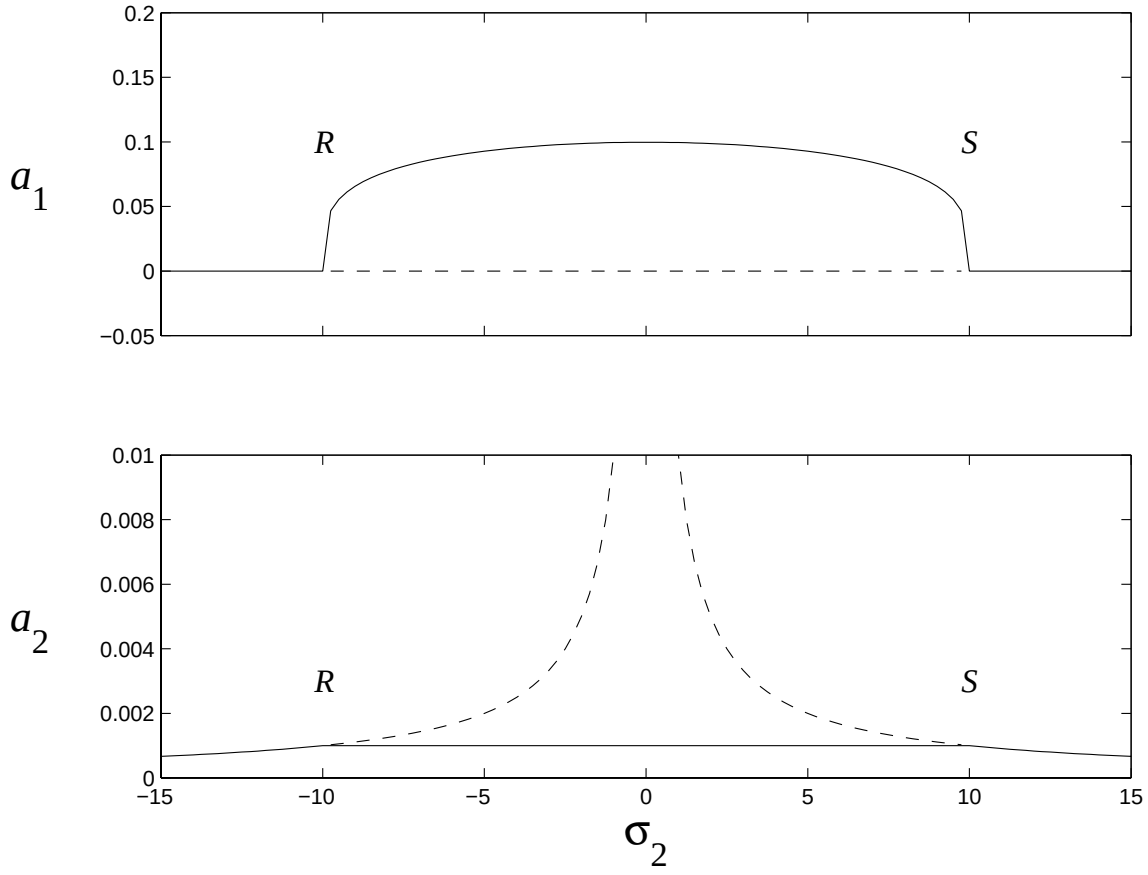

Figure 2-2. Frequency-response curves when $\mu = 0.05$, $\zeta = 0.001$, $\alpha = \delta = 1$, and $f = 0.01$. (—) Stable and (– –) unstable solutions.

for the critical value of σ_2 for which a_1^* admits a real solution. The bandwidth RS is given by

$$RS \;=\; 2\sqrt{\left(\frac{\alpha f}{\zeta}\right)^2 - \mu^2}. \tag{2.63}$$

Thus, the bandwidth is broadened as f increases. Alternatively, it can be broadened as α increases and/or as ζ decreases.

2.4.3 Transient Analysis

In this section, we investigate the transient response of the closed-loop system. The response is dependent on three factors: the eigenvalues of the linear unstable solution, the type of the fixed point associated with the saturation solution, and the controller initial conditions. First, we address these three issues, then we present numerical simulations illustrating the performance of the control scheme.

The response of the unstable linear solution depends on the positive eigenvalue in equations (2.44). The other three are always in the left-half of the complex plane and do not affect the transient response. The eigenvalue is given by

$$\lambda = -\zeta + \frac{\alpha f}{\sqrt{\mu^2 + \sigma_2^2}},$$

where we set $\nu_1 = 0$. The more positive this value is, the faster the repelling effect is. Thus, for a given forcing f, we expect that increasing α will accelerate the approach towards the stable saturated fixed point. We note that if the product αf is kept constant, the eigenvalue remains constant, in complete agreement with the findings of the scaling analysis. The transient response also depends on the type of the attracting fixed point.

The fixed point may be a stable focus or a stable node. In the former case, the response is oscillatory and exhibits a beating phenomenon as it decays, whereas, in the latter case, the response exhibits a smooth decay to steady state. The type of the fixed point can be determined by examining the roots of the characteristic equation (2.45). Substituting equation (2.36) into equation (2.45), we obtain

$$\begin{aligned}\lambda^4 &+ 2\,(\mu+\zeta)\lambda^3 + \left[\mu^2 + 4\,\mu\zeta + \sigma_2^2 + 4\left(-\zeta\mu + \sqrt{(\alpha f)^2 - (\sigma_2\zeta)^2}\right)\right]\lambda^2 \\ &+ \left[2\,\zeta(\mu^2+\sigma_2^2) + 4\,(\mu+\zeta)\left(-\mu\zeta + \sqrt{(\alpha f)^2 - (\sigma_2\zeta)^2}\right)\right]\lambda \\ &+ 4\left(-\mu\zeta + \sqrt{(\alpha f)^2 - (\sigma_2\zeta)^2}\right)\sqrt{(\alpha f)^2 - (\sigma_2\zeta)^2} = 0. \end{aligned} \tag{2.64}$$

For given μ and ζ, the roots of equation (2.64) depend only on σ_2 and the product αf, in agreement again with the scaling analysis. In Figure 2-3, we illustrate the loci of λ when α is varied. We note that in the case of $\sigma_2 = 0$, there is a value of α below which all of the

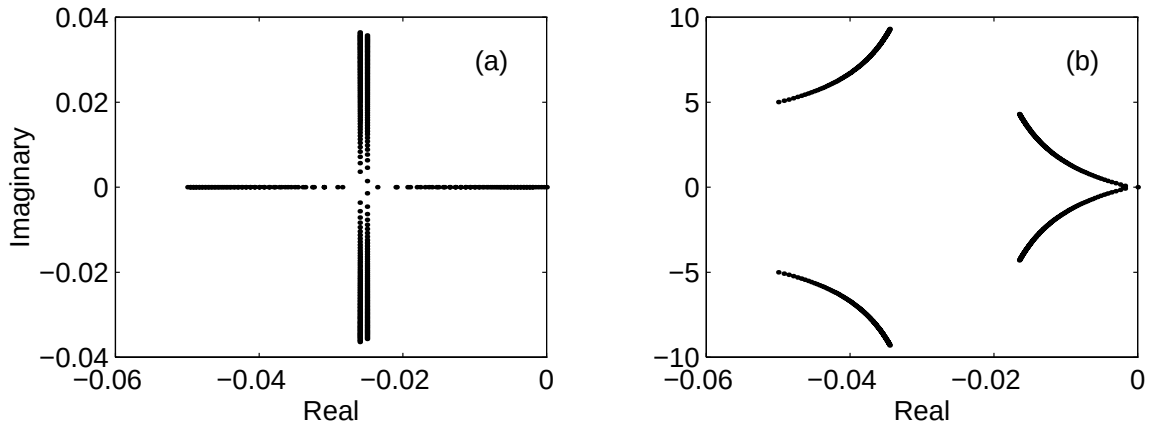

Figure 2-3. Root-locus of equation (2.64) as α is varied when $\mu = 0.05$, $\zeta = 0.001$. (a) $\sigma_2 = 0$ and (b) $\sigma_2 = 5$.

roots are real, as illustrated in Figure 2-3a. For the given parameters μ and ζ, the critical value $(\alpha f)_{cr}$ at which the first two roots are complex can be obtained numerically. Thus, if a nonoscillatory response is desired and the expected forcing level f is known by the user, a corresponding estimate of α may be determined by

$$\alpha = \frac{(\alpha f)_{cr}}{f}. \tag{2.65}$$

When $\sigma_2 \neq 0$, the numerical solution of the characteristic equation (2.64) indicates that it possesses at least two complex-conjugate roots, as shown in Figure 2-3b. Consequently, the transient response always contains an oscillatory component.

In either of the two cases, the approach to steady state is governed by the negative real part of the eigenvalues. Thus, depending on the plant's limitations, the user may elect to chose a gain that results in an oscillatory response but leads to a faster approach to the small-amplitude motion.

By examining the force- and frequency-response curves, we note that within the saturation regime, the controller possesses the trivial solution ($a_1 = 0$), but it is unstable. Thus, the suppression regime can only be activated with a non-zero controller initial condition. The initial conditions of the resonant mode are not available to be chosen in a real application. Nevertheless, if an estimate of the forcing level is available, equation (2.36) can be used

to calculate a controller initial condition based on its steady-state value. If neither $\sigma_2 = 0$ nor an estimate of f is available, it will be necessary for the user to resort to the previous methodology as a starting point for a trial and error approach to determine the optimal gains and initial conditions.

2.4.4 Numerical Simulations

In this section, we validate the results of the previous sections by numerically integrating the equations

$$\ddot{u} + 2\,\mu\,\dot{u} + u = F\cos(\Omega t) + \hat{\delta} v^2, \tag{2.66}$$

$$\ddot{v} + 2\,\zeta\,\dot{v} + \frac{1}{4}\,\Omega^2\,v = \hat{\alpha} u v, \tag{2.67}$$

where $\Omega \approx 1$. The constants F, $\hat{\alpha}$, and $\hat{\delta}$ are related to the parameters appearing in the modulation equations by

$$F = 2\,f, \quad \hat{\alpha} = 2\,\alpha, \quad \hat{\delta} = 4\,\delta, \tag{2.68}$$

and condition (2.65) is rewritten as

$$\hat{\alpha} = \frac{4(\alpha f)_{cr}}{F}. \tag{2.69}$$

One can show that the time scale of equations (2.66) and (2.67) is invariant when the product $\hat{\alpha}F$ is constant. For the purpose of the simulations, we set $\Omega = 1$, $\mu = 0.01$, $F = 0.02$, $v(0) = a_1^*$, $\dot{v}(0) = 0$, and choose $\zeta = 0.00001$. Using equation (2.69), we find that $\hat{\alpha} \approx 0.0026$.

In Figure 2-4, we show results for different values of $\hat{\alpha}$. Upon increasing $\hat{\alpha}$, the transient response is more oscillatory but the plant steady-state amplitude is reduced. Thus, the user may need to fine tune the gain in order to achieve a compromise between the two states.

In Figure 2-5, we illustrate the response of the system when $\hat{\delta}$ is varied. The gain affects only the amplitude of the controller. In all three cases, the response of the plant is unaltered. The choice of $\hat{\delta}$ depends on the characteristics of the actuator and its associated amplifier.

In Figure 2-6, we depict the response of the plant for different controller initial conditions. It is clear that the strategy is most effective when $v(0) \leq a_1^*$. When the initial conditions are

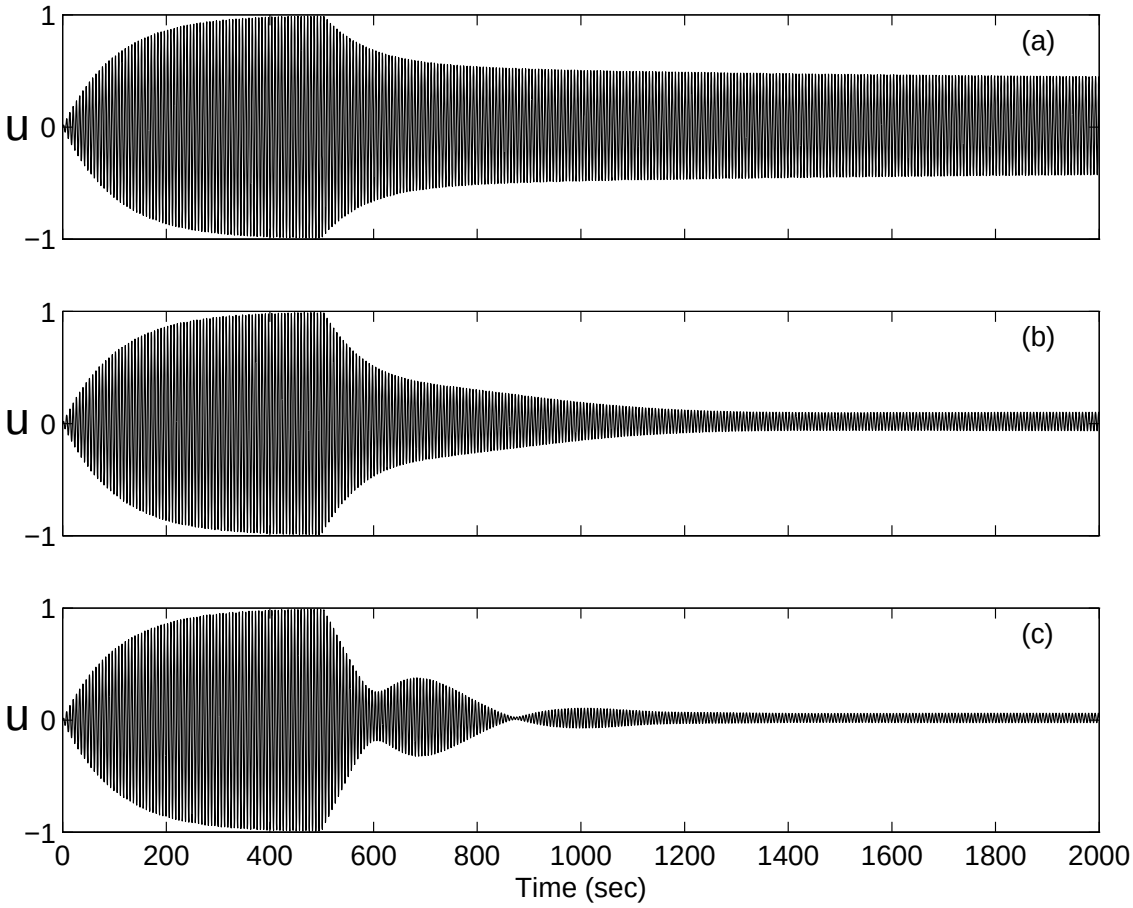

Figure 2-4. Time response of the plant for different $\hat{\alpha}$ when $F = 0.02$ and $\hat{\delta} = 0.0026$. (a) $\hat{\alpha}$=0.00052, (b) $\hat{\alpha}$=0.0026, and (c) $\hat{\alpha}$=0.013. The absorber is turned on at $t = 500$.

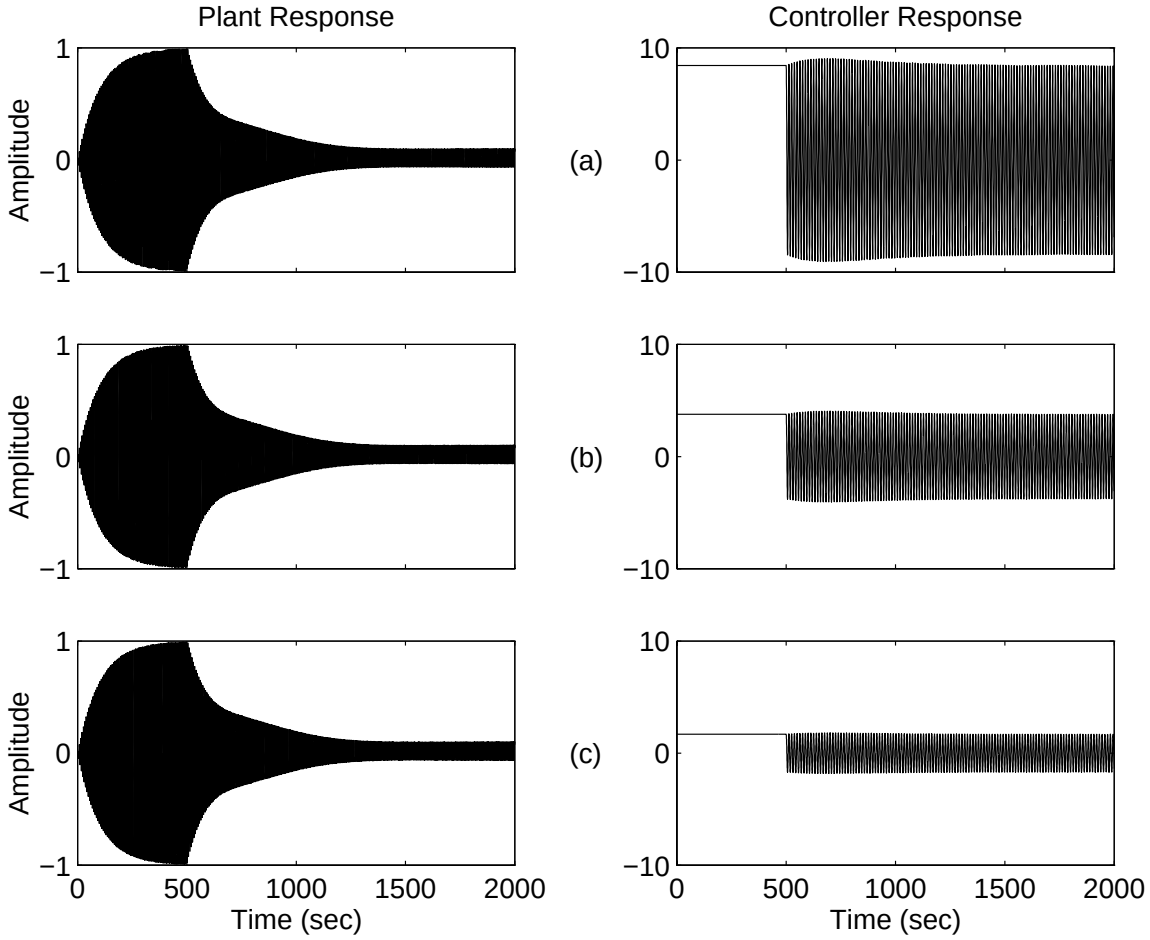

Figure 2-5. Time response of the system for different $\hat{\delta}$ when $F = 0.02$ and $\hat{\alpha} = 0.0026$. (a) $\hat{\delta} = 0.00052$, (b) $\hat{\delta} = 0.0026$, and (c) $\hat{\delta} = 0.013$. The absorber is turned on at $t = 500$.

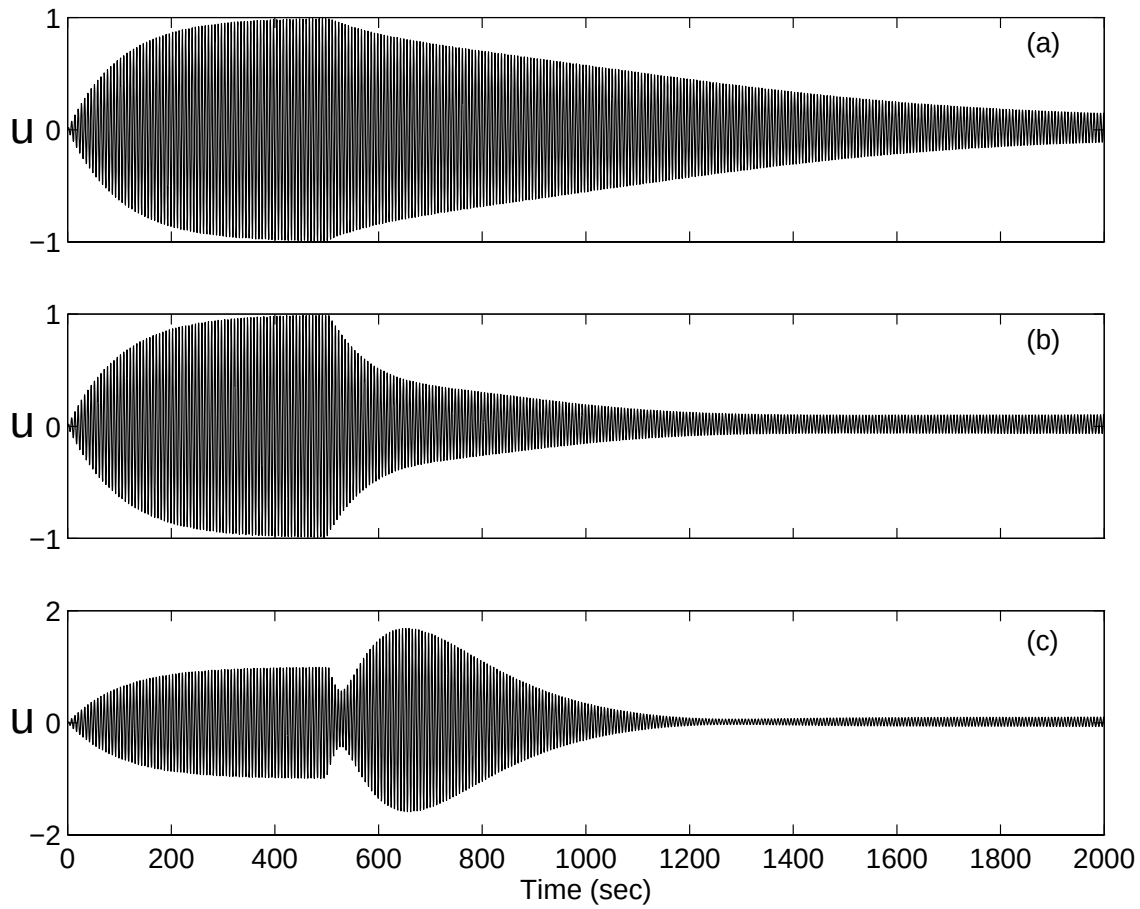

Figure 2-6. Time response of the plant for different controller initial conditions when $F = 0.02$ and $\hat{\alpha} = \hat{\delta} = 0.0026$. (a) $v(0) = \frac{1}{2}\, a_1^*$, (b) $v(0) = a_1^*$, and (c) $v(0) = 2\, a_1^*$. The absorber is turned on at $t = 500$.

too large, energy is detrimentally added to the system, while, when it is too small, the time to achieve a steady state is increased.

2.5 Comparison with the Linear Tuned Absorber

In this section, we compare the performance of the quadratic absorber with that of a linear tuned absorber. First, we develop the linear absorber. Then, we conduct theoretical studies and compare the characteristics and power requirements for both control techniques.

2.5.1 Development of the Linear Absorber

We consider controlling the system governed by

$$\ddot{u} + 2\,\mu\,\dot{u} + \omega_p^2\,u = F e^{i\Omega t} + F_c(t). \tag{2.70}$$

Following the development of the positive position feedback (PPF) filter by Fanson and Caughey [34], we introduce an absorber and a control force given by

$$\ddot{v} + 2\,\zeta\,\dot{v} + \omega_c^2\,v = \omega_c^2 u \quad \text{and} \quad F_c(t) = G\,\omega_p^2\,v, \tag{2.71}$$

respectively. Here, G is a constant gain. We follow Den Hartog [23], assume a solution of the form

$$\left\{ \begin{array}{c} u \\ v \end{array} \right\} = \left\{ \begin{array}{c} A_1 \\ A_2 \end{array} \right\} e^{i\Omega t}, \tag{2.72}$$

and transform equations (2.70) and (2.71) into the complex-valued algebraic system

$$\left[(\omega_p^2 - \Omega^2) + 2i\mu\Omega\right]\, A_1 = F + G\,\omega_p^2\,A_2, \tag{2.73}$$

$$\left[(\omega_c^2 - \Omega^2) + 2i\zeta\Omega\right]\, A_2 = \omega_c^2 A_1. \tag{2.74}$$

Solving for A_1 and A_2, we obtain

$$A_1 = \frac{F\,\left[(\omega_c^2 - \Omega^2) + 2i\zeta\Omega\right]}{\left[(\omega_c^2 - \Omega^2) + 2i\zeta\Omega\right]\left[(\omega_p^2 - \Omega^2) + 2i\mu\Omega\right] - \omega_p^2\,\omega_c^2\,G}, \tag{2.75}$$

$$A_2 = \frac{\omega_c^2\,F}{\left[(\omega_c^2 - \Omega^2) + 2i\zeta\Omega\right]\left[(\omega_p^2 - \Omega^2) + 2i\mu\Omega\right] - \omega_p^2\,\omega_c^2\,G}. \tag{2.76}$$

Similarly to the implementation of the quadratic absorber, the frequency of oscillation of the plant can be measured, and accordingly, the frequency of the linear absorber can be set such that

$$\omega_c = \Omega. \tag{2.77}$$

Then, the resulting amplitudes are

$$A_1 = \frac{2i\zeta\Omega\,F}{2i\zeta\Omega\,\left[(\omega_p^2 - \Omega^2) + 2i\mu\Omega\right] - \omega_p^2\,\Omega^2\,G}, \tag{2.78}$$

$$A_2 \;=\; \frac{\Omega^2\, F}{2i\zeta\Omega\,[(\omega_p^2 - \Omega^2) + 2i\mu\Omega] - \omega_p^2\,\Omega^2\, G}. \tag{2.79}$$

We note that, unlike the case of the nonlinear absorber, the amplitude of the plant A_1 is dependent on the forcing level F. If the absorber damping coefficient is set sufficiently small, then

$$A_1 \;\approx\; 0 \quad \text{and} \quad A_2 \;\approx -\frac{F}{\omega_p^2\, G}. \tag{2.80}$$

2.5.2 Stroke and Power Requirements

We consider controlling the following system:

$$\ddot{u} + \,2\,\mu\,\dot{u} \,+\, u \;=\; F\cos t \,+\, K_a F_c(t), \tag{2.81}$$

where K_a is a constant gain that is dependent on the actuator and amplifier parameters and $F_c(t)$ is a control signal. We introduce quadratic and linear absorbers given by

$$\ddot{v}_1 + 2\,\zeta_1\,\dot{v}_1 \,+\, \frac{1}{4}\,v_1 \;=\; \alpha_1 u v_1 \quad \text{and} \quad F_c \;=\; v_1^2, \tag{2.82}$$

and

$$\ddot{v}_2 + 2\,\zeta_2\,\dot{v}_2 \,+\, v_2 \;=\; \alpha_2 u \quad \text{and} \quad F_c \;=\; v_2, \tag{2.83}$$

respectively. In contrast with the development of Fanson and Caughey, we introduce a user-specified gain α_2 in the linear absorber, equation (2.83). The gain will allow for more flexibility in specifying the transient characteristics of the control law.

For a perfectly controlled plant (i.e., $u{=}0$), the stroke of each absorber is given by

$$v_1 \;=\; \sqrt{\frac{2F}{K_a}}\cos\,\frac{1}{2}\,t \quad \text{and} \quad v_2 \;=\; \frac{F}{K_a}\cos t. \tag{2.84}$$

Thus, for identical actuator and amplifier combination, $|v_1| \geq |v_2|$ when $0 \leq F \leq 2K_a$.

If the actuators are piezoceramics, then the $F_c(t)$ are voltage signals given by

$$F_c \;\equiv\; V_1 \;=\; -\frac{2F}{K_a}\left(\cos\,\frac{1}{2}\,t\right)^2 \quad \text{and} \quad F_c \;\equiv\; V_2 \;=\; -\frac{F}{K_a}\cos t. \tag{2.85}$$

The instantaneous power is defined by

$$P_i \;=\; V_i\, I_i \quad \text{for} \quad i = 1, 2. \tag{2.86}$$

Here, V_i is the control voltage, and the resulting current I_i is given by

$$I_i \;=\; C\,\frac{dV_i}{dt}, \tag{2.87}$$

where C is the effective capacitance of the actuators. Substituting equations (2.85) into equations (2.86) and (2.87), we obtain after a trigonometric manipulation

$$P_1 \;=\; -\frac{C\,F^2}{2\,K_a^2}(\sin 2t + 2\sin t) \quad \text{and} \quad P_2 \;=\; -\frac{C\,F^2}{2\,K_a^2}\sin 2t. \tag{2.88}$$

Clearly, $|P_1| > |P_2|$. The quadratic control signal in equation (2.82) introduces a DC shift that results in an additional harmonic component in the power equation. Next, we confirm the analysis.

The transient response is dependent on the initial conditions of the system. Therefore, we resort to numerical simulations to compare the characteristics of the quadratic and linear absorbers. For the purpose of this study, we design a linear absorber based on the results of the numerical simulations of Section 2.4.4.

To maintain consistency between the two techniques, we set $\zeta_1 = \zeta_2$ and use the same actuator gain K_a in both cases. In Figure 2-7, we show time traces of the plant and absorber responses and the control signal. We choose the gain α_2 to realize a settling time similar to the one achieved in the case of the quadratic absorber. Since $F > 2\,K_a$, the stroke of the linear absorber is larger than the stroke of the quadratic absorber, as shown in Figure 2-7b. In Figure 2-7c, we show time traces of the control force. For comparison purposes, we eliminate the DC shift associated with the nonlinear absorber. In both techniques, the magnitude of the control force is almost equal.

Next, we compare the power requirements. In Figure 2-8, we illustrate the instantaneous power calculated from equation (2.86). The figure indicates that the power requirement of the quadratic absorber is almost twice that of the linear technique.

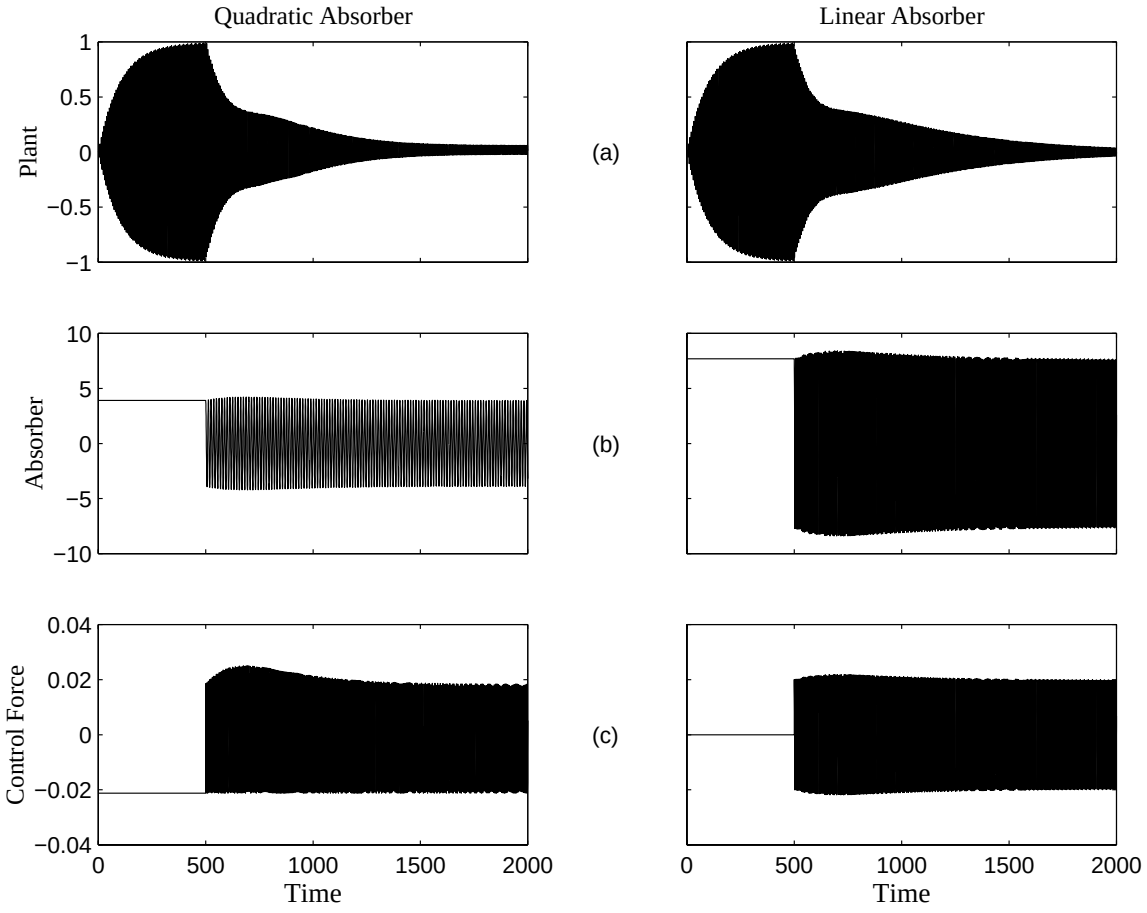

Figure 2-7. Performance comparison between the quadratic and linear absorbers when $F = 0.02,\ \mu = 0.01,\ \zeta_1 = \zeta_2 = 0.00001,\ K_a = 0.0026,\ \alpha_1 = 0.0026,\ \alpha_2 = 0.024,\ v_1(0) \approx \sqrt{\frac{2F}{K_a}}$, $v_2(0) = \frac{F}{K_a}$, and $\dot{v}_1(0) = \dot{v}_2(0) = 0$. (a) Plant response, (b) absorber response, and (c) control force.

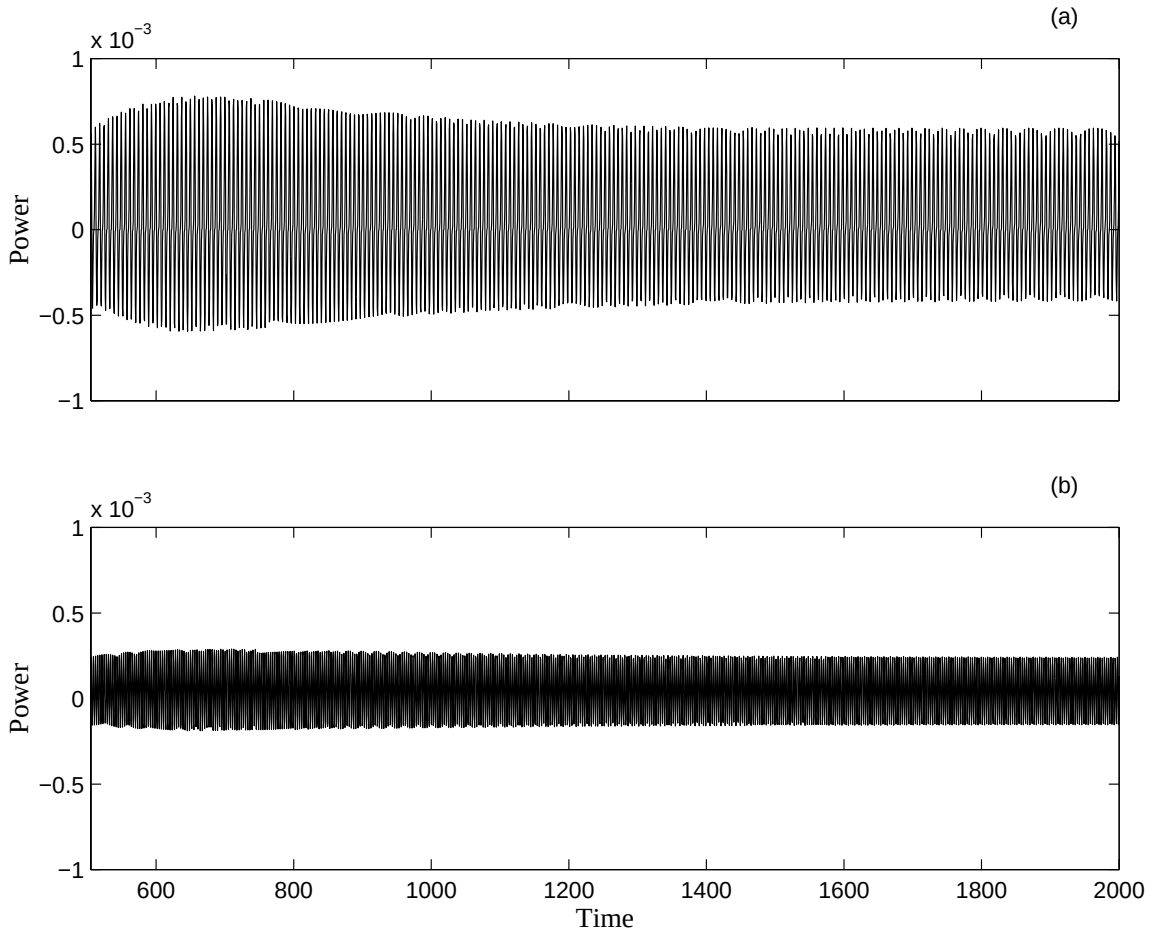

Figure 2-8. Time traces of the instantaneous power. (a) Quadratic absorber and (b) linear absorber.

2.6 Summary

In this chapter, we analyzed theoretically the quadratic vibration absorber. We developed the nonlinear differential equations governing the closed-loop response and used the method of multiple scale to obtain an approximate solution. Then, we investigated application of the control strategy by studying its steady-state and transient characteristics. Additionally, we compared the performance of the quadratic absorber with that of a linear absorber. We showed that the stroke of the nonlinear absorber may be larger or smaller, but its power requirement is always larger than its linear counterpart.

Chapter 3

Application of the Analog Quadratic Absorber

In this chapter, we validate the results of the theoretical studies and demonstrate experimentally the superiority of the quadratic absorber using linear and nonlinear actuators. We develop a mathematical model for each plant-actuator configuration and analyze the associated closed-loop system. Additionally, we present experimental results that substantiate the theoretical findings.

In order to apply the strategy, we design and build an analog electronic circuit that emulates the equation of the absorber. The circuit is used in conjunction with electromotive, piezoelectric, and magnetostrictive actuators. In the first case, we control the motion of a single-degree-of-freedom rigid arm attached to a DC motor. In the second case, we extend the strategy to multi-degree-of-freedom systems and utilize PZT ceramics to suppress the vibrations of flexible cantilever beams when subjected to single- and two-mode excitations. Furthermore, we report the results of an experimental parametric study in which we examine the effect of varying the control gains on the response of the closed-loop system. Finally, we employ a Terfenol-D strut, a nonlinear actuator, to suppress the vibrations of beams subjected to ideal and nonideal excitations.

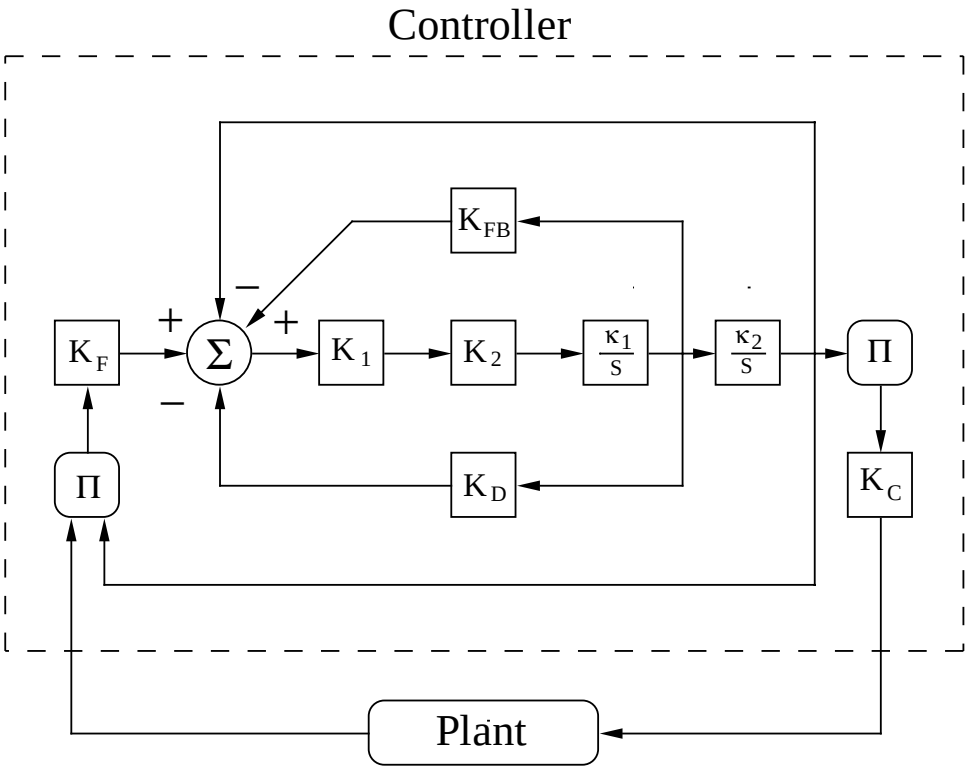

Figure 3-1. A block diagram of the circuit.

3.1 Controller Circuit

The circuit is comprised of operational amplifiers, analog multipliers, and various other electronic hardware. The block diagram depicting the implementation of the circuit is shown in Figure 3-1. The inverse of the time constants of the integrators are labeled κ_1 and κ_2. The natural frequency of the controller is adjusted through the two gains K_1 and K_2, where K_1 represents a coarse gain and K_2 represents a fine tuning gain. The term K_D represents the inherent damping associated with the electronic components. It is reduced by incorporating a positive velocity feedback loop in the circuit and adjusting its amplitude with the variable gain K_{FB}. Hence, the inherent damping of the circuit assembly is reduced by properly tuning K_{FB} such that $K_{FB} \approx K_D$. The nonlinear feedback and control signals are generated by the two multipliers Π. Their respective magnitudes are adjusted through the variable gains K_F and K_C.

3.2 Control of a Rigid Beam Attached to a DC Motor

As an initial proof-of-concept, we implement the strategy on a simple oscillatory system. To this end, we mount a rigid beam on a permanent magnet DC motor. The rigid-body motion of the shaft-beam assembly is rendered oscillatory by connecting a potentiometer to the motor shaft and using its signal as a position feedback signal.

3.2.1 Motor and Controller Equations

Neglecting the electrical time constant, we write the equation of motion of the motor as

$$J_m\,\ddot{\tilde{\theta}} + C_v\,\dot{\tilde{\theta}} + C_c\,\mathrm{sgn}(\dot{\tilde{\theta}}) = T_1 + T_2 + T_F\cos(\Omega t + \tau), \tag{3.1}$$

where $\tilde{\theta}$ represents the rotation of the motor shaft, J_m is the inertia of the shaft-beam assembly, C_v is a viscous damping term due to the back electromagnetic force, C_c models Coulomb friction in the brushes, T_1 is the control signal, T_2 provides the position feedback signal, T_F and Ω are the amplitude and frequency of excitation, respectively, and τ is a constant phase. The position feedback signal T_2 is defined by

$$T_2 = -K K_P\,\tilde{\theta}, \tag{3.2}$$

where K_P is the potentiometer constant and K is a variable gain. Dividing equation (3.1) by J_m, we describe the dynamics of the motor as

$$\ddot{\tilde{\theta}} + 2\,\tilde{\zeta}_2\,\dot{\tilde{\theta}} + \tilde{\mu}\,\mathrm{sgn}(\dot{\tilde{\theta}}) + \omega_2^2\,\tilde{\theta} = T_C + \omega_2^2\,\frac{V_{ref}}{K_P}\cos(\Omega t + \tau), \tag{3.3}$$

where

$$\tilde{\zeta}_2 = \frac{C_v}{2J_m},\quad \tilde{\mu} = \frac{C_c}{J_m},\quad \omega_2 = \sqrt{\frac{K K_P}{J_m}},\quad T_C = \frac{T_1}{J_m},\quad \text{and}\quad \omega_2^2\,\frac{V_{ref}}{K_P} = \frac{T_F}{J_m}.$$

Here, V_{ref} is the desired amplitude of the input voltage. We introduce an absorber governed by

$$\ddot{\tilde{v}} + 2\,\tilde{\zeta}_1\,\dot{\tilde{v}} + \omega_1^2\,\tilde{v} = \tilde{\alpha}\,\tilde{v}\,(K_P\,\tilde{\theta}), \tag{3.4}$$

and a control signal

$$T_C \;=\; \frac{\tilde{\delta}}{K_P}\,\tilde{v}^2, \tag{3.5}$$

where $\tilde{\alpha}$ and $\tilde{\delta}$ are positive constants.

3.2.2 Theoretical Analysis

We obtain an approximate solution of equations (3.3)–(3.5) by the method of averaging [1, 54]. To this end, we scale the state and control variables by letting

$$\tilde{\theta} \;=\; \epsilon\,\theta,\;\; \tilde{v} \;=\; \epsilon\,v,\;\; \tilde{\zeta}_i \;=\; \epsilon\,\zeta_i,\;\; \tilde{\mu} \;=\; \epsilon\,\hat{\mu},\;\; V_{ref} \;=\; \epsilon^2\,f_{ref}, \tag{3.6}$$

where ϵ is a dimensionless bookkeeping parameter. Then, we rewrite equations (3.3)–(3.5) as

$$\ddot{v} \;+\; \omega_1^2\,v \;=\epsilon\;\left(-2\,\zeta_1\,\dot{v} \;+\; K_P\,\tilde{\alpha}\,v\,\theta\right), \tag{3.7}$$

$$\ddot{\theta} \;+\; \omega_2^2\,\theta \;=\; \epsilon\;\left[-\,2\,\zeta_2\,\dot{\theta} \;-\; \hat{\mu}\,\mathrm{sgn}(\,\dot{\theta}) \;+\; \omega_2^2\,\frac{f_{ref}}{K_P}\,\cos\left(\Omega t+\tau\right) \;+\; \frac{\tilde{\delta}}{K_P}\,v^2\right]. \tag{3.8}$$

Following the method of variation of parameters, we let

$$v \;\approx\; a_1\,\cos\left(\omega_1 t+\beta_1\right) \quad\text{and}\quad \theta \;\approx\; \frac{a_2}{K_P}\,\cos\left(\omega_2 t+\beta_2\right), \tag{3.9}$$

subject to the constraints

$$\dot{v} \;=-\,\omega_1\,a_1\,\sin\left(\omega_1 t+\beta_1\right) \quad\text{and}\quad \dot{\theta} \;=-\,\omega_2\,\frac{a_2}{K_P}\,\sin\left(\omega_2 t+\beta_2\right). \tag{3.10}$$

Here, the amplitude a_1 defines the output voltage of the controller, and the amplitude a_2 measures the response of the motor as indicated by the potentiometer voltage. Using equations (3.9) and (3.10), we transform equations (3.7) and (3.8) into the standard form

$$\dot{a}_1 \;=\; -\;\frac{\epsilon}{\omega_1}\Big(2\,\zeta_1\omega_1\,a_1\,\sin\Phi_1 \;+\; \tilde{\alpha}\,a_1 a_2\,\cos\Phi_1\,\cos\Phi_2\Big)\sin\Phi_1, \tag{3.11}$$

$$\begin{aligned}\dot{a}_2 \;=\; -\;\frac{\epsilon}{\omega_2}\Big[&2\,\omega_2\,\zeta\,a_2\,\sin\Phi_2 \;+\; \mu\,K_P\,\mathrm{sgn}\left(\sin\Phi_2\right)\\ &+\;\tilde{\delta}\,a_1^2\,\cos^2\,\Phi_1 \;+\; \omega_2^2\,f_{ref}\,\cos\left(\Omega t+\tau\right)\Big]\,\sin\Phi_2,\end{aligned} \tag{3.12}$$

$$a_1\,\dot{\beta}_1 \;=\; -\;\frac{\epsilon}{\omega_1}\Big(2\,\zeta_1\omega_1\,a_1\;\sin\Phi_1 \;+\; \tilde{\alpha}\,a_1a_2\;\cos\Phi_1\;\cos\Phi_2\Big)\cos\Phi_1, \tag{3.13}$$

$$\begin{aligned} a_2\,\dot{\beta}_2 \;=\; -\;\frac{\epsilon}{\omega_2}\Big[&2\,\omega_2\,\zeta\,a_2\;\sin\Phi_2 \;+\; \mu\,K_P\,\mathrm{sgn}\,(\sin\Phi_2) \\ &+\; \tilde{\delta}\,a_1^2\;\cos^2\;\Phi_1 \;+\; \omega_2^2\;f_{ref}\;\cos\left(\Omega t+\tau\right)\Big]\;\cos\Phi_2, \end{aligned} \tag{3.14}$$

where

$$\Phi_1 \;=\; \omega_1 t+\beta_1 \quad\text{and}\quad \Phi_2 \;=\; \omega_2 t+\beta_2. \tag{3.15}$$

To describe quantitatively the nearness of $2\omega_1$ to ω_2 and Ω to ω_2, we introduce two detuning parameters σ_1 and σ_2 defined by

$$2\,\omega_1 \;=\; \omega_2 \;-\; \epsilon\,\sigma_1 \quad\text{and}\quad \Omega \;=\; \omega_2 \;+\; \epsilon\,\sigma_2. \tag{3.16}$$

Keeping the slowly varying terms on the right-hand sides of equations (3.11)–(3.14), we obtain the modulation equations

$$\dot{a}_1 \;=\; -\,\zeta_1 a_1 \;-\; \alpha\,a_1a_2\sin\gamma_1, \tag{3.17}$$

$$\dot{a}_2 \;=\; -\,\mu \;-\; \zeta_2 a_2 \;+\; \delta\,a_1^2\sin\gamma_1 \;+\; f\sin\gamma_2, \tag{3.18}$$

$$a_1\,\dot{\beta}_1 \;=\; \alpha\,a_1a_2\;\cos\gamma_1, \tag{3.19}$$

$$a_2\,\dot{\beta}_2 \;=\; \delta\,a_1^2\;\cos\gamma_1 \;-\; f\cos\gamma_2, \tag{3.20}$$

where

$$\gamma_1 \;=\; \sigma_1 t \;-\; 2\beta_1 \;+\; \beta_2 \quad\text{and}\quad \gamma_2 \;=\; \sigma_2 t \;-\; \beta_2 \;+\; \tau, \tag{3.21}$$

$$\alpha \;=\; \frac{\tilde{\alpha}}{4\,\omega_1},\;\; \delta \;=\; \frac{\tilde{\delta}}{4\,\omega_2},\quad \mu \;=\; \frac{2\,\hat{\mu}\,K_P}{\pi\,\omega_2},\;\; f \;=\; \frac{1}{2}\,\omega_2\,f_{ref}, \tag{3.22}$$

and ϵ is set equal to unity.

Except for the Coulomb friction term μ, appearing in equation (3.18), equations (3.17)–(3.21) are identical to equations (2.22)–(2.26) obtained in the previous chapter. Therefore, we expect that these equations will also exhibit the saturation phenomenon.

We proceed by solving for the fixed points of equations (3.17)–(3.21), which correspond to periodic solutions of equations (3.7) and (3.8). We set $\dot{a}_1 = \dot{a}_2 = 0$ and $\dot{\gamma}_1 = \dot{\gamma}_2 = 0$ and obtain

$$\zeta_1\,a_1 \;+\; \alpha\,a_1a_2\;\sin\gamma_1 \;=\; 0, \tag{3.23}$$

$$-\mu - \zeta_2 a_2 + \delta a_1^2 \sin\gamma_1 + f \sin\gamma_2 = 0, \tag{3.24}$$

$$\alpha a_1 a_2 \cos\gamma_1 = \frac{1}{2}(\sigma_1 + \sigma_2) a_1, \tag{3.25}$$

$$\delta a_1^2 \cos\gamma_1 - f \cos\gamma_2 = a_2 \sigma_2. \tag{3.26}$$

If we define a critical value of the forcing by $f = \mu$, there are four possible cases. First,

$$f < \mu,$$

and no steady-state solutions exist. Second,

$$f = \mu,$$

and the perturbation method yields the incorrect solution $a_1 = a_2 = 0$. In reality, the motion is dependent on the initial conditions, which are not modeled by equations (3.23)–(3.26). Third,

$$f > \mu, \tag{3.27}$$

$$a_1 = 0, \tag{3.28}$$

$$a_2 = -\frac{\mu\,\zeta_2}{\sigma_2^2 + \zeta_2^2} + \sqrt{\frac{f^2}{\sigma_2^2 + \zeta_2^2} - \left(\frac{\sigma_2\,\mu}{\sigma_2^2 + \zeta_2^2}\right)^2}. \tag{3.29}$$

Fourth,

$$a_1 = a_1(f, \alpha, \delta, \zeta_1, \zeta_2, \mu, \sigma_1, \sigma_2), \tag{3.30}$$

$$a_2 = \frac{1}{\alpha}\sqrt{\zeta_1^2 + \frac{1}{4}(\sigma_1 + \sigma_2)^2}. \tag{3.31}$$

We note that a_2 is independent of f, which suggests that the amplitude of motion of the motor reaches a constant ceiling. Using equations (3.16), we rewrite equation (3.31) as

$$a_2 = \frac{1}{\alpha}\sqrt{\zeta_1^2 + \frac{(\Omega - 2\omega_1)^2}{4\epsilon^2}}. \tag{3.32}$$

Hence, if we tune the absorber frequency such that $2\omega_1 = \Omega$, the motion of the motor can be virtually eliminated. Then, the resulting fixed points are

$$a_1 = \sqrt{\frac{-(\alpha\mu + \zeta_1\,\zeta_2) + (\alpha^2 f^2 - \sigma_2^2 \zeta_1^2)^{\frac{1}{2}}}{\alpha\,\delta}} \quad \text{and} \quad a_2 = \frac{\zeta_1}{\alpha}, \tag{3.33}$$

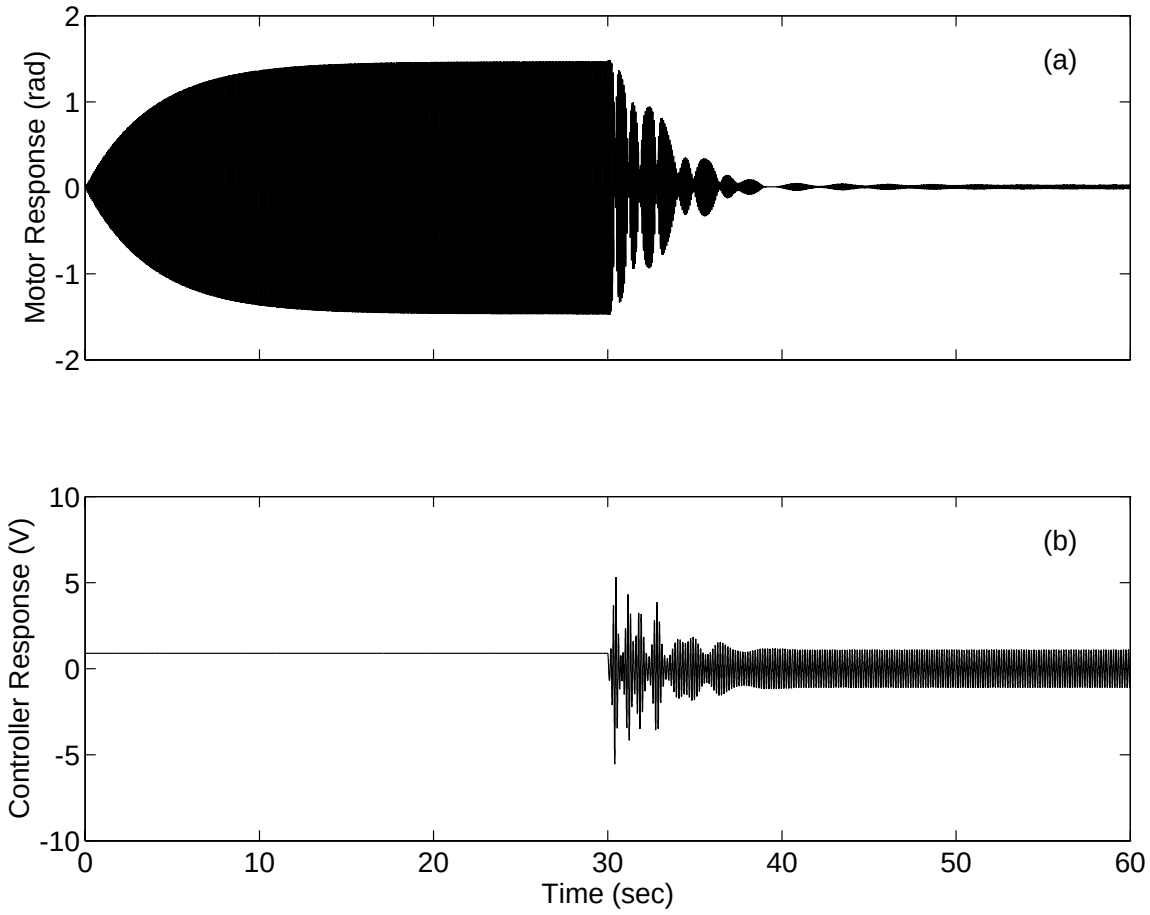

Figure 3-2. A numerical implementation of the control technique when $V_{ref} = 60\,mV$ and $v(0) = 0.9\,V$. (a) Motor and (b) controller.

when

$$f \geq \sqrt{\frac{(\alpha\mu + \zeta_1\zeta_2)^2 + \zeta_1^2\sigma_2^2}{\alpha^2}}. \tag{3.34}$$

To verify the solution derived in the fourth case, we integrate equations (3.3)–(3.5) numerically. In Figure 3-2, we illustrate the response of the motor and controller for $V_{ref} = 60\,mV$, $\Omega = \omega_2 = 88\,\text{rad/sec}$, and $2\,\omega_1 = \Omega$. The system is allowed to reach steady state, and the controller is activated at $t = 30\,\text{sec}$. The controller is very effective in reducing the amplitude of motion of the motor.

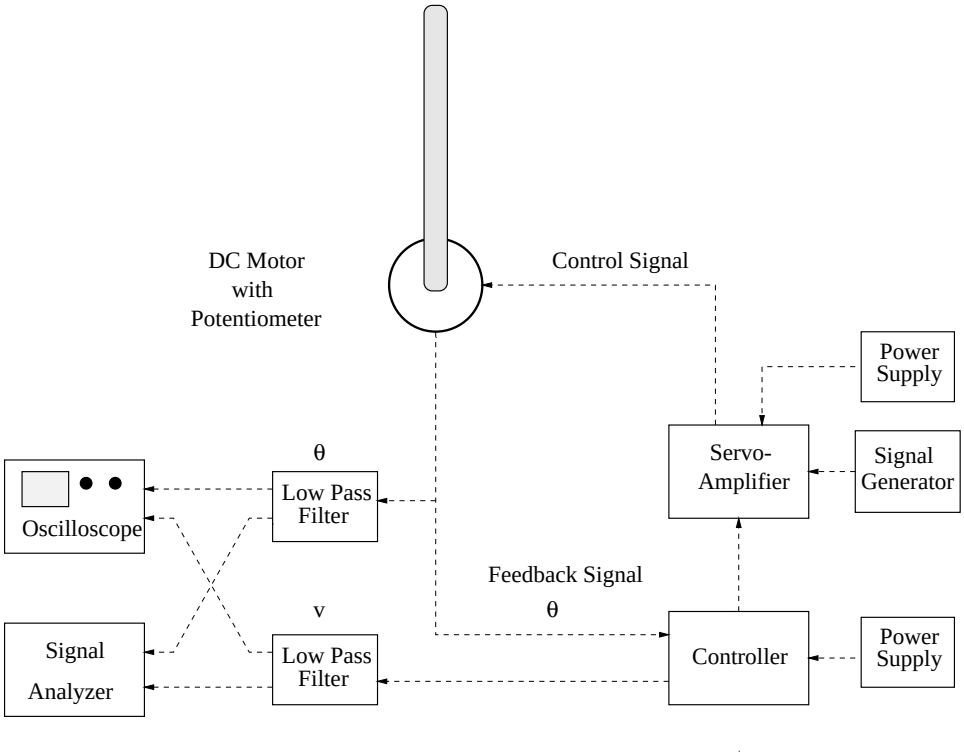

Figure 3-3. A schematic of the motor experimental setup.

3.2.3 Experiments

The experimental setup consists of a permanent magnet DC motor, a servo-amplifier, the electronic circuit, and a signal generator. A schematic of the setup is shown in Figure 3-3. A list of the equipment is included in Appendix A. We mount a rigid beam on one end of the motor shaft to provide an inertia load and connect a potentiometer to the other end to create the position feedback signal. The signal from the potentiometer is sent to the electronic circuit where the control and feedback signals, T_1 and T_2, are created and summed with the forcing term introduced by the signal generator. This total signal, the right-hand side of equation (3.1), is then sent to the servo-amplifier that drives the motor. The position signal of the motor and the response signal of the controller are monitored on a digital oscilloscope and an analyzer after being passed through two low-pass filters.

We adjust the motor position feedback gain K to obtain a free-oscillation frequency of

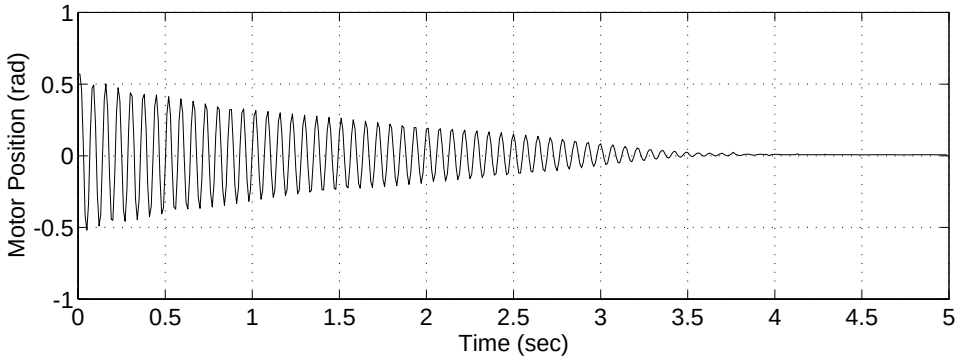

Figure 3-4. Free oscillations of the motor when $\theta(0) \approx 0.6\,\text{rad}$.

$\omega_2 \approx 88.0\,\text{rad/sec}$, which is equivalent to approximately 14 Hz. In Figure 3-4, we illustrate the free-vibration behavior of the motor.

The experiment is carried out by forcing the motor at its resonance frequency $\Omega \approx 88.0\,\text{rad/sec}$ ($\approx 14\,\text{Hz}$). Initially the forcing amplitude is set at $V_{ref} = 60\,mV$. We note that the steady-state amplitude is considerably less than that obtained through numerical simulation. This can be attributed to saturation in the motor, preventing it from achieving the resonant response. The controller is activated at $t \approx 35\,\text{sec}$. As illustrated in Figure 3-5, the controller is very successful in reducing the motor's amplitude of oscillations. To further examine the performance of the controller, we increase the forcing amplitude in steps of $20\,mV$ at $t \approx 75\,\text{sec}$, $t \approx 97\,\text{sec}$, and $t \approx 125\,\text{sec}$ to reach a value of $f = 120\,mV$. In all of these cases, the response amplitude of the motor remains almost constant as the controller response is increased. At $t \approx 135\,\text{sec}$, the controller is turned off for a period of 10 seconds, allowing the resonant response to develop at $V_{ref} = 120\,mV$. Upon the reactivation of the controller, the motion of the motor is again suppressed.

3.3 Control of Flexible Beams with PZT Actuators

Having applied successfully the control technique to a simple single-degree-of-freedom plant, we now investigate its implementation for continuous systems. We consider the problem

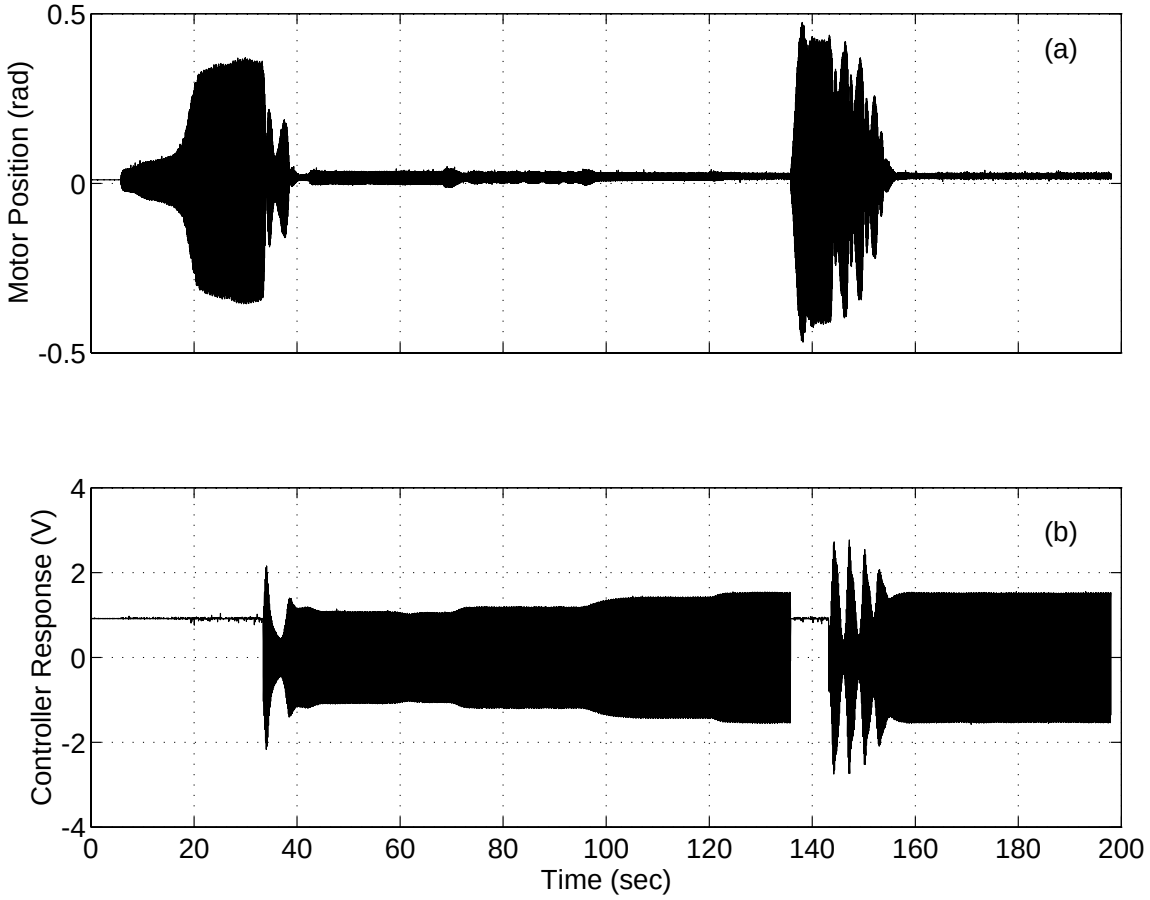

Figure 3-5. An experimental implementation of the control technique when $K_C = K_F = 0.1$, $\theta(0) = 0\,\text{rad}$, and $v(0) = 0.9\,V$. (a) Motor and (b) controller.

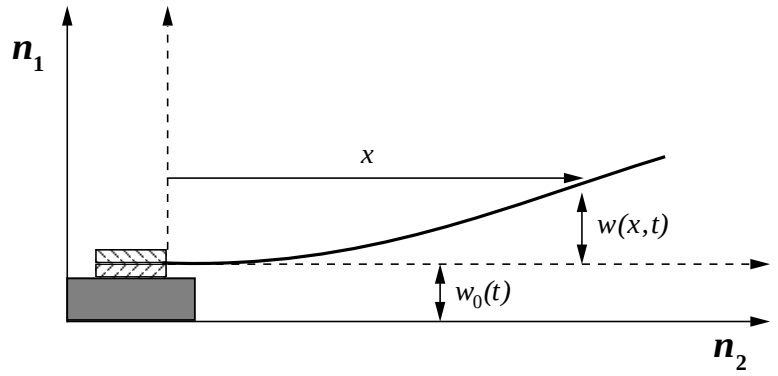

Figure 3-6. The beam and shaker configuration.

of suppressing the vibrations of flexible cantilever beams. We resort to PZT ceramics as actuators and use strain gages to generate the feedback signal.

3.3.1 Actuator and Beam Equations

The system consists of a beam mounted on a shaker that delivers the external excitation. The setup is shown in Figure 3-6. The deflection of the beam is denoted by $w(x,t)$, and the motion of the shaker is given by $w_0(t)$.

Application of the control effort is achieved by attaching two patches of piezoelectric material at both sides of the base of the beam, as illustrated in Figure 3-7. The actuators have width b and thickness t_a. They are attached to the beam such that they subject it to a bending moment. In this analysis, we consider the moment to be uniformly distributed over the length of the actuators and assume that it is defined by

$$M(x,t) \;=\; V_a(t)\, K_M \Big[H(x - x_1) \;-\; H(x - x_2) \Big], \tag{3.35}$$

where

$$K_M \;=\; b\, d_{31} E_a (t_a \;+\; t_b) K. \tag{3.36}$$

Here, d_{31} is a piezoelectric constant, E_a is the actuators' Young modulus, t_b is the thickness of the beam, K is an amplifier gain, $V_a(t)$ is the control voltage, and $H(x)$ is the Heaviside step function.

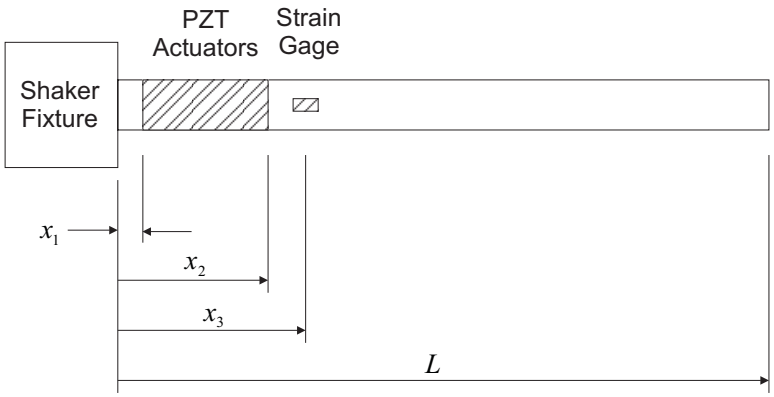

Figure 3-7. The locations of the actuators and the strain gage.

Following the developments by Meirovitch [57] and Fanson and Caughey [34] and including viscous damping, we write the equation of motion of the beam as

$$\rho A \frac{\partial^2 w}{\partial t^2} + C(x) \frac{\partial w}{\partial t} + EI \frac{\partial^4 w}{\partial x^4} = -\rho A \frac{d^2 w_0}{dt^2} + \frac{\partial^2 M}{\partial x^2}, \tag{3.37}$$

where A is the cross-sectional area of the beam, ρ is the mass density, EI is the flexural rigidity, and $C(x)$ is a damping coefficient. The boundary conditions associated with this formulation are

$$\begin{aligned} w(0,t) &= 0, \quad w'(0,t) = 0, \\ w''(L,t) &= 0, \quad w'''(L,t) = 0, \end{aligned} \tag{3.38}$$

where the prime indicates differentiation with respect to x.

We expand the beam deflection $w(x,t)$ as

$$w(x,t) = \sum_{n=1}^{\infty} \phi_n(x)\, u_n(t), \tag{3.39}$$

where the $\phi_n(x)$ are the linear undamped mode shapes and the u_n are generalized coordinates. Neglecting the stiffening effect of the actuators, we assume that the mode shapes are orthonormalized such that

$$\int_0^L \phi_r\, \phi_s\, dx = \delta_{rs}, \tag{3.40}$$

where δ_{rs} is the Kronecker delta. Substituting equations (3.35) and (3.39) into equation (3.37)

leads to

$$\sum_{n=1}^{\infty} \left[\rho A\,\phi_n\,\ddot{u}_n \,+\, C(x)\,\phi_n\,\dot{u}_n \,+\, EI\,\phi_n^{iv}\,u_n\right] = -\rho A\,\ddot{w}_0 + K_M\,V_a(t)\,\frac{\partial}{\partial\,x}\left[\delta(x-x_1) \,-\, \delta(x-x_2)\right]. \tag{3.41}$$

Multiplying equation (3.41) by $\phi_m(x)$ and integrating the result over the interval $[0, L]$ yields

$$\ddot{u}_m \,+\, 2\,\hat{\mu}_m\dot{u}_m \,+\, \omega_m^2\,u_m \,=\, P_m\,\ddot{w}_0 \,+\, M_m\,V_a(t), \quad m \,=\, 1, 2, \ldots, \infty \tag{3.42}$$

where the ω_m are the natural frequencies of the cantilever beam,

$$\hat{\mu}_m \,=\, \frac{1}{2\,\rho A}\int_0^L C(x)\,\phi_m^2\,dx, \tag{3.43}$$

$$P_m \,=\, -\int_0^L \phi_m\,dx, \quad M_m \,=\, \frac{K_M}{\rho A}\,\left[\phi_m'(x_2) \,-\, \phi_m'(x_1)\right], \tag{3.44}$$

and the damping is assumed to be modal.

3.3.2 Controller Equations

We consider the case of primary resonances and define the shaker acceleration $\ddot{w}_0$ by

$$\ddot{w}_0 = \sum_{j=1}^{N} \hat{F}_j\,\cos(\Omega_j\,t + \tau_j), \tag{3.45}$$

where the $\hat{F}_j$ and Ω_j are the amplitudes and frequencies of the excitation, respectively, the τ_j are constant phases, and N is the number of resonant modes. We assume, without loss of generality, that the first N modes of the beam are excited. Therefore, we let $\Omega_j \approx \omega_j$ and introduce N controllers taking the form

$$\ddot{v}_j \,+\, 2\,\hat{\zeta}_j\,\dot{v}_j \,+\, \hat{\omega}_j^2\,v_j \,=\, \hat{\alpha}_j\,v_j\,e(x_3,t), \qquad j \,=\, 1, 2, \ldots, N \tag{3.46}$$

and a control signal

$$V_a(t) \,=\, \sum_{j=1}^{N} \hat{\delta}_j\,v_j^2, \tag{3.47}$$

where the controllers' natural frequencies $\hat{\omega}_j$ are chosen such that $2\hat{\omega}_j \approx \omega_j$, the $\hat{\zeta}_j$ are the damping coefficients, the $\hat{\alpha}_j$ and $\hat{\delta}_j$ are constant gains, and $e(x_3, t)$ is the strain at the

surface of the beam at location x_3. Assuming simple beam theory, we approximate the strain measured by the gage by

$$e(x,t) \;=\; -\frac{1}{2}\,\frac{\partial^2 w}{\partial x^2}\,t_b. \tag{3.48}$$

Using equation (3.39), we write the strain as

$$e(x,t) \;=\; -\frac{1}{2}\,t_b \sum_{m=1}^{\infty} \phi_m''(x)\,u_m(t). \tag{3.49}$$

Inserting equations (3.45), (3.47), and (3.49) into equations (3.42) and (3.46) leads to

$$\ddot{u}_m \;+\; 2\,\hat{\mu}_m\,\dot{u}_m \;+\; \omega_m^2\,u_m \;=\; \sum_{j=1}^{N} \left[P_m\,\hat{F}_j\,\cos(\Omega_j t + \tau_j) + \; M_m\,\hat{\delta}_j\,v_j^2\right], \tag{3.50}$$

$$\ddot{v}_j \;+\; 2\,\hat{\zeta}_j\,\dot{v}_j \;+\; \hat{\omega}_j^2\,v_j \;=\; -\frac{1}{2}\,t_b\,\hat{\alpha}_j\,v_j \sum_{m=1}^{\infty} \phi_m''(x_3)\,u_m. \tag{3.51}$$

3.3.3 Perturbation Analysis

We use the method of multiple scales to obtain an approximate solution to equations (3.50) and (3.51). First, we scale the damping and forcing terms by letting

$$\hat{\mu}_m \;=\; \epsilon\,\mu_m, \quad \hat{\zeta}_j \;=\; \epsilon\,\zeta_j, \quad \hat{F}_j \;=\; \epsilon^2\,F_j, \tag{3.52}$$

where ϵ is a dimensionless bookkeeping parameter. Second, we seek expansions of the u_m and v_j in the form

$$u_m \;\approx\; \epsilon u_{m1}(T_0,T_1) + \epsilon^2 u_{m2}(T_0,T_1), \tag{3.53}$$

$$v_j \;\approx\; \epsilon v_{j1}(T_0,T_1) + \epsilon^2 v_{j2}(T_0,T_1), \tag{3.54}$$

where $T_0 = t$ and $T_1 = \epsilon\,t$. The derivatives with respect to time are expressed in term of the new time scales as

$$\frac{d}{dt} \;=\; D_0 \;+\; \epsilon\,D_1 \;+\cdots \quad \text{and} \quad \frac{d^2}{dt^2} \;=\; D_0^2 \;+\; 2\,\epsilon\,D_0\,D_1 \;+\cdots, \tag{3.55}$$

where $D_k \equiv \partial/\partial T_k$. Substituting equations (3.52)–(3.55) into equations (3.50) and (3.51) and equating coefficients of like powers of ϵ leads to

Order (ϵ):

$$D_0^2\, u_{m1} \,+\, \omega_m^2\, u_{m1} \,=\, 0, \tag{3.56}$$

$$D_0^2\, v_{j1} \,+\, \hat{\omega}_j^2\, v_{j1} \,=\, 0, \tag{3.57}$$

Order (ϵ^2):

$$\begin{aligned} D_0^2\, u_{m2} \,+\, \omega_m^2\, u_{m2} \,=&\, -\,2\, D_0\, (D_1\, u_{m1} \,+\, \mu_m\, u_{m1}) \\ &+ \sum_{j=1}^{N} \left[P_m\, F_j\, \cos(\Omega_j t + \tau_j) + M_m\, \hat{\delta}_j\, v_{j1}^2 \right], \end{aligned} \tag{3.58}$$

$$D_0^2\, v_{j2} \,+\, \hat{\omega}_j^2\, v_{j2} \,=\, -\,2\, D_0\, (D_1\, v_{j1} \,+\, \zeta_j\, v_{j1}) \,-\, \frac{1}{2}\, t_b\, \hat{\alpha}_j\, v_{j1} \sum_{m=1}^{\infty} \phi_m''(x_3)\, u_{m1}. \tag{3.59}$$

The solution of equations (3.56) and (3.57) can be expressed as

$$u_{m1} \,=\, A_m(T_1)\, e^{i\omega_m T_0} \,+\, \overline{A}_m(T_1)\, e^{-i\omega_m T_0}, \tag{3.60}$$

$$v_{j1} \,=\, B_j(T_1)\, e^{i\hat{\omega}_j T_0} \,+\, \overline{B}_j(T_1)\, e^{-i\hat{\omega}_j T_0}. \tag{3.61}$$

The quantities $A_m(T_1)$ and $B_j(T_1)$ are unknown at this stage of the analysis. They will be determined by eliminating the secular terms at the next level of approximation.

Substituting equations (3.60) and (3.61) into equations (3.58) and (3.59) yields

$$\begin{aligned} D_0^2\, u_{m2} \,+\, \omega_m^2\, u_{m2} \,=&\, -2\, i\, \omega_m\, (D_1 A_m \,+\, \mu_m\, A_m)\, e^{i\omega_m T_0} \\ &+ \sum_{j=1}^{N} \left[M_m\, \hat{\delta}_j\, \left(B_j^2\, e^{2i\hat{\omega}_j T_0} \,+\, B_j\, \overline{B}_j \right) \,+\, \frac{1}{2}\, P_m\, F_j\, e^{i(\Omega_j T_0 + \tau_j)} \right] \,+\, \text{cc}, \end{aligned} \tag{3.62}$$

$$\begin{aligned} D_0^2\, v_{j2} \,+\, \hat{\omega}_j^2\, v_{j2} \,=&\, -\,2\, i\, \hat{\omega}_j\, (D_1 B_j \,+\, \zeta_j\, B_j)\, e^{i\hat{\omega}_j T_0} \\ &-\, \frac{1}{2}\, t_b\, \hat{\alpha}_j\, \left(B_j\, e^{i\hat{\omega}_j T_0} \,+\, \overline{B}_j\, e^{-i\hat{\omega}_j T_0} \right) \sum_{m=1}^{\infty} \phi_m''(x_3)\, A_m\, e^{i\omega_m T_0} \,+\, \text{cc}, \end{aligned} \tag{3.63}$$

where cc stands for the complex conjugate of the preceding terms. To describe quantitatively the nearness of $2\,\hat{\omega}_j$ to ω_j and Ω_j to ω_j, we introduce two sets of detuning parameters $\hat{\sigma}_j$ and

σ_j defined by

$$2\,\hat{\omega}_j \;=\; \omega_j \;-\; \epsilon\,\hat{\sigma}_j \quad \text{and} \quad \Omega_j \;=\; \omega_j \;+\; \epsilon\,\sigma_j. \tag{3.64}$$

Then, inserting equations (3.64) in equations (3.62) and (3.63) and eliminating the terms that produce secular terms yields

$$D_1 A_m \;+\; \mu_m\, A_m \;=\; 0 \qquad\qquad \text{for} \;\; m > N \tag{3.65}$$

and

$$2\,i\,(D_1 A_j + \mu_j A_j) \;+\; 4\,\delta_j\, B_j^2\, e^{-i\hat{\sigma}_j T_1} \;-\; f_j\, e^{i(\sigma_j T_1 + \tau_j)} \;=\; 0, \tag{3.66}$$

$$2\,i\,(D_1 B_j + \zeta_j B_j) \;+\; 4\,\alpha_j\, A_j \overline{B}_j\, e^{i\hat{\sigma}_j T_1} \;=\; 0, \tag{3.67}$$

where

$$f_j \;=\; \frac{P_j F_j}{2\,\omega_j}, \quad \delta_j \;=\; -\,\frac{M_j\,\hat{\delta}_j}{4\,\omega_j}, \quad \alpha_j \;=\; \frac{t_b\;\hat{\alpha}_j\,\phi_j''(x_3)}{8\,\hat{\omega}_j}. \tag{3.68}$$

It follows from equation (3.65) that, to the first approximation, the A_m and hence the u_m for $m \neq j$ decay exponentially with time. Thus, the quadratic coupling creates a filtering process by which each of the controllers influences only the mode which is internally resonant with it, irrespective of the number of modes being monitored or any noise that may be contaminating the sensor signal $e(x_3, t)$. However, we note that the effectiveness of the strategy depends on the location of the sensor. The interaction coefficient α_j may be equal to zero if the jth mode possesses a node at $x = x_3$. Consequently, the strategy may not be capable of controlling that particular mode.

Next, we express equations (3.66) and (3.67) in real variables by letting

$$A_j \;=\; \frac{1}{2}\,a_j(T_1)\,e^{i\beta_j(T_1)} \quad \text{and} \quad B_j \;=\; \frac{1}{2}\,b_j(T_1)\,e^{i\varphi_j(T_1)}. \tag{3.69}$$

Substituting equations (3.69) into equations (3.66) and (3.67) and separating real and imaginary parts yields the following N sets of modulation equations:

$$a' \;=\; -\,\mu a \;+\; \delta\, b^2 \sin\Phi \;+\; f \sin\Psi, \tag{3.70}$$

$$b' \;=\; -\,\zeta b \;-\; \alpha\, a\, b \sin\Phi, \tag{3.71}$$

$$a\,\beta' \;=\; \delta\, b^2\, \cos\Phi \;-\; f \cos\Psi, \tag{3.72}$$

$$b\,\varphi' \;=\; \alpha\, a\, b\, \cos\Phi, \tag{3.73}$$

where

$$\Phi = \hat{\sigma}T_1 - 2\varphi + \beta \quad \text{and} \quad \Psi = \sigma T_1 - \beta + \tau, \tag{3.74}$$

the prime represents differentiation with respect to the slow time variable T_1, and the subscript j has been dropped for convenience.

Equations (3.70)–(3.74) are identical to equations (2.22)–(2.26). Thus, we have shown that by properly tuning each controller to the resonant mode associated with it, the solution of the nonlinearly coupled multi-degree-of-freedom problem reduces to the solution of a series of two quadratically coupled oscillators.

3.3.4 Experimental Setup and Procedure

A series of experiments are carried out to evaluate qualitatively the performance of the control strategy. We apply the strategy to control single- and multi-mode vibrations of two cantilever steel beams. Then, we conduct a parametric study to examine the effects of the gains $\hat{\alpha}$ and $\hat{\delta}$ on the response of the closed-loop system.

Two steel beams are used to carry out the experiments. Two patches of the piezoelectric material Lead-Zirconate-Titanate and a strain gage are attached near the root of each beam, as illustrated in Figure 3-7. The experimental setup is depicted in Figure 3-8. The setup consists of a 100-lb permanent magnet shaker and its driving power amplifier, a piezoamplifier, the controller circuits, a strain-gage signal conditioner, an accelerometer, and signal generators. The properties of the beams (No. I and II) and the actuators and the details of the equipment are listed in Appendix A.

The beams are attached to the shaker through a fixture, and the signal generators are used to drive the shaker at the desired amplitudes and frequencies. The base motion of the shaker is monitored by an accelerometer attached to the clamping fixture. The strain gage signal from the conditioner is fed to the controllers without any filtering, and the nonlinear control signal is generated, amplified, and sent to the actuators. The responses of the beam and the circuits are monitored by an oscilloscope and a signal analyzer and collected by a computer.

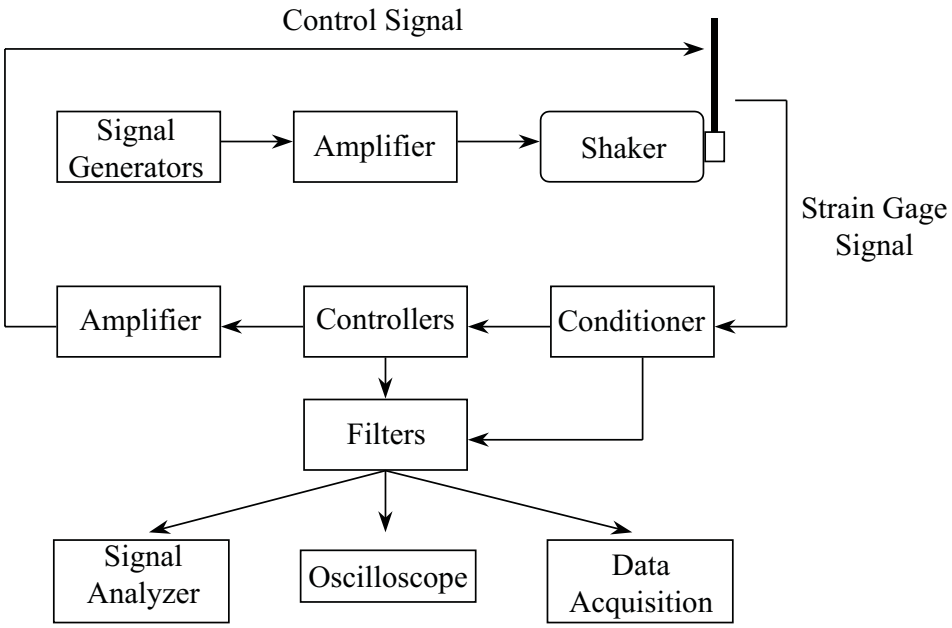

Figure 3-8. A schematic of the PZT experimental setup.

Each beam is mounted to the shaker and subjected to a random base excitation, and the first two natural frequencies are obtained by feeding the strain gage signal to the analyzer and monitoring the locations of the peaks on its screen. Then, the frequency of each circuit is adjusted, through the gain K_1, to one-half the frequency of the mode to be controlled.

The experiments are carried out in two steps. First, the shaker-beam setup is forced using the signal generators while fine tuning the forcing frequency to achieve the maximum steady-state peak-to-peak strain voltage signal. Second, the controllers are activated, and after the transients die out, the fine gain K_2 is adjusted to minimize the saturated response. Suitable values for the gains K_F and K_C are obtained by trial and error, and the controllers' initial conditions are chosen arbitrarily close to zero.

3.3.5 Control of Single- and Two-Mode Excitations

The first experiment consists of controlling the response of the first mode of beam I. The natural frequency is $\omega_1 \approx 72\,\text{rad/sec}$, which is equivalent to $11.5\,\text{Hz}$. We subject the beam

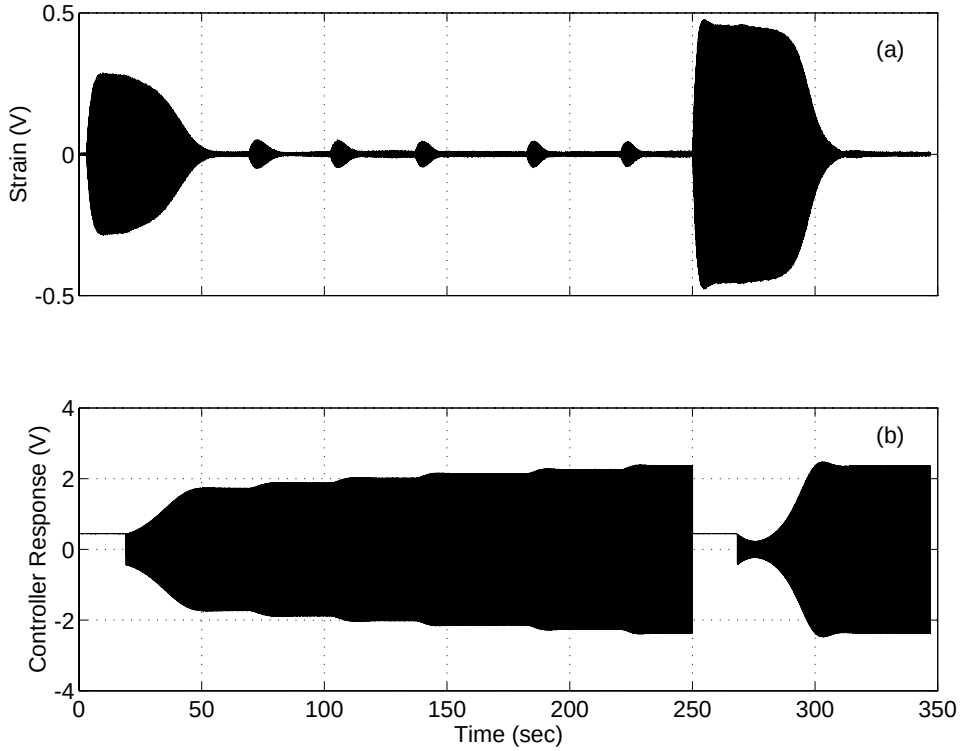

Figure 3-9. Control of the first mode of beam I: (a) strain voltage and (b) controller response.

to an initial base excitation of $5.8\,mg$ and increase it in five steps to $8.9\,mg$. In Figure 3-9, we illustrate the response of the beam when the controller is activated at $t \approx 20\,\text{sec}$. At $t \approx 250\,\text{sec}$, the controller is deactivated allowing the response to fully develop at $8.9\,mg$. The controller is activated again at $t \approx 260\,\text{sec}$.

In the second experiment, we simultaneously excite the first two modes of beam II. Here, we use two controllers. The natural frequencies are $\omega_1 \approx 27\,\text{rad/sec}$ and $\omega_2 \approx 166.5\,\text{rad/sec}$, which are equivalent to 4.3 Hz and 26.5 Hz, respectively. The beam is subjected to a base excitation of $43\,mg$. In Figure 3-10, we illustrate the response when the controllers are activated at $t \approx 60\,\text{sec}$. The saturated steady-state response is attained at $t \approx 190\,\text{sec}$. In Figure 3-11, we show the time response and power spectral density before and after the activation of the controllers. Clearly, the strategy is very effective in suppressing the vibrations of both structures.

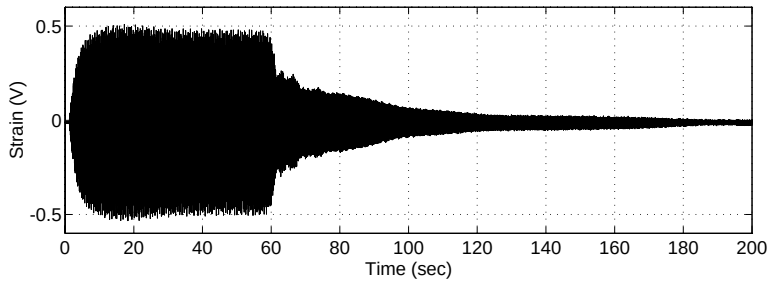

Figure 3-10. Control of the first and second modes of beam II.

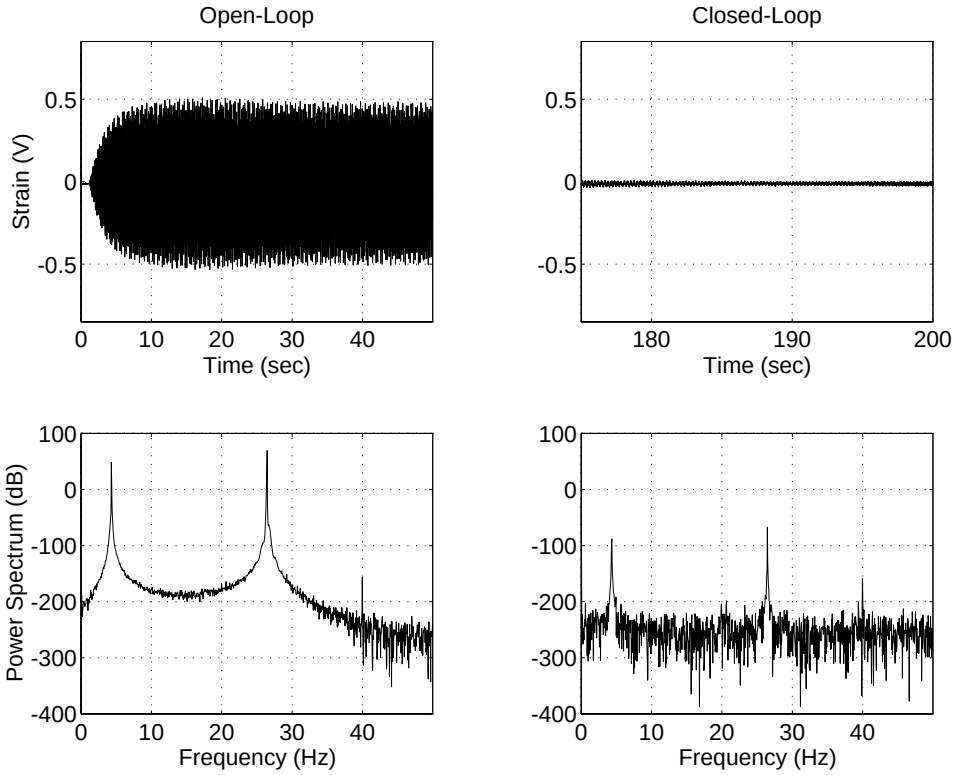

Figure 3-11. Time responses and power spectral densities of the open- and closed-loop systems.

3.3.6 Effect of Varying the Control Gains

Next, we investigate the effect of varying the gains K_F and K_C. We force beam I at approximately $4\,mg$ and perform two studies. First, we keep K_C constant and vary K_F. According to equation (2.34), the amplitude of the plant is $a_2 = \zeta/|\alpha|$. Thus, it is expected that increasing K_F reduces the response amplitude of the beam. In Figure 3-12, we show the response of the system for three values of K_F. In Figure 3-12a, the gain K_F is small enough such that the nonlinear coupling is lost, and the controller is rendered ineffective. However, it follows from Figures 3-12b and 3-12c that increasing K_F indeed reduces the vibration amplitude of the beam. We also note that increasing K_F introduces an oscillatory behavior in the response, in agreement with the theoretical findings.

Second, we fix K_F and vary K_C. For very small damping and detuning, recalling equation (2.36), we can approximate the amplitude of the controller by

$$a_1 \approx \sqrt{\frac{f}{\delta}}.$$

Hence, we expect that the response of the controller to be inversely related to the control gain K_C. In Figure 3-13, we illustrate the response of the beam and controller for three values of K_C. As K_C is increased, the peak-to-peak response of the controller decreases.

3.4 Control of Flexible Beams with Terfenol-D Actuators

In contrast with piezoelectric materials, Terfenol-D is a magnetostrictive material that exhibits a nonlinear constitutive relationship between the magnetic field and the strain. In Figure 3-14a, we show a drawing of a typical actuator assembly. In previously reported applications, a magnet is incorporated into the assembly of the actuator. The magnet introduces a bias field that allows for the operation of the actuator in a linear but small range. In the absence of a magnetic bias, Terfenol-D elongates for either a positively or a negatively

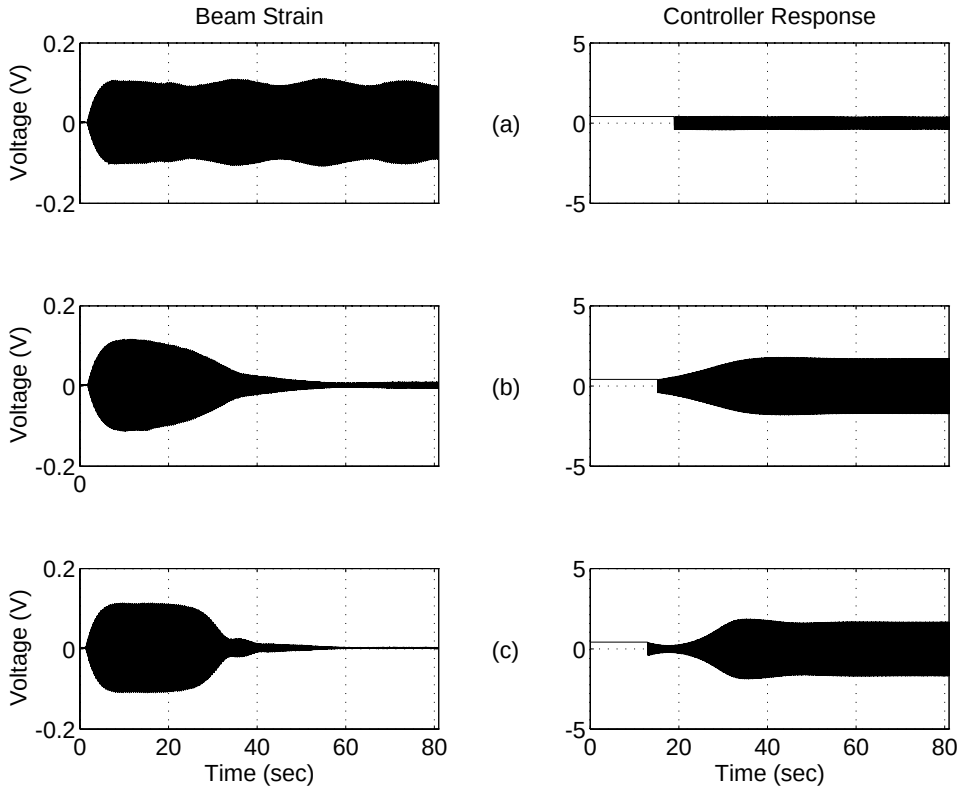

Figure 3-12. Effect of varying the feedback gain K_F on the response of beam I when $K_C = 10$. (a) $K_F = 0.1$, (b) $K_F = 1$, and (c) $K_F = 2$.

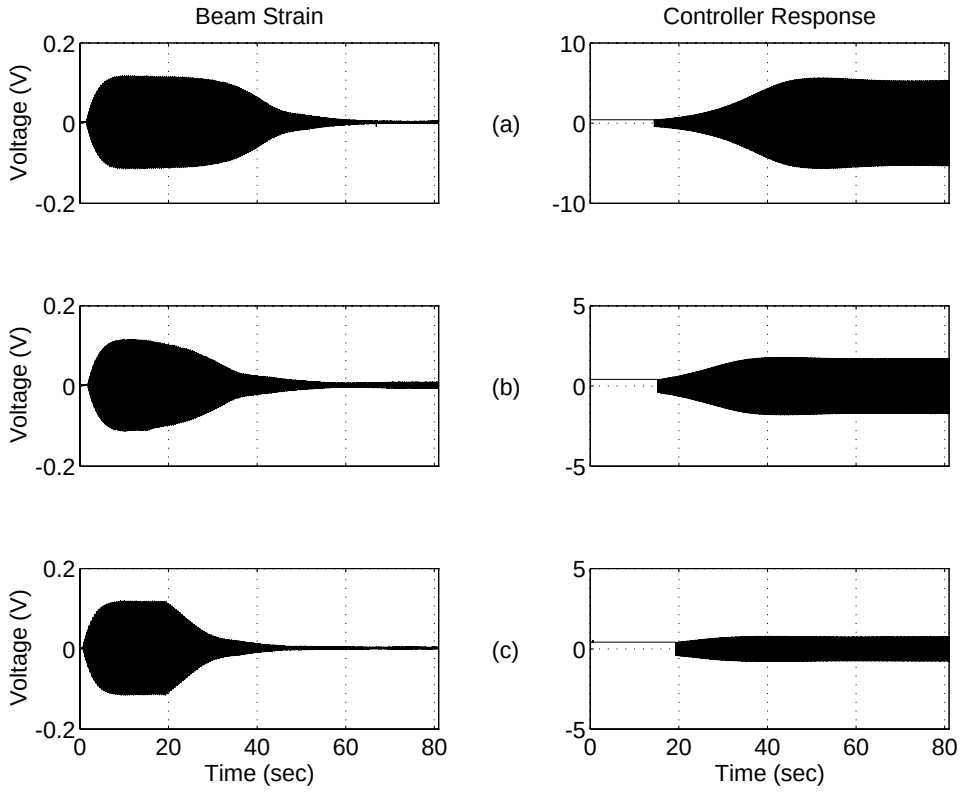

Figure 3-13. Effect of the control gain on the response of beam I when $K_F = 1$. (a) $K_C = 1$, (b) $K_C = 10$, and (c) $K_C = 50$.

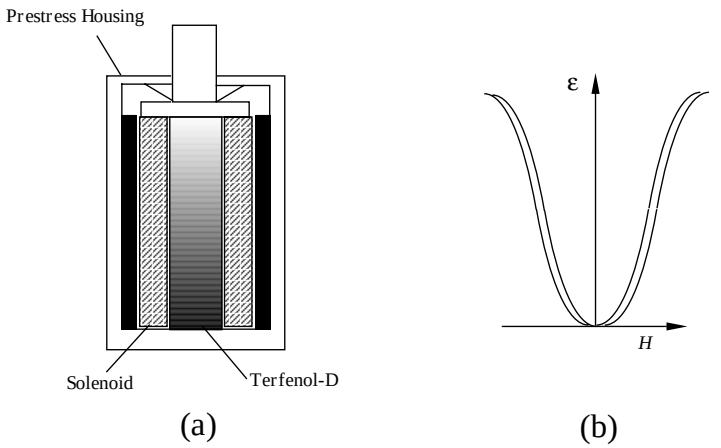

Figure 3-14. A Terfenol-D actuator. (a) Typical assembly and (b) strain-field relationship.

applied field, as illustrated in Figure 3-14b. To a first approximation, it can be shown that the nonlinear strain-field relationship is quadratic. Hence, if a nonbiased actuator is utilized, saturation may be achieved by allowing the actuator, and not the controller, to introduce the nonlinearity in the system. Though we develop the technique for Terfenol-D, the method can be easily applied to electrostrictive materials, such as Lead-Magnesium-Niobate (PMN), that also have quadratic constitutive laws.

3.4.1 Equations of Motion of the Beam

The structure consists of a flexible cantilever beam stiffened near its base with a Terfenol-D strut and subjected to an external excitation delivered by an electrodynamic shaker attached to the beam via a stinger. The configuration is shown in Figure 3-15. A mechanical model of the assembly is illustrated in Figure 3-16. The deflection of the beam at position x and time t is denoted by $w(x,t)$, m is the mass per unit length, EI is the flexural rigidity, k_a is the effective spring constant of the Terfenol-D actuator, and m_s and k_s are the effective mass and spring constants of the electrodynamic shaker, respectively.

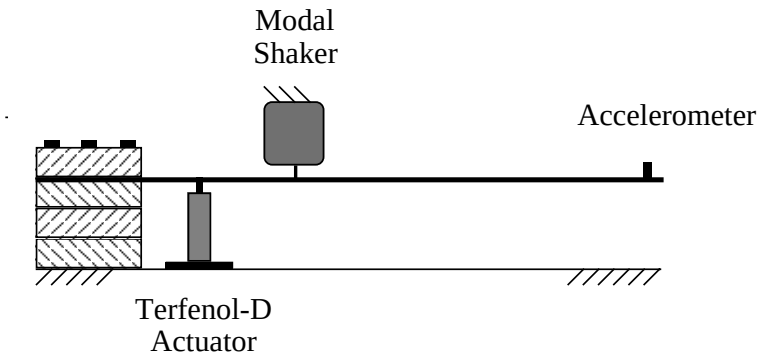

Figure 3-15. The beam and Terfenol-D actuator setup

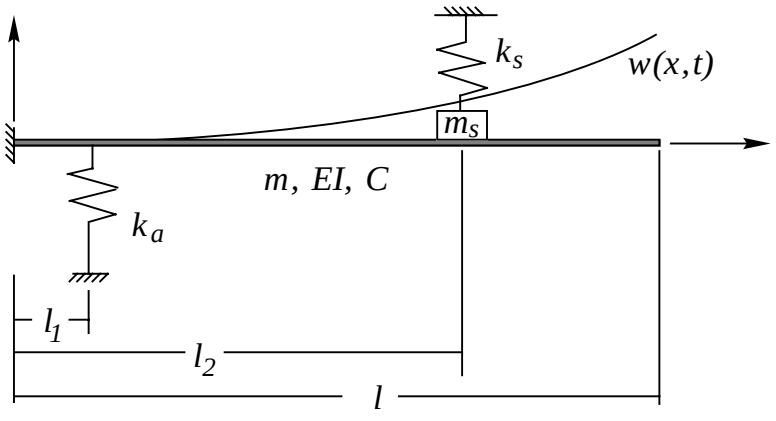

Figure 3-16. A mechanical model of the system.

The deflection $w(x,t)$ is divided into three components as follows:

$$w(x,t) \;=\; \begin{cases} w_1(x,t) & 0 \le x \le l_1 \\ w_2(x,t) & l_1 \le x \le l_2 \\ w_3(x,t) & l_2 \le x \le l \end{cases} \tag{3.75}$$

The kinetic and potential energies of the system are

$$T(t) \;=\; \frac{1}{2}\int_0^{l_1} m\dot{w}_1^2\,dx + \frac{1}{2}\int_{l_1}^{l_2} m\dot{w}_2^2\,dx + \frac{1}{2}\int_{l_2}^{l} m\dot{w}_3^2\,dx + \frac{1}{2}\,m_s\dot{w}_2^2(l_2,t), \tag{3.76}$$

$$V(t) \;=\; \frac{1}{2}\int_0^{l_1} EIw_1''^2\,dx + \frac{1}{2}\int_{l_1}^{l_2} EIw_2''^2\,dx + \frac{1}{2}\int_{l_2}^{l} EIw_3''^2\,dx \;+\; \frac{1}{2}k_a w_1(l_1,t)^2 + \frac{1}{2}\,k_s w_2(l_2,t)^2, \tag{3.77}$$

where the overdot indicates differentiation with respect to t and the prime indicates differentiation with respect to x.

Assuming that the system is viscously damped, we can write the virtual work of the non-conservative and external forces as

$$\delta W = -\int_0^{l} C(x)\dot{w}\,\delta w \;+\; f_a(t)\delta w(l_1,t) \;+\; f_s(t)\delta w(l_2,t), \tag{3.78}$$

where $C(x)$ is the damping coefficient per unit length of the beam and $f_a(t)$ and $f_s(t)$ are the actuation and excitation forces, respectively.

We expand the deflection $w(x,t)$ as

$$w(x,t) \;=\; \sum_{n=1}^{\infty} \phi_n(x)\,u_n(t), \tag{3.79}$$

where the $\phi_n(x)$ are the mode shapes of the system accounting for the discontinuities in the structure at $x = l_1$ and $x = l_2$.

Substituting equation (3.79) into equations (3.76)–(3.78), carrying out the integrations over the interval [0, l], then using Hamilton's extended principle [57], we obtain the following set of equations of motion for the forced problem:

$$\ddot{u}_j + 2\,\hat{\mu}_j\,\dot{u}_j + \omega_j^2 u_j \;=\; P_j\,f_a(t) + M_j\,f_s(t), \qquad j = 1, 2, \cdots, \infty \tag{3.80}$$

where the ω_j are the natural frequencies of the structure,

$$\hat{\mu}_j = \int_0^l \frac{C(x)\,\phi_j^2}{2\,m} dx, \quad P_j = \frac{\phi_j(l_1)}{m}, \quad M_j = \frac{\phi_j(l_2)}{m}, \tag{3.81}$$

and the mode shapes ϕ_n are orthonormalized such that

$$\int_0^l \phi_n \phi_m dx = \delta_{mn}. \tag{3.82}$$

Here, δ_{mn} is the Kronecker delta, and the damping is assumed to be modal.

3.4.2 Constitutive Law for Terfenol-D

The control force is applied using a nonbiased Terfenol-D actuator. Carman and Mitrovic [58] proposed a uniaxial nonlinear constitutive law for the material as follows:

$$\varepsilon_{33} = \sigma_{33}\, S_{3333}^{TH} + \alpha_{33}^{H}\, \Delta T + \frac{1}{2}\,(H_o + H)^2 \left(d_{3333}^{T} + \sigma_{33}\, S_{3333}^{T} + \alpha_{3333} \Delta T \right), \tag{3.83}$$

where ε_{33} is the axial strain, σ_{33} is the axial stress, S_{3333} is the compliance, ΔT is the change in temperature from a fixed reference, α_{33} and α_{3333} are coefficients of thermal expansion, d_{3333} is the piezomagnetic strain constant, H_o is the bias magnetic field, and H is the applied magnetic field. The superscripts on the constants define the physical constraints applied when the parameters are determined, such as constant temperature (T) or field (H).

We ignore the temperature effects and consider the case of zero magnetic bias. Then, equation (3.83) becomes

$$\varepsilon_{33} = \sigma_{33} S_{3333}^{TH} + \frac{1}{2} H^2 (\sigma_{33} S_{3333}^{T} + d_{3333}^{T}). \tag{3.84}$$

The equivalent force developed by the actuator is defined by

$$f_a(t) = \frac{\overline{\varepsilon}_{33} A}{S_{3333}^{TH}}, \tag{3.85}$$

where $\overline{\varepsilon}_{33} = \varepsilon_{33} - \sigma_{33} S_{3333}^{TH}$ and A is the cross-sectional area of the Terfenol rod. Approximating the applied magnetic field H by

$$H = \frac{N}{L}\, i_a(t), \tag{3.86}$$

and using equation (3.84), we express the actuator force as

$$f_a(t) \;=\; K_a\, i_a^2(t), \tag{3.87}$$

where

$$K_a \;=\; \frac{(\sigma_{33} S^T_{3333} \;+\; d^T_{3333}+)\, N^2 A}{2\, S^{TH}_{3333}\, L^2}. \tag{3.88}$$

Here, N is the number of turns in the solenoid, L is the length of the solenoid, and $i_a(t)$ is the applied electrical current. We note that this quadratic force-current model neither accounts for magnetic hysteresis nor includes eddy current losses, factors that might be important for high-frequency operation. For low frequencies, the actuator stiffness k_a may be approximated by

$$k_a = \frac{A}{L\, S^T_{3333}}. \tag{3.89}$$

3.4.3 Controller Equations

We define the forcing by

$$f_s(t) \;=\; \hat{F} \cos(\Omega t + \tau), \tag{3.90}$$

where $\hat{F}$ and Ω are the forcing amplitude and frequency, respectively, and τ is a constant phase. We consider the case of primary resonance and let $\Omega \approx \omega_k$, where ω_k is the natural frequency of the kth mode. Then, we introduce a controller taking the form

$$\ddot{v} \;+\; 2\,\hat{\zeta}\,\dot{v} \;+\; \omega_c^2\, v \;=\; \hat{\alpha}\, v\, \left.\frac{\partial^2 w}{\partial t^2}\right|_{x=l} \tag{3.91}$$

In this case, the feedback signal is generated by an accelerometer located at the tip of the beam. The control signal is given by

$$i_a(t) \;=\; \hat{\delta} v. \tag{3.92}$$

In contrast with the original definition of the control law, the current signal is linear in v. Since Terfenol exhibits a quadratic constitutive law, we let the actuator, and not the circuit, perform the "squaring" operation.

Inserting equations (3.90) and (3.92) into equations (3.80) and (3.91) leads to

$$\ddot{u}_j \,+\, 2\,\hat{\mu}_j\,\dot{u}_j \,+\, \omega_j^2\,u_j \,=\, P_j\,\hat{F}\,\cos(\Omega t+\tau) \,+\, M_j\,K_a\,\hat{\delta}^2\,v^2, \tag{3.93}$$

$$\ddot{v} \,+\, 2\,\hat{\zeta}\,\dot{v} \,+\, \omega_c^2\,v \,=\, \hat{\alpha}\,v\,\sum_{j=1}^{\infty}\,\phi_j(l)\,\ddot{u}_j. \tag{3.94}$$

3.4.4 Perturbation Analysis

In this section, we use the method of multiple scales to determine an approximate solution of equations (3.93) and (3.94). First, we scale the damping and forcing terms by letting

$$\hat{\mu}_j \,=\, \epsilon\,\mu_j, \quad \hat{\zeta} \,=\, \epsilon\,\zeta, \quad \hat{F} \,=\, \epsilon^2\,F, \tag{3.95}$$

where ϵ is a dimensionless bookkeeping parameter. Second, we seek expansions of u_j and v in the form

$$u_j \,\approx\, \epsilon\,u_{j1}(T_0,T_1) \,+\, \epsilon^2\,u_{j2}(T_0,T_1), \tag{3.96}$$

$$v \,\approx\, \epsilon\,v_1(T_0,T_1) \,+\, \epsilon^2\,v_2(T_0,T_1). \tag{3.97}$$

The derivatives with respect to time are expressed in terms of the new time scales as

$$\frac{d}{dt} \,=\, D_0 \,+\, \epsilon\,D_1 \,+\cdots \quad \text{and} \quad \frac{d^2}{dt^2} \,=\, D_0^2 \,+\, 2\,\epsilon\,D_0\,D_1 \,+\cdots, \tag{3.98}$$

where $D_k \equiv \partial/\partial T_k$. Substituting equations (3.95)–(3.98) into equations (3.93) and (3.94) and equating coefficients of like powers of ϵ leads to

Order (ϵ):

$$D_0^2\,u_{j1} \,+\, \omega_j^2\,u_{j1} \,=\, 0, \tag{3.99}$$

$$D_0^2\,v_1 \,+\, \omega_c^2\,v_1 \,=\, 0, \tag{3.100}$$

Order (ϵ^2):

$$\begin{aligned} D_0^2\,u_{j2} \,+\, \omega_j^2\,u_{j2} \,=&-\, 2\,D_0\,(D_1\,u_{j1} \,+\, \mu_j\,u_{j1}) + P_j\,F\,\cos(\Omega t+\tau) \\ &+\, M_j\,K_a\,\hat{\delta}^2\,v_1^2, \end{aligned} \tag{3.101}$$

$$D_0^2\,v_2 \,+\, \omega_c^2\,v_2 \,=\, -\, 2\,D_0\,(D_1\,v_1 \,+\, \zeta\,v_1) \,+\, \hat{\alpha}\,v_1\,\sum_{j=1}^{\infty}\,\phi_j(l)\,D_0^2\,u_{j1}. \tag{3.102}$$

The solutions of equations (3.99) and (3.100) can be expressed as

$$u_{j1} \;=\; A_j(T_1)\, e^{i\omega_j T_0} \;+\; \text{cc} \quad \text{and} \quad v_1 \;=\; B(T_1)\, e^{i\omega_c T_0} \;+\; \text{cc}, \tag{3.103}$$

where cc stands for the complex conjugate of the preceding term. The quantities $A_j(T_1)$ and $B(T_1)$ are unknown at this stage of the analysis. They are determined by eliminating the secular terms at the next level of approximation. To describe quantitatively the nearness of $2\,\omega_c$ to ω_k and Ω to ω_k, we introduce two detuning parameters σ_1 and σ_2 defined by

$$2\,\omega_c \;=\; \omega_k \;-\; \epsilon\,\sigma_1 \quad \text{and} \quad \Omega \;=\; \omega_k \;+\; \epsilon\,\sigma_2. \tag{3.104}$$

Then, substituting equations (3.103) into equations (3.101) and (3.102), using equations (3.104), and eliminating the terms that produce secular terms yields

$$A_j' \;+\; \mu_j\, A_j \;=\; 0, \qquad \text{for } j \neq k \tag{3.105}$$

$$2\,i\,(A_k' + \mu_k A_k) \;+\; 4\,\gamma\, B^2\, e^{-i\sigma_1 T_1} \;-\; f\, e^{i\sigma_2 T_1} \;=\; 0, \tag{3.106}$$

$$2\,i\,(B' + \zeta B) \;+\; 4\,\alpha\, A_k \overline{B}\, e^{i(\sigma_1 T_1 + \tau)} \;=\; 0, \tag{3.107}$$

where the prime represents differentiation with respect to the slow time variable T_1 and

$$f \;=\; \frac{P_k\, F}{2\,\omega_k}, \quad \delta \;=\; -\,\frac{M_k\, K_a\, \hat{\delta}^2}{4\,\omega_k}, \quad \alpha \;=\; \frac{1}{2}\,\omega_k\,\hat{\alpha}\,\phi_k(l). \tag{3.108}$$

It follows from equation (3.105) that, to the first approximation, the A_j and hence the u_j for $j \neq k$ decay exponentially with time.

Next, we express equations (3.106) and (3.107) in real variables by letting

$$A_k \;=\; \frac{1}{2}\, a_2(T_1)\, e^{i\beta_2(T_1)} \quad \text{and} \quad B \;=\; \frac{1}{2}\, a_1(T_1)\, e^{i\beta_1(T_1)}. \tag{3.109}$$

Substituting equations (3.109) into equations (3.106) and (3.107) and separating real and imaginary parts yields

$$a_1' \;=\; -\,\zeta a_1 \;-\; \alpha\, a_1 a_2 \sin\gamma_1, \tag{3.110}$$

$$a_2' \;=\; -\,\mu_k a_2 \;+\; \delta\, a_1^2 \sin\gamma_1 \;+\; f \sin\gamma_2, \tag{3.111}$$

$$a_1 \beta_1' \;=\; \alpha\, a_1 a_2 \cos\gamma_1, \tag{3.112}$$

$$a_2 \beta_2' \;=\; \delta\, a_1^2 \cos\gamma_1 \;-\; f \cos\gamma_2, \tag{3.113}$$

where

$$\gamma_1 = \sigma_1 T_1 - 2\beta_1 + \beta_2 \quad \text{and} \quad \gamma_2 = \sigma_2 T_1 - \beta_2 + \tau. \tag{3.114}$$

Again, we find that the solution of the multi-degree-of-freedom problem reduces to the solution of two quadratically coupled oscillators.

3.4.5 Experimental Setup and Procedure

The control technique is implemented experimentally using a cantilever beam and the analog circuit. We use a cantilever steel beam measuring $0.75m \times 0.05m \times 0.004m$ to carry out the experiments. We attach a Terfenol-D actuator and a 50-lb electrodynamic modal shaker to the structure. The experimental setup is depicted in Figure 3-17. It consists of the shaker and its driving power amplifier, a power amplifier, an accelerometer mounted at the tip of the beam, and a signal generator. The details of the equipment are listed in Appendix A.

We clamp the beam at one end and use the signal generator to drive the shaker at the desired amplitude and frequency. The signal from the accelerometer conditioning amplifier is fed to the circuit, and the output of the circuit is amplified and sent to the actuator. The responses of the beam and the circuit are monitored by an oscilloscope and a signal analyzer and collected by a computer.

3.4.6 Single-Mode Control

We conduct two experiments where we control resonant oscillations of the first and second modes of the beam-actuator assembly. In Figure 3-18, we show the response of the first mode before and after activation of the controller. The time trace reveals that the system does not reach steady state. We run the experiment for an extended period of time, and the controller response continues to grow. However, a considerable reduction in the response of the beam is observed. We suspect that this anomaly is due to the influence of higher-order nonlinear terms in the constitutive law for Terfenol-D at this frequency and amplitude. The responses shown in Figure 3-18 do not exhibit the saturation phenomenon. We suspect

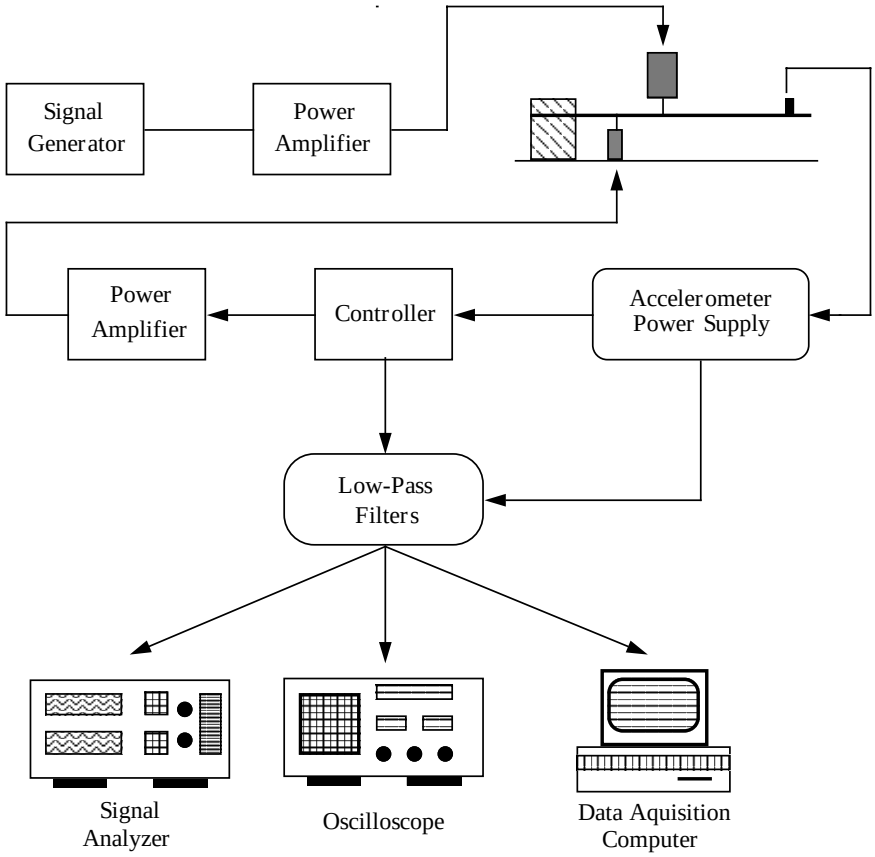

Figure 3-17. A schematic of the Terfenol-D experimental setup.

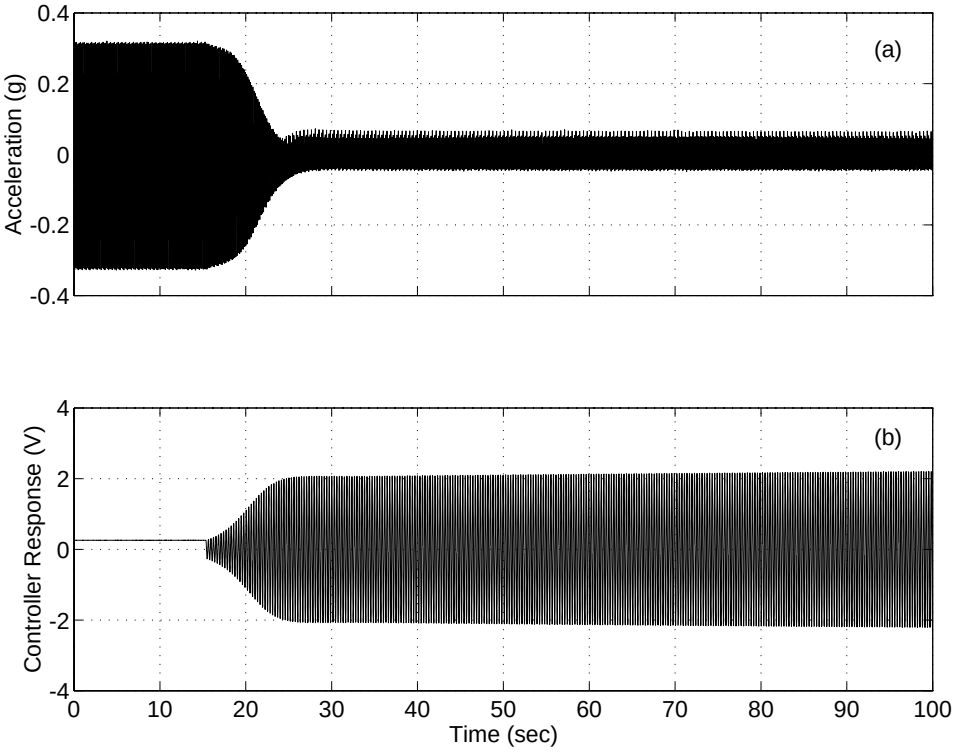

Figure 3-18. Control of the first mode when $\Omega \approx 6.8\,\mathrm{Hz}$. (a) Acceleration at the tip of the beam and (b) controller response.

that the saturated response is unstable via a Hopf bifurcation, leading to small large-period oscillations about the saturated response. In contrast, when the actuator is used to control the second mode of the beam, saturation is achieved, as depicted in the time traces of Figure 3-19.

3.4.7 Control of a Nonideal System

To further examine the utility of the control strategy, we carry out an experiment in which the excitation is provided by a nonideal source. We shorten the beam to $0.31m$, remove the electrodynamic shaker from the assembly, and replace it by an electric motor with a rotating imbalance. In Figure 3-20, we show the time trace of the response before and after application of the control. In this case, the beam response appears to be nonstationary.

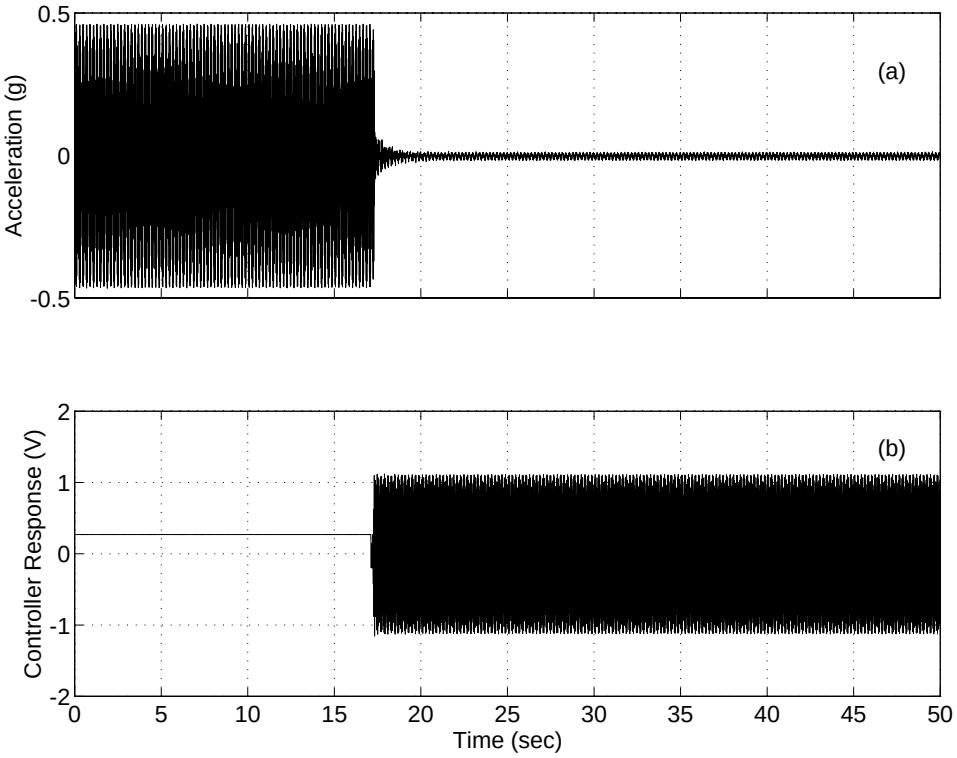

Figure 3-19. Control of the second mode when $\Omega \approx 47.5\,\mathrm{Hz}$. (a) Acceleration at the tip of the beam and (b) controller response.

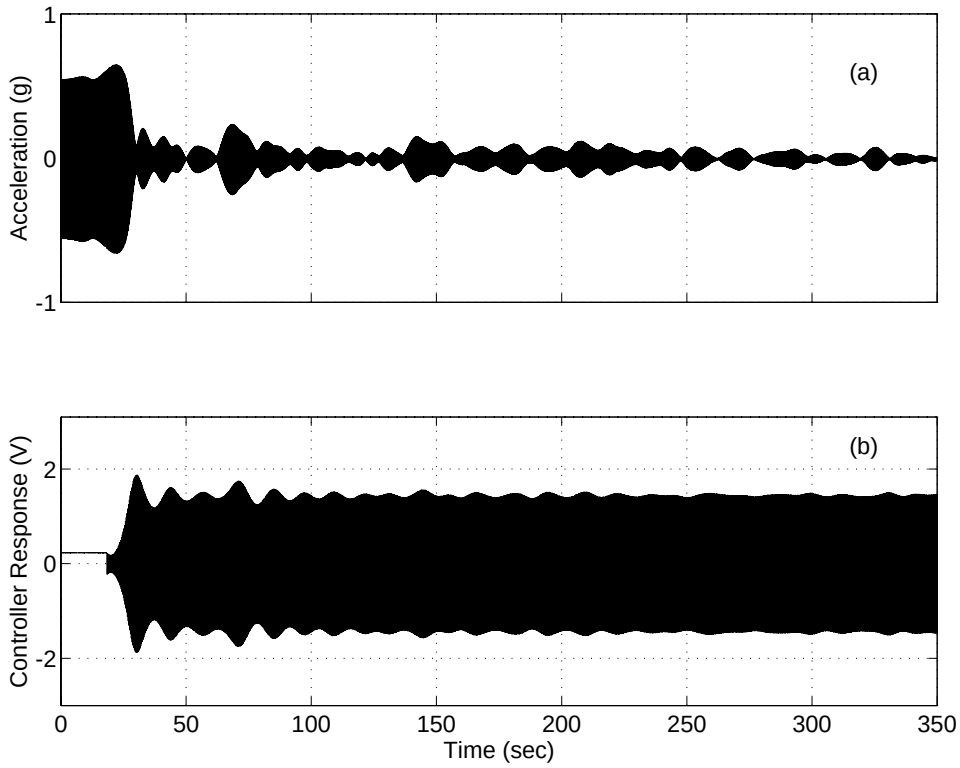

Figure 3-20. Control of a nonideal system when $\Omega \approx 7\,\text{Hz}$. (a) Acceleration at the tip of the beam and (b) controller response.

As the amplitude of oscillations decreases, the rotational frequency of the motor is visually observed to increase. Thus, the excitation continuously detunes itself from the controller, causing the response to expand and contract alternately as the control system goes "in and out of tune". This is an example of a lock-in phenomenon associated with nonideal energy sources [3]. Nevertheless, the controlled response is greatly attenuated and it should be possible to devise an adaptive system that can tune the compensator frequency in a quasistatic manner based on a tachometer signal.

3.5 Summary

In this chapter, we presented theoretical and experimental results that demonstrate the versatility of the quadratic absorber. We devised an electronic circuit to emulate the absorber and used a variety of sensors and actuators to implement the active control strategy.

First, we used a motor and a potentiometer to control the vibration of a rigid beam. We developed a plant model that includes Coulomb friction and demonstrated theoretically and experimentally that the closed-loop system exhibited the saturation phenomenon.

Second, we extended the strategy to multi-degree-of-freedom systems. We used PZT ceramics and strain gages to suppress the vibrations of flexible steel beams when subjected to single- and simultaneous two-mode excitations. In the case of the two-mode excitation, we used two circuits. Furthermore, we investigated the effect of varying the absorber gains on the response of the closed-loop system. Our experimental results agree well with the theoretical analysis.

Third, we employed a nonlinear actuator. We used Terfenol-D and accelerometers to control the vibrations of flexible beams. We considered the cases of ideal and nonideal excitations. In the first case, the structure was excited with a shaker through a stinger. In the second case, we removed the shaker and mounted a motor with a rotating imbalance on the beam. In both instances, the technique was successful in significantly reducing the response amplitude of the structures.

Chapter 4

Application of the Digital Absorber

In the previous chapter, we applied the control strategy through a series of analog circuits. Although successful, the implementation was not complete. By design, the analog circuit suffers from an operational disadvantage. Since the various gains are adjusted through potentiometers, the user's intervention is required to change parameters, such as the natural frequency, damping, and feedback gains. Consequently, automatic tracking of the plant's frequency of oscillation, a major design requirement, is not possible. Therefore, a more flexible and versatile implementation is imperative.

To facilitate application of the strategy, we resort to a digital signal processing (DSP) board. The DSP board is a programmable input/output device that is installed in a host computer. This technology has two advantages. First, it enables us to achieve a more user-friendly implementation of the control law. Second, its flexibility allows us to apply easily other techniques, such as the linear tuned absorber, for comparison purposes. Another similar application has been implemented by Pai *et al.* [59]. They developed a code in the Matlab-based SIMULINK modeling software and designed a hybrid quadratic/linear technique using a digital board manufactured by dSPACE. Their approach is successful, but it does not allow for automatic tuning of the absorber frequency.

4.1 Hardware

The hardware consists of an ADC64 input/output board developed by Innovative Integration and installed in a Pentium-based personal computer. In addition to its software controlled analog-to-digital (A/D) and digital-to-analog (D/A) converters, the board is supported by a Texas Instruments C3X micro-processor chip. The board's functions, such as signal input and output and data manipulation, are specified by composing a code in C. Then, the resulting executable file is downloaded to the micro-processor, which performs all of the mathematical calculations and executes the A/D and D/A conversions at any user-specified rate. Since the DSP board is a self-contained modular device, the speed of execution of the code depends on the speed of the C3X processor, and not the host processor.

4.2 Algorithms

We develop a code that automates implementation of the absorber. The program is structured around an interrupt service routine (ISR). An ISR is a function that is executed (serviced) whenever a certain condition is met. In our program, the ISR is invoked when a hardware-timer runs out, thereby executing its content at a specified frequency. The ISR sets the basis for sampling the feedback signal from the plant, outputting the control signal to the actuator amplifier, and performing all of the necessary mathematical calculations. In order for the program to operate properly, all commands within the interrupt routine must be executed in a time span that is less or equal to the time period between invocation of the ISR. The routine calls functions that perform the following tasks:

1. emulation of the absorber equation;
2. detection of the plant frequency and coarse-tuning of the absorber frequency; and
3. detection of the plant amplitude and fine-tuning of the absorber frequency.

In Figure 4-1, we show a flow-diagram illustrating the structure of the program. First, the program detects the frequency of oscillation of the plant, sets the frequency of the absorber, and activates the controller. Second, after the initial transients die out, it fine-tunes the absorber frequency to maintain small-amplitude motion. The algorithm operates within two amplitude bounds, a_{max} and a_{min}. If the amplitude of the plant is greater than a_{max}, the controller is turned off and a new coarse frequency is calculated. If the amplitude is greater than a_{min}, the program seeks to minimize the response amplitude by continously fine-tuning the frequency, otherwise it is idle. The functions performing these operations are described next.

4.2.1 Absorber Algorithm

The function executes a fourth-order Runge-Kutta [60] algorithm that, given a set of software-specified initial conditions, solves the second-order differential equation given by equation (2.2). By design, the algorithm requires four previously sampled values of the plant feedback signal in order to evaluate the solution of the differential equation at the next time step. We find that such restriction is not necessary for successful implementation of the scheme. We conjecture that the sampling rate we use is fast enough, thereby allowing us to apply correctly the algorithm using only the value of the feedback signal sampled at the previous time step.

4.2.2 Detection of Plant Frequency and Coarse-Tuning of Absorber

Since the frequency resolution of an FFT algorithm is inversely proportional to the length of the time sample [61], we opt against using such an approach. Assuming a single-frequency carrier signal, we develop a function that calculates the frequency of the plant to within an accuracy of $10m$Hz. The function is based on detecting zero-crossings over a certain time span. Therefore, it does not require the 100 second sample length otherwise needed by the

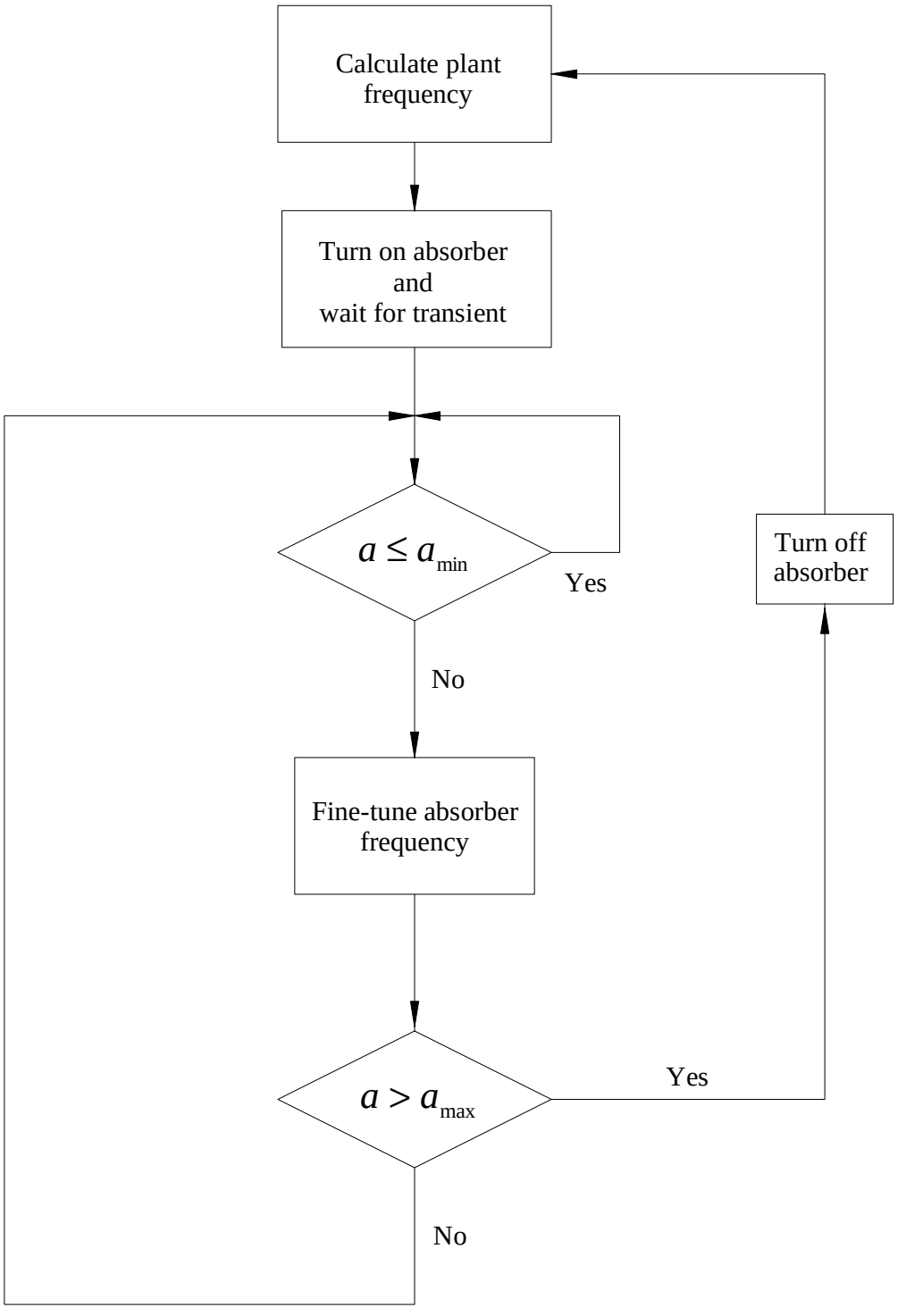

Figure 4-1. Flow-chart of a digital implementation of the absorber.

FFT scheme. To insure redundancy, positive-to-negative and negative-to-positive crossings are counted separately and two average frequencies are calculated. The higher of the two values is used to coarse-tune the frequency of the absorber. This algorithm is successful, and hence only used when the uncontrolled plant is oscillating with high-amplitude response. Once the controller is activated, the small signal-to-noise ratio hinders proper detection of the zero-crossings. In this case, we resort to an amplitude detection scheme to fine tune the absorber frequency.

4.2.3 Detection of Plant Amplitude and Fine-Tuning of Absorber

The amplitude detection algorithm processes the plant feedback signal and calculates the amplitude of oscillation to within an accuracy of $50mV$. The function detects the maximum amplitude over a one-second time span, calculates the average amplitude over a longer user-specified time interval, and stores the previously calculated average amplitude.

Fine-tuning of the absorber frequency is performed heuristicly. The algorithm compares the old average amplitude a_{old} with the current amplitude a_0 and determines the change in the frequency $\Delta\omega$ according to the following set of rules:

$$\begin{aligned}
&\text{if} \quad a_0 > a_{old} \quad \text{and} \quad (\Delta\omega)_{old} > 0 \quad \text{then} \quad (\Delta\omega)_{new} < 0,\\
&\text{if} \quad a_0 < a_{old} \quad \text{and} \quad (\Delta\omega)_{old} > 0 \quad \text{then} \quad (\Delta\omega)_{new} > 0,\\
&\text{if} \quad a_0 > a_{old} \quad \text{and} \quad (\Delta\omega)_{old} < 0 \quad \text{then} \quad (\Delta\omega)_{new} > 0,\\
&\text{if} \quad a_0 < a_{old} \quad \text{and} \quad (\Delta\omega)_{old} < 0 \quad \text{then} \quad (\Delta\omega)_{new} < 0.
\end{aligned}$$

4.3 Application of the Quadratic and Linear Absorbers

In this section, we apply the quadratic absorber and compare its performances with that of a linear absorber. We present results of frequency- and force-response sweeps that we conduct to suppress vibrations of a steel beam fitted with piezoceramic actuators and a strain gage. The properties of the beam (No. III) and the actuators are listed in Appendix A.

4.3.1 Quadratic Absorber

The algorithms are tested by mounting the cantilever beam to a 100-lb shaker and subjecting it to a base excitation whose frequency is near the natural frequency of its first mode. In Figures 4-2 and 4-3, we show open- and closed-loop frequency-response curves when the beam is subjected to forcing levels of 50 and $70mg$, respectively. In both cases, the absorber is very effective in suppressing the motion of the beam, even when the excitation is away from resonance. Although very small, the closed-loop amplitude of the beam is neither equal to zero nor a constant as the forcing frequency is varied. This stems from the fact that the algorithm relies on the measured plant amplitude to tune the frequency of the absorber. The scheme does not insure that the absorber frequency is set equal to exactly one-half the frequency of vibration of the beam. In fact, it seeks only to minimize the response by tuning the absorber. We find that, in some instances, the maximum difference between the ideal and actual frequency is in the order of $10m$Hz. Such an error can be minimized by specifying a smaller condition amplitude a_{min}.

4.3.2 Comparison between the Quadratic and Linear Absorbers

We compare the performance of the quadratic absorber with that of a linear tuned absorber. We modify the program and apply both techniques. However, in this study, we manually set the frequency of each absorber. In the case of the linear scheme, we set the absorber frequency equal to the excitation frequency. In Figures 4-4 and 4-5, we show open- and closed-loop frequency-response curves when the beam is subjected to forcing levels of 50 and $70mg$, respectively. In both figures, the data points labeled "Closed-Loop" refer to the response amplitudes when either of the techniques is used. Clearly, both control schemes lead to comparable performances. In Figure 4-6, we illustrate the response of the absorbers. The stroke of the linear absorber is larger than the stroke of the quadratic absorber. In Figure 4-7a, we depict force-response curves when the forcing frequency is equal to 11.5Hz. Again, both techniques lead to similar results. However, the stroke of the linear absorber

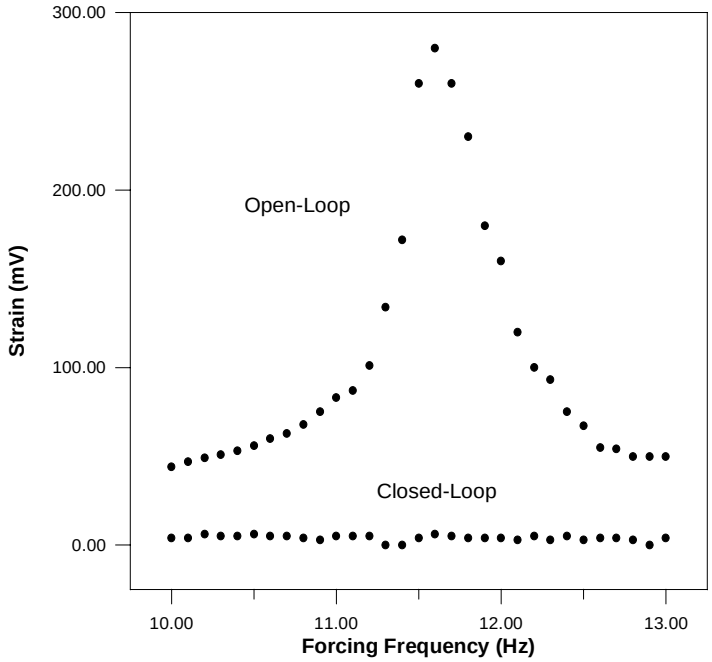

Figure 4-2. Application of the quadratic absorber. Frequency-response curves when $F = 50mg$.

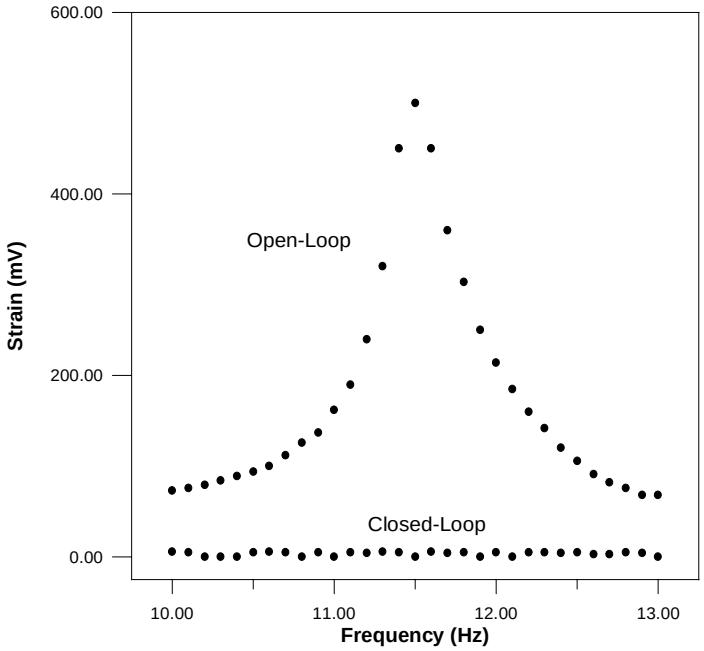

Figure 4-3. Application of the quadratic absorber. Frequency-response curves when $F = 70mg$.

increases more rapidly as the forcing level is increased, as shown in Figure 4-7b.

4.4 Saturation of the Actuators

In this section, we investigate the effect of saturation (clipping) of the actuator on the performance of the quadratic absorber. Since neither an exact nor an approximate analytical solution to the problem is possible to obtain, we tackle the issue through numerical and experimental studies.

4.4.1 Numerical Simulations

We consider the closed-loop system given by

$$\ddot{u} + 2\,\mu\,\dot{u} + \omega_2^2\,u = F\cos(\Omega t) + F_c(t), \tag{4.1}$$

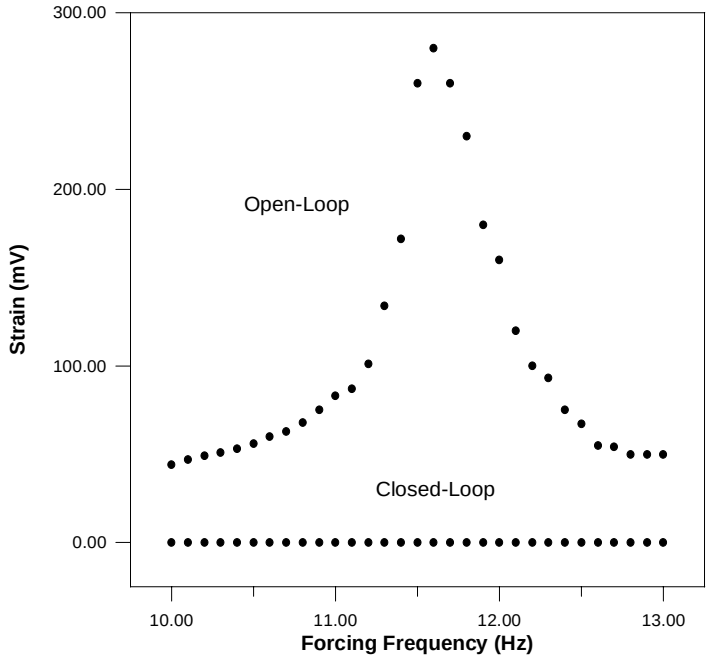

Figure 4-4. Application of the quadratic and linear absorbers. Frequency-response curves when $F = 50mg$.

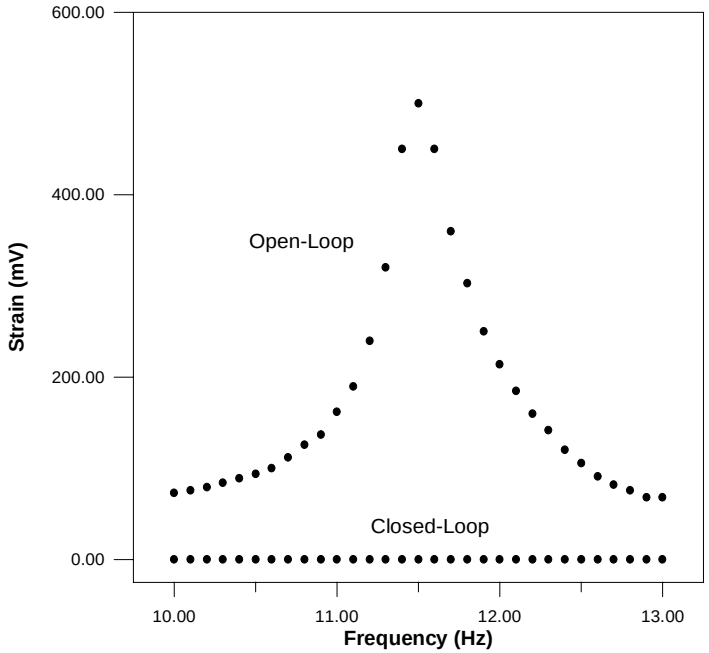

Figure 4-5. Application of the quadratic and linear absorbers. Frequency-response curves when $F = 70mg$.

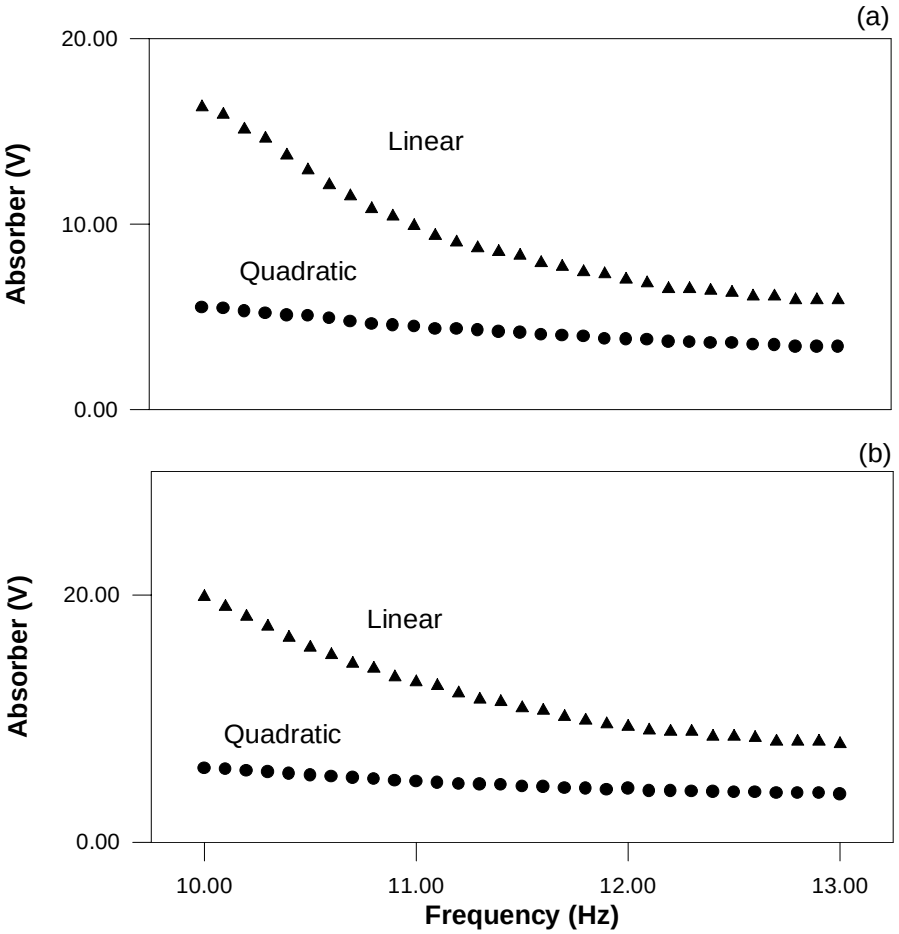

Figure 4-6. Frequency-response curves of the quadratic and linear absorbers. (a) $F = 50mg$ and (b) $F = 70mg$.

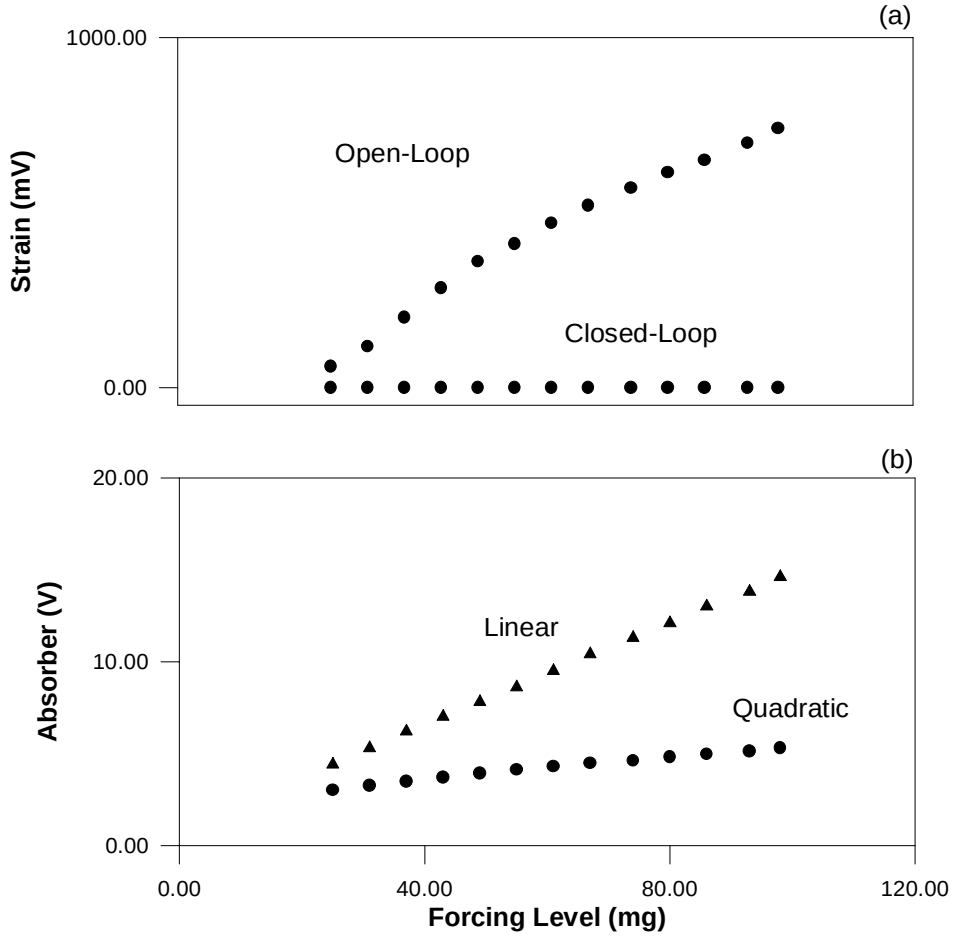

Figure 4-7. Application of the quadratic and linear absorbers. Force-response curves when $\Omega = 11.5$Hz.

$$\ddot{v} + 2\zeta\dot{v} + \omega_1^2 v = \alpha u v, \tag{4.2}$$

where u and v are the plant and absorber coordinates, respectively. The control signal $F_c(t)$ is defined by

$$F_c(t) = \begin{cases} K_a v^2 & \text{when} \quad K_a v^2 \leq K_{sat} \\ K_{sat} & \text{when} \quad K_a v^2 > K_{sat} \end{cases} \tag{4.3}$$

where K_{sat} is a constant that represents possible limitations in the operation of the actuator. Here, K_{sat} may be equal to the maximum force (or moment) the actuator can impart to the structure. Alternatively, it may be related to the maximum value of the signal (voltage or current) that the system's electronic devices can input or output.

In Figure 4-8, we show results of a numerical simulation of the responses of the plant and the absorber when $K_{sat}=0.1$. Initially, $F=0.05$ and effective control is achieved. When the forcing is increased to $F=0.07$ at $t=150$, the value of the control signal F_c exceeds K_{sat}, the solution loses stability, and the response of the absorber increases exponentially with time. Since the magnitude of F_c cannot exceed the limiting value K_{sat}, the plant oscillates at the open-loop amplitude.

4.4.2 Experiments

To verify the results of the numerical simulations, we perform several experiments where we utilize the digital absorber. First, we control the response of a second-order electronic circuit emulating the plant given by equation (4.1). The values of the plant and absorber parameters are identical to the ones used in the numerical simulations. In Figure 4-9, we show the response of the circuit and the absorber. The numerical and experimental results are in good agreement.

In the second set of experiments, we consider suppressing the response of beam No. III but modify the control algorithm to artificially limit the value of the control signal. Restricting the amplitude of the signal in this case is mathematically equivalent to imposing upper and lower bounds on the moment delivered by the PZT actuators. It follows from equation (4.3)

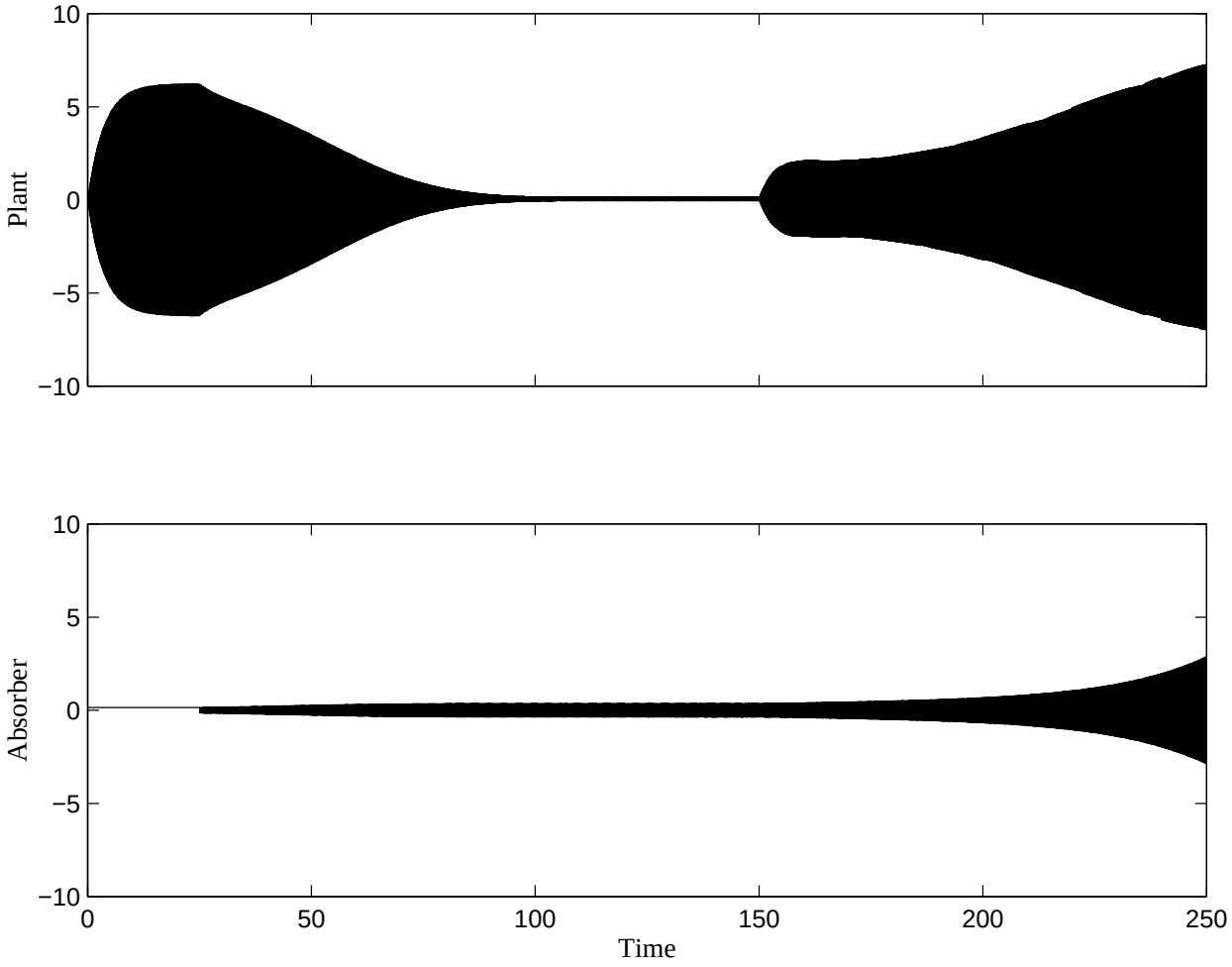

Figure 4-8. A numerical simulation of actuator saturation when $\Omega = \omega_2 = 68.3$ rad/sec, $\omega_1 = \Omega/2$, $\mu = 0.004$, $\zeta = 10^{-6}$, and $\alpha = K_a = 0.75$.

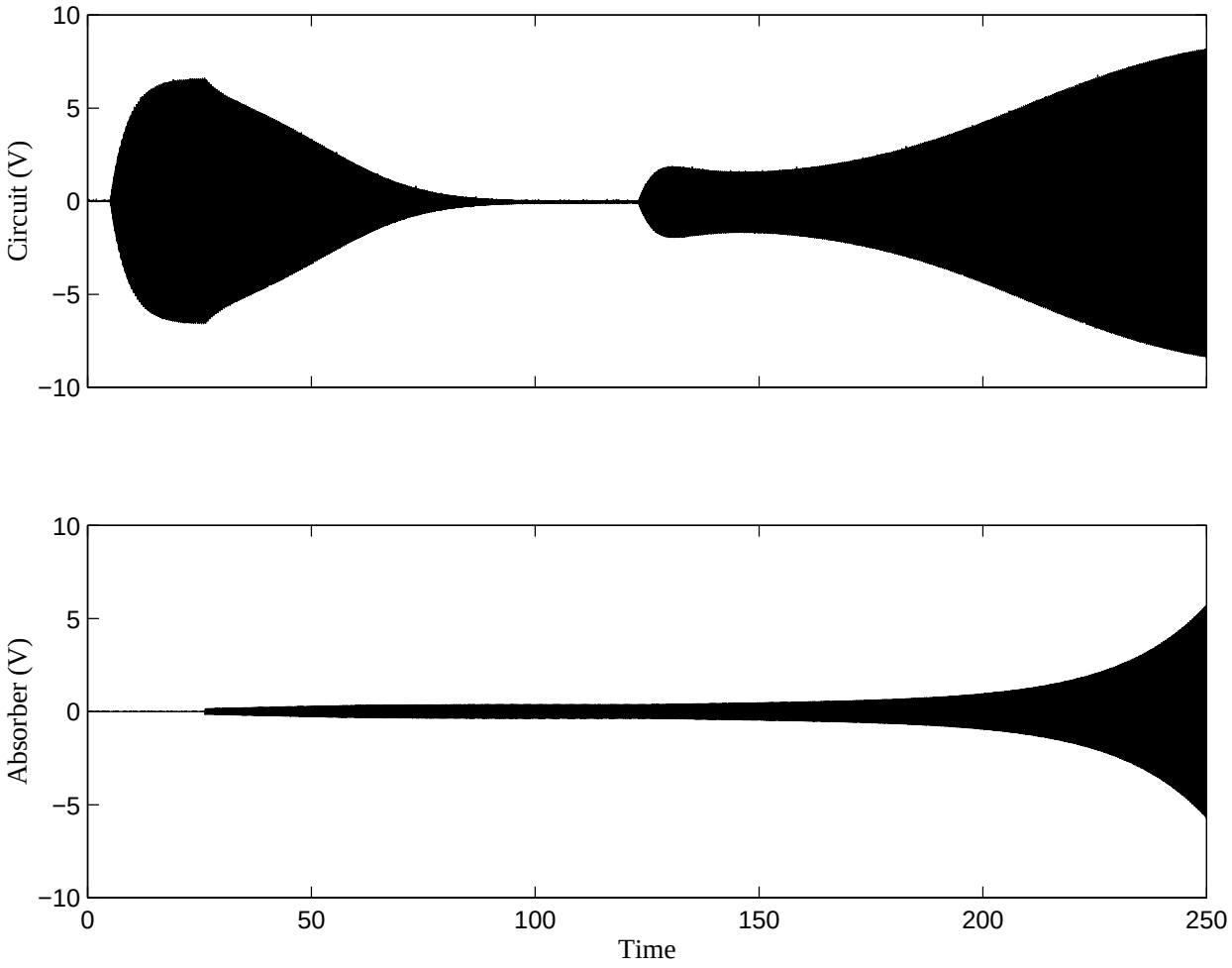

Figure 4-9. Experimental time traces of the circuit and absorber responses illustrating actuator saturation when $\Omega = \omega_2 = 68.3$ rad/sec, $\omega_1 = \Omega/2$, $\mu = 0.004$, $\zeta = 10^{-6}$, and $\alpha = K_a = 0.75$.

that the control signal is either strictly positive or strictly negative. For a perfectly controlled beam, the signal is given by

$$\begin{aligned} F_c &= -K_a \left[\sqrt{\frac{2\,F}{K_a}} \cos\left(\frac{1}{2}\Omega\, t\right) \right]^2 , \\ &= -F\,(\cos\Omega t + 1)\,. \end{aligned} \tag{4.4}$$

This fact is illustrated in Figure 4-10a. It is clear from the figure that only half of the actuator's capability can be exploited. The root of the problem lies in the constant term in equation (4.4).

It seems plausible to assume that the harmonic term is solely responsible for attenuation of the response, while the constant term contributes only to a static displacement. Therefore, a possible solution amounts to eliminating the DC component mathematically or through a filter. Pai *et al.* [59] reported that the latter approach resulted in instabilities. We conjecture that the filters they used altered significantly the phase of the signal, thereby degrading the performance of the technique. In contrast, our experimental tests show that elimination of the DC component yields successful results.

We propose two methods for carrying out this task. The easiest of the two consists of running the control signal through a band-pass filter and properly choosing the corner frequencies to minimize the unavoidable phase shift. The second method is based on modifying the signal by calculating an average of $max(v^2)$ and subtracting its value from the control signal. The resulting time responses when applying this algorithm are shown in Figure 4-10b. Eliminating the DC shift is only applicable when using linear actuators. In this case, the actuators are fully exploited and the techniques's power requirement becomes equal to that of a linear absorber.

Our experimental tests also show that the quadratic absorber is capable of maintaining control authority even when the signal is clipped. In both cases, there is a forcing level above which the controlled response is lost and replaced with the open-loop response, as illustrated in Figure 4-11. However, the nonbiased control signal allows for longer sustained operations in the clipped range (i.e., larger input forces).

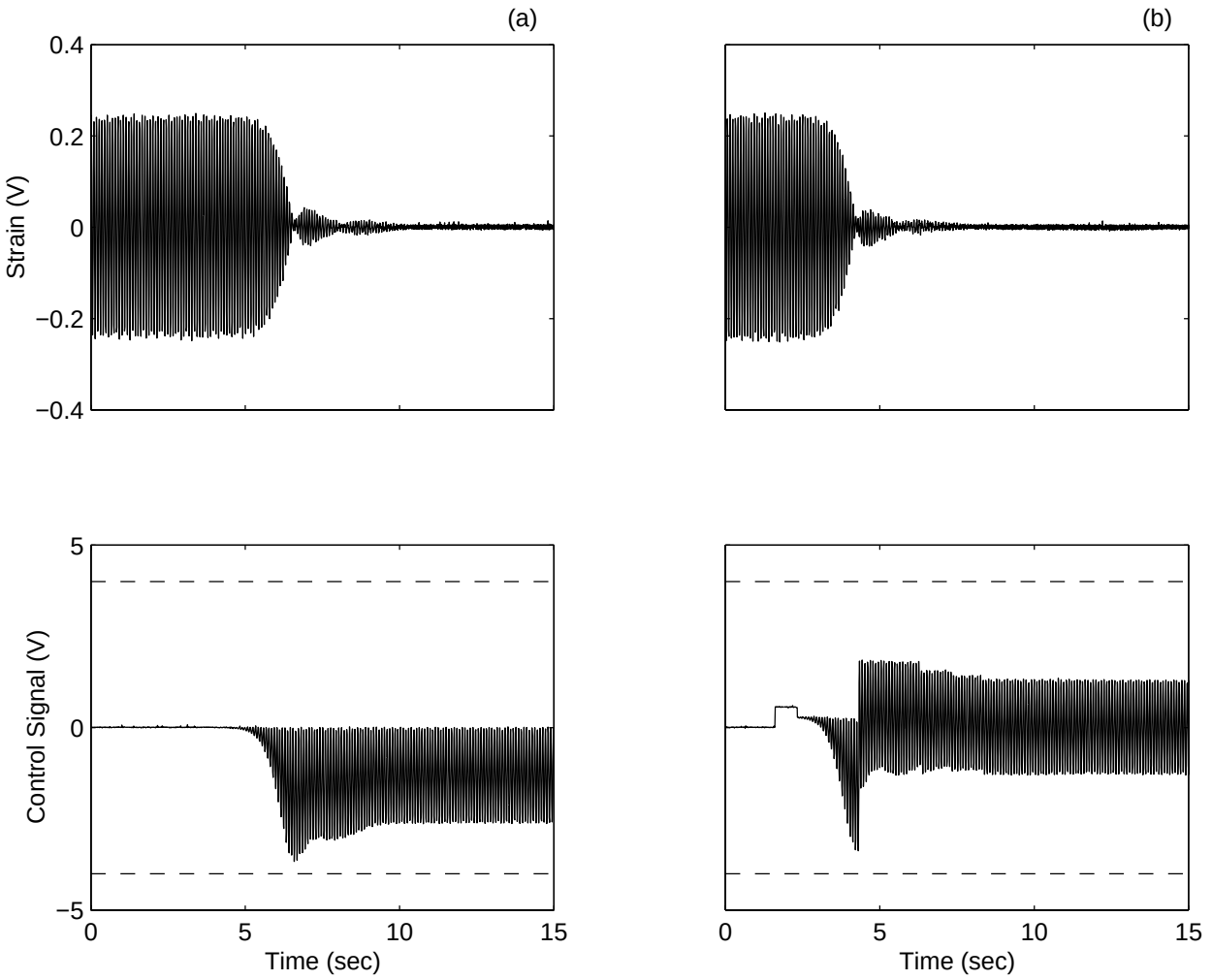

Figure 4-10. Experimental transient time traces of the beam response and the control signal when $\Omega = 11.5$Hz. (a) Biased control signal and (b) nonbiased control signal. The dashed line indicates the maximum allowed signal value.

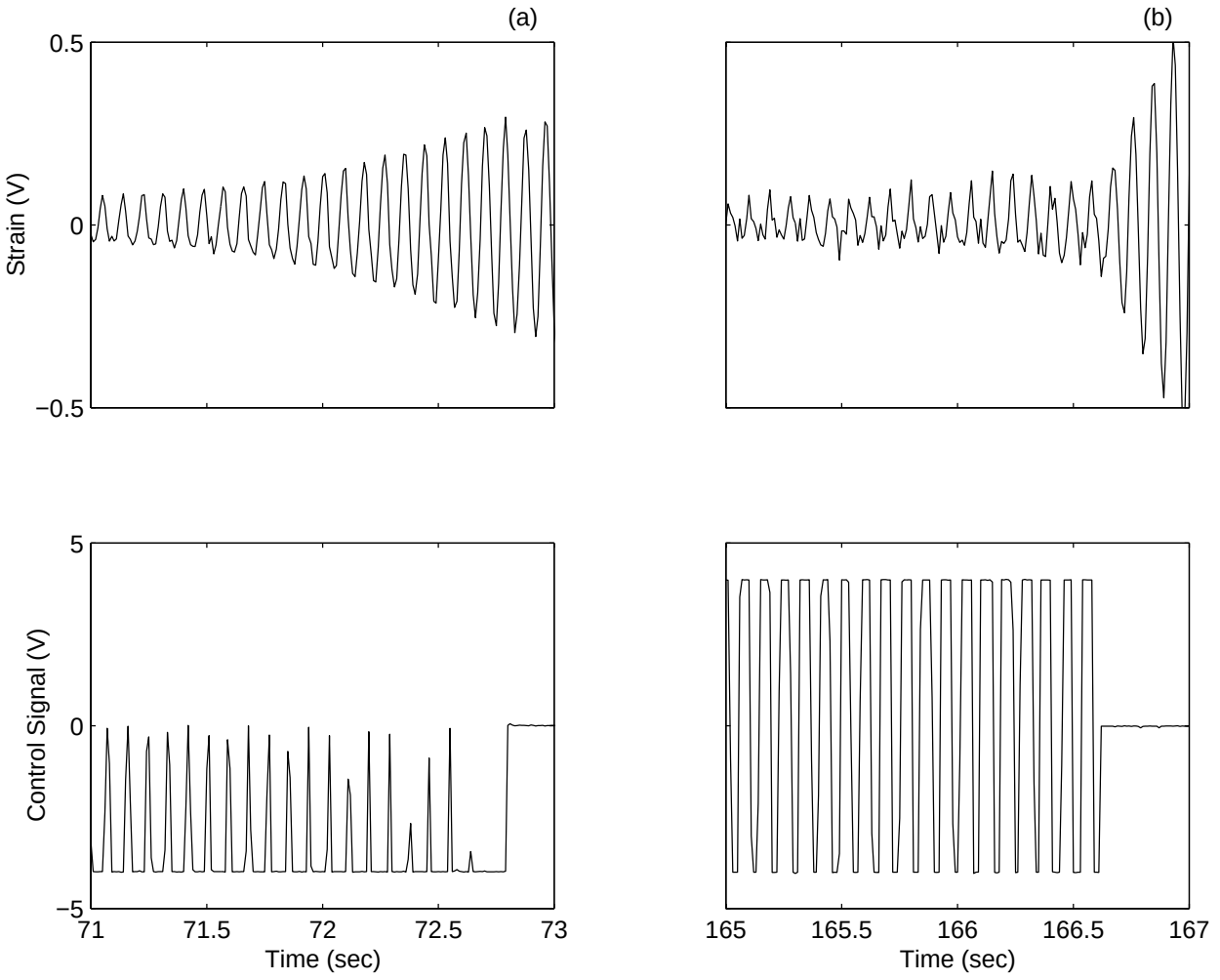

Figure 4-11. Experimental time traces of the beam response and the control signal when $\Omega = 11.5$Hz. (a) Biased control signal and (b) nonbiased control signal.

4.5 Summary

In this chapter, we developed and implemented nonlinear and linear vibration absorbers using a digital signal processing (DSP) device. First, we described the DSP board and outlined the software algorithms. Then, we reported results of application of the techniques for controlling the high-amplitude response of a cantilever beam fitted with piezoceramic actuators. Once the absorbers' frequencies were properly tuned, we showed that both control schemes possess a wide suppression bandwidth. In addition, we analyzed the effect of actuator saturation on the performance of the quadratic absorber. By judicially modifying the control signal, we were able to expand the effective force output of the absorber and reduce its power requirements.

Chapter 5

Development of the Cubic Absorber

Unlike previous studies that investigated the saturation phenomenon in quadratic systems, we propose to "reverse-engineer" the saturation phenomenon using cubic terms. We consider a plant modeled by a second-order nonlinear differential equation and introduce an active vibration absorber coupled with the plant via a specific set of cubic nonlinearities. We analyze the resulting equations of motion using the method of multiple scales and show that a saturation phenomenon occurs when a one-to-one internal resonance is imposed between the plant and the absorber. To our knowledge, this is the first instance in which the saturation phenomenon is encountered in cubicly coupled systems.

5.1 System Model

We consider a plant model that includes curvature and inertia nonlinearities, introduce a second-order absorber, and couple it with the plant through a user-defined cubic feedback control law. Then, the equations governing the dynamics of the coupled oscillators are given by

$$\ddot{u}_1 \,+\, 2\,\epsilon^2\,\tilde{\mu}_1\dot{u}_1 \,+\, \omega_1^2\,u_1 \,=\, \tilde{\alpha}_1\,F_f(t), \tag{5.1}$$

$$\ddot{u}_2 \,+\, 2\,\epsilon^2\,\tilde{\mu}_2\dot{u}_2 \,+\, \omega_2^2\,u_2 + \,\tilde{\delta}_1\,u_2^3 \,+\, \tilde{\delta}_2\,\ddot{u}_2u_2^2 \,+\, \tilde{\delta}_3\,\dot{u}_2^2u_2 \,=\, \tilde{\alpha}_2\,F_c(t) \,+\, \epsilon^3 F\cos(\Omega t), \tag{5.2}$$

Table 5-1. Feedback and control signals for the cubic absorber.

Sensor	$F_f(t)$	$F_c(t)$
Position	$u_1u_2^2$, $\ddot{u}_1u_2^2$	$u_2u_1^2$, $u_2\dot{u}_1^2$, $u_2\ddot{u}_1^2$, $u_2u_1\ddot{u}_1$
Velocity	$u_1\dot{u}_2^2$, $\ddot{u}_1\dot{u}_2^2$	$\dot{u}_2u_1\dot{u}_1$, $\dot{u}_2\dot{u}_1\ddot{u}_1$
Acceleration	$u_1\ddot{u}_2^2$, $\ddot{u}_1\ddot{u}_2^2$	$\ddot{u}_2u_1^2$, $\ddot{u}_2\dot{u}_1^2$, $\ddot{u}_2\ddot{u}_1^2$, $\ddot{u}_2u_1\ddot{u}_1$

where u_1 is the absorber coordinate and u_2 is the generalized coordinate of the plant, the $\tilde{\mu}_i$ are damping coefficients, the ω_i are the natural frequencies, the $\tilde{\delta}_i$ and the $\tilde{\alpha}_i$ are constants, F and Ω are the forcing amplitude and frequency, respectively, $F_f(t)$ and $F_c(t)$ are feedback and control signals, respectively, and ϵ is a dimensionless bookkeeping parameter. The term $\tilde{\delta}_1\,u_2^3$ is due to nonlinear curvature, and the terms $\tilde{\delta}_2\ddot{u}_2u_2^2$ and $\tilde{\delta}_3\dot{u}_2^2u_2$ are due to nonlinear inertia [7]. We consider the case of one-to-one internal resonance (i.e., $\omega_1 \approx \omega_2$) and primary resonance of the plant (i.e., $\Omega \approx \omega_2$).

To realize saturation of the plant response, the signals $F_f(t)$ and $F_c(t)$ may take different forms depending on the available sensor signal from the plant. Table 5-1 lists the possible forms of these signals.

5.2 Perturbation Analysis

We consider the case of position feedback and analyze, without loss of generality, the system of equations

$$\ddot{u}_1 + 2\,\epsilon^2\tilde{\mu}_1\dot{u}_1 + \omega_1^2\,u_1 = \tilde{\alpha}_1\,\ddot{u}_1u_2^2, \tag{5.3}$$

$$\ddot{u}_2 + 2\,\epsilon^2\tilde{\mu}_2\dot{u}_2 + \omega_2^2\,u_2 + \tilde{\delta}_1u_2^3 + \tilde{\delta}_2\,\ddot{u}_2u_2^2 + \tilde{\delta}_3\,\dot{u}_2^2u_2 = \tilde{\alpha}_2\,\dot{u}_1^2u_2 + \epsilon^3F\cos(\Omega t). \tag{5.4}$$

Using the method of multiple scales, we seek expansions of u_1 and u_2 in the form

$$u_1 \approx \epsilon\,u_{11}(T_0,T_2) + \epsilon^3\,u_{13}(T_0,T_2), \tag{5.5}$$

$$u_2 \;\approx\; \epsilon\, u_{21}(T_0, T_2) \;+\; \epsilon^3\, u_{23}(T_0, T_2), \tag{5.6}$$

where $T_0 = t$ is a fast time scale and $T_2 = \epsilon^2 t$ is a slow time scale describing the time evolution of the amplitudes and phases of the response. The time derivatives are recast in terms of the new time scales as

$$\frac{d}{dt} \;=\; D_0 \;+\; \epsilon^2\, D_2 \;+\cdots \quad \text{and} \quad \frac{d^2}{dt^2} \;=\; D_0^2 \;+\; 2\,\epsilon^2\, D_0\, D_2 \;+\cdots, \tag{5.7}$$

where $D_k \equiv \partial/\partial T_k$. Substituting equations (5.5)–(5.7) into equations (5.3) and (5.4) and equating coefficients of like power of ϵ yields

Order (ϵ):

$$D_0^2 u_{11} \;+\; \omega_1^2\, u_{11} \;=\; 0, \tag{5.8}$$

$$D_0^2 u_{21} \;+\; \omega_2^2\, u_{21} \;=\; 0, \tag{5.9}$$

Order (ϵ^3):

$$D_0^2 u_{13} \;+\; \omega_1^2\, u_{13} \;=\; -\; 2\, D_0\, (D_2 u_{11} + \tilde{\mu}_1\, u_{11}) + \tilde{\alpha}_1\, D_0^2 u_{11} u_{21}^2, \tag{5.10}$$

$$\begin{aligned} D_0^2 u_{23} \;+\; \omega_2^2\, u_{23} \;=\; &-\; 2\, D_0\, (D_2 u_{21} + \tilde{\mu}_2\, u_{21}) - \tilde{\delta}_1\, u_{21}^3 \;-\; \tilde{\delta}_2 D_0^2 u_{21}\, u_{21}^2 \;-\; \tilde{\delta}_3\, (D_0 u_{21})^2 u_{21} \\ &-\; \tilde{\alpha}_2\, (D_0 u_{11})^2\, u_{21} + F\cos(\Omega t). \end{aligned} \tag{5.11}$$

The solutions of equations (5.8) and (5.9) can be expressed as

$$u_{11} \;=\; A_1(T_2)\, e^{i\omega_1 T_0} \;+\; \overline{A}_1(T_2)\, e^{-i\omega_1 T_0}, \tag{5.12}$$

$$u_{21} \;=\; A_2(T_2)\, e^{i\omega_2 T_0} \;+\; \overline{A}_2(T_2)\, e^{-i\omega_2 T_0}, \tag{5.13}$$

where the A_i are unknown complex-valued functions that will be determined by imposing the solvability conditions at the next level of approximation. Substituting equations (5.12) and (5.13) into equations (5.10) and (5.11) yields

$$\begin{aligned} D_0^2 u_{13} \;+\; \omega_1^2\, u_{13} \;=\; &-\; 2\, i\, \omega_1\, (\, D_2 A_1 + \tilde{\mu}_1\, A_1)\, e^{i\omega_1 T_0} \\ &-\; \omega_1^2\, \tilde{\alpha}_1\, \left(A_1\, e^{i\omega_1 T_0} \;+\; \overline{A}_1\, e^{-i\omega_1 T_0}\right) \left(A_2^2\, e^{2i\omega_2 T_0} + A_2 \overline{A}_2\right) + \text{cc}, \end{aligned} \tag{5.14}$$

$$D_0^2 u_{23} \;+\; \omega_2^2\, u_{23} \;=\; -\; 2\, i\, \omega_2\, (\, D_2 A_2 + \tilde{\mu}_2\, A_2)\, e^{i\omega_2 T_0} - (\tilde{\delta}_1 - \omega_2^2 \tilde{\delta}_2)\, \left(A_2^3\, e^{3i\omega_2 T_0} \;+\; 3 A_2^2 \overline{A}_2\, e^{i\omega_2 T_0}\right)$$

$$
\begin{aligned}
&+\ \omega_2^2\,\tilde{\delta}_3\left(A_2^2\,e^{2i\omega_2 T_0}\ -\ A_2\overline{A}_2\right)\left(A_2\,e^{i\omega_2 T_0}\ +\ \overline{A}_2\,e^{-i\omega_2 T_0}\right)\\
&-\ \omega_1^2\,\tilde{\alpha}_2\ \left(A_1^2\,e^{2i\omega_1 T_0}-A_1\overline{A}_1\right)\left(A_2\,e^{i\omega_2 T_0}\ +\ \overline{A}_2\,e^{-i\omega_2 T_0}\right)\\
&+\ \frac{1}{2}\,F\,e^{i\Omega T_0}+\text{cc},
\end{aligned}
\tag{5.15}
$$

where cc stands for the complex conjugate of the preceding terms. To express the nearness of ω_1 to ω_2 and Ω to ω_2, we introduce two detuning parameters $\tilde{\sigma}_1$ and $\tilde{\sigma}_2$ defined by

$$
\omega_1\ =\ \omega_2\ -\ \epsilon^2\,\tilde{\sigma}_1\quad\text{and}\quad\Omega\ =\ \omega_2\ +\ \epsilon^2\,\tilde{\sigma}_2. \tag{5.16}
$$

Inserting equations (5.16) into equations (5.14) and (5.15) and eliminating terms that lead to secular terms yields

$$
2\,i\,(D_2A_1+\tilde{\mu}_1A_1)+\ 8\,\hat{\alpha}_1\left(2\,A_2\overline{A}_2A_1+\overline{A}_1A_2^2e^{2i\tilde{\sigma}_1T_2}\right)\ =\ 0, \tag{5.17}
$$

$$
2\,i\,(D_2A_2+\tilde{\mu}_2A_2)+8\,\delta_eA_2^2\overline{A}_2\ +\ 8\,\hat{\alpha}_2\left(-2A_1\overline{A}_1A_2+A_1^2\overline{A}_2e^{-2\,i\tilde{\sigma}_1T_2}\right)\ -\ f\,e^{i\tilde{\sigma}_2T_2}\ =\ 0, \tag{5.18}
$$

where

$$
\hat{\alpha}_1\ =\ \frac{1}{8}\,\omega_1\,\alpha_1,\quad\hat{\alpha}_2\ =\ \frac{1}{8}\,\omega_1\,\alpha_2,\quad\delta_e\ =\ \frac{1}{8\,\omega_2}\left[3\,\tilde{\delta}_1-\omega_2^2(3\,\tilde{\delta}_2+\tilde{\delta}_3)\right],\quad\text{and}\quad f\ =\ \frac{F}{2\,\omega_2}. \tag{5.19}
$$

To facilitate the analysis, we reduce the number of the parameters in equations (5.17) and (5.18) by introducing the scalings

$$
A_1\ =\ c_1\,B_1,\ \ A_2\ =\ c_2\,B_2,\ \ \text{and}\ \ T_2\ =\ c_3\,T, \tag{5.20}
$$

where the c_i are constants. Then, equations (5.17) and (5.18) become

$$
2\,i\,(B_1'+\mu_1B_1)+\ 8\,\hat{\alpha}_1\,c_2^2\,c_3\left(2\,B_2\overline{B}_2B_1+\overline{B}_1B_2^2e^{2i\sigma_1T}\right)\ =\ 0, \tag{5.21}
$$

$$
2\,i\,(B_2'+\mu_2B_2)\ +\ 8\,c_2^2\,c_3\,\delta_e\,B_2^2\overline{B}_2\ +\ 8\,\hat{\alpha}_2c_1^2c_3\left(-2B_1\overline{B}_1B_2+B_1^2\overline{B}_2e^{-2i\sigma_1T}\right)\ -\ \frac{c_3f}{c_2}e^{i\sigma_2T}\ =\ 0, \tag{5.22}
$$

where

$$
\mu_i\ =\ c_3\,\tilde{\mu}_i\quad\text{and}\quad\sigma_i\ =\ c_3\,\tilde{\sigma}_i. \tag{5.23}
$$

To keep the forcing amplitude f as a control parameter, we set $c_2=c_3$. Furthermore, we let

$$
\hat{\alpha}_1\,c_3^3\ =\ 1\quad\text{and}\quad\hat{\alpha}_2\,c_1^2\,c_3\ =\ 1. \tag{5.24}
$$

Solving for the constants, we obtain

$$c_1 = \sqrt{\frac{|\hat{\alpha}_1|^{\frac{1}{3}}}{|\hat{\alpha}_2|}} \quad \text{and} \quad c_2 = c_3 = |\hat{\alpha}_1|^{-\frac{1}{3}}. \tag{5.25}$$

Moreover, we define

$$\delta = \frac{\delta_e}{\hat{\alpha}_1}. \tag{5.26}$$

Next, we express $B_1(T)$ and $B_2(T)$ in the polar form

$$B_1 = \frac{1}{2}\, a_1(T)\, e^{i\beta_1(T)} \quad \text{and} \quad B_2 = \frac{1}{2}\, a_2(T)\, e^{i\beta_2(T)}. \tag{5.27}$$

Substituting equations (5.25)–(5.27) into equations (5.21) and (5.22) and separating real and imaginary parts yields

$$a_1' = -\,\mu_1\, a_1 - a_1 a_2^2 \sin\gamma_1, \tag{5.28}$$

$$a_2' = -\,\mu_2\, a_2 + a_1^2 a_2 \sin\gamma_1 + f \sin\gamma_2, \tag{5.29}$$

$$a_1\, \beta_1' = a_1 a_2^2\, (2 + \cos\gamma_1), \tag{5.30}$$

$$a_2\, \beta_2' = \delta a_2^3 + a_1^2 a_2\, (\cos\gamma_1 - 2) - f \cos\gamma_2, \tag{5.31}$$

where

$$\gamma_1 = 2\,(\beta_2 - \beta_1 + \sigma_1 T) \quad \text{and} \quad \gamma_2 = \sigma_2 T - \beta_2. \tag{5.32}$$

5.3 Equilibrium and Dynamic Solutions

In this section, we study the equilibrium and dynamic solutions of equations (5.28)–(5.32) and their bifurcations. To determine the equilibrium solutions, we set $a_1' = a_2' = 0$ and $\gamma_1' = \gamma_2' = 0$ and obtain the algebraic equations

$$\mu_1\, a_1 = -\, a_1 a_2^2 \sin\gamma_1, \tag{5.33}$$

$$\mu_2\, a_2 = a_1^2 a_2 \sin\gamma_1 + f \sin\gamma_2, \tag{5.34}$$

$$\nu_1\, a_1 = a_1 a_2^2\, (2 + \cos\gamma_1), \tag{5.35}$$

$$\nu_2\, a_2 = \delta\, a_2^3 + a_1^2 a_2\, (\cos\gamma_1 - 2) - f \cos\gamma_2, \tag{5.36}$$

where

$$\nu_1 \;=\; \sigma_1 + \sigma_2 \quad \text{and} \quad \nu_2 = \sigma_2. \tag{5.37}$$

There are two possibilities: $a_1 = 0$ and $a_1 \neq 0$. When $a_1 = 0$, it follows from equations (5.34) and (5.36) that

$$\left[\mu_2^2 + \left(\nu_2 \;-\; \delta\, a_2^2\right)^2\right] a_2^2 \;-\; f^2 \;=\; 0. \tag{5.38}$$

This is the single-mode solution. Equation (5.38) is similar to the frequency-response equation of the forced Duffing oscillator. The unexcited mode does not oscillate while the directly excited mode oscillates with an amplitude that is dependent on the detuning ν_2, the magnitude of the forcing f, and the system's initial conditions [62]. When $a_1 \neq 0$, it follows from equations (5.33)–(5.36) that

$$\mu_1^2 \;+\; \left(\nu_1 - 2\, a_2^2\right)^2 - a_2^4 = 0, \tag{5.39}$$

$$\left(\mu_1 a_1^2 + \mu_2 a_2^2\right)^2 + \left[\nu_2\, a_2^2 - a_1^2\left(\nu_1 - 4\, a_2^2\right) \;-\; \delta\, a_2^4\right]^2 \;-\; a_2^2\, f^2 \;=\; 0, \tag{5.40}$$

which is a two-mode solution. The solutions of equation (5.39) are

$$a_2^{(1)} \;=\; \sqrt{\frac{2\,\nu_1 - \sqrt{\nu_1^2 - 3\mu_1^2}}{3}} \quad \text{and} \quad a_2^{(2)} \;=\; \sqrt{\frac{2\,\nu_1 + \sqrt{\nu_1^2 - 3\mu_1^2}}{3}}. \tag{5.41}$$

Thus, the directly excited mode may oscillate at two distinct amplitudes that are functions of the detuning parameter ν_1 and the damping coefficient μ_1, but independent of the excitation amplitude f. In contrast, the amplitude of the indirectly excited mode is dependent on the excitation amplitude.

To study the stability of the equilibrium solutions, we express B_1 and B_2 in the form

$$B_1 \;= \frac{1}{2}\,(p_1 - iq_1)\, e^{i\nu_1 T} \quad \text{and} \quad B_2 \;=\; \frac{1}{2}\,(p_2 - iq_2)\, e^{i\nu_2 T}, \tag{5.42}$$

where the p_n and q_n are real and write the modulation equations in Cartesian form as

$$p_1' \;=\; -\,\mu_1\, p_1 - \nu_1\, q_1 + \; q_1(p_2^2 + 3q_2^2) \;+\; 2p_1 p_2 q_2, \tag{5.43}$$

$$q_1' \;=\; -\,\mu_1\, q_1 + \nu_1\, p_1 - \; p_1(q_2^2 + 3p_2^2) \;-\; 2q_1 q_2 p_2, \tag{5.44}$$

$$p_2' \;=\; -\,\mu_2\, p_2 - \nu_2\, q_2 - \; q_2\,(q_1^2 + 3p_1^2) \;+\; 2p_1 p_2 q_1 \;+\; \delta\, q_2\,(p_2^2 + q_2^2), \tag{5.45}$$

$$q_2' \;=\; -\,\mu_2\, q_2 + \nu_2\, p_2 + \; p_2\,(p_1^2 + 3q_1^2) \;-\; 2p_1 q_1 q_2 \;-\; \delta p_2\,(p_2^2 + q_2^2) \;+\; f. \tag{5.46}$$

The stability of a particular equilibrium solution is ascertained by investigating the eigenvalues of the Jacobian matrix of the right-hand sides of equations (5.43)–(5.46). Then, a pseudo-arclength scheme is used to trace branches of the equilibrium solutions [63].

The purpose of this study is to investigate active implementation of the vibration absorber. In this case, the frequency at which the plant oscillates can be measured, and, accordingly, the frequency of the absorber can be adjusted. Guided by the fact that the amplitudes $a_2^{(1)}$ and $a_2^{(2)}$ in equation (5.41) are only functions of μ_1 and ν_1, we choose ν_1 to be a small non-zero number. Consequently, the magnitude of a_2 will be constant in both the frequency- and force-response curves. Furthermore, we set the absorber damping coefficient equal to a small but non-zero value.

In Figure 5-1, we show the frequency-response curves when $\mu_1 = 0.0005$, $\mu_2 = 0.001$, $\nu_1 = 0.01$, $\delta = -1$, and $f = 0.0001$. The plant exhibits a softening-type behavior. In Figure 5-1b, we illustrate an enlargement of the boxed area labeled "I" in Figure 5-1a. Initially, the response consists of the single-mode solution. As σ_2 is increased beyond the value at point F, shown in Figure 5-1b, and in the presence of large disturbances, a jump to a high-amplitude plant response is possible. In this case, the response consists of the two-mode solution along the branch FG, and the amplitude of the plant is $a_2^{(2)}$. The two-mode solution experiences a supercritical pitchfork bifurcation at G, where the single-mode solution is reached. It is maintained until point H, where it undergoes a subcritical pitchfork bifurcation, leading to a jump to the single-mode solution along the branch EA. In the absence of large disturbances, the response consists of the single-mode solution, which is stable. At A, the single-mode solution undergoes a saddle-node bifurcation, and the response jumps to B where the two-mode solution is sustained. As σ_2 is increased, the response traces the curve BC. Here, the amplitude of the plant is equal to $a_2^{(1)}$. When $\sigma_2 = \sigma_2^{(C)}$, the response undergoes a supercritical pitchfork bifurcation after which only the single-mode solution exists. When σ_2 is decreased from a high value, the single-mode response experiences a supercritical pitchfork bifurcation at C, and the resulting two-mode solution traces the curve CBD. At D, the solution undergoes a saddle-node bifurcation, leading to a jump to point E, where the

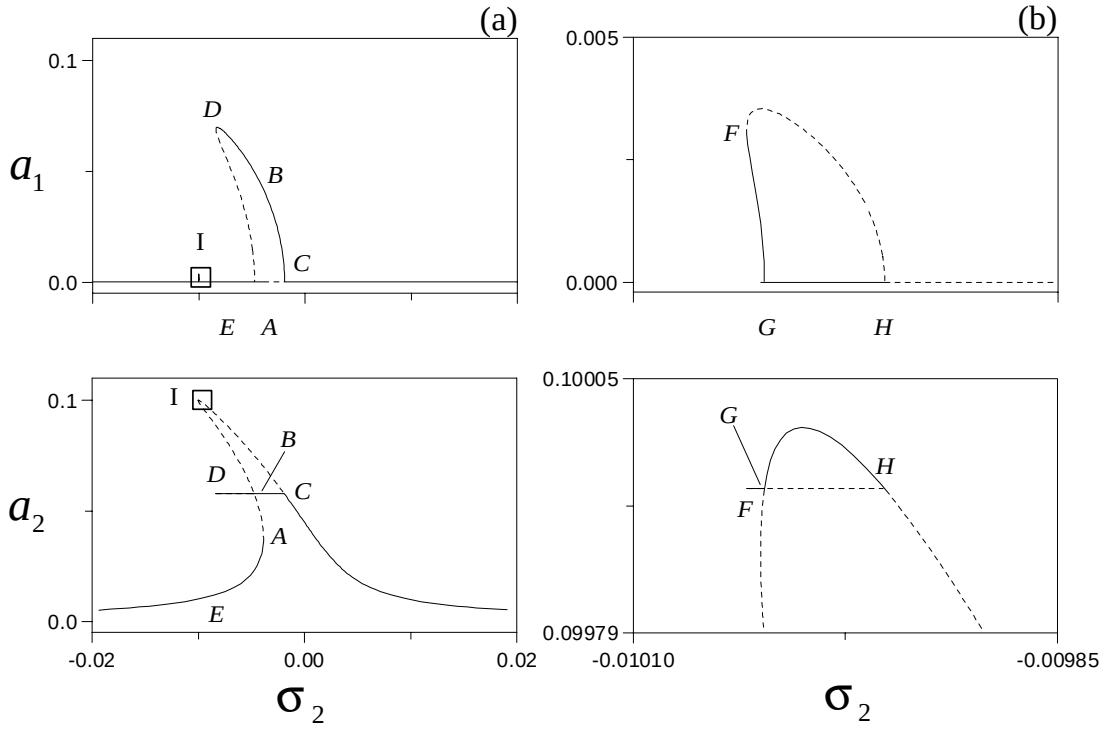

Figure 5-1. Frequency-response curves when $\mu_1 = 0.0005$, $\mu_2 = 0.001$, $\nu_1 = 0.01$, $\delta = -1$, and $f = 0.0001$. (a) Overall frequency-response curves and (b) an enlargement of area "I". Solid (dotted) lines denote stable nodes (saddles).

response consists of the single-mode solution thereafter. If σ_2 is set at a value between the points H and F and a large disturbance is imparted to the system, single- or two-mode solutions may be possible, as discussed previously.

In Figure 5-2, we show the frequency-response curves when $\mu_1 = 0.0005$, $\mu_2 = 0.001$, $\nu_1 = 0.01$, $\delta = 1$, and $f = 0.0001$. The plant exhibits a hardening-type behavior. In Figure 5-2b, we illustrate an enlargement of the boxed area labeled "II" in Figure 5-2a. As σ_2 is increased, the response consists of the single-mode solution, which is stable. At point A ($\sigma_2 = 0.001935458$), the response undergoes a subcritical pitchfork bifurcation, which leads to a jump to a two-mode dynamic solution. The dynamic solution is maintained until E is reached, after which the response jumps to the single-mode solution. The branch EF is unstable (saddle) and,

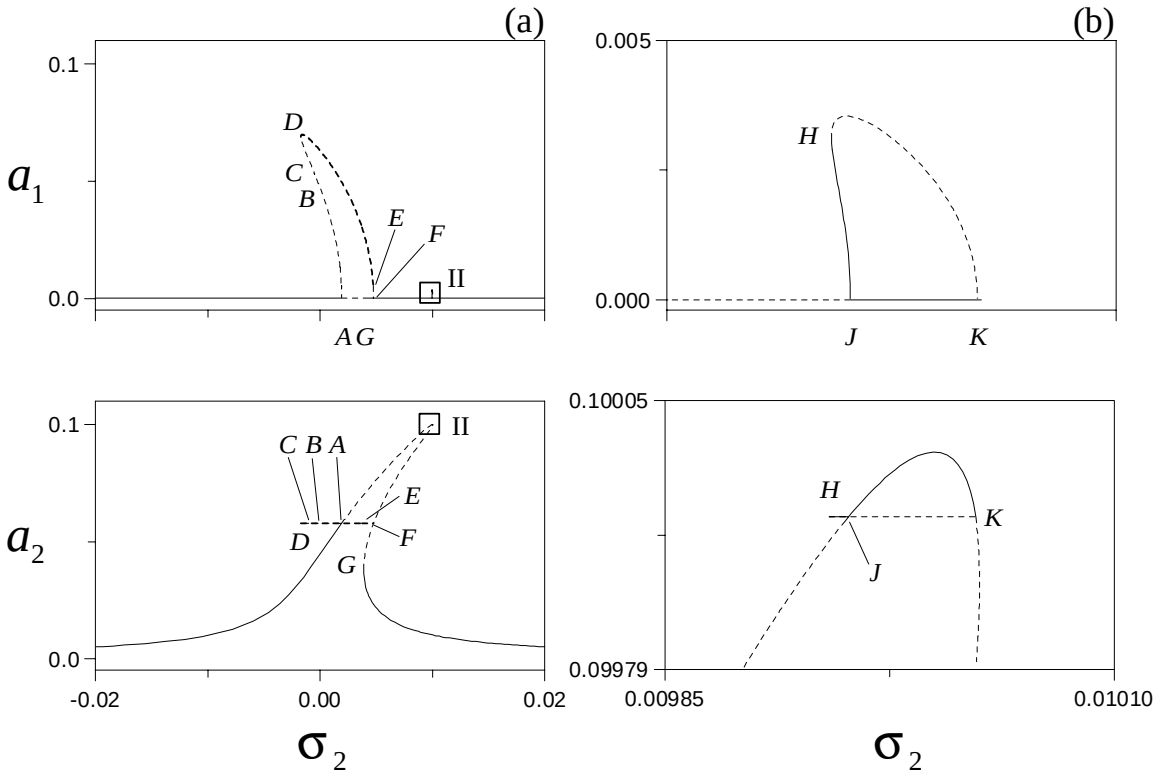

Figure 5-2. Frequency-response curves when $\mu_1 = 0.0005$, $\mu_2 = 0.001$, $\nu_1 = 0.01$, $\delta = 1$, and $f = 0.0001$. (a) Overall frequency-response curves and (b) an enlargement of area "II". Solid (dotted) lines denote stable nodes (saddles) and bold-dashed lines denote unstable foci.

therefore, cannot be attained. Similarly to the case when $\delta = -1$, there exists a region between points H and K where high-amplitude single- or two-mode solutions may be reached in the presence of large disturbances. In the case of reverse sweep, and in the absence of large disturbances, the single-mode solution is initially stable. It experiences a saddle-node bifurcation at G ($\sigma_2 = 0.003878544$), leading to a jump to a two-mode dynamic solution. When σ_2 is in the region AD, the dynamic solution might coexist with the single-mode solution. When σ_2 is less than the value at D, only the single-mode solution exists.

In Figure 5-3, we illustrate the loci of the unstable eigenvalues of the two-mode solution shown in Figure 5-2a as σ_2 is varied. In Figure 5-3a, we show the locus of the eigenvalues

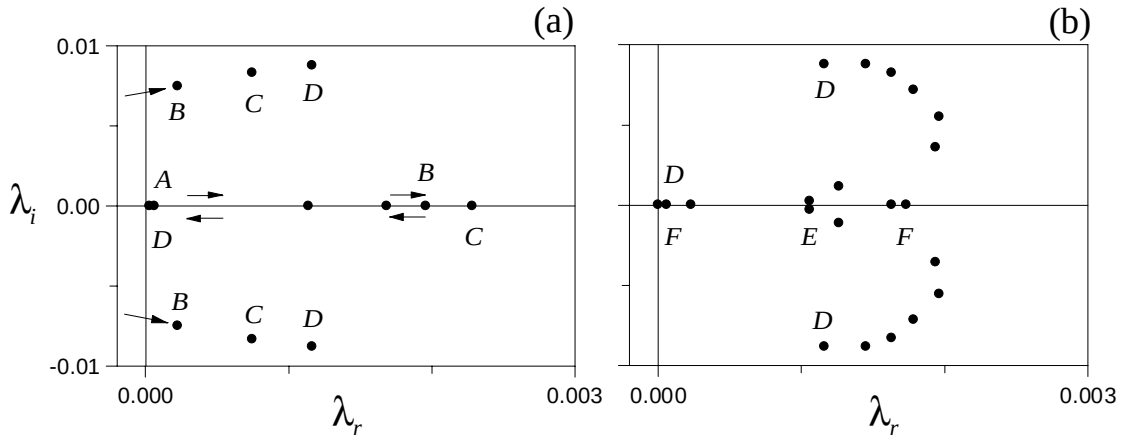

Figure 5-3. Loci of the unstable eigenvalues of the two-mode solution when $\mu_1 = 0.0005$, $\mu_2 = 0.001$, $\nu_1 = 0.01$, $f = 0.0001$, and $\delta = 1$. (a) Locus along branch $ABCD$ and (b) locus along branch DEF.

along the branch $ABCD$. At point A, a single eigenvalue goes through zero, indicating a subcritical pitchfork bifurcation. It remains real and positive as σ_2 is decreased. As point B is approached, two complex conjugate eigenvalues move to the right-hand side of the complex plane. As σ_2 is decreased further, the real eigenvalue moves to the right until point C is reached, where it reverses direction. At point D, it crosses to the left-hand plane through zero, indicating a turning point. Two complex eigenvalues remain in the right-hand side, and the equilibrium solution becomes an unstable focus. In Figure 5-3b, we illustrate the locus of the unstable eigenvalues for branch DEF. As σ_2 is increased, the imaginary parts of the eigenvalues decrease until they become zero beyond point E, where the fixed point becomes a saddle. Then, the remaining two positive real eigenvalues split and move in opposite directions. At point F, one eigenvalue is equal to zero, and a non-classical pitchfork bifurcation occurs where the branches of the unstable single and two-mode solutions meet.

To investigate the nature of the dynamic solutions, we integrate numerically equations (5.43)–(5.46) between A and G and find that the response is chaotic. Therefore, we analyze the system between and in the neighborhood of points A and G. In Figure 5-4, we show two-

Table 5-2. Values of the ratio r on branch AB.

σ_2	0.001872	0.001899	0.001918	0.001930	0.001935
r	1.10	1.59	2.74	7.42	242

dimensional projections of the phase portraits and Poincaré sections for two values of σ_2 that lie in the region between points A and G. Clearly, the system exhibits high-amplitude chaotic responses.

Next, we study the system dynamics near point A. When σ_2 is increased beyond A, the response jumps to a chaotic attractor. However, when σ_2 is decreased, the chaotic response is maintained for a small region to the left of point A. Further decreases in σ_2 lead to the single-mode solution. Here, the chaotic attractor may be destroyed through a Shilnikov scenario or a boundary crisis [62]. In the presence of orbits homoclinic to a saddle-focus, Shilnikov's theorem predicts chaotic behavior on the outer side of the orbit if the ratio

$$r = \frac{|\rho|}{\lambda_1}$$

is less than one, where ρ is the value of the real part of the stable complex conjugate eigenvalues and λ_1 is the value of the unstable real eigenvalue. We look for orbits homoclinic to the saddle-focus close to point A. To this end, we search for limit cycles by choosing initial conditions in both directions on the unstable manifolds of the saddle-focus on branch AB. In Figure 5-5, we show time traces of the responses. All initial conditions lead to the single-mode solution. In the event that a homoclinic orbit existed, we monitor the ratio r. In Table 5-2, we list the value of the ratio r as A is approached. Since the value is greater than one and increasing, we conclude that a Shilnikov scenario is not possible. Therefore, the chaotic attractor is destroyed by a boundary crisis.

Finally, we investigate the system dynamics near point G, where the single-mode response undergoes a saddle-node bifurcation at $\sigma_2 = 0.003878544$. Beyond G, the system exhibits an intermittent response. The response of the plant alternates between two single-mode states: the old (ghost) solution near G and the unstable solution on branch AH. As σ_2 is

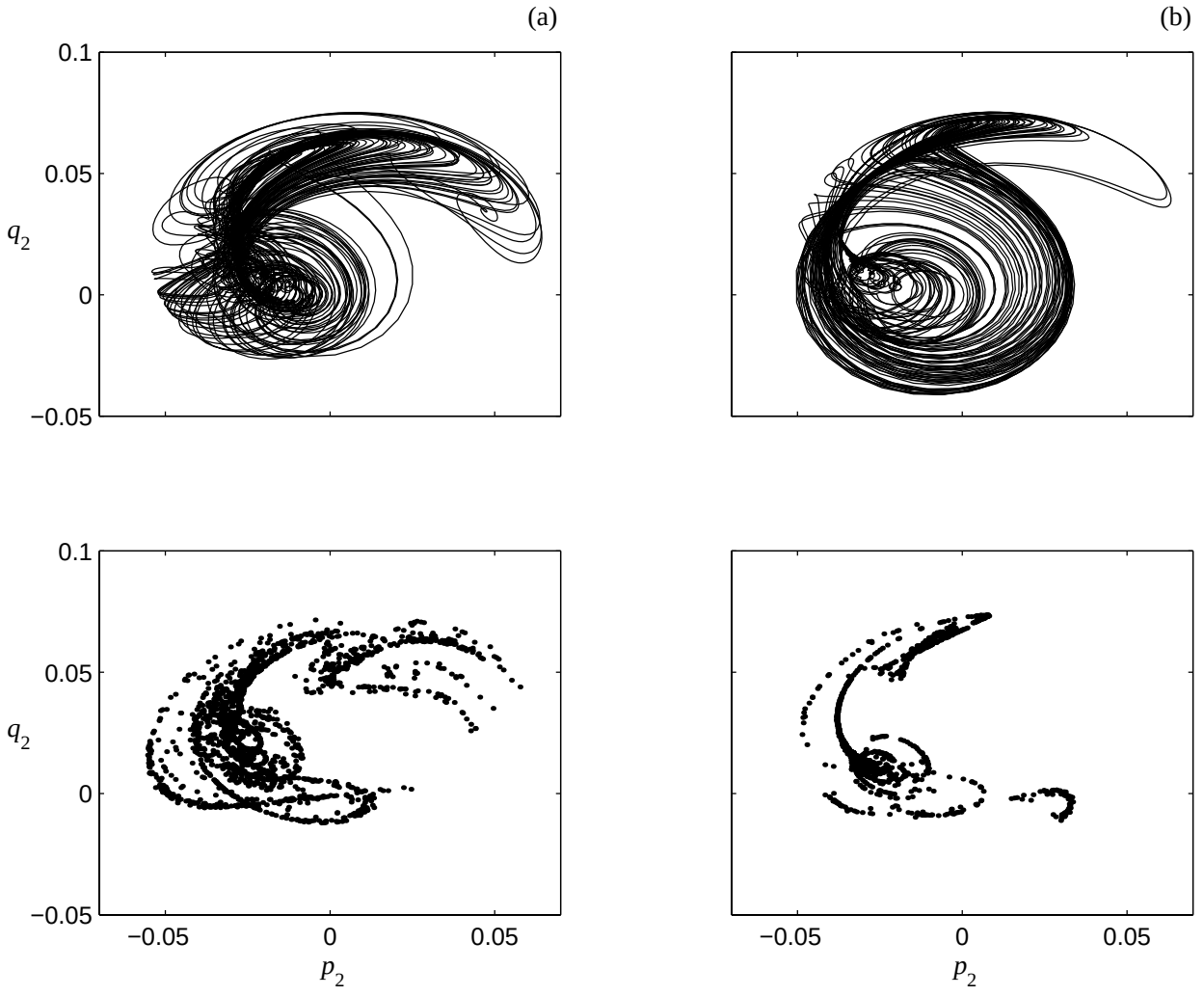

Figure 5-4. Two-dimensional projections of the phase portraits and Poincaré sections of the response when $\delta = 1$, $\mu_1 = 0.0005$, $\mu_2 = 0.001$, $\nu_1 = 0.01$, and $f = 0.0001$. (a) $\sigma_2 = 0.002$ and (b) $\sigma_2 = 0.0036$.

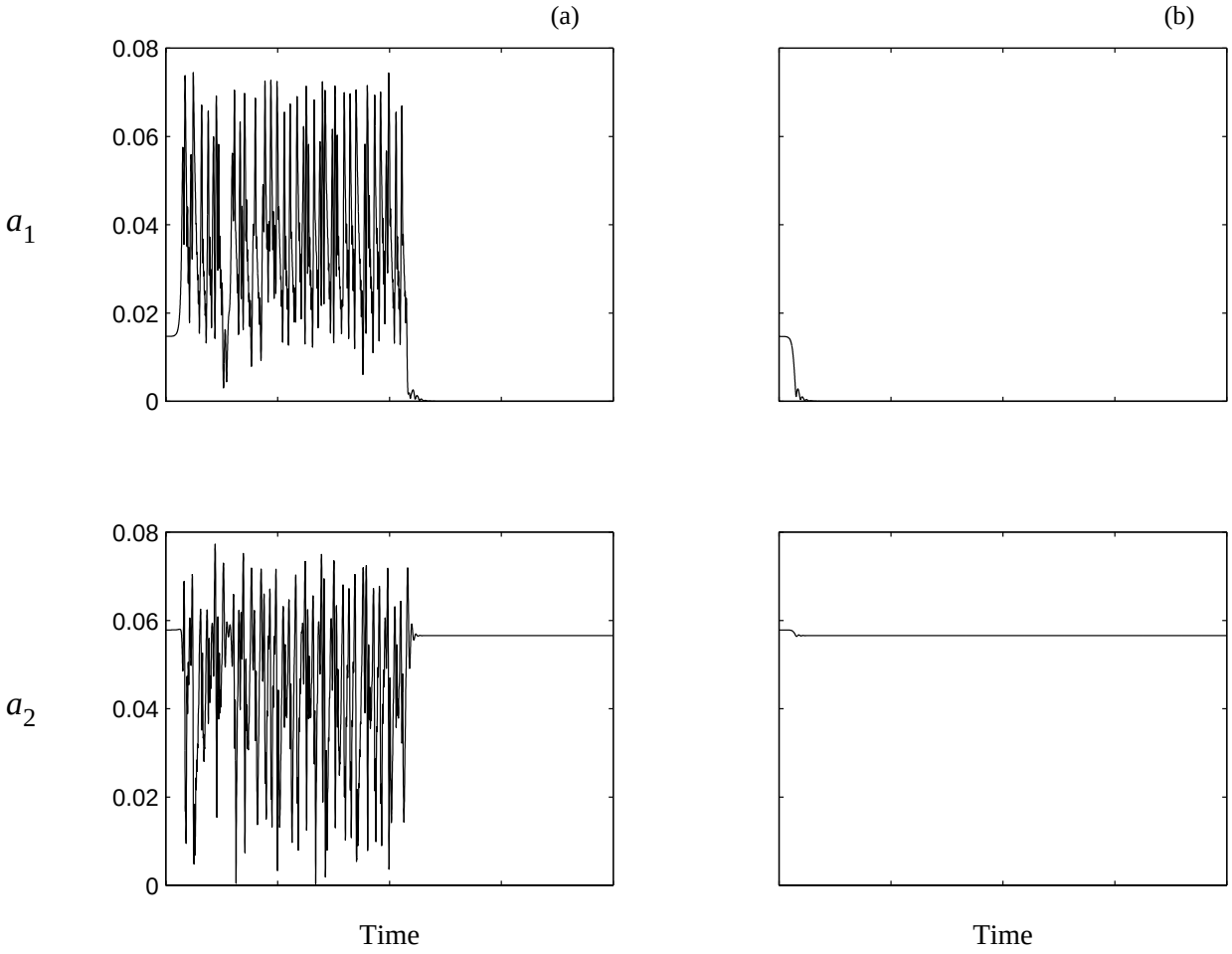

Figure 5-5. Time responses when $\delta = 1$, $\mu_1 = 0.0005$, $\mu_2 = 0.001$, $\nu_1 = 0.01$, $f = 0.0001$, and $\sigma_2 = 0.001740453$. Initial conditions are chosen on the unstable manifold of branch AB.

decreased, the frequency of intermittency increases, as illustrated in Figure 5-6. Chaos is reached through a type I intermittency.

Based on the frequency-response analysis, it appears that it is possible to implement the proposed absorber when $\delta < 0$ and the forcing amplitude is small. Consequently, we study the effect of varying the forcing amplitude on the response of the system. In Figure 5-7, we display the force-response curves when $\mu_1 = 0.0005$, $\mu_2 = 0.001$, and $\nu_1 = 0.01$. The system exhibits a two-valued saturation phenomenon.

First, we analyze the case when $\delta = -1$ and $\sigma_2 = -0.005$, which is shown in Figure 5-7a. Initially, as f is increased from zero and in the absence of large disturbances, the response consists of the single-mode solution, which is stable. The solution goes through a saddle-node bifurcation at A, leading to a stable two-mode solution at B. As f is increased beyond f_B, the response of the directly excited mode saturates at the value $a_2^{(1)}$, and the response of the unexcited mode increases. At point H, the response experiences a subcritical Hopf bifurcation leading to a jump to a dynamic solution. When $f > f_C$, the system may be attracted to either the constant single-mode solution or to a two-mode dynamic solution. When f is decreased, there are two possible paths for the solutions. If the initial conditions are small, the system response will consist of the single-mode solution. This solution loses stability through a subcritical pitchfork bifurcation at $f = f_C$. When $f < f_C$, the responses of both modes undergo jumps and are attracted to a dynamic solution. If the initial conditions are large, the system may be attracted directly to a dynamic solution. Because the Hopf bifurcation at H is subcritical, a dynamic solution may coexist with the stable two-mode solution when $f < f_H$. If the constant two-mode solution is reached, then as f is decreased, the solution will trace the curve BD and will undergo a saddle-node bifurcation at D, leading to a jump to the single-mode solution at E.

In Figure 5-7b, we show force-response curves when $\delta = 1$ and $\sigma_2 = 0.005$. We note the emergence of a new region of dynamic solutions between the points H_1 and H_2. Furthermore, the subcritical pitchfork bifurcation at C is replaced with a supercritical pitchfork bifurcation. When $0 < f < f_A$ and in the absence of large disturbances, the response consists of the

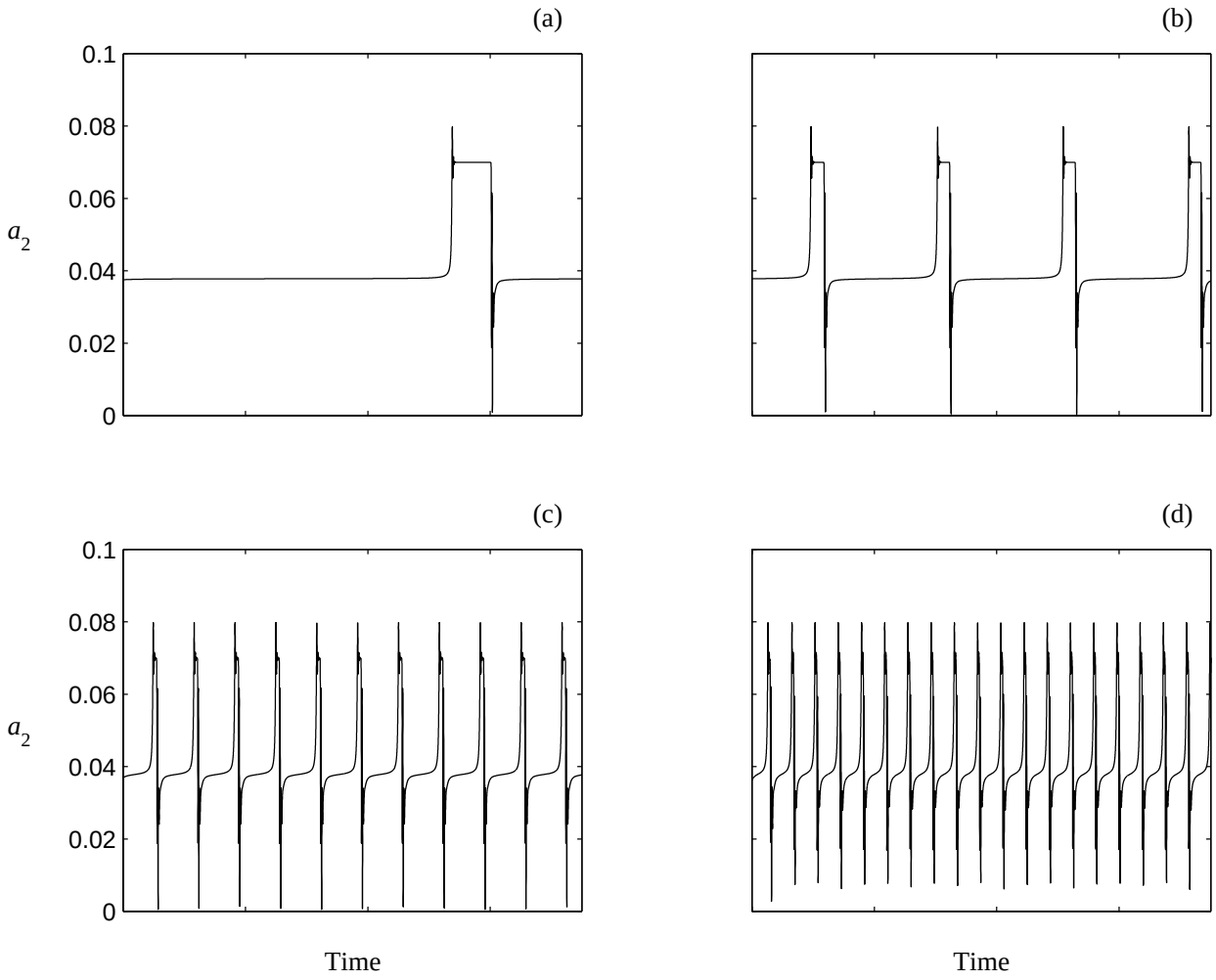

Figure 5-6. Time evolution of the plant amplitude when $\delta = 1$, $\mu_1 = 0.0005$, $\mu_2 = 0.001$, $\nu_1 = 0.01$, and $f = 0.0001$. (a) $\sigma_2 = 0.003878056$, (b) $\sigma_2 = 0.00387801$, (c) $\sigma_2 = 0.0038775$, and (d) $\sigma_2 = 0.003876$.

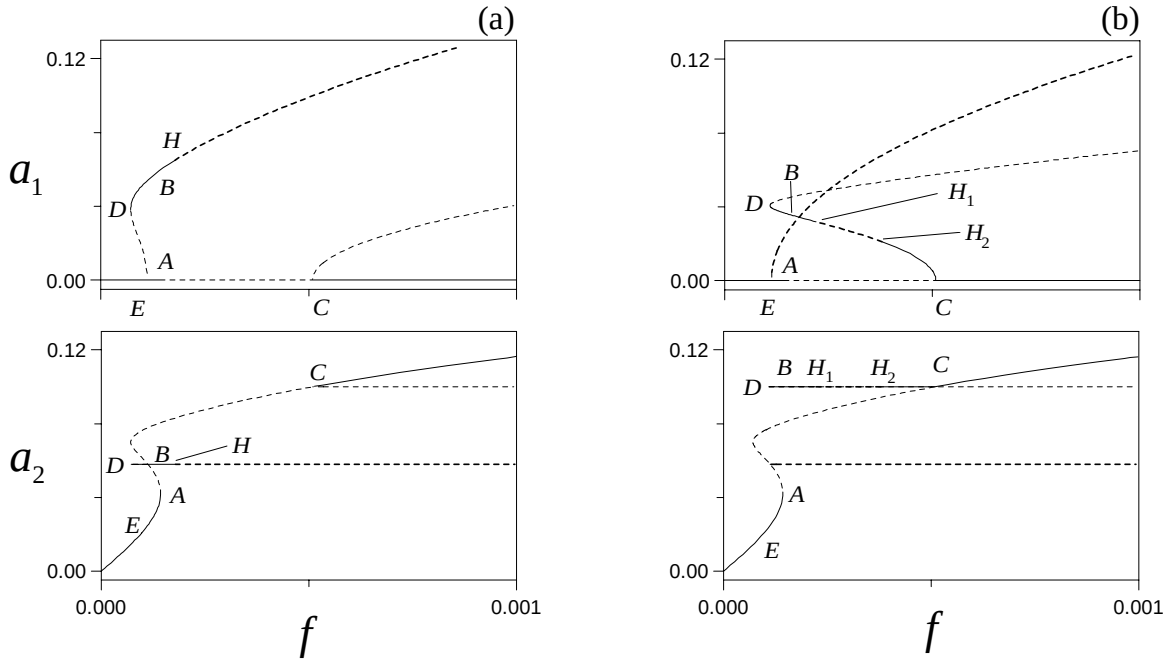

Figure 5-7. Force-response curves when $\mu_1 = 0.0005$, $\mu_2 = 0.001$, and $\nu_1 = 0.01$. (a) $\delta = -1$ and $\sigma_2 = -0.005$ and (b) $\delta = 1$ and $\sigma_2 = 0.005$. Solid (dotted) lines denote stable nodes (saddles) and bold-dashed lines denote unstable foci.

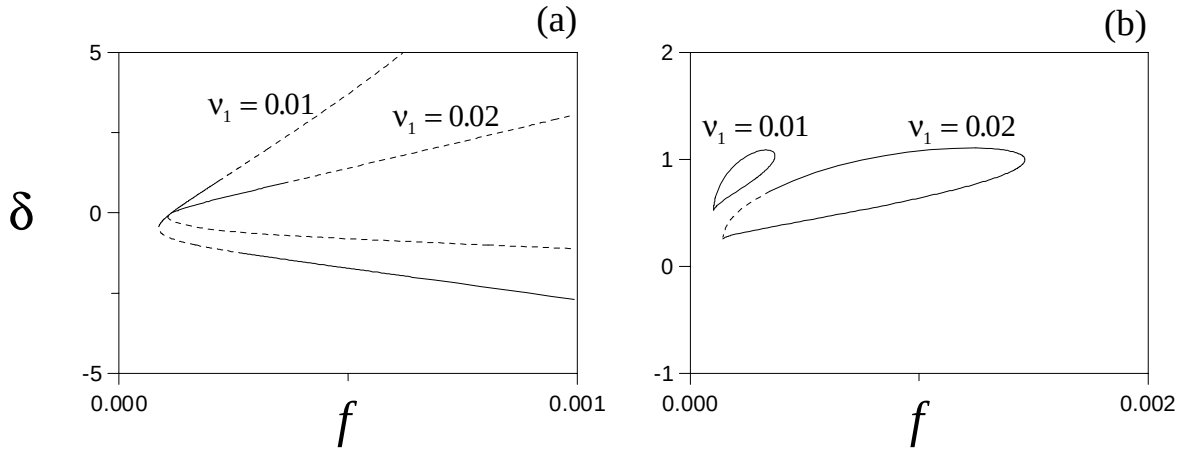

Figure 5-8. Projection of the Hopf bifurcation loci on the δ–f plane when $\mu_1 = 0.0005$ and $\mu_2 = 0.001$. (a) $\sigma_2 = -0.005$ and (b) $\sigma_2 = 0.005$. Solid (dotted) lines denote supercritical (subcritical) bifurcations.

single-mode solution. When $f > f_A$ and depending on the amplitude of the motion, the response may be attracted to either a dynamic or a constant solution in the region BH_1. In this case, the plant's amplitude may saturate at the value $a_2^{(2)}$. Subsequently, the solution undergoes a supercritical Hopf bifurcation at H_1. At H_2, the system experiences a reverse supercritical Hopf bifurcation after which the two-mode solution is attained. Then, the single-mode solution is reached through a supercritical pitchfork bifurcation at C. Similar results are expected when f is decreased. However, a stable two-mode constant solution may be attained along branch H_1D.

Based on the results of the force-response analysis, we conclude that implementation of the absorber is possible only for small forcing amplitudes when $\delta < 0$. In Figure 5-8, we display the loci of the Hopf bifurcation points in the δ–f plane for different values of the detuning parameter ν_1. It is clear that Hopf bifurcations that may lead to high-amplitude periodic or chaotic motions are possible.

5.4 Summary

In this chapter, we studied the dynamics of a cubic vibration absorber. We developed the equations of motion and obtained an approximate solution to the nonlinear differential equations using the method of multiple scales. Then, we conducted bifurcation analyses and investigated theoretically the performance of the control strategy. We showed that a saturation phenomenon exists and that it can be used, in a very limited range, for successful application of the control technique. Additionally, we demonstrated the existence of dynamic solutions that may lead to high-amplitude or chaotic responses.

Part II

Parametric Excitation

Chapter 6

Quadratic Absorber

Motivated by the results of Part I of the Dissertation, we investigate in this chapter application of the quadratic absorber for controlling a parametrically excited system. Nayfeh [64] analyzed the response of a system of two quadratically coupled oscillators in the case of simultaneous principal parametric and internal resonances. He found that, for certain detunings, the response of the system experiences Hopf bifurcations, leading to nonperiodic motions. In the context of studying multi-mode dynamics of buckled beams, Chin, Nayfeh, and Lacarbonara [65] derived and analyzed modulation equations identical to the ones derived by Nayfeh [64]. They reported the occurences of Hopf and period-doubling bifurcations, type I intermittency, chaos, and crises. They also found regimes where the system exhibited unbounded responses. Consequently, we do not expect that the strategy to be successful in the case of parametric excitation. Nevertheless, we take advantage of the developments of the previous chapters.

We analyze a system similar to the one investigated by Chin, Nayfeh, and Lacarbonara and conduct experiments on such systems. We develop an experimental testbed that consists of a cantilever beam and an electronic second-order circuit. The beam is fitted with a strain gage and piezoceramic actuators. It is coupled with the circuit through electronically generated quadratic nonlinearities.

6.1 System Model and Perturbation Solution

We model the dynamics of the two oscillators with the differential equations

$$\ddot{u} + 2\epsilon\tilde{\mu}_1\dot{u} + \omega_1^2 u = \epsilon\tilde{\alpha}_1 uv, \tag{6.1}$$

$$\ddot{v} + 2\epsilon\tilde{\mu}_2\dot{v} + \tilde{\mu}_3|\dot{v}|\dot{v} + \omega_2^2 v = \epsilon vF\cos(\Omega t) + \epsilon\tilde{\alpha}_2 u^2, \tag{6.2}$$

where u and v are generalized coordinates, $\tilde{\mu}_1$ and $\tilde{\mu}_2$ are viscous damping coefficients, $\tilde{\mu}_3$ is the air drag damping coefficient, the ω_i are the natural frequencies, F and Ω are the forcing amplitude and frequency, respectively, $\tilde{\alpha}_1$ and $\tilde{\alpha}_2$ are constants, and ϵ is a bookkeeping parameter. We consider the case of principal parametric resonance of the second mode (i.e., $\Omega \approx 2\omega_2$) in the presence of a two-to-one internal resonance (i.e., $2\omega_1 \approx \omega_2$). Nayfeh[64] and Chin, Nayfeh, and Lacarbonara [65] analyzed the case when $\tilde{\mu}_3 = 0$. Because we are conducting experimental studies with a cantilever beam, we include the air drag term to obtain a realistic model that does not exhibit unbounded responses. However, since we are carrying out our analysis only to the second-order approximation, we do not include cubic terms. Their effect would be to influence the phase, thereby limiting the amplitude of the response.

Using the method of multiple scales, we seek expansions of u and v in the form

$$u \approx u_0(T_0, T_1) + \epsilon u_1(T_0, T_1), \tag{6.3}$$

$$v \approx v_0(T_0, T_1) + \epsilon v_1(T_0, T_1), \tag{6.4}$$

where $T_0 = t$ and $T_1 = \epsilon t$. The time derivatives are recast in terms of the new time scales as

$$\frac{d}{dt} = D_0 + \epsilon D_1 + \cdots \quad \text{and} \quad \frac{d^2}{dt^2} = D_0^2 + 2\epsilon D_0 D_1 + \cdots, \tag{6.5}$$

where $D_k \equiv \partial/\partial T_k$. Substituting equations (6.3)–(6.5) into equations (6.1) and (6.2) and equating coefficients of like power of ϵ yields

Order (1):

$$D_0^2 u_0 + \omega_1^2 u_0 = 0, \tag{6.6}$$

$$D_0^2 v_0 + \omega_2^2 v_0 = 0, \tag{6.7}$$

Order (ϵ):

$$D_0^2 u_1 \,+\, \omega_1^2\, u_1 \;=\; -\; 2\, D_0\, (D_1 u_0 + \tilde{\mu}_1\, u_0) + \tilde{\alpha}_1\, u_0 v_0, \tag{6.8}$$

$$\begin{aligned} D_0^2 v_1 \,+\, \omega_2^2\, v_1 \;=\; &-\; 2\, D_0\, (D_1 v_0 + \tilde{\mu}_2\, v_0) - \tilde{\mu}_3\, |D_0 v_0| D_0 v_0 \\ &+\; v_0 F \cos(\Omega t) \,+\, \tilde{\alpha}_2\, u_0^2\,. \end{aligned} \tag{6.9}$$

The solutions of equations (6.6) and (6.7) can be expressed as

$$u_0 \;=\; A_1(T_1)\, e^{i\omega_1 T_0} \,+\, \overline{A}_1(T_1)\, e^{-i\omega_1 T_0}, \tag{6.10}$$

$$v_0 \;=\; A_2(T_1)\, e^{i\omega_2 T_0} \,+\, \overline{A}_2(T_1)\, e^{-i\omega_2 T_0}, \tag{6.11}$$

where the $A_i(T_1)$ are unknown complex-valued quantities that will be determined by imposing the solvability conditions at the next level of approximation.

To express the nearness of $2\,\omega_1$ to ω_2 and Ω to $2\,\omega_2$, we introduce two detuning parameters $\tilde{\sigma}_1$ and $\tilde{\sigma}_2$ defined by

$$2\,\omega_1 \;=\; \omega_2 \,-\, \epsilon\,\tilde{\sigma}_1 \quad \text{and} \quad \Omega \;=\; 2\,\omega_2 \,+\, \epsilon\,\tilde{\sigma}_2. \tag{6.12}$$

Inserting equations (6.10)–(6.12) into equations (6.8) and (6.9) and eliminating terms that lead to secular terms yields

$$2\,i\,(D_1 A_1 + \tilde{\mu}_1 A_1) - 4\alpha_1 \overline{A}_1 A_2 e^{i\tilde{\sigma}_1 T_1} \;=\; 0, \tag{6.13}$$

$$2\,i\,(D_1 A_2 + \tilde{\mu}_2 A_2) + \frac{\tilde{\mu}_3}{2\,\pi} \int_0^{2\pi/\omega_2} D_0 v_1 |D_0 v_1| e^{-i\omega_2 T_0} dT_0 - \,4\,\alpha_2 A_1^2\, e^{-i\tilde{\sigma}_1 T_1} \,-\, 2\, f\, \overline{A}_2 e^{i\tilde{\sigma}_2 T_1} \;=\; 0, \tag{6.14}$$

where

$$\alpha_1 \;=\; \frac{\hat{\alpha}_1}{4\omega_1}, \quad \alpha_2 \;=\; \frac{\hat{\alpha}_2}{4\omega_2}, \quad \text{and} \quad f \;=\; \frac{F}{4\omega_2}. \tag{6.15}$$

We seek to reduce the number of parameters in equations (6.13) and (6.14) by introducing the scalings

$$A_1 \;=\; c_1 B_1, \quad A_2 \;=\; c_2\, B_2, \quad \text{and} \quad T_1 \;=\; c_3 T. \tag{6.16}$$

Then, we rewrite equations (6.13) and (6.14) as

$$2\,i\,(D_1 B_1 + \mu_1 B_1) - 4\, c_2 c_3 \alpha_1 \overline{B}_1 B_2 e^{i\sigma_1 T} \;=\; 0, \tag{6.17}$$

$$2\,i\,(D_1B_2+\mu_2B_2)\;+\;\Upsilon(T)-\;\frac{4\,c_1^2\,c_3\,\alpha_2}{c_2}B_1^2\,e^{-i\sigma_1T}\;-\;2\,c_3\,f\,\overline{B}_2e^{i\sigma_2T}\;=\;0, \tag{6.18}$$

where

$$\Upsilon(T)\;=\;i\,\frac{\tilde{\mu}_3\,c_2c_3\omega_2^2}{2\,\pi}\int_0^{2\pi/\omega_2}(B_2e^{i\omega_2T_0}-\overline{B}_2e^{-i\omega_2T_0})\left|B_2e^{i\omega_2T_0}-\overline{B}_2e^{-i\omega_2T_0}\right|e^{-i\omega_2T_0}dT_0, \tag{6.19}$$

$$\mu_1\;=\;c_3\,\tilde{\mu}_1,\quad \mu_2\;=\;c_3\,\tilde{\mu}_2,\quad \text{and}\quad \sigma_i\;=\;c_3\,\tilde{\sigma}_i. \tag{6.20}$$

To keep the forcing f as a bifurcation parameter, we let $c_3 = 1$. To eliminate the gains α_1 and α_2, we set

$$c_2c_3\alpha_1\;=1\quad\text{and}\quad\frac{c_1^2\,c_3\,\alpha_2}{c_2}\;=\;1. \tag{6.21}$$

Solving for the constants, we obtain

$$c_1\;=\frac{1}{\sqrt{\alpha_1\alpha_2}}\quad\text{and}\quad c_2\;=\;\frac{1}{|\alpha_1|}. \tag{6.22}$$

Next, we express $B_1(T)$ and $B_2(T)$ in the polar form

$$B_1\;=\;\frac{1}{2}\,a_1(T)\,e^{i\beta_1(T)}\quad\text{and}\quad B_2\;=\;\frac{1}{2}\,a_2(T)\,e^{i\beta_2(T)}. \tag{6.23}$$

Substituting equations (6.23) into equations (6.17) and (6.18), performing the integration, and separating real and imaginary parts yields

$$a_1'\;=\;-\mu_1\,a_1\;+\;a_1a_2\,\sin\gamma_1, \tag{6.24}$$

$$a_2'\;=\;-\,\mu_2\,a_2\;-\mu_3a_2^2-\;a_1^2\,\sin\gamma_1\;+\;fa_2\sin\gamma_2, \tag{6.25}$$

$$a_1\,\beta_1'\;=\;-\,a_1a_2\,\cos\gamma_1, \tag{6.26}$$

$$a_2\,\beta_2'\;=\;-\,a_1^2\,\cos\gamma_1\;-\;fa_2\cos\gamma_2, \tag{6.27}$$

where

$$\mu_3=\frac{4\,\omega_2\,\tilde{\mu}_3}{3|\alpha_1|\pi},$$

$$\gamma_1\;=\;\sigma_1T-2\beta_1+\beta_2\quad\text{and}\quad\gamma_2\;=\;\sigma_2T-2\beta_2, \tag{6.28}$$

and the prime indicates differentiation with respect to the slow time T_1.

6.2 Equilibrium and Dynamic Solutions

In this section, we investigate the fixed points of equations (6.24)–(6.28) and determine their bifurcations. To find the fixed points, we set $a_1' = a_2' = 0$ and $\gamma_1' = \gamma_2' = 0$ and obtain the algebraic equations

$$\mu_1\, a_1 \;=\; a_1 a_2\, \sin\gamma_1, \tag{6.29}$$

$$\mu_2\, a_2 \;=\; -\,\mu_3 a_2^2 -\; a_1^2\, \sin\gamma_1 \;+\; f a_2 \sin\gamma_2, \tag{6.30}$$

$$\nu_1\, a_1 \;=\; -\,a_1 a_2\, \cos\gamma_1, \tag{6.31}$$

$$\nu_2\, a_2 \;=\; -\,a_1^2\, \cos\gamma_1 \;-\; f a_2 \cos\gamma_2, \tag{6.32}$$

where

$$\nu_1 \;=\; \frac{1}{2}\Big(\sigma_1 + \frac{1}{2}\sigma_2\Big) \quad \text{and} \quad \nu_2 = \frac{1}{2}\sigma_2. \tag{6.33}$$

There are three possibilities. First, the trivial solution

$$a_1 \;=\; a_2 \;=\; 0. \tag{6.34}$$

Second, a single-mode solution

$$a_1 \;=\; 0 \quad \text{and} \quad a_2 \;=\; \frac{-\mu_2 \;+\; \sqrt{f^2 - \nu_2^2}}{\mu_3}. \tag{6.35}$$

And third, a two-mode solution

$$\big(a_1^2\mu_1 + \mu_2 a_2^2 + \mu_3 a_2^3\big)^2 + \big(a_1^2\nu_1 - \nu_2 a_2^2\big)^2 - a_2^4 f^2 \;=\; 0 \quad \text{and} \quad a_2 \;=\; \sqrt{\mu_1^2 \;+\; \nu_1^2}. \tag{6.36}$$

We note that a_2 in equation (6.36) is independent of f.

To study the stability of the fixed points, we express B_1 and B_2 in the form

$$B_1 \;= \frac{1}{2}\,(p_1 - i q_1)\, e^{i\nu_1 T} \quad \text{and} \quad B_2 \;=\; \frac{1}{2}\,(p_2 - i q_2)\, e^{i\nu_2 T}, \tag{6.37}$$

where the p_n and q_n are real and write the modulation equations in the Cartesian form

$$p_1' \;=\; -\,\mu_1\, p_1 - \nu_1\, q_1 \;+\; (p_2 q_1 \;-\; p_1 q_2), \tag{6.38}$$

$$q_1' \;=\; -\,\mu_1\, q_1 + \nu_1\, p_1 \;+\; (p_1 p_2 \;+\; q_1 q_2), \tag{6.39}$$

$$p_2' \;=\; -\,\mu_2\, p_2 -\; \mu_3 p_2 \sqrt{p_2^2 + q_2^2} -\; \nu_2\, q_2 -\; 2\, p_1 q_1 +\; q_2 f \tag{6.40}$$

$$q_2' \;=\; -\,\mu_2\, q_2 -\; \mu_3 q_2 \sqrt{p_2^2 + q_2^2} +\; \nu_2\, p_2 +\; (p_1^2 - q_1^2) + p_2 f. \tag{6.41}$$

The stability of a particular equilibrium solution is ascertained by investigating the eigenvalues of the Jacobian matrix of the right-hand sides of equations (6.38)–(6.41). Then, a pseudo-arclength scheme is used to trace branches of the equilibrium solutions

6.2.1 Frequency-Response Curves

In Figure 6-1, we show frequency-response curves when $\mu_1 = 0.01$, $\mu_2 = 0.05$, $\mu_3 = 0.2$, $\sigma_1 = -0.07$, and $f = 0.1$. As σ_2 is increased from a negative value, the response consists of the trivial solution, which is stable. When $\sigma_2 = \sigma_2^{(A)}$, the trivial solution experiences a transcritical bifurcation, after which the response consists of the single-mode solution. Although, we do not prove the nature of this bifurcation rigorously, it can be inferred from the structure of the solution. By manipulating equation (6.35), we find that the amplitude a_2 is given by the roots of the expression

$$(a_2\mu_3 + \mu_2)^2 + \nu_2^2 = f^2, \tag{6.42}$$

which is the equation of an ellipse with axes of symmetry $\nu_2 = 0$ and $a_2 = -\frac{\mu_2}{\mu_3}$. Since $a_2 = 0$ is not an axis of symmetry, $a_2^{(A)}$ is not an inflection point, and therefore, the bifurcation cannot be of the pitchfork type.

As σ_2 is increased, the solution traces the curve AB; a_2 increases while a_1 remains equal to zero. At point B, the single-mode solution loses stability through a subcritical pitchfork bifurcation, and the amplitude of the lower mode jumps from zero to the value at point C. Subsequently, the response consists of the two-mode solution, which traces the branch CD. When $\sigma_2 = \sigma_2^{(D)}$, the response undergoes a supercritical Hopf bifurcation, leading to a two-mode dynamic response. This response is maintained until $\sigma_2 = \sigma_2^{(E)}$. Our analysis reveals the existence of a subcritical Hopf bifurcation at point E, where we expect the dynamic solution to transform into a two-mode equilibrium solution. Later in this section, we investigate the nature of the response in the neighborhood of the Hopf bifurcation points D and E. Once the equilibrium solution is attained and as σ_2 is increased, the response will trace all or portion of the branch EF. When $\sigma_2 = \sigma_2^{(F)}$, the response undergoes a saddle-node

bifurcation leading to the single-mode solution, which traces the branch GH. At point H, the solution experiences a transcritical bifurcation, after which the response consists of the trivial solution. When $\sigma_2^{(J)} \leq \sigma_2 \leq \sigma_2^{(K)}$ and in the presence of disturbances that lie within the appropriate domain of attraction, the response may jump to a high-amplitude response that traces the branch JK. As σ_2 is increased beyond $\sigma_2^{(K)}$, the response consists of the trivial solution only.

As σ_2 is decreased from a positive value, initially the response is similar to the case of the forward sweep. When $\sigma_2 = \sigma_2^{(H)}$, the trivial solution loses stability through a transcritical bifurcation, after which the single-mode solution is attained. This response is maintained until $\sigma_2 = \sigma_2^{(L)}$, where a subcritical pitchfork bifurcation occurs that leads to a jump of the amplitude of the lower mode from zero to the value at point M. Subsequently, the response consists of the two-mode solution, which traces the branch ME. As σ_2 is further decreased, the response becomes dynamic in the region ED, as discussed previously. After experiencing the supercritical Hopf bifurcation at point D, the response consists of the two-mode equilibrium solution, which traces the branch DN. When $\sigma_2 = \sigma_2^{(N)}$, the solution undergoes a saddle-node bifurcation that results in a jump to the trivial solution.

To better understand the nature of the dynamic responses, we investigate the characteristics of the solution in the neighborhood of points D and E. In the first case, we found that the dynamic solution resulting from the supercritical Hopf bifurcation experiences a cyclic-fold bifurcation. In Figure 6-2, we show time evolution of the amplitude of the lower mode as σ_2 is increased beyond the cyclic-fold. In Figures 6-2, we illustrate an intermittent response that culminates into chaos, as shown in Figure 6-2d. The corresponding Lyiapunov exponents are 0.018, 0, -0.098, and -0.154. The power spectrum is shown Figure 6-3. The route to chaos is through a type I intermittency. In the second case, we find that the response is chaotic to the left of the subcritical Hopf bifurcation point. As σ_2 is increased, the two-mode equilibrium solution is attained through a reverse type II intermittency mechanism, as shown in Figure 6-4.

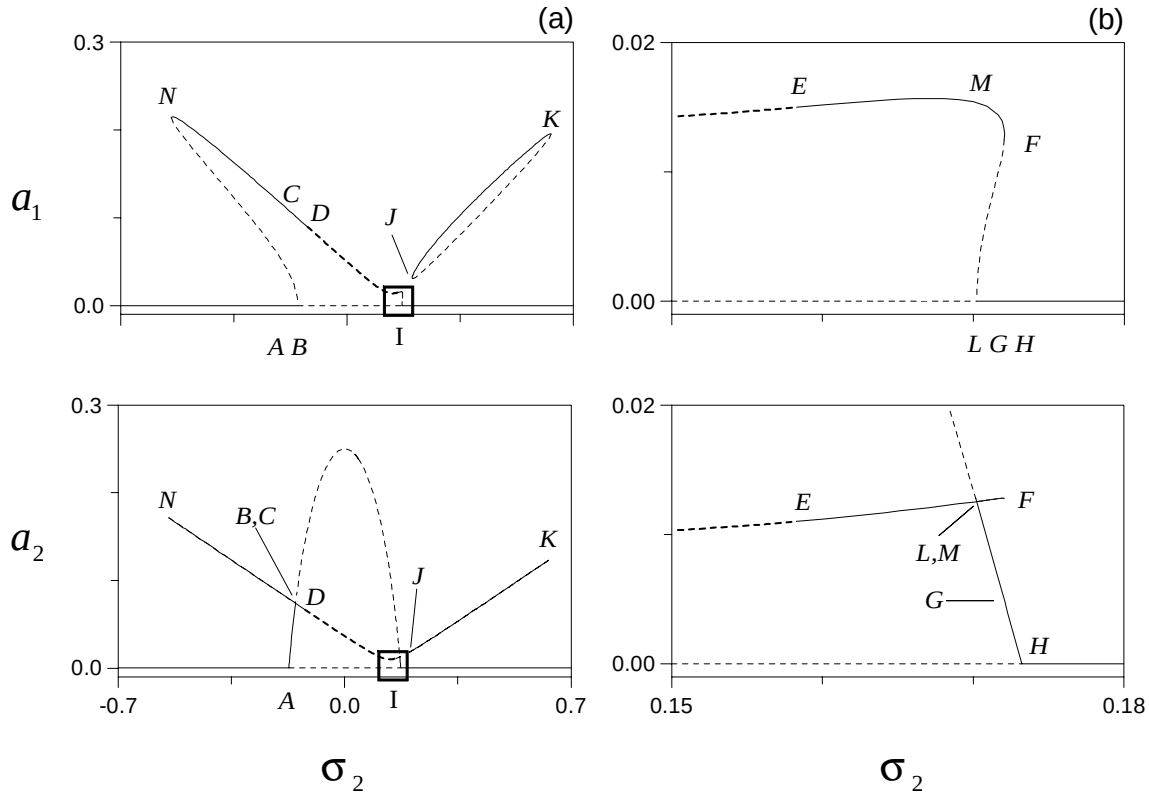

Figure 6-1. Theoretical frequency-response curves when $\mu_1 = 0.01$, $\mu_2 = 0.05$, $\mu_3 = 0.2$, $\sigma_1 = -0.07$, and $f = 0.1$. (a) Overall frequency-response curves and (b) an enlargement of area "I". Solid (dotted) lines denote stable nodes (saddles) and bold-dashed lines denote unstable foci.

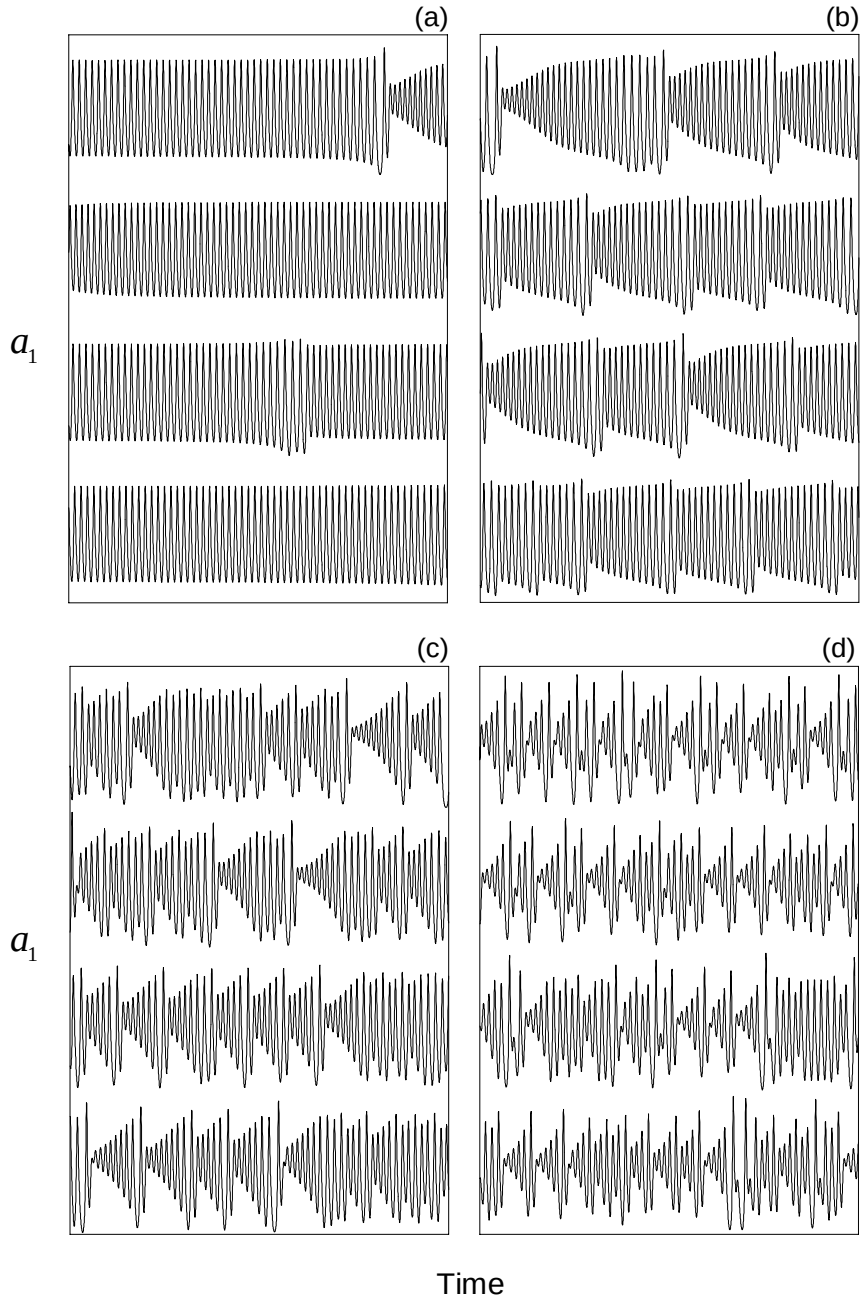

Figure 6-2. Time evolution of a_1 for varying σ_2 when $\mu_1 = 0.01$, $\mu_2 = 0.05$, $\mu_3 = 0.2$, $\sigma_1 = -0.07$, and $f = 0.1$. (a) $\sigma_2 = -0.11435$, (b) $\sigma_2 = -0.114$, (c) $\sigma_2 = -0.11$, and (d) $\sigma_2 = -0.1$. Each plot contains a single continuous time history, with the four rows consecutively including time intervals of 4000 each.

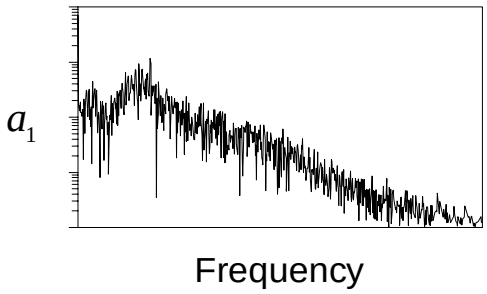

Figure 6-3. Power spectrum of a_1 when $\mu_1 = 0.01$, $\mu_2 = 0.05$, $\mu_3 = 0.2$, $\sigma_1 = -0.07$, $\sigma_2 = -0.1$, and $f = 0.1$.

6.2.2 Force-Response Curves

In Figure 6-5, we show force-response curves when $\mu_1 = 0.01$, $\mu_2 = 0.05$, $\mu_3 = 0.2$, $\sigma_1 = -0.07$, and $\sigma_2 = -0.1$. As f is increased from zero, only the trivial solution exists, which is stable. When $f = f_A$, the trivial solution experiences a transcritical bifurcation, after which the response consists of the single-mode solution. As f is increased, a_2 increases, while a_1 remains equal to zero. When $f = f_B$, the single-mode solution loses stability through a subcritical pitchfork bifurcation, and the amplitude of the lower mode jumps from point B to point C. As f is increased, the response traces the branch CD; a_1 increases, while a_2 remains constant (saturates). When $f = f_D$, the two-mode solution undergoes a supercritical Hopf bifurcation, leading to a small-amplitude limit-cycle response. When $f > f_D$, only the two-mode dynamic solution exists. As f is decreased, the two-mode equilibrium solution is attained through a reverse supercritical Hopf bifurcation at D. Subsequently, the response traces the brach DE. When $f = f_E$, the two-mode solution experiences a saddle-node bifurcation, leading to a jump to the trivial solution.

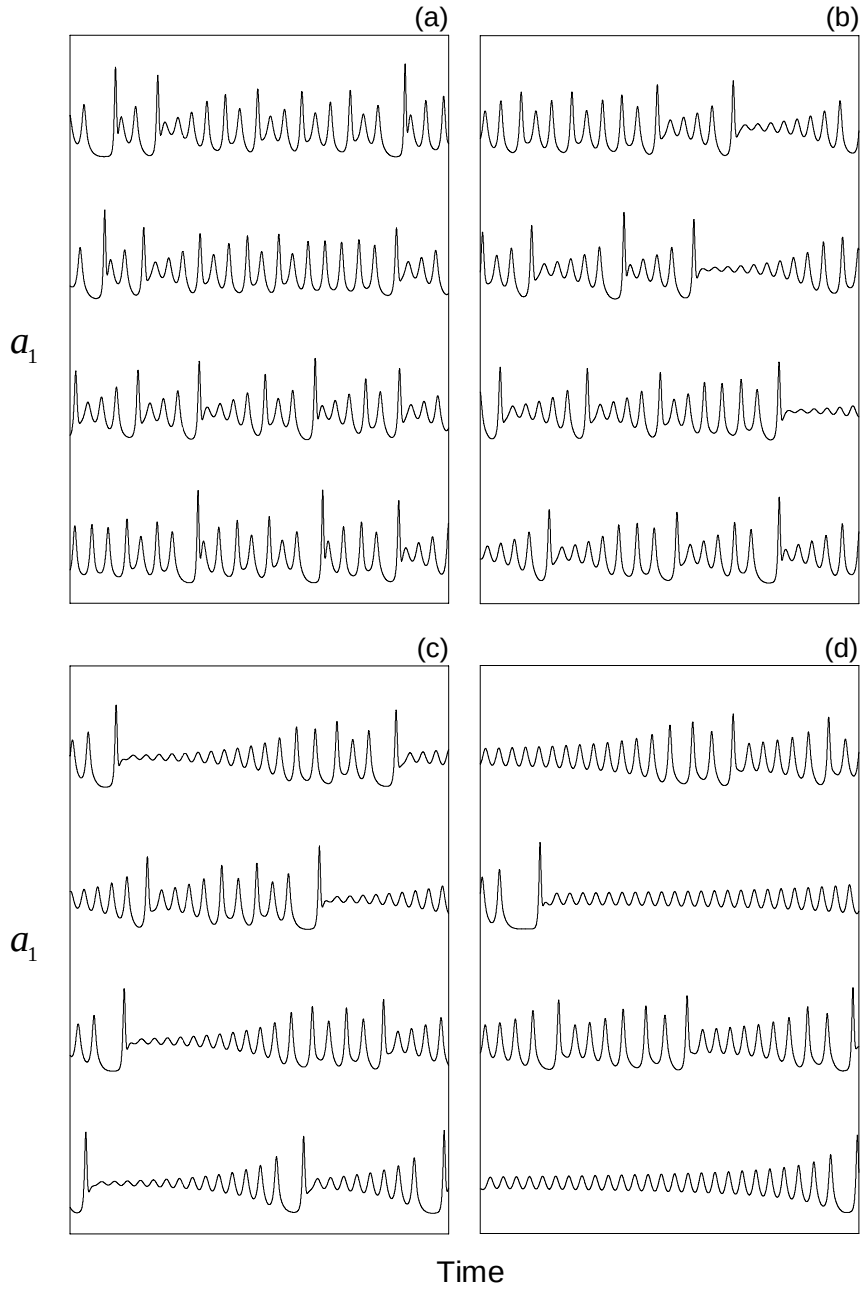

Figure 6-4. Time evolution of a_1 for varying σ_2 when $\mu_1 = 0.01$, $\mu_2 = 0.05$, $\mu_3 = 0.2$, $\sigma_1 = -0.07$, and $f = 0.1$. (a) $\sigma_2 = 0.157$, (b) $\sigma_2 = 0.1575$, (c) $\sigma_2 = 0.158$, and (d) $\sigma_2 = 0.1587$. Each plot contains a single continuous time history, with the four rows consecutively including time intervals of 10000 each.

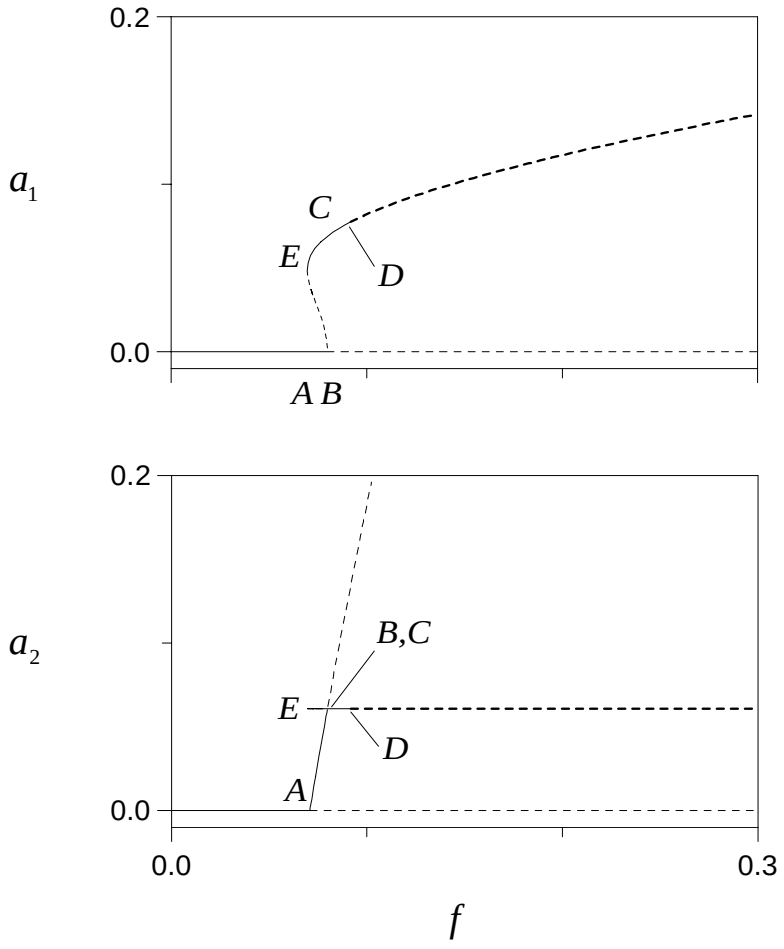

Figure 6-5. Theoretical force-response curves when $\mu_1 = 0.01$, $\mu_2 = 0.05$, $\mu_3 = 0.2$, $\sigma_1 = -0.07$, and $\sigma_2 = -0.1$. Solid (dotted) lines denote stable nodes (saddles) and bold-dashed lines denote unstable foci.

6.3 Experiments

The theoretical analysis is verified experimentally. A steel beam (No. IV) is fitted with a strain gage and piezoceramic actuators. The beam is excited vertically by a shaker subjecting its first mode to a principal parametric resonance. To create the second oscillatory mode and the quadratic coupling, we use a circuit that we developed previously for implementing a quadratic absorber.

6.3.1 Setup

The properties of the beam and the actuators are listed in Appendix A. The natural frequency of the first mode is approximately 11.3 Hz. The clamping fixture and the configuration of the actuators and the strain gage are shown in Figure 6-6. An accelerometer is positioned on the shaker head to measure the forcing amplitude. The setup for the experiment is shown in Figure 6-7. The beam and clamping fixture are attached to a 100-lb permanent-magnet shaker that is driven through a signal generator and a power amplifier. The signal from the strain gage conditioner is fed to the circuit, and the output of the circuit is sent to the actuators after being amplified. The details of the equipment are listed in Appendix A.

6.3.2 Frequency-Response Curves

We force the beam at an amplitude of $1.75g$. We monitor the acceleration of the shaker head and adjust the input voltage driving the shaker to maintain a constant forcing amplitude.

In Figure 6-8, we show the frequency-response curves. First, we discuss results of the forward sweep. Initially, as the forcing frequency is increased, the trivial response is maintained. At $\Omega \approx 22.5$Hz, the trivial response loses stability, and the response jumps to a nonperiodic motion. As the forcing frequency approaches 22.72Hz, the frequency of modulation of the response decreases. At $\Omega = 22.72$Hz, a reverse supercritical Hopf bifurcation occurs, resulting in a small-amplitude periodic motion. As the forcing frequency is increased, the amplitude of

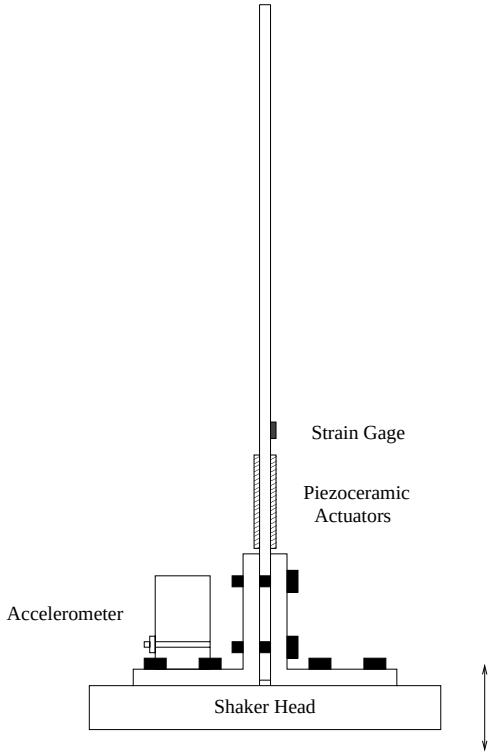

Figure 6-6. Beam fixture and instrumentation.

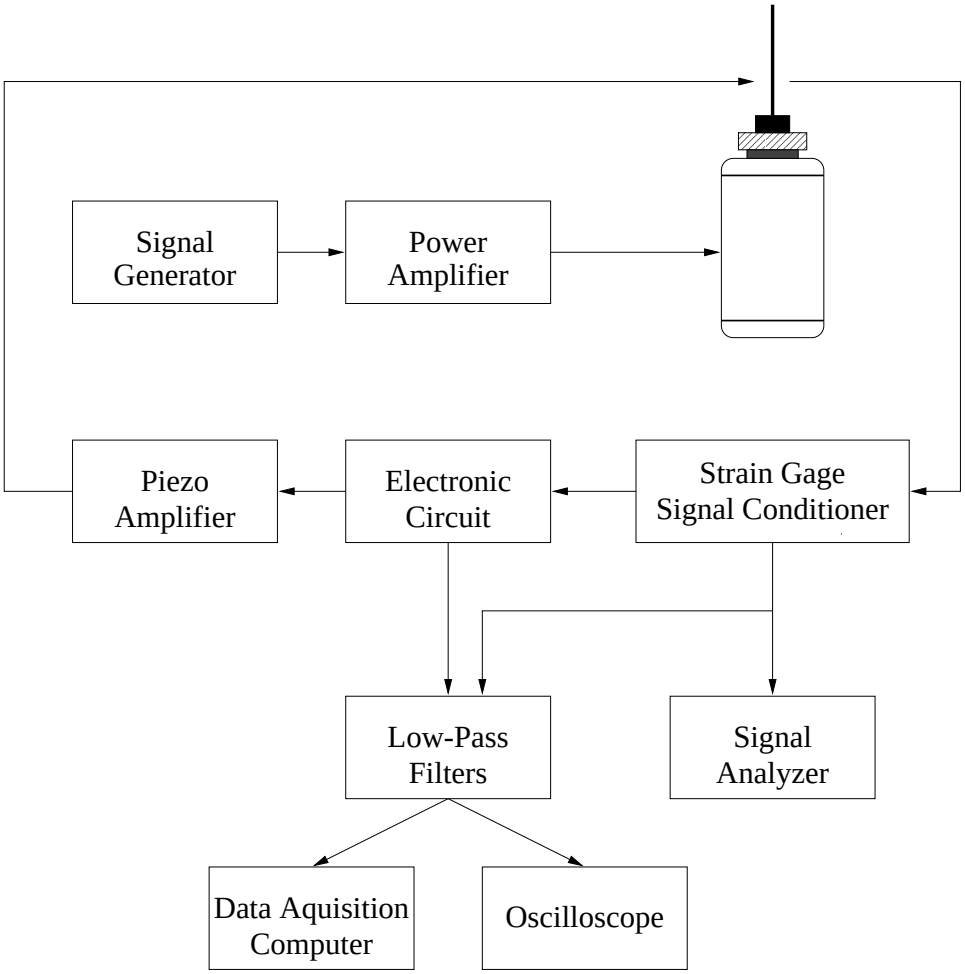

Figure 6-7. The experimental setup.

the response of the beam and the circuit increases. At $\Omega = 22.84$Hz, the response experiences a cyclic-fold bifurcation, leading to a jump to the trivial response that persists thereafter. We are unsuccessful in activating the isolated branch predicted theoretically and depicted as the branch JK in Figure 6-1a.

Second, we describe results of the reverse sweep. As the forcing frequency is decreased, the trivial motion loses stability at $\Omega = 22.68$Hz, and a jump to a nonperiodic motion occurs. At $\Omega \approx 22.26$Hz, the response experiences a reverse supercritical Hopf bifurcation, leading to a periodic motion. As Ω is further decreased, the response of the beam and circuit increases until $\Omega = 21.44$Hz. At $\Omega \approx 21.40$Hz, the response experiences a cyclic-fold bifurcation, leading to a jump to the trivial response.

In both sweeps, we are unable to capture the single-mode responses, identified by the branches AC and HF in Figure 6-1. We conjecture that, for the experimental-setup we have at hand, these branches are steep and therefore may require a very fine frequency-sweep resolution in order to capture them.

In order to investigate the nature of the nonperiodic responses observed during the experiment, we analyze the response of the system at two forcing frequencies. We sample the strain gage and circuit voltage signals at a frequency equal to ten times the forcing frequency, and we generate time histories, Poincaré sections, and power spectra of the responses. The Poincaré sections are created by plotting every tenth pair of data. In Figure 6-9, we show the response at $\Omega = 22.62$Hz. The time trace of the circuit voltage shown in Figure 6-9a indicates that the response is periodically modulated. This fact is confirmed by the Poincaré section and the power spectrum presented in Figures 6-9b and 6-9c, respectively. The response of the system at $\Omega = 22.5$Hz is shown in Figure 6-10. The time trace in Figure 6-10a indicates that the response is chaotically modulated, which is verified by examining the Poincaré section and power spectrum in Figures 6-10b and 6-10c.

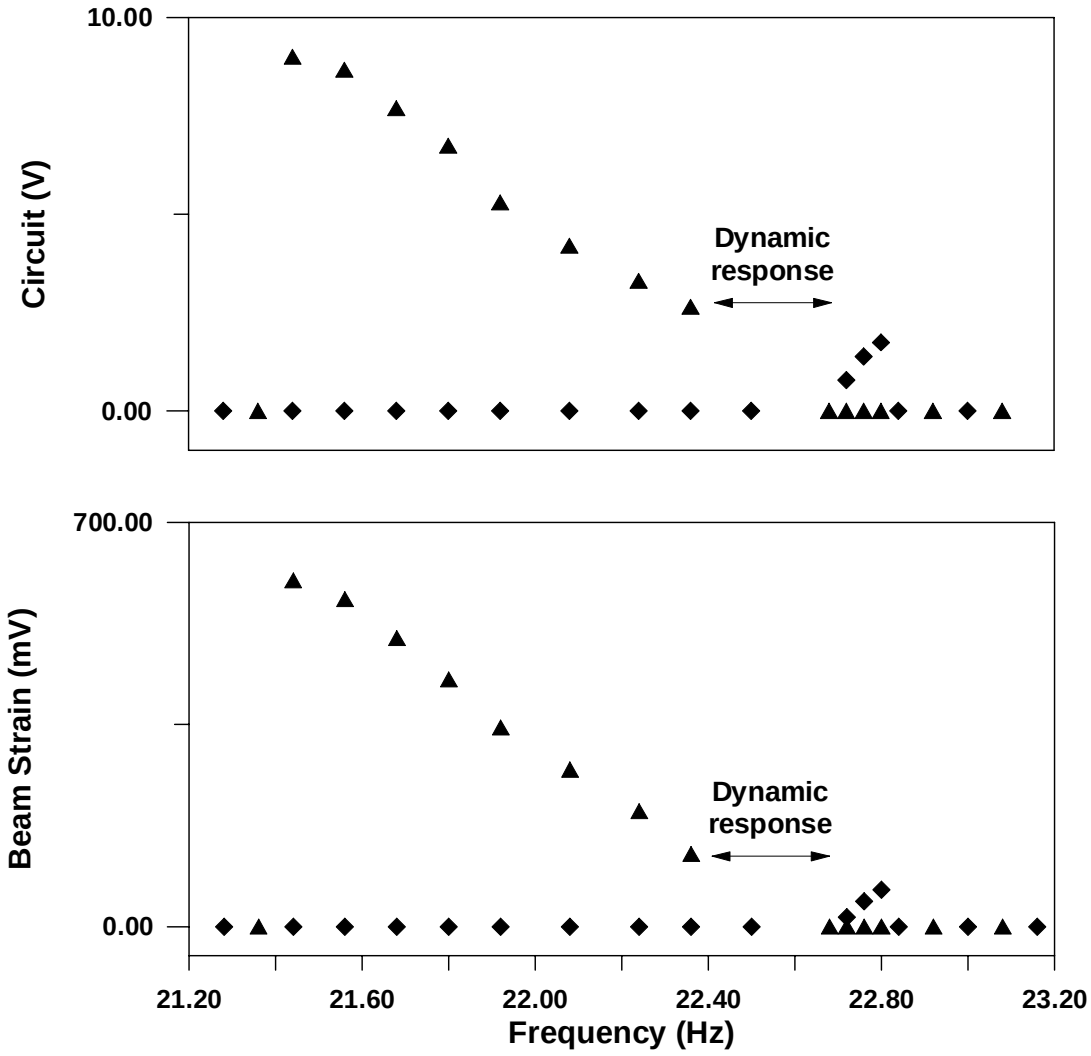

Figure 6-8. Experimental frequency-response curves. (♦) Forward sweep and (▲) reverse sweep.

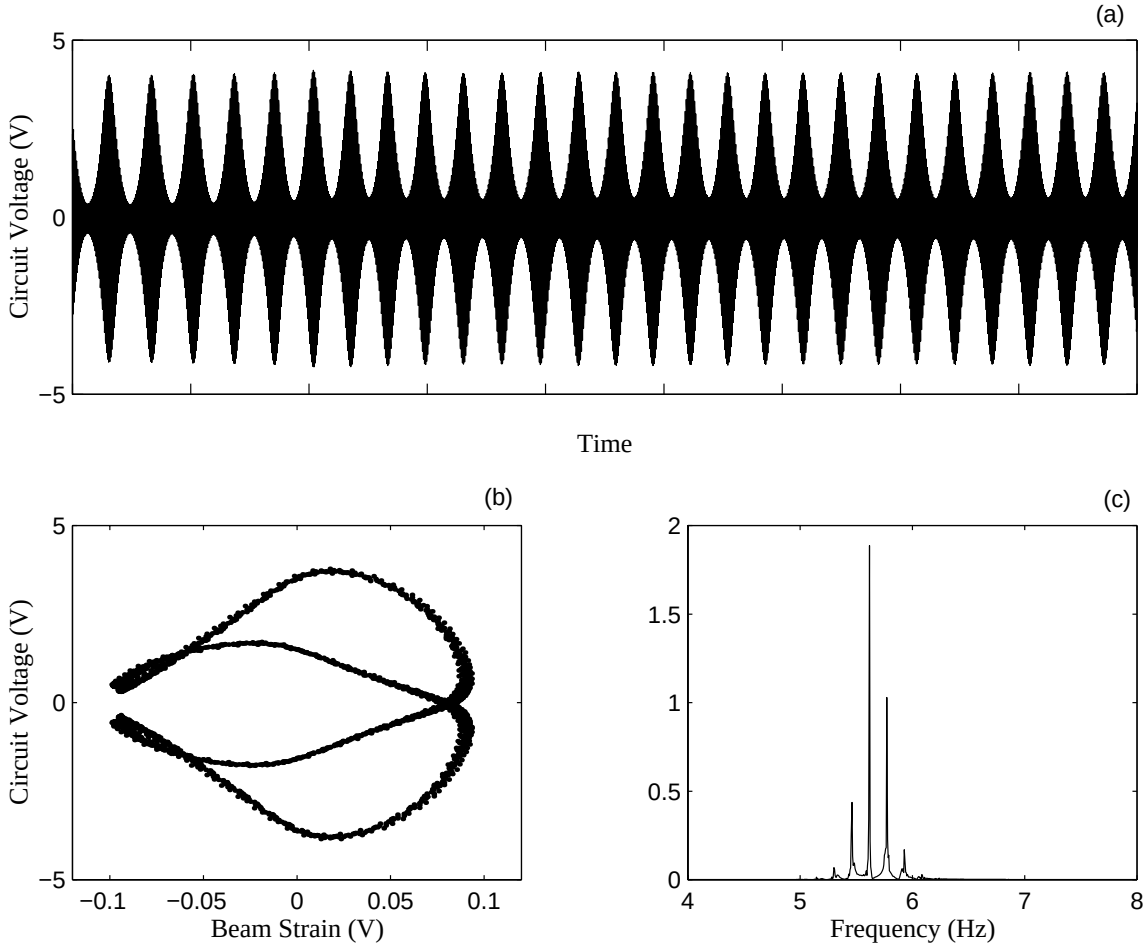

Figure 6-9. Response of the system when $\Omega = 22.62$Hz. (a) Time trace, (b) two-dimensional projection of the Poincaré section, and (c) power spectrum.

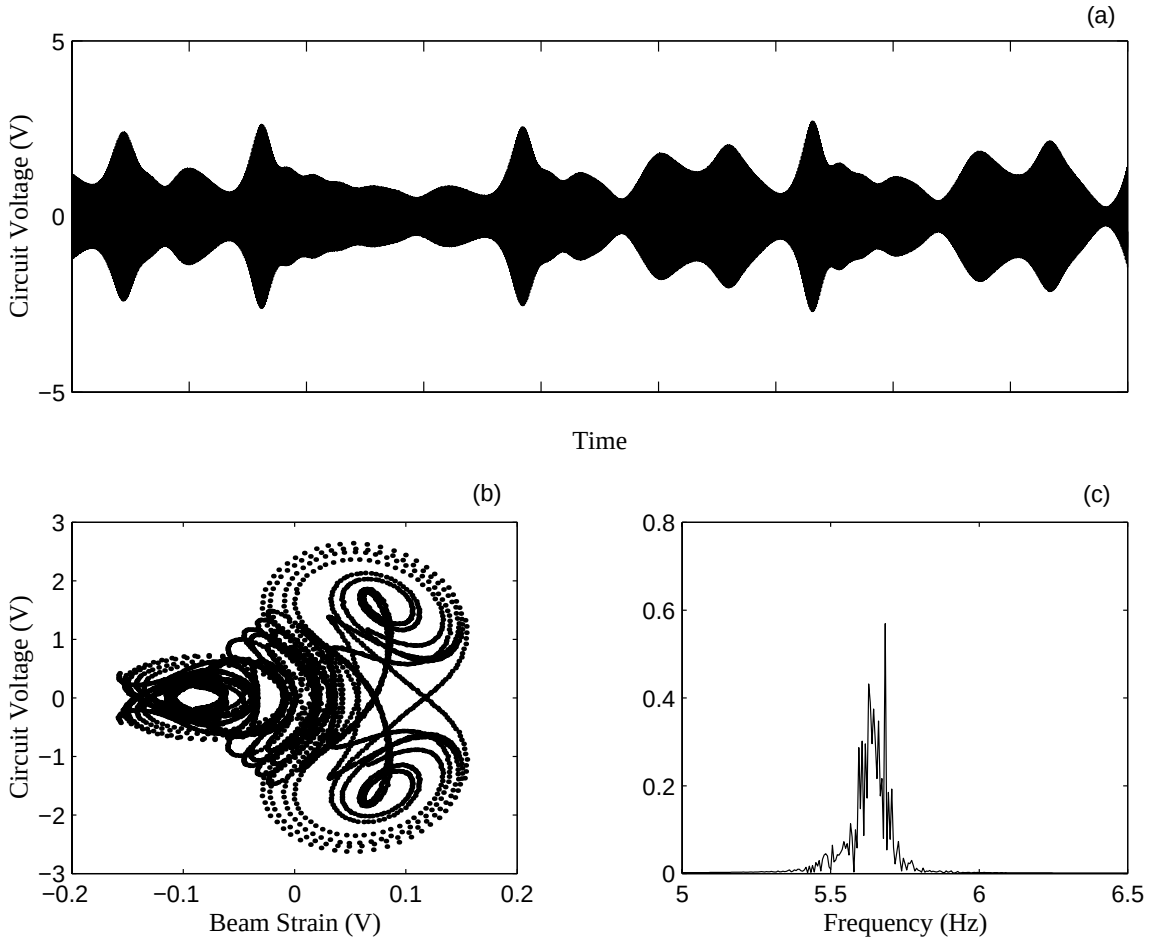

Figure 6-10. Response of the system when $\Omega = 22.5$Hz. (a) Time trace, (b) two-dimensional projection of the Poincaré section, and (c) power spectrum.

6.3.3 Force-Response Curves

We force the system at 22.52Hz and perform forward and reverse sweeps. In Figure 6-11, we show the force-response curves. As the forcing level is increased from zero, the response of the beam and circuit remains at zero. When the forcing amplitude reaches a value close to $1.4g$, the trivial response loses stability, resulting in a two-mode nonperiodic response. In the reverse sweep, the response experiences a reverse supercritical Hopf bifurcation when the forcing level reaches $1.16g$, leading to a periodic motion. As the forcing amplitude is decreased further, we observe a saturation phenomenon; the amplitude of motion of the beam remains constant, while the amplitude of the response of the circuit decreases. When the forcing level reaches approximately $1.09g$, the response of the system experiences a cyclic-fold bifurcation, leading to a jump to the trivial response.

6.4 Summary

In this chapter, we considered application of the quadratic absorber for parametric excitation. Specifically, we investigated the response of two oscillators coupled with quadratic nonlinearities in the presence of two-to-one internal resonance when the higher mode is subjected to a principal parametric excitation. We analyzed a model and showed that the system exhibits trivial, single- and two-mode periodic motions, a saturation phenomenon, periodically and chaotically modulated motions, and type I and II intermittency.

Additionally, we validated the theoretical results experimentally. We used a beam fitted with piezoceramic actuators and a strain gage and built a second-order analog circuit to represent the second oscillator. We subjected the beam to a parametric excitation whose frequency was approximately equal to twice the natural frequency of its first mode and coupled it with the circuit through electronically created quadratic nonlinearities. Our experimental results are in good agreement with the theoretical findings.

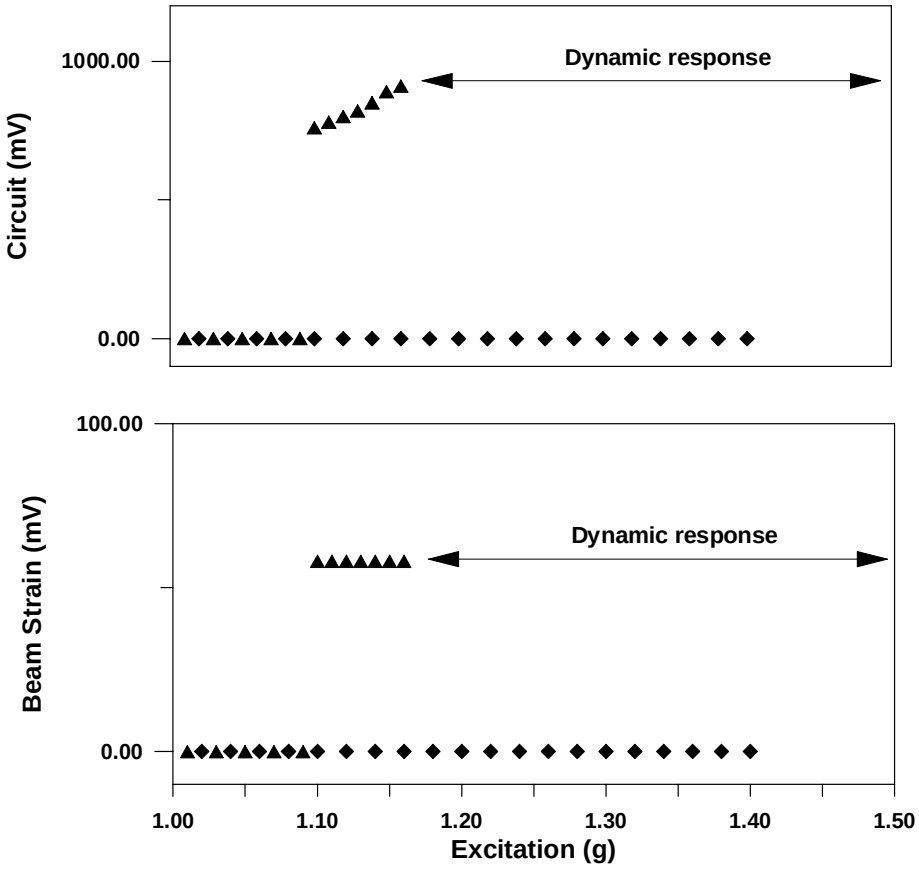

Figure 6-11. Experimental force-response curves. (⧫) Forward sweep and (▲) reverse sweep.

Chapter 7

Cubic Velocity Feedback

In the preceding chapter, we demonstrated that the quadratic absorber strategy is not effective for controlling principal parametric resonance. In this chapter, we offer an alternate approach for controlling this resonance.

We consider the problem of suppressing the vibrations of a single-degree-of-freedom system. We model its dynamics with a second-order nonlinear ordinary-differential equation and introduce a control law based on cubic velocity feedback. Using the method of multiple scales, we obtain an approximate solution to the differential equation and investigate the stability of the response. Then, we verify the results of the perturbation solution through numerical simulations.

To validate the theoretical findings, we investigate the performance of the control law through experiments. We fit a cantilever steel beam with piezoceramic actuators and subject its first mode to a principal parametric excitation. We perform frequency and amplitude sweeps and investigate the effect of varying the control gain on the response of the closed-loop system.

7.1 System Model and Control Law

We model the dynamics of the structure with the following nondimensional equation:

$$\ddot{u} + u + 2\,\epsilon\mu_1\,\dot{u} + \epsilon\hat{\mu}_2\,|\dot{u}|\dot{u} + \epsilon\alpha_1 u^3 + \epsilon\alpha_2 u^2\ddot{u} + \epsilon\alpha_3 u\dot{u}^2 = \epsilon\, uF_p\cos(\Omega t) + T, \tag{7.1}$$

where u is the generalized coordinate, μ_1 is the viscous damping coefficient, $\hat{\mu}_2$ is the air drag coefficient, the α_i are constants, F_p and Ω are the forcing amplitude and frequency, respectively, T is a control input, and ϵ is a bookkeeping parameter. The term $\alpha_1\,u^3$ is due to nonlinear curvature, and the terms $\alpha_2 u^2\ddot{u}$ and $\alpha_3 u\dot{u}^2$ are due to nonlinear inertia [7].

We consider the case of principal parametric resonance (i.e., $\Omega \approx 2$) and propose a control law given by

$$T = -\epsilon\, G\dot{u}^3, \tag{7.2}$$

where G is a positive constant.

7.2 Perturbation Analysis

To obtain an approximate solution to equations (7.1) and (7.2), we use the method of multiple scales and seek an expansion of u in the form

$$u(T_0, T_1) \approx u_0(T_0, T_1) + \epsilon u_1(T_0, T_1), \tag{7.3}$$

where $T_0 = t$ and $T_1 = \epsilon t$. The time derivatives are recast in terms of the new time scales as

$$\frac{d}{dt} = D_0 + \epsilon\, D_1 + \cdots \quad \text{and} \quad \frac{d^2}{dt^2} = D_0^2 + 2\,\epsilon\, D_0\, D_1 + \cdots, \tag{7.4}$$

where $D_k \equiv \partial/\partial T_k$. Substituting equations (7.3) and (7.4) into equations (7.1) and (7.2) and equating coefficients of like power of ϵ yields

Order (1):

$$D_0^2\, u_0 + u_0 = 0, \tag{7.5}$$

Order (ϵ):

$$D_0^2\, u_1 \,+\, u_1 \;=\; -\; 2\, D_0 D_1 u_0 - 2\,\mu_1\, D_0 u_0 \;-\hat{\mu}_2\, |D_0\, u_0\,|\, D_0\, u_0 - \alpha_1\, u_0^3$$
$$-\; \alpha_2 u_0^2\, D_0^2 u_0 - \alpha_3 u_0\, (D_0 u_0)^2 - G(D_0 u_0)^3 + \; u_0\, F_p \cos(\Omega T_0). \qquad (7.6)$$

The solution of equation (7.5) can be expressed as

$$u_0 \;=\; A(T_1)\, e^{iT_0} \;+\; \overline{A}(T_1)\, e^{-iT_0}, \qquad (7.7)$$

where $A(T_1)$ is a complex-valued quantity that will be determined by imposing the solvability condition at the next level of approximation.

To express the nearness of Ω to 2, we introduce a detuning parameter σ such that

$$\Omega \;=\; 2 + \;\epsilon\, \sigma. \qquad (7.8)$$

Substituting equations (7.7) and (7.8) into equation (7.6) and eliminating the terms that produce secular term leads to

$$2i(D_1 A + \mu_1 A) + \frac{\hat{\mu}_2}{2\pi} \int_0^{2\pi} D_0 u_0 |D_0 u_0| e^{-iT_0} dT_0 + 8\,(\alpha_e + i\mu_3) A^2 \overline{A} - 2\overline{A} f e^{i\sigma T_1} = 0, \qquad (7.9)$$

where

$$\alpha_e \;= \frac{1}{8}(3\,\alpha_1 - 3\,\alpha_2 + \alpha_3), \quad \mu_3 = \frac{3\,G}{8}, \quad \text{and} \quad f = \frac{F_p}{4}.$$

Next, we express A in the polar form

$$A \;=\; \frac{1}{2}\, a(T_1)\, e^{i\beta(T_1)}. \qquad (7.10)$$

Inserting equation (7.10) into equation (7.9), performing the integration, and separating real and imaginary parts yields

$$a' \;=\; -\mu_1 a - \mu_2 a^2 - \mu_3\, a^3 + af \sin\gamma, \qquad (7.11)$$

$$a\gamma' \;=\; \sigma a - \; 2\,\alpha_e\, a^3 + 2\, af \cos\gamma, \qquad (7.12)$$

where the prime denotes differentiation with respect to T_1,

$$\gamma \;=\; \sigma\, T_1 - 2\,\beta \quad \text{and} \quad \mu_2 \;=\; \frac{4\,\hat{\mu}_2}{3\,\pi}.$$

7.3 Performance of the Control Law

The performance of the control technique is ascertained by calculating the fixed points of equations (7.11) and (7.12) and examining their stability as a function of the parameters f, σ, and the gain G (μ_3). Setting $a' = 0$ and $\gamma' = 0$ yields

$$af \sin\gamma \;=\; \mu_1 a + \mu_2 a^2 + \mu_3\, a^3, \tag{7.13}$$

$$-af \cos\gamma \;=\; \frac{1}{2}\sigma\, a - \;\alpha_e\, a^3. \tag{7.14}$$

There are two possibilities: $a = 0$ and $a \neq 0$. The nontrivial fixed points are given by the roots of

$$\left(\mu_1 + \mu_2 a + \mu_3\, a^2\right)^2 \;+\; \left(\frac{1}{2}\sigma - \;\alpha_e\, a^2\right)^2 \;-\; f^2 \;=\; 0. \tag{7.15}$$

The stability of the fixed points is investigated by evaluating the eigenvalues of the Jacobian matrix of equations (7.11) and (7.12). In the case of the trivial solution, the form of these equations is not suitable for the stability analysis. Therefore, we express A in the Cartesian form

$$A \;=\; \frac{1}{2}(p - iq)\, e^{\nu T_1}, \tag{7.16}$$

where p and q are real and $\nu = \frac{1}{2}\sigma$. Substituting equation (7.16) into equation (7.9) and separating real and imaginary parts yields

$$p' \;=\; -\mu_1 p - \mu_2 p\sqrt{p^2+q^2} - \mu_3 p\left(p^2+q^2\right) - \nu q + \alpha_e\, q\left(p^2+q^2\right) + q\, f, \tag{7.17}$$

$$q' \;=\; -\mu_1 q - \mu_2 q\sqrt{p^2+q^2} - \mu_3 q\left(p^2+q^2\right) + \nu p - \alpha_e\, p\left(p^2+q^2\right) + p\, f. \tag{7.18}$$

The stability of the trivial solution ($p = q = 0$) to a disturbance proportional to $e^{\lambda T_1}$ is ascertained by the roots of

$$\begin{vmatrix} -\mu_1 - \lambda & -\nu + f \\ \nu + f & -\mu_1 - \lambda \end{vmatrix} = 0, \tag{7.19}$$

that is

$$\lambda \;=\; -\mu_1 \pm \sqrt{f^2 - \nu^2}. \tag{7.20}$$

The trivial solution is stable if

$$f \leq \sqrt{\mu_1^2 + \nu^2}, \tag{7.21}$$

when f is the control parameter, or if

$$|\sigma| \geq 2\sqrt{f^2 - \mu_1^2}, \tag{7.22}$$

when σ is the control parameter.

Due to the complexity in obtaining a closed-form solution to equation (7.15), we resort to numerical methods to investigate the stability of the nontrivial solutions. In the next three sections, we perform the stability analysis and evaluate the control law.

7.3.1 Frequency-Response Curves

In Figure 7-1, we show frequency-response curves of the open- and closed-loop system, and in Figure 7-2, we show an enlargement of the response curves. The amplitude of the response depends on the value of σ and the system's initial conditions.

We consider first the open-loop response (i.e., $G = 0$). When $\sigma > \sigma_B$, only the trivial solution exists, which is stable. As σ is decreased from point A, the trivial solution loses stability at point B through a transcritical bifurcation. The response amplitude increases as σ is decreased. The nontrivial solution loses stability through a saddle-node bifurcation at point C, and the response amplitude jumps down to point D, where only the trivial solution exists thereafter. In the case where σ is increased, there are two possible paths for the solution. If the initial conditions are small, the system does not oscillate initially, and the response traces the curve DE. When $\sigma = \sigma^{(E)}$, the trivial solution loses stability through a transcritical bifurcation. The bifurcation is shown in Figure 7-2. As σ is increased, the amplitude increases. When $\sigma = \sigma^{(J)}$, the response experiences a saddle-node bifurcation, leading to a jump up to the value at point F . Upon further increasing σ, the amplitude traces the curve FBA, where the trivial solution is reached through a transcritical bifurcation at point B. If the initial conditions are large, a high-amplitude response is sustained initially.

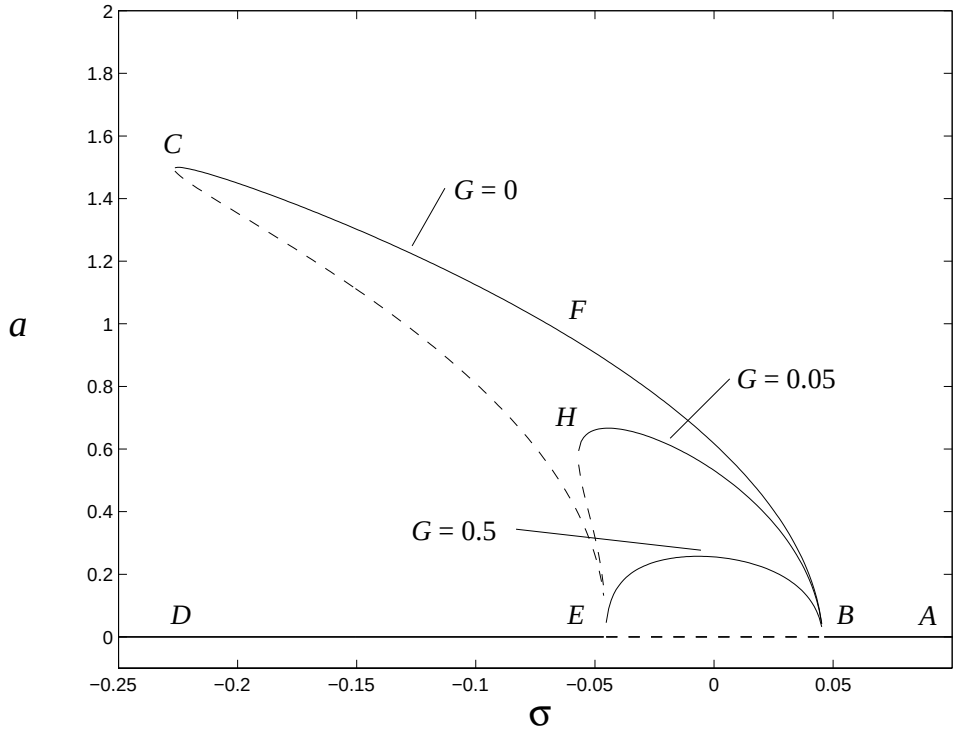

Figure 7-1. Theoretical frequency-response curves when $f = 0.025$, $\mu_1 = 0.01$, $\mu_2 = 0.01$, and $\alpha_e = -0.05$, (—) stable solution and (– –) unstable solution.

Here, a jump phenomenon does not occur, and the response traces portions of or all the curve $CFBA$. We note that the overhang region FC exhibits high-amplitude responses.

Next, we analyze the response of the closed-loop system (i.e., $G \neq 0$). We consider two cases, $G = 0.05$ and $G = 0.5$. In the first case, the response undergoes bifurcations similar to those of the open-loop system. However, the response amplitude is decreased, and the saddle-node bifurcations are shifted from point C to point H (Figure 7-1) and from point J to point L (Figure 7-2). In the second case, superior results are achieved. The saddle-node bifurcations are replaced with one transcritical bifurcation at point E. The overhang region and the jump phenomenon are eliminated, and the response is suppressed further, tracing the curve EB.

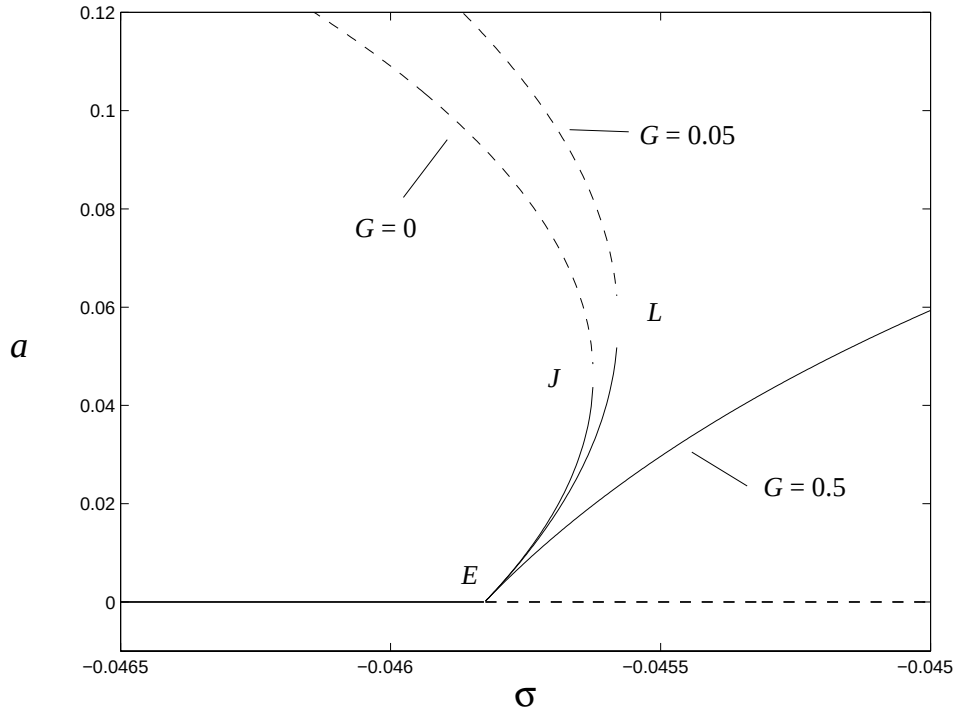

Figure 7-2. An enlargement of the frequency-response diagram near the transcritical bifurcation point E. (—) Stable solution and (– –) unstable solution.

7.3.2 Force-Response Curves

In Figure 7-3, we show open- and closed-loop force-response curves. In Figure 7-4, we depict an enlargement of the response diagram near point B. Since an exact resonance ($\sigma = 0$) is difficult to achieve realistically, we show response curves that exhibit the more interesting hysteretic effect when $\sigma < 0$.

First, we consider the open-loop response. If $f < f_E$, only the trivial solution exists, which is stable. In the absence of large disturbances, it is maintained as f is increased along the curve AB. When $f = f_B$, the trivial solution loses stability through a transcritical bifurcation, and the solution traces the branch BM (Figure 7-4). When $f = f_M$, the response experiences a saddle-node bifurcation, leading to a jump to point C (Figure 7-3). A further increase in f leads to higher response amplitudes, tracing the curve CD. When f is decreased, the amplitude traces the curve DE. At point E, the solution undergoes a saddle-node bifurcation, leading to a jump down, where only the trivial solution exists thereafter.

Second, we analyze the response for two values of the feedback gain. When $G = 0.05$, the response curve is similar to the uncontrolled response curve. The bifurcations are identical, however, the locations of the saddle-node bifurcation points are shifted from points E and M to points J and N, respectively, resulting in a smaller hysteretic region. Furthermore, the response amplitude is reduced from the curve ECD to the curve JFH. When $G = 0.5$, the saddle-node bifurcations at points J and M are eliminated. Additionally, the amplitude of the response is further reduced, tracing the curve BPL.

7.3.3 Numerical Simulations

To validate the perturbation results, we integrate numerically the equation

$$\ddot{u} + u + 2\,\mu_1\,\dot{u} + \frac{3}{4}\,\pi\,\mu_2\,|\dot{u}|\dot{u} + \frac{8}{3}\,\alpha_1\,u^3 \;=\; u\,F_p\,\cos(\Omega t) - G\,\dot{u}^3, \tag{7.23}$$

where $\mu_1 = 0.01$, $\mu_2 = 0.01$, $\alpha_1 = -0.05$, $\alpha_2 = \alpha_3 = 0$, and $F_p = 0.1$ for different values of the forcing frequency Ω and the velocity feedback gain G. In Figure 7-5, we show time responses

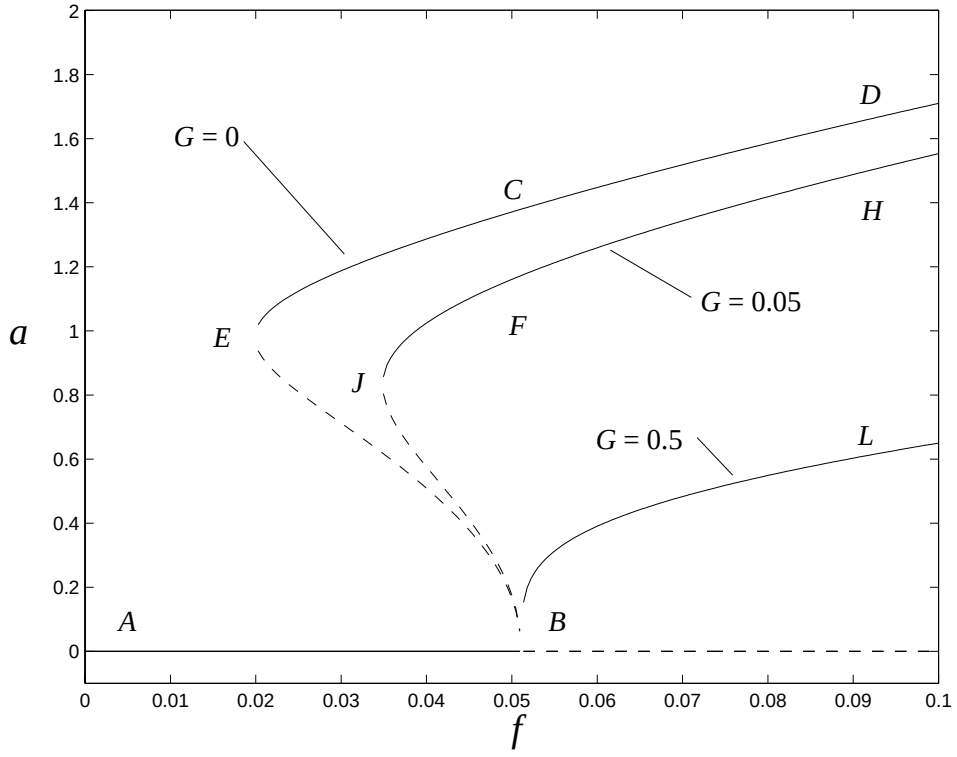

Figure 7-3. Theoretical force-response curves when $\sigma = -0.1$, $\mu_1 = 0.01$, $\mu_2 = 0.01$, and $\alpha_e = -0.05$. (—) Stable solution and (– –) unstable solution.

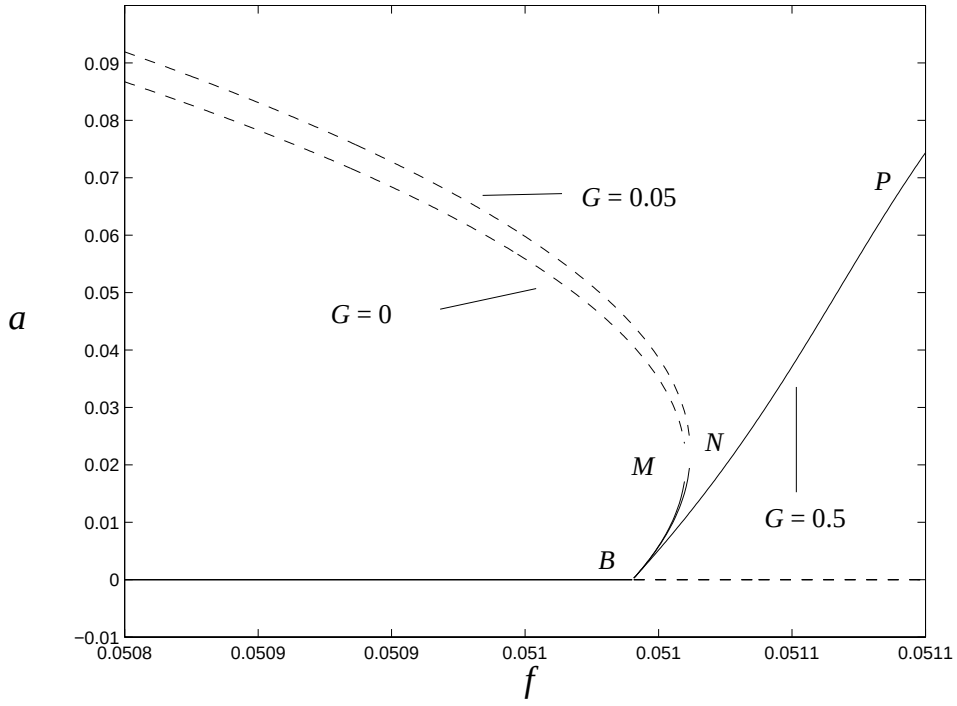

Figure 7-4. An enlargement of the force-response diagram near the transcritical bifurcation point B. (—) Stable solution and (– –) unstable solution.

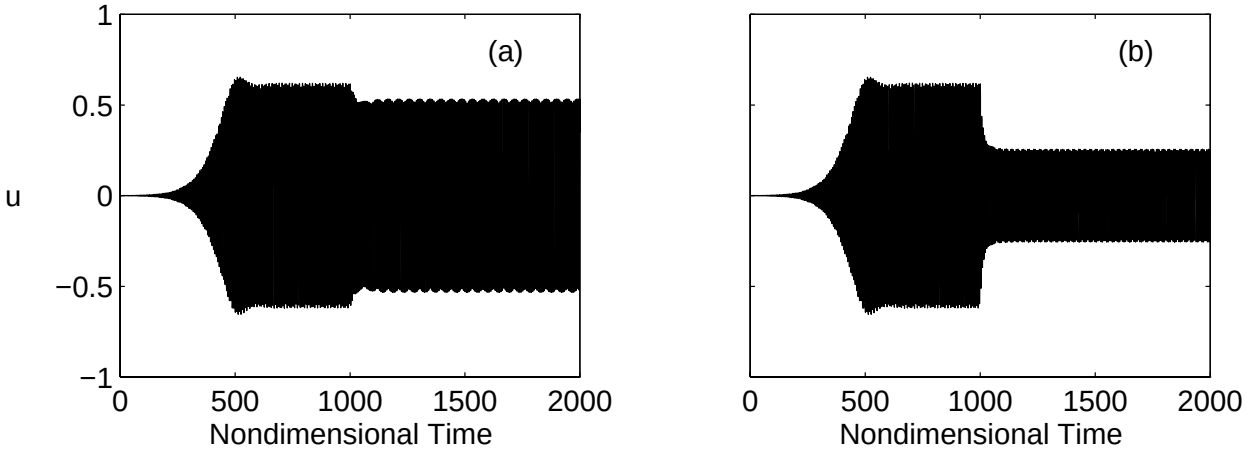

Figure 7-5. Numerical simulations of the time response when $\Omega = 2$. (a) $G = 0.05$ and (b) $G = 0.5$.

when $\Omega = 2$ (i.e., $\sigma = 0$) for $G = 0.05$ and $G = 0.5$. Comparing Figure 7-1 and Figure 7-5, we note that the open- and closed-loop response amplitudes predicted by the perturbation solution are in agreement with the results of the numerical simulations. In Figure 7-6, we show results when $\Omega = 1.9$ (i.e., $\sigma = -0.1$) for $G = 0.05$ and $G = 0.5$. In this case, the system possesses two stable states: the trivial solution and a high-amplitude limit-cycle solution (the system is operating in the overhang region CF shown in Figure 7-1). Thus, the initial conditions for this simulation are chosen to insure that the system is attracted to the nontrivial solution. Here, the addition of velocity feedback eliminates the high-amplitude motion. Since only the trivial solution exists, the amplitude of the closed-loop response is not influenced by the magnitude of the gain G. However, the gain affects the transient behavior. The higher the gain is, the faster is the approach to the trivial solution.

7.4 Experiments

The theoretical analysis is verified by implementing the control strategy on a cantilever beam (No. V) fitted with piezoceramic actuators and a strain gage. The beam is excited vertically by a shaker subjecting its first mode to a principal parametric resonance.

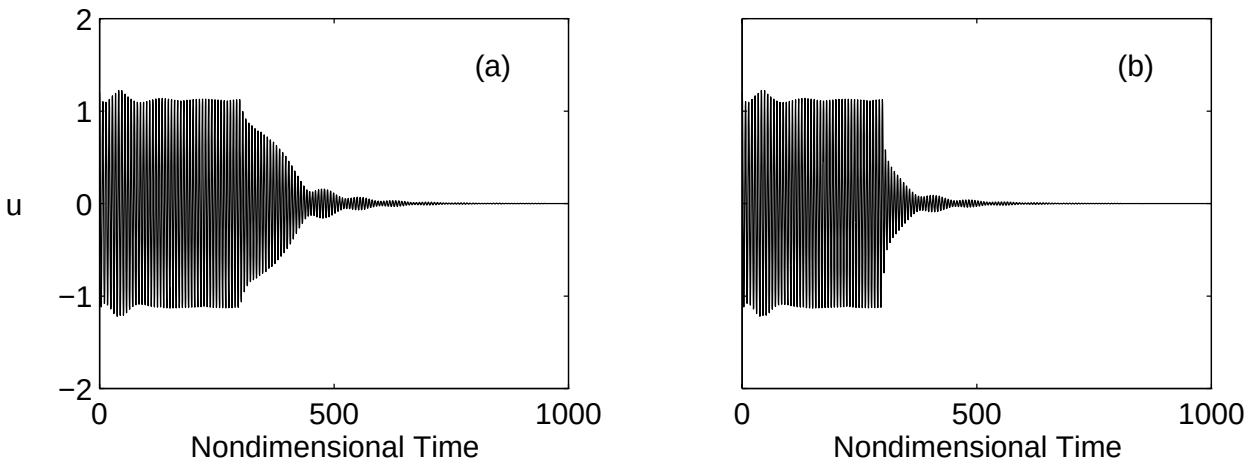

Figure 7-6. Numerical simulations of the time response when $\Omega = 1.9$. (a) $G = 0.05$ and (b) $G = 0.5$.

7.4.1 Setup

The properties of the beam and the actuators are listed in Appendix A. The natural frequency of the first mode is approximately 7 Hz. The clamping fixture and the configuration of the actuators and the strain gage are shown in Figure 7-7. An accelerometer is positioned on the shaker head to measure the forcing amplitude. The setup for the experiment is shown in Figure 7-8. The beam and clamping fixture are attached to a 100-lb permanent-magnet shaker that is driven through a signal generator and a power amplifier. The signal from the strain gage is filtered and sampled by a digital computer using the software LabView. The signal is manipulated, and the cubic velocity signal is generated, amplified, and sent to the actuators. The details of the equipment are listed in Appendix A.

7.4.2 Frequency-Response Curves

We force the beam at an amplitude of $1.2\,g$ and conduct forward and reverse frequency sweeps. The acceleration of the shaker head is monitored, and the input voltage driving the shaker is adjusted to maintain a constant forcing amplitude. In Figure 7-9, we illustrate open- and closed-loop frequency-response curves.

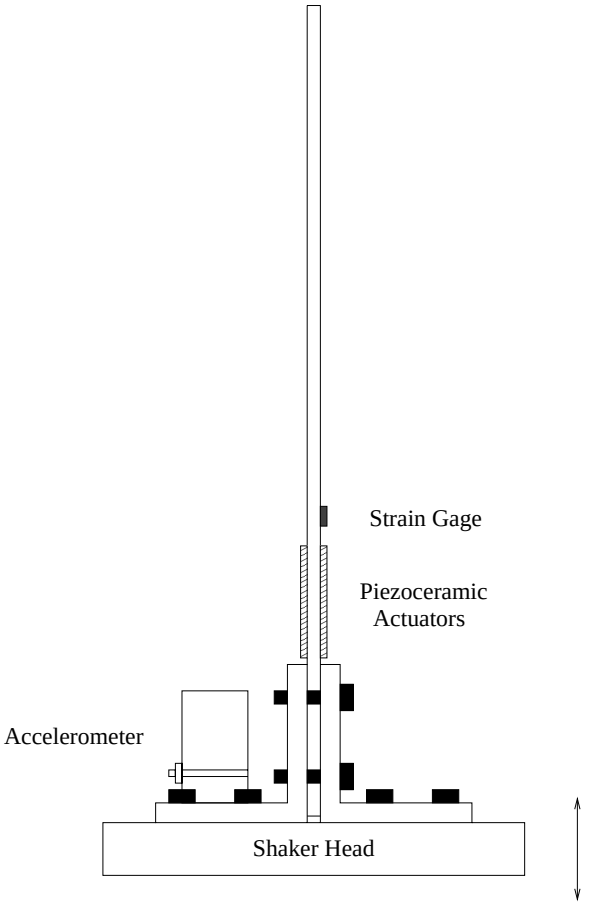

Figure 7-7. Beam fixture and instrumentation.

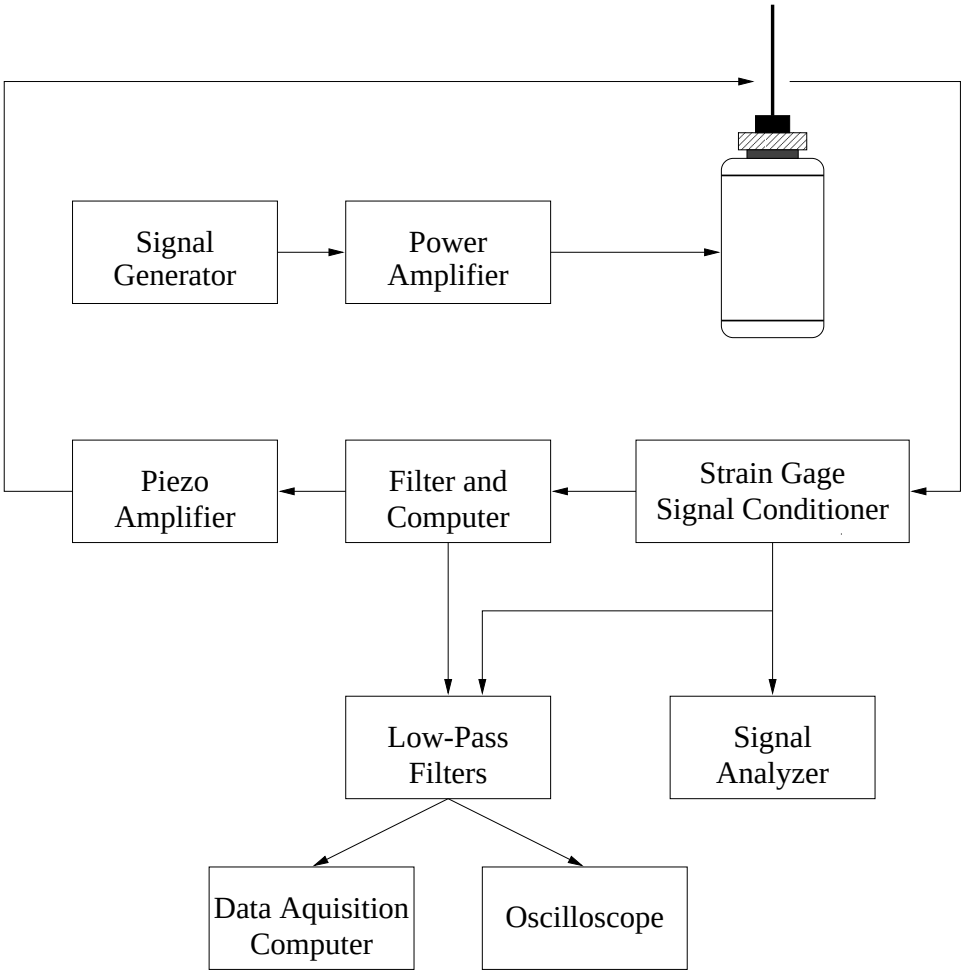

Figure 7-8. The experimental setup.

First, we discuss the open-loop case. Initially, as the forcing frequency is increased, the amplitude remains at zero. When the frequency reaches a value close to 13.9 Hz, the response jumps up to a value of $0.3\,V$. Further increase in the frequency leads to a decrease in the amplitude. When the frequency is approximately 14.1 Hz, the beam stops oscillating. Subsequently, the response remains at zero. In the reverse sweep, the response is similar to the one observed during the forward sweep. However, the response amplitude does not experience a jump down at 13.9 Hz. Instead, a growth rate is observed, leading to a very high response amplitude reaching $2.9\,V$. A jump down to zero occurs at 13.6 Hz. Thereafter, the response remains at zero.

Second, we consider the closed-loop case. As the frequency is increased, the response remains at zero until a gradual increase is observed at 13.9 Hz. Further increases in the frequency result in a decrease in the response amplitude leading to a zero response at 14.1 Hz. During the reverse sweep, the response amplitude traces the same path observed during the closed-loop forward sweep. The high-amplitude motion attained in the open-loop system is eliminated.

7.4.3 Force-Response Curves

We excite the beam at a constant frequency of 13.88 Hz and conduct forward and reverse excitation amplitude sweeps. In Figure 7-10, we show open- and closed-loop force-response curves.

First, we describe the open-loop response. As the forcing level is increased, the beam does not oscillate initially. When the forcing amplitude reaches approximately $1.5\,g$, the response experiences a jump to a high amplitude ($0.5\,V$). Further increases in the excitation amplitude lead to an increase in the response. During the reverse sweep, the response amplitude decreases until a jump down to zero is observed at approximately $1.2\,g$. The response remains at zero as the forcing level is further decreased.

Second, we discuss the closed-loop response. As the forcing level is increased, the beam remains motionless until the forcing amplitude reaches $1.5\,g$. Subsequently, the response

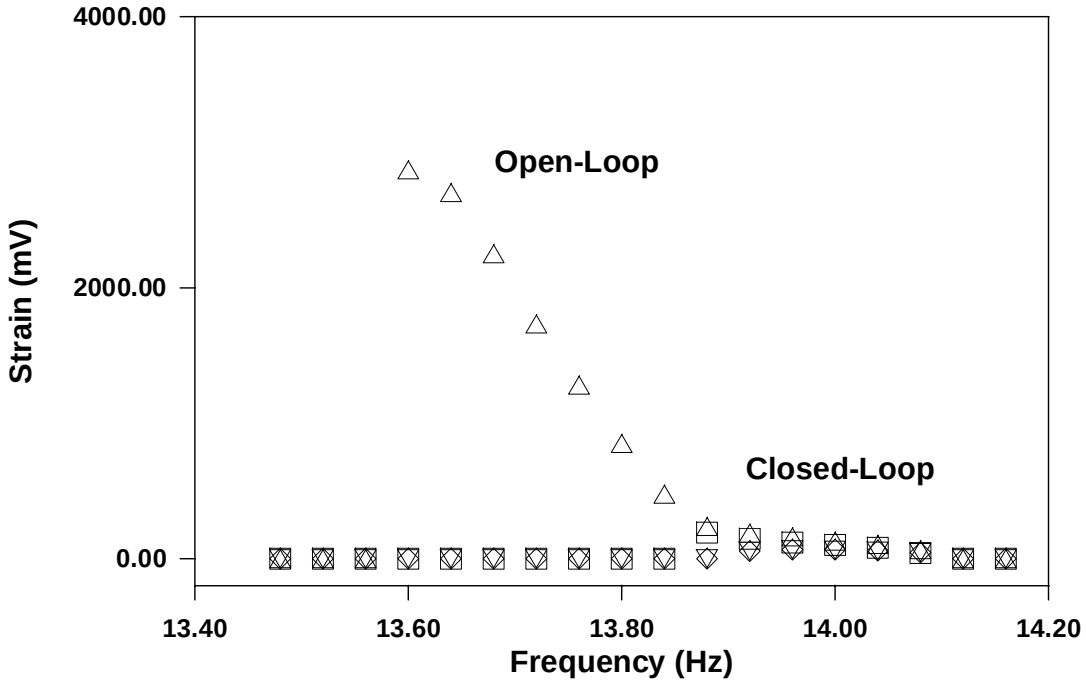

Figure 7-9. Experimental open- and closed-loop frequency-response curves. Open-loop: □ forward sweep, △ reverse sweep, closed-loop: ▽ forward sweep, and ◊ reverse sweep.

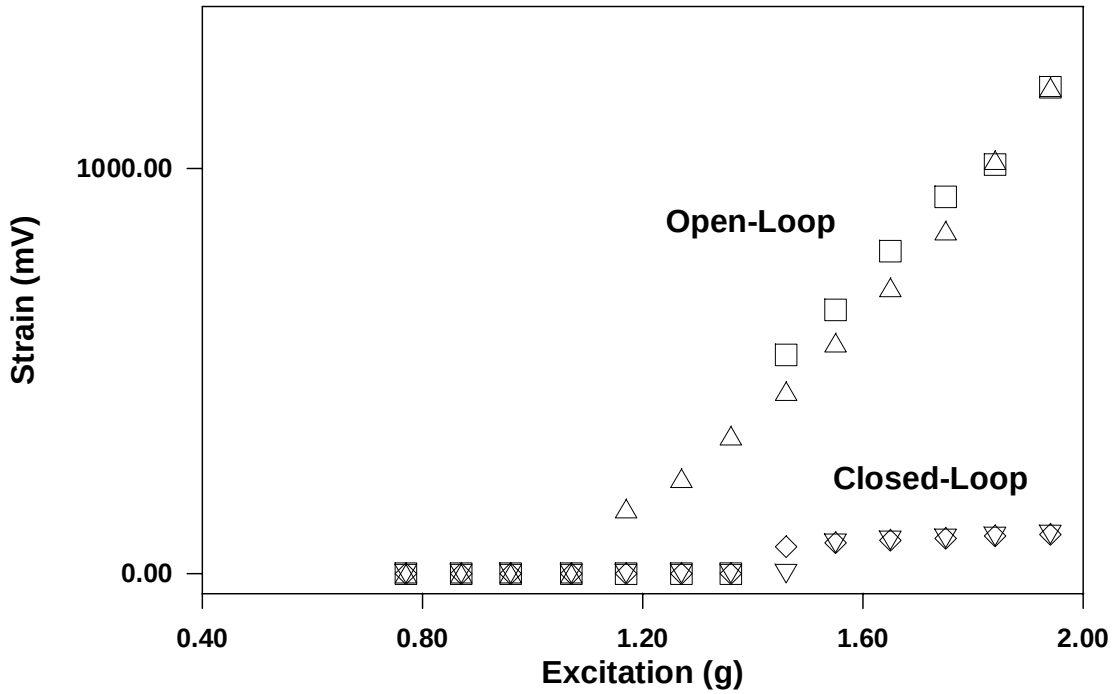

Figure 7-10. Experimental open- and closed-loop force-response curves. Open-loop: □ forward sweep, △ reverse sweep, closed-loop: ▽ forward sweep, and ◊ reverse sweep.

amplitude gradually increases, but the amplitude is significantly smaller than in the open-loop case. In the reverse sweep, the amplitude of the response traces identically the response observed in the forward sweep. However, a very small hysteresis area is observed around $1.5\,g$.

7.4.4 Effect of Varying the Feedback Gain

In Figures 7-11 to 7-13, we compare the response curves and time traces for two feedback gains that differ by an order of magnitude. The gain K shown in the figures is proportional to the gain G. The curves labeled "$K = 10$" in Figures 7-11 and 7-12 correspond to the ones labeled "Closed-Loop" in Figures 7-9 and 7-10, respectively. In both figures, increasing the gain results in a decrease in the response amplitudes. In the case of the force-response

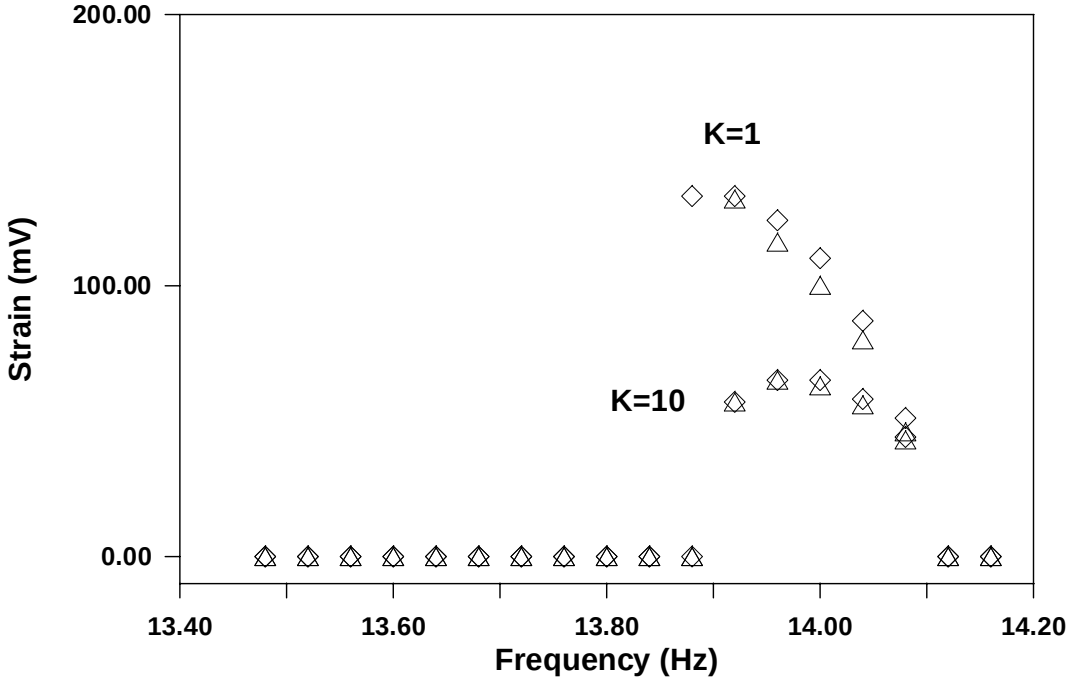

Figure 7-11. Effect of varying the feedback gain on the frequency-response curve. △ Forward sweep and ◊ reverse sweep.

curves, increasing the gain leads to a more noticeable reduction in the hysteretic region.

To examine the transient characteristics of the control law, we subject the beam to a forcing level of $1.2\,g$ at 13.8 Hz. Since the system is operating in the overhang region, the closed-loop response amplitude is expected to be zero. In Figure 7-13, we illustrate two time traces for $K = 1$ and $K = 10$. Clearly, increasing the feedback gain results in better transient performance.

7.5 Summary

In this chapter, we proposed a nonlinear control law to suppress the vibrations of a system subjected to a principal parametric excitation. We modeled the dynamics of the system

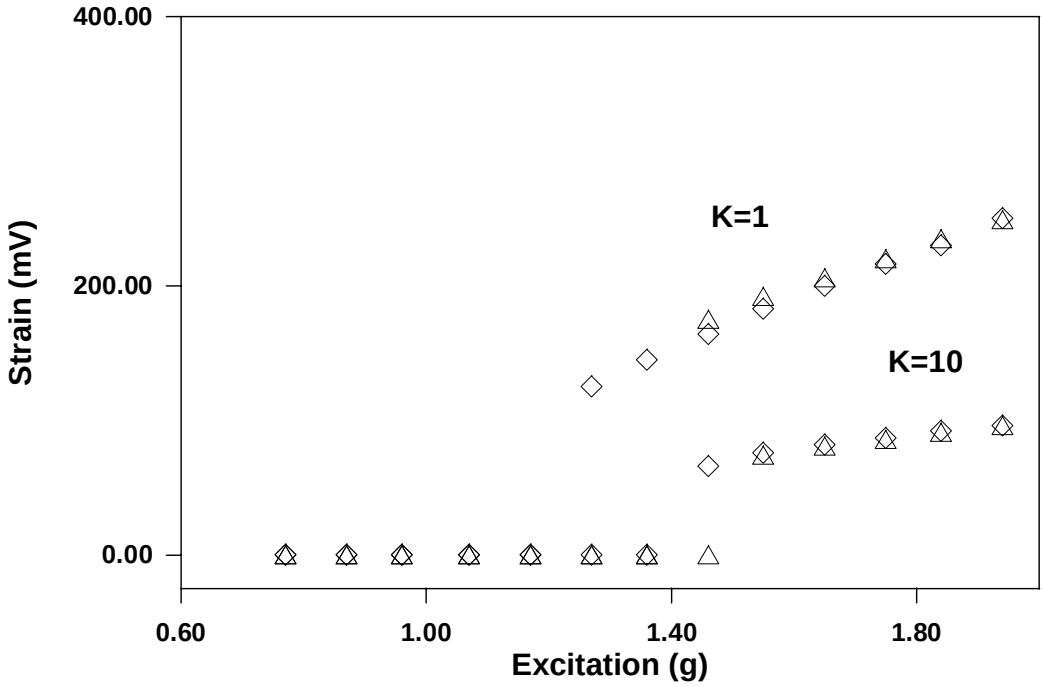

Figure 7-12. Effect of varying the feedback gain on the force-response curve. △ Forward sweep and ◊ reverse sweep.

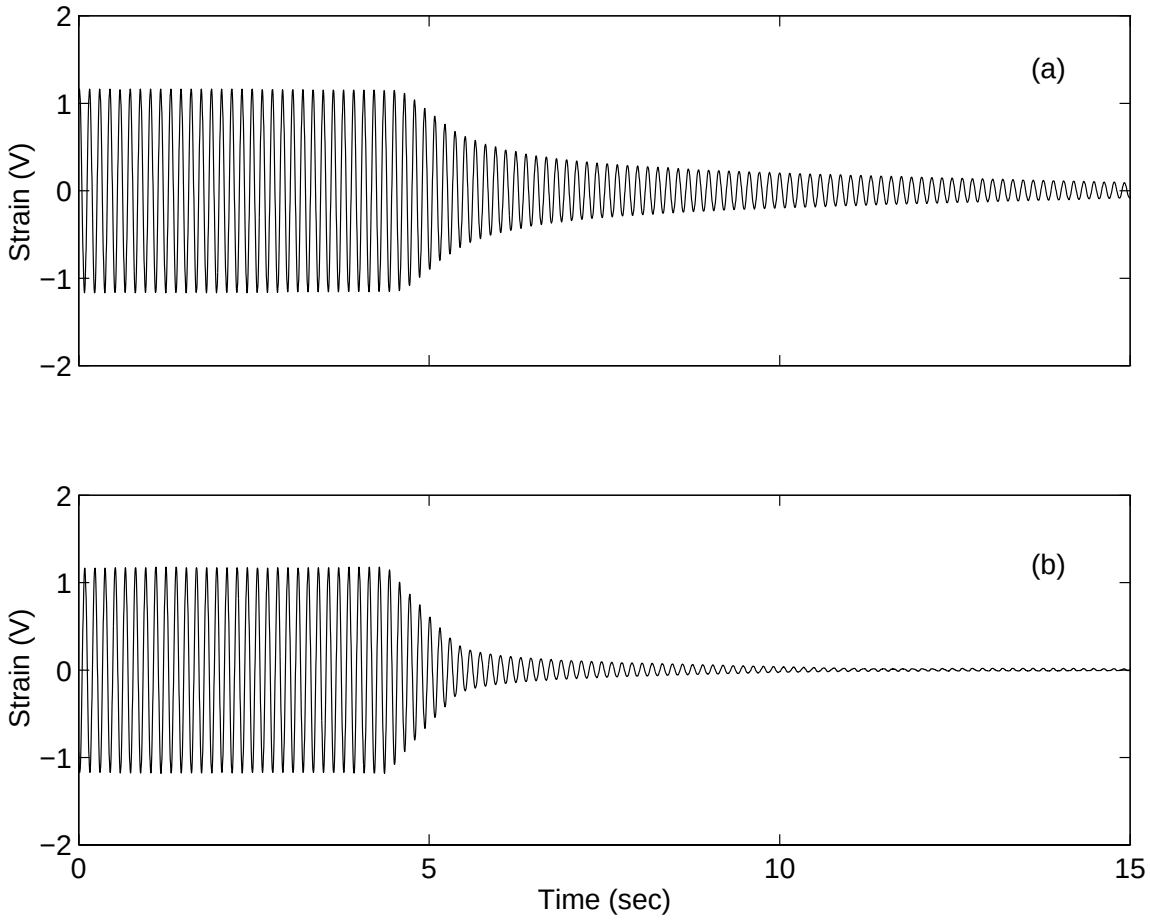

Figure 7-13. Transient time responses. (a) $K = 1$ and (b) $K = 10$.

with a second-order nonlinear ordinary-differential equation and introduced a control law based on cubic velocity feedback. Using the method of multiple scales, we derived two first-order differential equations governing the time evolution of the amplitude and phase of the response and conducted a bifurcation analysis to investigate the performance of the control law. Our analysis revealed that cubic velocity feedback reduces the amplitude of the response. Furthermore, it eliminates the saddle-node bifurcations in the frequency- and force-response curves.

To verify the theoretical analysis, we conducted experiments. We attached piezoceramic actuators to a cantilever steel beam and subjected it to a parametric excitation having a frequency equal to twice the natural frequency of its first mode. We utilized a computer and a series of analog filters to generate the cubic velocity feedback signal. The experimental frequency- and force-response curves are in excellent qualitative agreement with our theoretical results.

Chapter 8

Concluding Remarks

8.1 Summary

We consider suppression of high-amplitude vibrations of single- and multi-degree-of-freedom structures when subjected to either primary external or principal parametric excitations. We develop and investigate application of three active nonlinear control laws: a quadratic absorber, a cubic absorber, and a nonlinear velocity feedback strategy. By resorting to perturbation techniques, namely, the method of multiple scales or averaging, we obtain approximate solutions to the equations governing the response of the closed-loop systems. Then, using modern tools of nonlinear dynamics, we analyze the performance of the control laws. Moreover, we design mechatronic systems of sensors, actuators, and electronic devices, carry out experiments, and report results that substantiate our theoretical studies.

8.1.1 Quadratic Absorber

We develop an active absorber that exploits the saturation phenomenon first identified in ship dynamics. The control strategy is implemented by artificially introducing a second-order system (i.e., absorber) and coupling it to the plant through a sensor and an actuator, where

the user-defined coupling terms are quadratic. Once the structure is forced at resonance, the quadratic terms create an energy transfer mechanism that limits the response of the plant.

We show analytically that, by setting the frequency of the absorber equal to one-half the excitation frequency and properly adjusting the feedback gains, the plant resonant response can be virtually eliminated. Additionally, we conduct stability analyses and investigate the transient and steady-state response of the closed-loop system.

As a proof of concept, we design and build an analog circuit that emulates the absorber and use a variety of sensors and actuators to implement the active control strategy.

First, we use a motor and a potentiometer to control the vibration of a rigid beam. We develop a plant model that includes Coulomb friction and demonstrate theoretically and experimentally that the closed-loop system exhibits the saturation phenomenon.

Second, we extend the strategy to multi-degree-of-freedom systems. We use PZT ceramics and strain gages to suppress the vibrations of flexible steel beams when subjected to single- and simultaneous two-mode excitations. In the case of the two-mode excitation, we use two circuits. Furthermore, we investigate the effect of varying the absorber gains on the response of the closed-loop system. Our experimental results agree well with the theoretical analysis.

Third, we employ a nonlinear actuator. We use Terfenol-D and accelerometers to control the vibrations of flexible beams. We consider the cases of ideal and nonideal excitations. In the first case, the structure is excited with a shaker through a stinger. In the second case, we remove the shaker and mount a motor with a rotating imbalance on the beam. In both instances, the technique is successful in reducing significantly the response amplitudes of the structures.

Lastly, we compare theoretically and experimentally the performance of the quadratic absorber with that of a linear tuned absorber. We show analytically the existence of a forcing value above which the stroke of the linear absorber is greater than the stroke of the quadratic one. Additionally, our results indicate that the "square" control signal of the nonlinear technique introduces a DC component that leads to higher power requirements.

To verify the theoretical results, we fit a cantilever beam with PZT actuators, use a signal processing board, and implement both techniques digitally. We develop an automatic tuning algorithm and show that, when each the absorber's frequency is adjusted properly, they both possess a wide suppression bandwidth. Furthermore, our experimental tests reveal that the nonlinear absorber's power requirement can be reduced by eliminating the DC component in its corresponding control signal.

Motivated by the successful implementation of the quadratic absorber in the case of external excitation, we explore application of the strategy in the case of parametric excitation. We analyze a model of the closed-loop system and show that it exhibits trivial, single- and two-mode periodic motions, a saturation phenomenon, periodically and chaotically modulated motions, and type I and II intermittency. Then, we validate the theoretical results experimentally. We use a beam fitted with piezoceramic actuators and a strain gage, use a second-order analog circuit to represent the absorber, and subject the beam to a parametric excitation whose frequency is approximately twice the natural frequency of its first mode. Our experimental results are in good agreement with the theoretical findings.

8.1.2 Cubic Absorber

Guided by the topology of the equations governing the dynamics of the quadratic absorber, we identify a set of cubic nonlinearities that also induce a saturation phenomenon. We consider for analysis a plant model that includes curvature and inertia nonlinearities, introduce a cubic absorber, and obtain an approximate solution to the nonlinear differential equations. We conduct bifurcation analyses and show that, when the frequency of the absorber is almost equal to the frequency of the plant, there exists a two-valued saturation phenomenon. However, our analysis reveals that the absorber creates regimes of high-amplitude or chaotic responses, thereby limiting its utility.

8.1.3 Cubic Velocity Feedback

To remedy the failure of the quadratic absorber in controlling parametric resonances, we propose a nonlinear control law based on cubic velocity feedback. We revisit the task of suppressing the vibrations of a cantilever beam and model the dynamics of its first flexural mode by a second-order nonlinear ordinary-differential equation that accounts for inertia and curvature cubic nonlinearities and quadratic air damping. We obtain an approximate solution to the governing equation and study the stability of the closed-loop system.

The analysis reveals that cubic velocity feedback reduces the amplitude of the response. Furthermore, it leads to the elimination of the saddle-node bifurcations in the frequency- and force-response curves. Moreover, we show that increasing the velocity feedback gain results in better transient performance.

We verify the theoretical analysis experimentally. We fit a cantilever steel beam with piezoceramic actuators and subject it to a parametric excitation having a frequency equal to twice the natural frequency of its first mode. We apply the strategy using a computer and a series of analog filters. Our experimental frequency- and force-response curves are in excellent qualitative agreement with the theoretical results.

8.2 Future Work

We believe that the work presented in this Dissertation can be expanded and enhanced by undertaking the following tasks:

- During our evaluation of the quadratic absorber, the absorber's initial velocity is set equal to zero. The theory should be extended to derive expressions that, given the plant's position and velocity, evaluate the absorber's both initial states.
- Analytical and possibly experimental studies should be conducted to investigate the performance of the quadratic and cubic absorbers when the plant is nonlinearly coupled with a third mode through an internal resonance. The coupling may be quadratic and/or cubic.

- Our experimental tests show that, when the actuator is saturated, there exists a forcing level below which the performance of the quadratic absorber is nonetheless maintained. Therefore, theoretical studies should be performed to identify the threshold forcing level above which the strategy is rendered ineffective.
- Our studies focus on controlling plants that are somewhat linear. The superiority of the quadratic absorber can be emphasized if it is shown to be effective in controlling highly cubic systems, such as fixed-fixed beams or plates.
- The convergence of the frequency detection algorithm is slow. Furthermore, the noise introduced by the analog-to-digital converters renders the algorithm unusable when the amplitude of the sampled signal is small (i.e., small signal-to-noise ratio). An investigation into the development and implementation of a faster and robust tuning method, such as phased-locked loop, should be undertaken. If such a method is proven successful, it can be used in conjunction with more advanced digital hardware to control the response of plants possessing very high frequencies.
- Although we show that the cubic absorber possess a limited application range, experimental studies should be conducted to verify the theoretical results.

Bibliography

[1] A. H. Nayfeh, *Introduction to Perturbation Techniques*. Wiley, New York, 1981.

[2] N. Minorsky, *Nonlinear Oscillations*. Van Nostrand, Princeton, N.J., 1962.

[3] A. H. Nayfeh and D. T. Mook, *Nonlinear Oscillations*. Wiley, New York, 1979.

[4] M. Faraday, "On a peculiar class of acoustical figures and on certain forms assumed by a group of particles upon vibrating elastic surfaces," *Philosophical Transactions of the Royal Society of London*, vol. 121, pp. 299–318, 1831.

[5] E. Mathieu, "Mémoire sur le mouvement vibratoire d'une membrane de forme elliptique," *Journal de Mathématiques Pures et Appliquées*, vol. 13, pp. 137–203, 1868.

[6] L. D. Zavodney, A. H. Nayfeh, and N. E. Sanchez, "The response of a single-degree-of-freedom system with quadratic and cubic non-linearities to a principal parametric resonance," *Journal of Sound and Vibration*, vol. 129, pp. 417–442, 1989.

[7] L. D. Zavodney and A. H. Nayfeh, "The non-linear response of a slender beam carrying a lumped mass to a principal parametric excitation: Theory and experiment," *International Journal of Non-Linear Mechanics*, vol. 24, pp. 105–125, 1989.

[8] T. J. Anderson, A. H. Nayfeh, and B. Balachandran, "Experimental verification of the importance of the nonlinear curvature in the response of a cantilever beam," *Journal of Vibration and Acoustics*, vol. 118, pp. 21–27, 1996.

[9] H. Yabuno, Y. Ide, and N. Aoshima, "Nonlinear analysis of a parametrically excited cantilever beam," *JSME International Journal*, vol. 41, Series C, pp. 555–562, 1998.

[10] A. H. Nayfeh and D. T. Mook, "Energy transfer from high-frequency to low-frequency modes in structures," *Journal of Mechanical Design and Journal of Vibration and Acoustics, 50th Anniversary Design Engineering Division Issue*, vol. 117, pp. 186–195, 1995.

[11] H. N. Arafat, A. H. Nayfeh, and C. M. Chin, "Nonlinear nonplanar dynamics of parametrically excited cantilever beams," *Nonlinear Dynamics*, vol. 15, pp. 31–61, 1998.

[12] T. J. Anderson, A. H. Nayfeh, and B. Balachandran, "Coupling between high-frequency modes and a low-frequency mode: Theory and experiment," *Nonlinear Dynamics*, vol. 11, pp. 17–36, 1996.

[13] S. A. Nayfeh and A. H. Nayfeh, "Nonlinear interactions between widely spaced modes - External excitation," *International Journal of Bifurcation and Chaos*, vol. 3, pp. 417–427, 1993.

[14] S. A. Nayfeh and A. H. Nayfeh, "Energy transfer from high- to low-frequency modes in a flexible structure via modulation," *Journal of Vibration and Acoustics*, vol. 116, pp. 203–207, 1994.

[15] A. H. Nayfeh and C. M. Chin, "Nonlinear interactions in a parametrically excited system with widely spaced frequencies," *Nonlinear Dynamics*, vol. 7, pp. 195–216, 1995.

[16] P. R. Sethna, "Vibrations of dynamical systems with quadratic nonlinearities," *Journal of Applied Mechanics*, vol. 32, pp. 576–582, 1965.

[17] A. H. Nayfeh, D. T. Mook, and L. R. Marshall, "Nonlinear coupling of pitch and roll modes in ship motion," *Journal of Hydronautics*, vol. 7, pp. 145–152, 1973.

[18] A. G. Haddow, A. D. S. Barr, and D. T. Mook, "Theoretical and experimental study of modal interaction in a two degree-of-freedom structure," *Journal of Sound and Vibration*, vol. 97, pp. 451–473, 1984.

[19] A. H. Nayfeh and L. D. Zavodney, "Experimental observation of amplitude- and phase-modulated responses of two internally coupled oscillators to a harmonic excitation," *Journal of Applied Mechanics*, vol. 55, pp. 706–710, 1988.

[20] B. Balachandran and A. H. Nayfeh, "Observations of modal interactions in resonantly forced beam-mass structures," *Nonlinear Dynamics*, vol. 2, pp. 77–117, 1991.

[21] J. Q. Sun, M. R. Jolly, and M. A. Norris, "Passive, adaptive and active tuned vibration absorbers — A survey," *Journal of Mechanical Design and Journal of Vibration and Acoustics, 50th Anniversary Design Engineering Division Issue*, vol. 117, pp. 234–242, 1995.

[22] H. Frahm, "Device for damping vibrations of bodies." US Patent No. 989958, 1909.

[23] J. P. Den Hartog, *Mechanical Vibrations*. McGraw-Hill, New York, 1934.

[24] R. E. Roberson, "Synthesis of a nonlinear dynamic vibration absorber," *Journal of the Franklin Institute*, vol. 254, pp. 205–220, 1952.

[25] F. R. Arnold, "Steady-state behavior of systems provided with nonlinear dynamic vibration absorbers," *Journal of Applied Mechanics*, vol. 22, pp. 487–492, 1955.

[26] J. B. Hunt and J. C. Nissen, "The broadband dynamic absorber," *Journal of Sound and Vibration*, vol. 83, pp. 573–578, 1982. Letter to the editor.

[27] S. E. Semercigil, D. Lammers, and Z. Ying, "A new tuned vibration absorber for wide-band excitations," *Journal of Sound and Vibration*, vol. 156, pp. 445–459, 1992.

[28] L. E. Galhoud, S. F. Masri, and J. C. Anderson, "Transfer function of a class of nonlinear multidegree of freedom oscillators," *Journal of Applied Mechanics*, vol. 54, pp. 215–225, 1987.

[29] D. H. Gonsalves, R. D. Neilson, and A. D. S. Barr, "The dynamics and design of a non-linear vibration absorber," *Journal of Mechanical Engineering Science*, vol. 207, pp. 363–374, 1993.

[30] H. Luo and S. Hanagud, "On the dynamics of vibration absorbers with motion-limiting stops," *Journal of Applied Mechanics*, vol. 65, pp. 223–233, 1998.

[31] S. Natsiavas, "Steady state oscillations and stability of non-linear dynamic vibration absorbers," *Journal of Sound and Vibration*, vol. 156, pp. 227–245, 1992.

[32] N. Olgac and B. T. Holm-Hansen, "A novel active vibration absorption technique: Delayed resonator," *Journal of Sound and Vibration*, vol. 176, pp. 93–104, 1994.

[33] N. Olgac, H. Elmali, and S. Vijayan, "Introduction to the dual frequency fixed delayed resonator," *Journal of Sound and Vibration*, vol. 189, pp. 355–367, 1996.

[34] J. L. Fanson and T. K. Caughey, "Positive position feedback control for large space structures," *AIAA Journal*, vol. 28, pp. 717–724, 1990.

[35] N. W. Hagood and A. von Flotow, "Damping of structural vibrations with piezoelectric materials and passive electrical networks," *Journal of Sound and Vibration*, vol. 146, pp. 243–268, 1991.

[36] J. J. Dosch, D. J. Inman, and E. Garcia, "A self-sensing piezoelectric actuator for collocated control," *Journal of Intelligent Material Systems and Structures*, vol. 3, pp. 166–185, 1992.

[37] J. J. Hollkamp and T. F. Starchville, Jr., "A self-tuning piezoelectric vibration absorber," *Journal of Intelligent Material Systems and Structures*, vol. 5, pp. 559–566, 1994.

[38] G. S. Agnes, *Performance of Nonlinear Mechanical, Resonant-Shunted Piezoelectric, and Electronic Vibration Absorbers for Multi-Degree-of-Freedom Structures*. PhD thesis, Virginia Tech, Department of Engineering Science and Mechanics, 1997.

[39] M. W. Hiller, M. D. Bryant, and J. Umegaki, "Attentuation and transformation of vibration through active control of magnetostrictive terfenol," *Journal of Sound and Vibration*, vol. 134, pp. 507–519, 1989.

[40] A. B. Flatau, D. L. Hall, and J. M. Schlesselman, "Magnetostrictive active vibration control systems (A preliminary investigation)," in *Recent Advances in Adaptive and Sensory Materials and their Applications* (C. A. Rogers and R. C. Rogers, eds.), pp. 419–429, TECHNOMIC, Lancaster, PA, 1992.

[41] J. R. Pratt and A. H. Nayfeh, "Experimental system identification and active vibration control of a smart machine tool." *Eleventh VPI&SU Symposium on Structural Dynamics and Control*, Blacksburg, VA, 1997.

[42] R. S. Haxton and A. D. S. Barr, "The autoparametric vibration absorber," *Journal of Engineering for Industry*, vol. 94, pp. 119–225, 1972.

[43] H. Hatwal, A. K. Mallik, and A. Ghosh, "Non-linear vibrations of a harmonically excited autoparametric system," *Journal of Sound and Vibration*, vol. 81, pp. 153–164, 1982.

[44] H. Hatwal, A. K. Mallik, and A. Ghosh, "Forced nonlinear oscillations of an autoparametric system — Part 1: Periodic responses," *Journal of Applied Mechanics*, vol. 50, pp. 657–662, 1983.

[45] A. K. Bajaj, S. I. Chang, and J. M. Johnson, "Amplitude modulated dynamics of a resonantly excited autoparamtric two dgree-of-freedom system," *Nonlinear Dynamics*, vol. 5, pp. 433–457, 1994.

[46] B. Banerjee, A. K. Bajaj, and P. Davies, "Second order averaging study of an autoparamtric system," in *Nonlinear Vibrations DE-Vol. 54* (R. A. Ibrahim, A. K. Bajaj, and L. A. Bergman, eds.), pp. 127–138, ASME, 1993.

[47] M. Cartmell and J. Lawson, "Performance enhancement of an autoparametric vibration absorber by means of computer control," *Journal of Sound and Vibration*, vol. 177, pp. 173–195, 1994.

[48] O. Cuvalci and A. Ertas, "Pendulum as vibration absorber for flexible structures: Experiments and theory," *Journal of Vibration and Acoustics*, vol. 118, pp. 558–566, 1996.

[49] A. Khajepour and M. F. Golnaraghi, "Experimental control of flexible structures using nonlinear modal coupling: Forced and free vibrations," *Journal of Intelligent Material Systems and Structures*, vol. 8, pp. 697–710, 1997.

[50] K. R. Asfar and K. K. Masoud, "Damping of parametrically excited single-degree-of-freedom systems," *International Journal of Non-Linear Mechanics*, vol. 29, pp. 421–428, 1994.

[51] G. Mustafa and A. Ertas, "Experimental evidence of quasiperiodicity and its breakdown in the column-pendulum oscillator," *Journal of Dynamic Systems, Measurement and Control*, vol. 117, pp. 218–225, 1995.

[52] J. J. Thomsen, "Vibration suppression by using self-arranging mass: Effects of adding restoring force," *Journal of Sound and Vibration*, vol. 197, pp. 403–425, 1996.

[53] H. Yabuno, "Bifurcation control of parametrically excited duffing system by a combined linear-plus-nonlinear feedback control," *Nonlinear Dynamics*, vol. 12, pp. 263–274, 1997.

[54] A. H. Nayfeh, *Perturbation Methods*. Wiley, New York, 1973.

[55] A. H. Nayfeh, "Application of the method of multiple scales to nonlinearly coupled oscillators," in *Lasers, Molecules, and Methods, Advances in Chemical Physics Volume LXXIII* (J. O. Hirschfelder, R. E. Wyatt, and R. D. Coalson, eds.), ch. 3, pp. 137–196, Wiley, New York, 1989.

[56] A. H. Nayfeh, *Nonlinear Interactions*. Wiley, New York, 1999, in press.

[57] L. Meirovitch, *Analytical Methods in Vibrations*. Macmillan, New York, 1967.

[58] G. P. Carman and M. Mitrovic, "Nonlinear constitutive relations for magnetostrictive materials with applications to 1-D problems," *Journal of Intelligent Material Systems and Structures*, vol. 6, pp. 673–683, 1995.

[59] P. F. Pai, B. Wen, A. S. Naser, and M. J. Schultz, "Structural vibration control using PZT patches and non-linear phenomena," *Journal of Sound and Vibration*, vol. 215, pp. 273–296, 1998.

[60] R. W. Hornbeck, *Numerical Methods*. Prentice-Hall, Englewood Cliffs, N.J., 1975.

[61] K. G. McConnell, *Vibration Testing*. Wiley, New York, 1995.

[62] A. H. Nayfeh and B. Balachandran, *Applied Nonlinear Dynamics*. Wiley, New York, 1995.

[63] R. Seydel, *Practical Bifurcation and Stability Analysis: From Equilibrium to Chaos*. Springer-Verlag, New York, 1994.

[64] A. H. Nayfeh, "Parametric excitation of two internally resonant oscillators," *Journal of Sound and Vibration*, vol. 119, pp. 95–109, 1987.

[65] C. Chin, A. H. Nayfeh, and W. Lacarbonara, "Two-to-one internal resonances in parametrically excited buckled beam," 1997. AIAA Paper No. 97–1081.

Appendix A

Experimental Equipment and Beam Properties

Table A-1. Components for the motor experiment.

Item	Manufacturer	Model Number
Motor	Litton - Clifton Precision	JDH–2250–BX–1C
Servo-amplifier	Advanced Motions Control	25A8
Power supply	Pertec Peripheral Corp.	PSX01
Potentiometer	Bourns	3438S–1–102
Filters	Krohn-Hite Corp.	3905

Table A-2. Components for the Terfenol-D experiment.

Item	Manufacturer	Model Number
Actuator	ETREMA Products Inc.	OTY77
Amplifier	MB Dynamics	SS250
Shaker	MB Dynamics	Modal 50A Exciter
Accelerometer	PCB	308B02
Filters	Krohn-Hite Corp.	3905

Table A-3. Components for the PZT experiments.

Item	Manufacturer	Model Number
Actuators	Piezo Systems, Inc.	PSI–5H–S4–ENH
Piezoamplifier	Piezo Systems, Inc.	EPA–102
Shaker	MB Dynamics	PM100
Amplifier	MB Dynamics	SS250
Strain gage	Measurements Group	WK–06–062AP–350
Conditioner	Measurements Group	2310
Filters	Krohn-Hite Corp.	3905

Table A-4. Properties of the beams.

Property	I	II	III	IV	V
Length (m)	0.21	0.41	0.21	0.21	0.26
Thickness ($10^{-4}m$)	5.1	8.89	5.1	5.1	6.0
	All beams				
Width ($10^{-2}m$)	1.27				
Density (kg/m^3)	7800				
Elastic modulus (GPa)	208				

Table A-5. Properties of the PZT actuators.

Property	I	II	III	IV	V
Length ($10^{-2}m$)	2.7	3.0	3.0	3.0	3.0
Width ($10^{-2}m$)	1.07	1.27	1.27	1.27	1.27
	All actuators				
Thickness (m)	1.91×10^{-4}				
Elastic modulus (GPa)	6.20				
Strain Coefficient (m/V)	-190×10^{-12}				

VITA

Shafic Sami Oueini was born on October 15, 1968 in Beirut, Lebanon. In 1986, he moved to Ontario, Canada. One year later, he enrolled in the Department of Mechanical Engineering at the University of Waterloo, where he obtained his Bachelor's degree in 1992 and his Master's degree in 1994. Subsequently, he joined the Department of Engineering Science and Mechanics at Virginia Tech, where he completed his doctoral studies in April of 1999.